

NUMERICAL EXPERIMENTS ON THE SENSITIVITY
OF AN ATMOSPHERIC HYDROLOGIC CYCLE
TO THE EQUILIBRIUM TEMPERATURE

by

JOHN OWEN ROADS

B.A., University of Colorado
(1972)

SUBMITTED IN PARTIAL FULFILLMENT OF THE
REQUIREMENTS FOR THE DEGREE OF
DOCTOR OF PHILOSOPHY

at the

MASSACHUSETTS INSTITUTE OF TECHNOLOGY

January, 1977

Signature of Author.....
Department of Meteorology, January 1977

Certified by.....
Thesis Supervisor

Accepted by.....
Chairman, Departmental Committee on Graduate Students

WITHDRAWN
FROM
MIT LIBRARIES
LIBRARIES
JAN 6 1977
Lindgren

To my wife

Anastasia

NUMERICAL EXPERIMENTS ON THE SENSITIVITY
OF AN ATMOSPHERIC HYDROLOGIC CYCLE
TO THE EQUILIBRIUM TEMPERATURE

by

JOHN OWEN ROADS

Submitted to the Department of Meteorology on January 12, 1977 in partial fulfillment of the requirements for the degree of Doctor of Philosophy.

ABSTRACT

Numerical solutions to the time-dependent primitive equations and equations for water vapor and cloud water are obtained on a self-contained, differentially-heated, ocean-covered, mid-latitude, two-level, periodic f plane. Circulations are calculated in domains of small and large latitudinal extent with low and high-resolution grids for climates with both high and low radiative-convective equilibrium temperatures and for climates with a small and large absolute meridional temperature gradient (AMTG). Estimates of standard deviations of time-averaged results are calculated in order to determine statistical significance.

Qualitatively, for our model, we find that the circulation of either a cold climate or a climate with a relatively small AMTG is weak and cloudy. A warm climate or a climate with a relatively large AMTG is vigorous, with clearer skies and darker storms.

Because of the Clausius-Clapeyron relationship, components of the water cycle, such as evaporation, water transport, and condensation, increase with increasing temperature. Water vapor increases everywhere while cloud water increases only in cloudy regions. Similar effects were obtained for an increasing AMTG.

Conversely, fractional areal coverage of positive-condensation regions, fractional areal coverage of total cloud cover, and average relative humidity decrease with increasing temperature and AMTG. These results are analyzed by means of a simple wave model. Although clouds, condensation, and relative humidity increase with increasing surface winds and increasing radiative and sensible cooling, they decrease, in regions of subsidence with an increasing subsidence rate, an increasing static stability, an increasing temperature, and a decreasing boundary-layer temperature differential. Also, the areally-averaged relative humidity decreases with decreasing fractional coverage because of an increase in the dry area.

The horizontal advection of dry and moist air has an important influence on cloudiness and relative humidity in our model. For increasing advectons, the relative humidity increased and the fractional cloud cover decreased. And, although the ratio of the horizontal advection to the change due to vertical motion decreased with increasing temperature and AMTG, the greater decrease in the relative humidity in dry regions may have resulted in an increase in the transport of dry air into regions which might otherwise produce cloud, by rising motion and other processes.

The zonal winds increase with increasing temperature and AMTG. The temperature effect is related, in part, to the relative increase of condensation in the southern part of the domain and a concomitant increase in the AMTG. Other dynamical components are similarly affected.

Thesis Supervisor: Edward N. Lorenz, Professor of Meteorology

ACKNOWLEDGEMENTS

Without the profound and inspirational guidance from my advisor, Professor Edward N. Lorenz, this thesis would not have been done. I especially thank him for the support and help that he gave me when I needed it the most. I thank Professor Ronald G. Prinn for suggesting the thesis, for his constant support of the study, and for his help. I thank Professor Eugenia Kalnay-Rivas for teaching me some of her numerical methodology and for her help. I thank Dr. Edward S. Sarachik for his profound questions, discussions, and help. I thank Dr. Jagadish Shukla for his many critical discussions and help. I thank Diana Spiegel and Dr. Fred Alyea for much computing help. I thank Anne Edeleanu, my friends, and my teachers for their help. I thank Marshall Potter and Isabelle Kole for their magnificent work. I thank my parents, my brother and sisters, Anne's parents, brother and sister, and all others who gave me their support, encouragement, and prayers. Most of all, I thank my wife Anastasia for the unselfish support, encouragement, and help that she has always given me. In addition to her full-time job and household management, she typed the preliminary drafts of this thesis. I thank the Goddard Institute for Space Studies for providing me with my computer time. My financial support at MIT has come in part from an NSF graduate fellowship, in part from NSF grant DES-74-14116, in part from NASA grant NSG-2010, and in part from NSF grant NSF-g 74-03969ATM.

TABLE OF CONTENTS

ABSTRACT	2
DEDICATION	4
ACKNOWLEDGEMENTS	5
TABLE OF CONTENTS	6
LIST OF FIGURES AND TABLES	8
1. Introduction	18
2. Numerical Model	41
2.1 Basic Equations	41
2.2 Heating and Friction Parameterizations	43
2.2.1 Heating	43
2.2.2 Friction	45
2.2.3 Summary	46
2.3 Horizontal Boundary Conditions	48
2.4 Finite Differences	51
3. Water Model	61
3.1 Atmospheric Water	61
3.2 Surface Fluxes	63
3.3 Condensation	65
3.4 Precipitation	69
3.5 Summary	76
4. Sensitivities of the Water Distribution	84
4.1 Relative-Humidity Equation	84
4.2 Principal Approximation to the Relative-Humidity Equation	92
4.2.1 Fractional Coverage	92
4.2.2 Relative Humidity	96
4.2.3 Precipitation	100
4.2.4 Cloud Formulae	101
4.3 Entrainment and Detrainment	103
4.3.1 Entrainment	103
4.3.2 Detrainment	114
4.3.3 Summary	116

5.	Description of Experiments	143
5.1	Time Series	143
5.2	Vertical-Velocity, Cloud-Water, and Relative-Humidity Fields	145
5.3	Statistics of Time Averages	147
6.	Sensitivities of the Numerical Model	170
6.1	Sensitivities of the Zonal Temperature and Zonal Winds	170
6.1.1	Evaporation	170
6.1.2	Average Temperature	171
6.1.3	Condensation	171
6.1.4	Absolute Meridional Temperature Gradient	172
6.1.5	Zonal Winds	173
6.1.6	Summary	175
6.2	Sensitivities of the Cloud and Relative-Humidity Fields	176
6.2.1	Cloud Water	176
6.2.2	Precipitation and Cloud Water Transports	177
6.2.3	Fractional Coverages and Relative Humidity	177
6.2.4	Vertical Velocities	178
6.2.5	Static Stabilities	179
6.2.6	Calculated Fractional Cloud Cover	180
6.2.7	Calculated Relative Humidity	182
6.2.8	Calculated Precipitation	183
6.2.9	Entrainment Parameter	184
6.2.10	Cloud Formulae	186
6.2.11	Summary	188
6.3	Sensitivity of Model Results to Various Parameteriza- tions and Model Scales	189
6.3.1	Domain Size	189
6.3.2	Horizontal Grid Resolution	190
6.3.3	Precipitation Function	190
6.3.4	Critical Relative Humidity	191
6.3.5	Newtonian Time Constant	192
6.3.6	Summary	192
7.	Summary and Conclusions	255
APPENDIX A	Symbols, Subscripts, and Operators	264
APPENDIX B	Parity Budget	273
APPENDIX C	Finite-Difference Budgets	276
REFERENCES	283
BIOGRAPHY	287

LIST OF FIGURES AND TABLES

Figure 1.1.	Linear relationships between fractional cloud cover and relative humidity obtained by Smagorinsky for high clouds - H,S; middle level clouds - M,S; and low clouds - L,S; and those derived for the NCAR model for high clouds - H,N; and for low clouds - L,N.	26
Figure 1.2.	Precipitation ($\text{g cm}^{-2} \text{ day}^{-1}$) for northern and southern hemisphere winter and summer. (After Schutz and Gates, 1974) Precipitation is greatest in midlatitudes during the winter.	27
Figure 1.3.	Evaporation ($\text{g cm}^{-2} \text{ day}^{-1}$) for northern and southern hemisphere winter and summer. (After Schutz and Gates, 1974) Evaporation is greatest in midlatitudes during the winter.	28
Figure 1.4.	Atmospheric vertically-averaged meridional transport of water vapor ($\text{m sec}^{-1} \text{ g kg}^{-1}$) for northern hemisphere winter and summer. (After Oort and Rasmusson, 1971) Absolute flux convergence is greatest during the winter in polar and middle latitudes.	29
Figure 1.5.	Time-and-longitude averaged relative humidity $ \overline{q/q^*} $ in northern summer (solid line) and winter (dashed line). (After Lorenz, 1967) Relative humidity is greatest in middle latitudes during the winter.	30
Figure 1.6a.	Total zonal cloud fractional coverage (space and time) (percent) for northern and southern hemisphere winter and summer. (After Landsburg, 1945) Cloudiness is greatest during the winter in midlatitudes.	31
Figure 1.6b.	Same as Figure 1.6a. (After Clapp, 1967)	32
Figure 1.6c.	Same as Figure 1.6a, but for northern hemisphere only.	33
Figure 1.7a.	Altostratus and Nimbostratus plus stratus zonal fractional cloud coverage for northern hemisphere winter and summer. (After London, 1957) Cloudiness is greatest during the winter in midlatitudes.	34

Figure 1.7b.	Cirrus zonal fractional cloud cover for northern hemisphere winter and summer. (After London, 1957) Cloud cover is greatest during the winter in mid-latitudes.	35
Figure 1.7c.	Cumulus plus cumulonimbus for northern hemisphere winter and summer. (After London, 1957) Cloudiness is greatest during the summer.	36
Figure 1.8a.	Polar stereographic satellite relative cloud cover, 1400 local, northern hemisphere, mean octas, June through August 1967-1970. (From Miller, 1971)	37
Figure 1.8b	Polar stereographic satellite relative cloud cover, 1400 local, northern hemisphere, mean octas, December through February 1967-1970. (From Miller, 1971)	38
Figure 1.8c.	Polar stereographic satellite relative cloud cover, 1400 local, southern hemisphere, mean octas, June through August 1967-1970. (From Miller, 1971)	39
Figure 1.8d.	Polar stereographic satellite relative cloud cover, 1400 local, southern hemisphere, mean octas, June through August 1967-1970. (From Miller, 1971)	40
Figure 2.1a.	A mid-latitude f plane channel with a vertical sigma coordinate.	55
Figure 2.1b.	The horizontal domain.	55
Figure 2.2a.	Typical equilibrium temperature structure for the model.	56
Figure 2.2b.	Surface temperature gradient.	57
Figure 2.2c.	Atmospheric and boundary-layer static stability. ...	57
Figure 2.3.	Relative damping of ∇^2 and $-\nabla^4$ operators versus grid-point wavelengths.	58
Figure 2.4.	The unbounded domain and associated symmetry.	59
Figure 2.5a.	Vertical differencing in the computational domain. ..	60
Figure 2.5b.	Horizontal differencing in the computational domain.	60
Figure 3.1.	Evaporation parameterization.	81
Figure 3.2.	Precipitation functions and precipitation time constant.	82

Figure 3.3.	The atmospheric hydrologic cycle.	83
Table 4.1a.	Magnitudes of parameters in the relative-humidity equation for the hot climate.	118
Table 4.1b.	Magnitudes of coefficients in the relative-humidity equation for the hot climate.	119
Figure 4.1.	An idealized condensation field and cloud water field at a particular time, t_0 , in the model domain.	120
Figure 4.2.	Interaction of the eddy vertical velocity with the mean field terms. Regions of clear sky occur where $\omega' > B$. Cloud regions occur when $\omega' < B$	121
Figure 4.3.	Fractional cloud cover, C , versus the factor B - which includes the evaporation, sensible and radiative heating and mean field transports, for various velocities, W	122
Figure 4.4a.	The decrease in q_a with temperature is plotted for various boundary-layer temperature differences, ΔT , and static stabilities, S	123
Figure 4.4b.	The decrease in q_b with temperature is plotted for various boundary-layer temperature difference, ΔT , and static stabilities, S	124
Figure 4.5a.	Fractional cloud cover, C , versus the zonal relative humidity for various ratios of a measure of the surface turbulent transport, to a measure of the free atmosphere water vapor transport and dynamical heating η	125
Figure 4.5b.	Fractional cloud cover, C , versus the inverse of the of the zonal average of the inverse relative humidity for various η	126
Figure 4.5c.	The relationship between the inverse of the zonally averaged inverse relative humidity and the zonally averaged relative humidity is different for the various η	127
Figure 4.6.	Ratio of the average precipitation versus fractional cloud cover, C	128
Figure 4.7.	Relation between the precipitation, relative humidity and surface turbulent transports as a function of cloud cover, C	129

Figure 4.8.	Relative humidity when entrainment is present. The dashed line is the solution of the relative humidity for no entrainment effects.	130
Figure 4.9a.	For $C=.05$ and $\eta=1.0$, H - as a function of θ - is shown for various ϵ . The dashed line is the scaled sigma velocity.	131
Figure 4.9b.	For $C=.4$ and $\eta=1$, H - as a function of θ - is shown for various ϵ . The dashed line is the scaled sigma velocity.	132
Figure 4.9c.	For $C=.4$ and $\eta=.125$, H - as a function of θ - is shown for various ϵ . The dashed line is the scaled sigma velocity.	133
Figure 4.9d.	For $C=.4$ and $\epsilon=.3$, H - as a function of θ - is shown or various η . The dashed line is the scaled sigma velocity.	134
Figure 4.9e.	The cloud cover, C_c - resulting from entrainment - is plotted as a function of the cloud cover which would result if no entrainment were present - for various entrainment rates, ϵ . $\eta=1$	135
Figure 4.9f.	The cloud cover resulting from entrainment is plotted as a function of the cloud cover - which would result if no entrainment were present - for various η . $\epsilon=1$	136
Figure 4.9g.	Equilibrium fractional cloud cover - as a function of zonally averaged relative humidity - for $\eta=1$ and various ϵ	137
Figure 4.9h.	Equilibrium fractional cloud cover - as a function of zonally averaged relative humidity - for $\epsilon=1$ and various η	138
Figure 4.9i.	Fractional cloud cover, C , as a function of the relative humidity for various η and ϵ	139
Figure 4.10a.	For $\delta=3 \times 10^4$, $\chi=2/3$, $\psi=.1$, $\eta=1$, q_{cc} - as a function of θ - is shown for various C and ϵ	140
Figure 4.10b.	The cloud cover, C_c - resulting from entrainment and detrainment - is plotted as a function of the cloud cover which would result if $\epsilon=0$ for various ϵ . $\delta=3 \times 10^4$, $\chi=2/3$, $\psi=.1$, and $\eta=1$	141

Figure 4.10c.	The cloud cover, C - resulting from entrainment and detrainment - is plotted as a function of the cloud cover which would result if $\epsilon=0$ for various η . $\epsilon=1$. 142
Table 5.1.	Basic sensitivity tests' parameterizations and model scales. 152
Figure 5.1a.	Equilibrium temperature (T_E) at the upper (1) and lower levels (2) as a function of y are shown for the hot (H), normal (N) and cold (C) climates. 153
Figure 5.1b.	Equilibrium temperatures as a function of y are shown for the climates with a large AMTG (9), normal AMTG (6), and a small AMTG (3). 154
Figure 5.2a	Model TPE as a function of time for the hot, normal and cold climates. Curves plotted from points 12.5 days apart. Dashed lines indicate the averaging period and the numbers refer to the experiment numbers. See Table 5.1. 155
Figure 5.2b.	Model TKE as a function of time for the hot, normal, and cold climates. 156
Figure 5.3a.	Model TPE as a function of time for the climates with a large, normal and small AMTG. 157
Model 5.3b.	Model TKE as a function of time for the climates with a large, normal and small AMTG. 158
Figure 5.4a.	Ψ_1 at day 447.5 for the hot climate (tape I.D. - 0335,1473/272267,272627/); 1 \Rightarrow $-25. \leq \Psi_1 < -22.5$, 2 \Rightarrow $-20 \leq \Psi_1 < -17.5$, ..., 9 \Rightarrow $17.5 \leq \Psi_1 < 20$ g sec^{-1} . Numbers 1-5 represent the cyclonic circulation whereas 6-9 represent the anti-cyclonic circulation. 159
Figure 5.4b.	Ψ_2 at day 447.5 for the hot climate. 160
Figure 5.4c.	$p_{s\dot{\sigma}}$ at day 447.5 for the hot climate (tape I.D. - 0335,1473/272267/). Minus signs denote upward motion, asterisks denote regions where the upward vertical sigma velocities exceed $-2\text{gcm}^{-1}\text{sec}^{-3}$, blank regions denote regions of subsidence. Unlike the upward motions, downward motions never exceeded $2\text{gcm}^{-1}\text{sec}^{-3}$.161
Figure 5.4d.	$\{q_c\}$ at day 447.5 for the hot climate, blank \Rightarrow 0. $< \{q_c\} < 5 \times 10^{-2}$, 1 \Rightarrow $5 \times 10^{-2} \leq \{q_c\} < 1.5 \times 10^{-2}$, ..., 9 \Rightarrow $8.5 \leq \{q_c\} < 9.5 \times 10^{-2}$, + \Rightarrow $9.5 \times 10^{-2} \leq \{q_c\} < 10 \times 10^{-2}$ 162

Figure 5.4e.	H at day 447.5 for the hot climate, blank => $0 < H < .05$, 1 => $.05 \leq H < .15$, ..., 9 => $.85 \leq H < .95$, + => $.95 \leq H$.	163
Figure 5.4f.	Ψ_1 at day 451.25 for the hot climate.	164
Figure 5.4g.	Ψ_2 at day 451.25 for the hot climate.	165
Figure 5.4h.	$p_s \dot{\sigma}$ at day 451.25 for the hot climate.	166
Figure 5.4i.	{ q_c } at day 451.25 for the hot climate.	167
Figure 5.4j.	H at day 451.25 for the hot climate.	168
Figure 5.5a.	Ψ_1 at day 447.5 for the cold climate (tape I.D. - 0845,6044/272267-272627/).	169
Figure 5.5b.	Ψ_2 at day 447.5 for the cold climate.	170
Figure 5.5c.	$p_s \dot{\sigma}$ at day 447.5 for the cold climate. (Tape I.D. - 6044,0845/272267/).	171
Figure 5.5d.	{ q_c } at day 447.5 for the cold climate.	172
Figure 5.5e.	H at day 447.5 for the cold climate.	173
Figure 5.6a.	Lag-time correlation for the upper level areally-averaged and meridionally-averaged temperatures for the normal climate. Solid lines are model values and dashed lines are estimated from $R(\tau)=e^{-\nu\tau}$.	174
Figure 5.6b.	Lag-time correlations for the areally-averaged and meridionally averaged lower-level temperatures for the normal climate. Solid lines are model values and dashed lines are estimated from $R(\tau)=e^{\nu\tau}$.	175
Figure 5.6c.	Lag-time correlations for the areally-averaged and meridionally averaged upper-level zonal momentum for the normal climate. Solid lines are model values and dashed lines are estimated from $R(\tau)=e^{\nu\tau}$.	176
Figure 6.1a.	Sensitivity of the positive evaporation to the equilibrium temperature.	200
Figure 6.1b.	Sensitivity of the positive evaporation to the equilibrium absolute meridional temperature gradient.	201
Figure 6.2a.	Sensitivity of dew deposition to equilibrium temperature.	202

Figure 6.2b.	Sensitivity of dew deposition to the equilibrium absolute meridional temperature gradient.	203
Figure 6.3a.	Sensitivity of the surface wind speed and zonal wind to the equilibrium temperature.	204
Figure 6.3b.	Sensitivity of the surface wind speed and zonal wind to the equilibrium absolute meridional temperature gradient.	205
Figure 6.4a.	Sensitivity of boundary-layer temperature difference ($T_g - T_2$) to the equilibrium temperature. Dashed line is at the T of the imposed equilibrium temperature.	206
Figure 6.4b.	Sensitivity of the boundary-layer temperature difference to the equilibrium absolute meridional temperature gradient. Dashed line is at the T of the imposed equilibrium temperatures.	207
Figure 6.5a.	Sensitivity of the integrated temperature to the equilibrium temperature. Dashed lines are the imposed equilibrium temperatures.	208
Figure 6.5b.	Sensitivity of the integrated temperature to the equilibrium absolute meridional temperature gradient. Dashed lines are the imposed equilibrium temperatures. .	209
Figure 6.6a.	Sensitivity of positive condensation to the equilibrium temperature.	210
Figure 6.6b.	Sensitivity of the positive condensation to the equilibrium absolute meridional temperature gradient. ...	211
Figure 6.7a.	Sensitivity of the cloud evaporation to the equilibrium temperature.	212
Figure 6.7b.	Sensitivity of the cloud evaporation to the equilibrium absolute meridional temperature gradient.	213
Figure 6.8a.	Sensitivity of the meridional transport of latent heat to the equilibrium temperature.	214
Figure 6.8b.	Sensitivity of the meridional transport of latent heat to the equilibrium absolute meridional temperature gradient.	215
Figure 6.9a.	Sensitivity of the total energy transport to the equilibrium temperature.	216
Figure 6.9b.	Sensitivity of the total energy transport to the equilibrium absolute meridional temperature gradient.	217
Figure 6.10a.	Sensitivity of the upper and lower-level zonal winds to the equilibrium temperature.	218

Figure 6.10b.	Sensitivity of the upper and lower-level zonal winds to the equilibrium absolute meridional temperature gradient.	219
Figure 6.11a.	Sensitivity of the transport of zonal momentum to the equilibrium temperature.	220
Figure 6.11b.	Sensitivity of the transport of zonal momentum to the equilibrium absolute meridional temperature gradient.	221
Figure 6.11c.	Sensitivity of the mean cell to the equilibrium temperature. Contours placed every 2×10^{12} gsec ⁻¹ . Numbers less than or equal to 0 represent a Ferrell cell.	222
Figure 6.11d.	Sensitivity of the mean cell to the equilibrium absolute meridional temperature gradient.	223
Figure 6.12a.	Sensitivity of the cloud water in positive condensation regions to the equilibrium temperature.	224
Figure 6.12b.	Sensitivity of average cloud water in positive condensation regions to the equilibrium absolute meridional temperature gradient.	225
Figure 6.13a.	Sensitivity of the average cloud water in the cloudy regions to the equilibrium temperature.	226
Figure 6.13b.	Sensitivity of the average cloud water in the cloudy regions to the equilibrium absolute meridional temperature gradient.	227
Figure 6.14a.	Sensitivity of the precipitation to the equilibrium temperature.	228
Figure 6.14b.	Sensitivity of the precipitation to the equilibrium absolute meridional temperature gradient.	229
Figure 6.15a.	Sensitivity of the precipitation to the equilibrium absolute meridional temperature gradient.	230
Figure 6.15b.	Sensitivity of the meridional transport of cloud water to the equilibrium absolute meridional temperature gradient.	231
Figure 6.16a.	Sensitivity of the fractional coverage of the positive-condensation regions to the equilibrium temperatures.	232
Figure 6.16b.	Sensitivity of the fractional coverage of the positive-condensation regions to the equilibrium absolute meridional temperature gradient.	233

Figure 6.17a.	Sensitivity of the total cloud fractional coverage to the equilibrium temperature.	234
Figure 6.17b.	Sensitivity of the total cloud fractional coverage to the equilibrium absolute meridional temperature gradient.	235
Figure 6.18a.	Sensitivity of the relative humidity to the equilibrium temperature.	236
Figure 6.18b.	Sensitivity of the relative humidity to the equilibrium absolute meridional temperature gradient.	237
Figure 6.19a.	Sensitivity of the eddy vertical velocity to the equilibrium temperature.	238
Figure 6.19b.	Sensitivity of the eddy vertical velocity to the equilibrium absolute meridional temperature gradient.	239
Figure 6.20a.	Sensitivity of the atmospheric static stability to the equilibrium temperature.	240
Figure 6.20b.	Sensitivity of the static stability to the equilibrium absolute meridional temperature gradient.	241
Figure 6.21a.	Sensitivity of the upper (1) and lower (2) level temperature to the equilibrium temperature.	242
Figure 6.21b.	Sensitivity of the upper and lower-level temperatures to the equilibrium absolute meridional temperature gradient.	243
Figure 6.22a.	Sensitivity of the convective condensation to the equilibrium temperature.	244
Figure 6.22b.	Sensitivity of the convective condensation to the equilibrium absolute meridional temperature gradient.	245
Figure 6.23a.	Sensitivity of $C = 1 - \frac{\cos^{-1}(B/W)}{\pi}$ to the equilibrium temperature.	246
Figure 6.23b.	Sensitivity of $C = 1 - \frac{\cos^{-1}(B/W)}{\pi}$ to the equilibrium absolute meridional temperature gradient.	247
Figure 6.24a.	Sensitivity to η to the equilibrium temperature. η is a measure of the ratio of the surface turbulent transport to the atmospheric transport and adiabatic heating.	248

Figure 6.24b.	Sensitivity of η to the equilibrium absolute meridional temperature gradient.	249
Figure 6.25a.	Sensitivity of $[H^{-1}]^{-1} = [1 + \frac{1}{\eta}(\frac{\sin\pi C}{\pi} + (1-C)\cos\pi C)]^{-1}$ to the equilibrium temperature.	250
Figure 6.25b.	Sensitivity of $[H^{-1}]^{-1} = [1 + \frac{1}{\eta}(\frac{\sin\pi C}{\pi} + (1-C)\cos\pi C)]^{-1}$ to the equilibrium absolute meridional temperature gradient.	251
Figure 6.26a.	Sensitivity of the calculated precipitation rate to the equilibrium temperature.	252
Figure 6.26b.	Sensitivity of the calculated precipitation to the equilibrium absolute meridional temperature gradient.	253
Figure 6.27a.	Sensitivity of ϵ to the equilibrium temperature. ..	254
Figure 6.27b.	Sensitivity of ϵ to the equilibrium absolute meridional temperature gradient.	255
Figure 6.28a.	Sensitivity of C_E to the equilibrium temperature. .	256
Figure 6.28b.	Sensitivity of C_E to the equilibrium absolute meridional temperature gradient.	257
Figure 6.29a.	Sensitivity of Sellers' cloud parameterization, C_S , to the equilibrium temperature.	258
Figure 6.29b.	Sensitivity of Sellers' cloud parameterization, C_S , to the equilibrium absolute meridional temperature gradient.	259
Figure 6.30a.	Sensitivity of the fractional coverage of positive-condensation regions to the equilibrium temperature for the experiment with $\tau_2 = 5 \times 10^5$ sec.	260
Figure 6.30b.	Sensitivity of the fractional coverage of positive-condensation regions to the equilibrium absolute meridional gradient for the experiment with $\tau_2 = 5 \times 10^5$ sec.	261

1. Introduction

Of the estimated 3.4×10^5 ergs $\text{cm}^{-2} \text{sec}^{-1}$ that the earth, on the average, receives from the sun, about 35% is reflected back to space with approximately 75% of the reflection due to clouds. Clouds have, on the average, an albedo of 50% and cover, roughly, 50% of the earth. (See London and Sasamori, 1971.) It may be shown that an increase in cloud albedo or cloud fractional coverage by 1% will decrease the earth's radiative equilibrium temperature by about $.5^\circ\text{K}$. The lower atmospheric temperatures are not directly related to the radiative equilibrium temperature because of the atmospheric "greenhouse" mechanism, which is strongly influenced by clouds. Since the tropospheric temperatures decrease upward, the clouds which act as blackbodies on the average, can reduce the infrared flux to space by emitting at a colder temperature than the lower atmosphere, from which the planetary radiation would otherwise escape. In order to maintain the planetary radiative equilibrium, the temperatures of the lower atmosphere must therefore be greater.

Schneider (1972) showed that for an idealized, globally-averaged, constant lapse-rate, radiative equilibrium model, surface temperatures increase 2° for a 1/2 kilometer increase in cloud top height. Because of the competing influences, Schneider also found that an increase in middle-level cloud fractional coverage of 1% would result in a surface temperature decrease of only $.25^\circ$. Manabe and Strickler (1964) and Manabe and Wetherald (1967) showed that for their idealized radiative-convective models, a greater change in surface temperature would result from a change in lower level cloudiness which tends to have a greater characteristic albedo and a warmer cloud-top temperature. In fact, they obtain an increase

in surface temperatures for increased high-level (greater than nine kilometer altitude) cloudiness. This latter result also depends on the characteristic infrared emissivity of the high-level clouds. Cess (1976) found from his empirically-derived expressions for the outgoing flux of infrared radiation and the absorption of solar radiation that an increase in the fractional cloud cover gives rise to a slight increase of surface temperature in the northern hemisphere and a slight decrease in the southern hemisphere. The infrared feedback is the stronger in Cess's formulas.

Also because of the competing influences, the effects are different in different latitude belts. Schneider showed that in polar latitudes, increased middle-level clouds result in increased surface temperatures, in contrast to his results for middle latitudes, equatorial latitudes, and global averages.

The preceding models describe various influences of cloud on surface temperature. But the effect of surface temperature change on the cloud field cannot be answered without additional information. This is required if a complete climate solution is to be obtained. For example, suppose that the air temperatures are increased through some course. It is unknown if the resulting change in cloud field would amplify the temperature increase, a positive feedback, or whether it would damp the increase, a negative feedback. We note that a positive feedback need not destabilize an entire system if negative feedbacks are also present.

Cess (1976) found that by comparing the differences in the outgoing flux at a particular latitude belt with variations in the surface temperature that the fractional cloud cover had an inverse relationship with surface temperature, decreasing with increasing temperature. Relating the planetary

albedo, and assumed variations of cloud albedo with respect to the zenith angle, to the surface temperature, Cess (1976) obtained another formula which could be used to find the relationship between fractional cloud cover and surface temperature. Both formulas give approximately a one percent decrease in fractional cloud cover for a one degree increase in surface temperature.

Another approach used to determine the climatic sensitivity of cloudiness involves the construction of a model with a hydrologic cycle. Weare and Snell (1974) determined the climatic sensitivities of a radiative-moist-convective model with a thin diffuse cloud (a major disparity between their model results and observations was that the calculated water content was less, by two orders of magnitude, than the amount observed). For an increased surface temperature, they obtained increased cloud-water content which resulted in increased solar reflectivity and increased infrared emission. Their model has great climatic stability to changes in solar constant. It cannot determine changes in fractional coverage. (For a discussion of cloud and radiation interaction, see also Gierasch and Goody, 1971, and Herman and Goody, 1971.)

Schneider and Washington (1973) discussed the response of the parameterized clouds in the National Center for Atmospheric Research General Circulation Model to sea-surface temperature perturbations. They found that an increase of 2°K in the sea-surface temperature, globally, resulted in a decrease of low-level fractional cloud cover

of 2%. Various other experiments dealing with local changes in sea-surface temperature have been performed and will be reported elsewhere.*

The NCAR model cloudiness (see Kasahara and Washinton, 1971) is based on a linear relationship between fractional cloud cover and relative humidity. This type of parameterization was suggested by Smagorinsky (1960) from a study of synoptic data. The relationships for the NCAR model and Smagorinsky's study are shown in Figure 1.1. Quantitative differences are especially noticeable for the high-level clouds since the NCAR model also assumes that the upper clouds are black-bodies and hence their total coverage must be substantially reduced in order to maintain a proper radiation budget. Because of the assumed relationship (which has been studied more extensively by Sanders - personal communication) we can examine other models that determine relative humidity and infer their cloud sensitivity.

Manabe and Wetherald (1975) obtained an increased temperature throughout the atmosphere by doubling the CO_2 content in an idealized three-dimensional general circulation model. They found that for increased evaporation and condensation the boundary layer relative humidity increased while the free atmosphere relative humidity decreased. Wetherald and Manabe (1976) found, for a similiar model, that an increase in the solar constant resulted in an increase in tropospheric temperatures, an increase in boundary layer relative humidity, a decrease in free atmosphere relative humidity and an increase in evaporation and condensation. The opposite results were obtained for a decrease in solar content.

* Schneider and Washington (1976), personal communication.

Wetherald and Manabe suggested that an increase in the magnitude of the downward as well as the upward motion accompanying increased precipitation may result in greater drying in regions of subsidence than moistening in ascent regions and hence a lower overall average relative humidity and cloudiness.

Manabe found in a recent study (personal communication) in which cloud cover was determined from regions of positive condensation, that the cloud cover also decreased with increasing temperature.

Sellers (1976) discussed a speculative relationship between fractional cloud cover, relative humidity, evaporation, and precipitation. For an increased solar constant, his model gave greater temperatures and less cloudiness. He indicated that for warm climates there may be less stratus, more cumulus, and less total cloudiness.

Part of the earth's hydrologic cycle may be examined seasonally. Figure 1.2 gives the precipitation for northern and southern hemisphere winter and summer. Precipitation is greatest in middle latitudes during the winter. The strongest seasonal differences occur in the southern hemisphere. Similar seasonal behavior occurs for evaporation in the northern hemisphere whereas evaporation is greater everywhere in southern latitudes during the southern hemisphere winter (see Figure 1.3). The greatest absolute convergence of moisture occurs in middle latitudes during the winter (see Figure 1.4). Seasonal changes in relative humidity (Figure 1.5) shows that the relative humidity is least in middle latitudes during the summer. Figure 1.6 shows that middle-latitude fractional cloud cover is greatest during the winter. Figure 1.7 shows

that cirrus and stratus have the same seasonal variation as total cloudiness whereas cumulus and cumulonimbus are more predominant everywhere during the summer. Seasonal variations of individual cloud type were unavailable for the southern hemisphere. Figure 1.8 gives satellite brightness photographs for the various seasons. The fractional coverage estimation in these pictures was obtained by correlation of subjective observations of cloud cover with measured brightness values in satellite photographs. Variations in cloud brightness with the same fractional coverage were not considered, although different correlation coefficients were derived for different seasons. The figures indicate that there is more longitudinal asymmetry in brightness for northern hemisphere summer than in northern hemisphere winter and southern hemisphere winter and summer. Qualitatively, cloudiness increases in middle latitudes during the winter but decreases in equatorial latitudes.

It is difficult to infer the causes for the climatic variations in cloud cover from seasonal behavior and empirical formulas. The straightforward way to determine cloud sensitivities is to construct a model that has various characteristics of the cloud field modeled explicitly and to determine the response under different external conditions. In this way, all components pertaining to the cloud distribution are obtained in a consistent fashion.

Since the cloud field is influenced by the large scale dynamics, it was decided to construct a model applicable to middle latitudes - where dynamical systems have been extensively studied. Lorenz (1970) suggested

that small numerical models that have atmospheric-like behavior, can be appropriate for long-range climate experiments. The model has to be large enough, however, to contain the large scale synoptic systems. The size and resolution of the model was tested and the resulting climate variations are discussed in Chapter 6.

The model is self-contained, with a saturated ocean surface and atmospheric hydrologic cycle. The sea-surface temperature is fixed. No explicit radiative feedbacks were allowed and only the dynamical redistribution of heat and latent heat release ensured that the model temperatures were different from the equilibrium temperature.

The sea-surface and radiative equilibrium temperature, hereafter denoted T_E , between very cold and very warm values and also varied the sea-surface and atmospheric radiative equilibrium absolute meridional temperature gradient, hereafter denoted \underline{AMTG}_E , between very small and very large values.

We discussed the cloud-water content, relative humidity, areal coverage of cloud water and positive-condensation regions, evaporation, precipitation, and other hydrologic components. Other model variables are also discussed, especially if they relate to the water distribution or are affected by the latent heat of condensation.

The absolute magnitudes obtained depend upon the various modelling assumptions described in the body of the thesis. Chapter 2 describes the numerical model, the domain, and the boundary conditions. Chapter 3 describes the model for the water substance and associated components of the atmospheric hydrologic cycle. Chapter 4 discusses relationships between the fractional coverages of cloud and condensation and

the relative humidity, and the sensitivities of these quantities to the model variables. Chapter 5 describes the basic sensitivity experiments; Chapter 6 discusses the numerical model results; and Chapter 7 gives the conclusions.

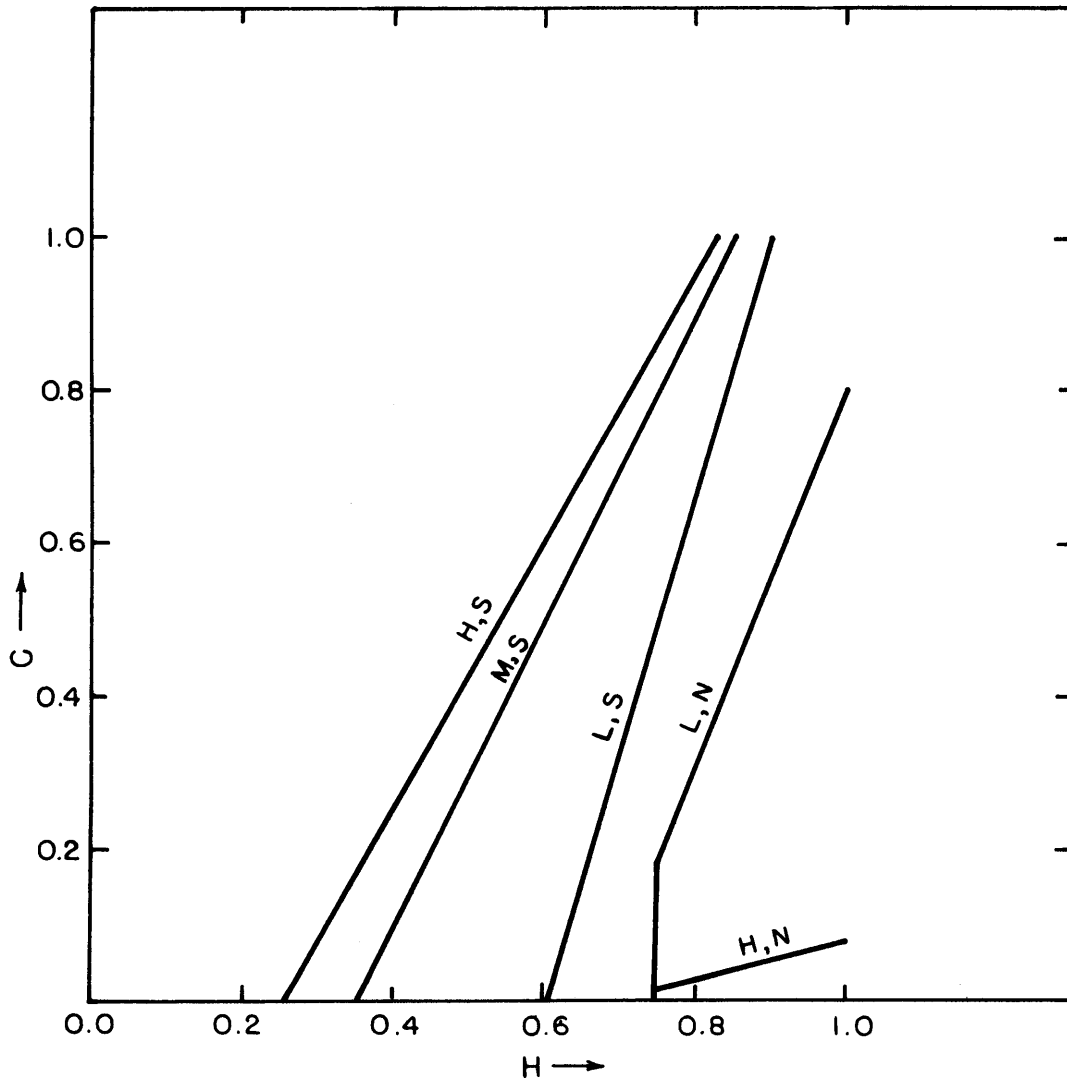


Figure 1.1. Linear relationships between fractional cloud cover and relative humidity obtained by Smagorinsky for high clouds - H,S; middle level clouds - M,S; and low clouds - L,S; and those derived for the NCAR model for high clouds - H,N; and for low clouds - L,N.

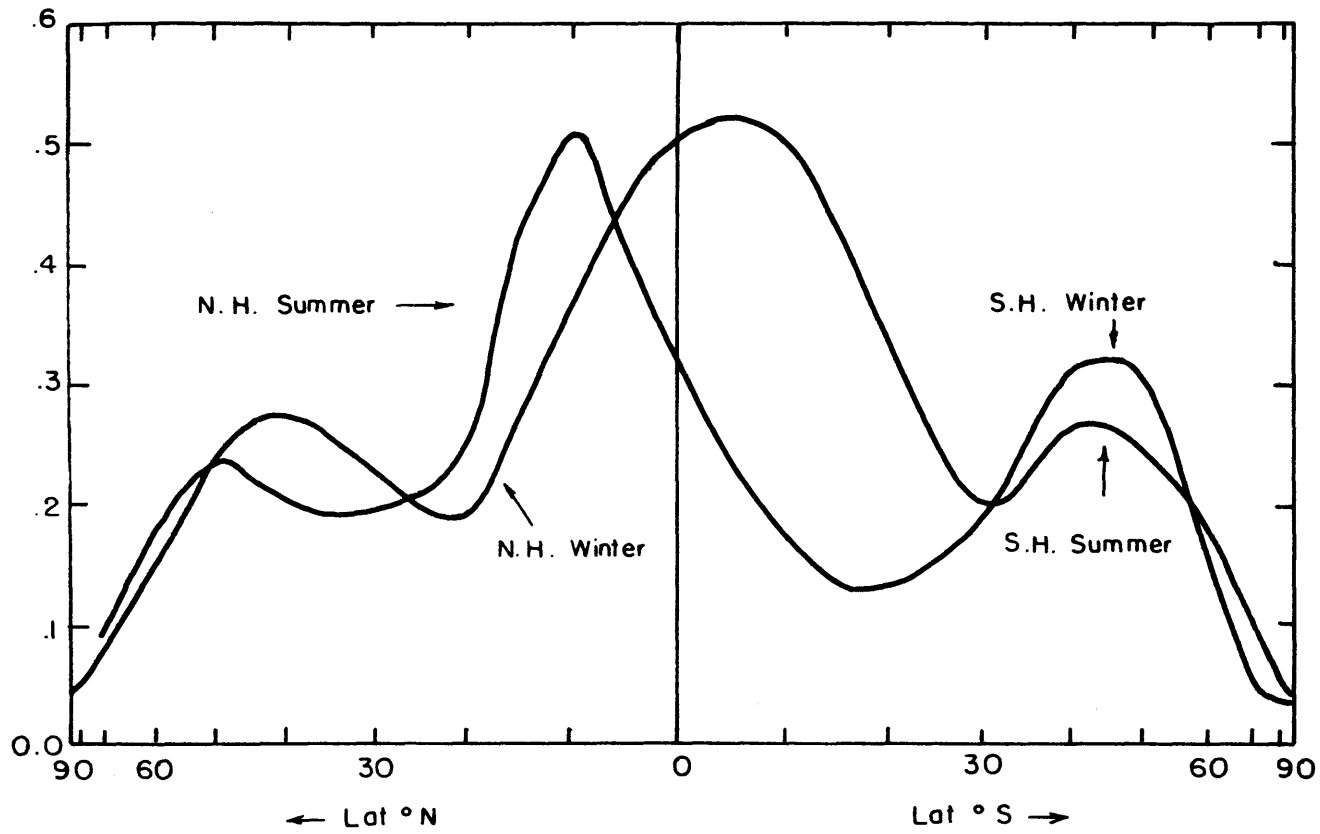


Figure 1.2. Precipitation ($\text{g cm}^{-2} \text{ day}^{-1}$) for northern and southern hemisphere winter and summer. (After Schutz and Gates, 1974) Precipitation is greatest in midlatitudes during the winter.

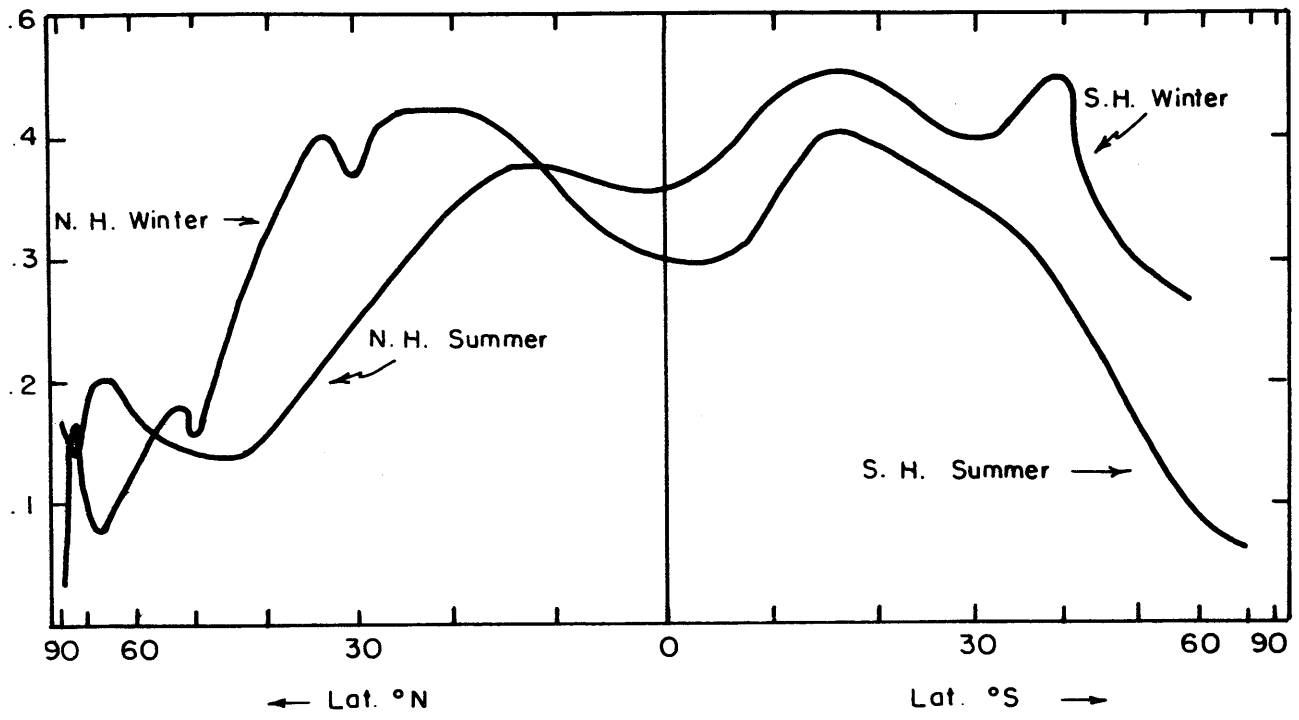


Figure 1.3. Evaporation ($\text{g cm}^{-2}\text{day}^{-1}$) for northern and southern hemisphere winter and summer. (After Schutz and Gates, 1974) Evaporation is greatest is midlatitudes during the winter.

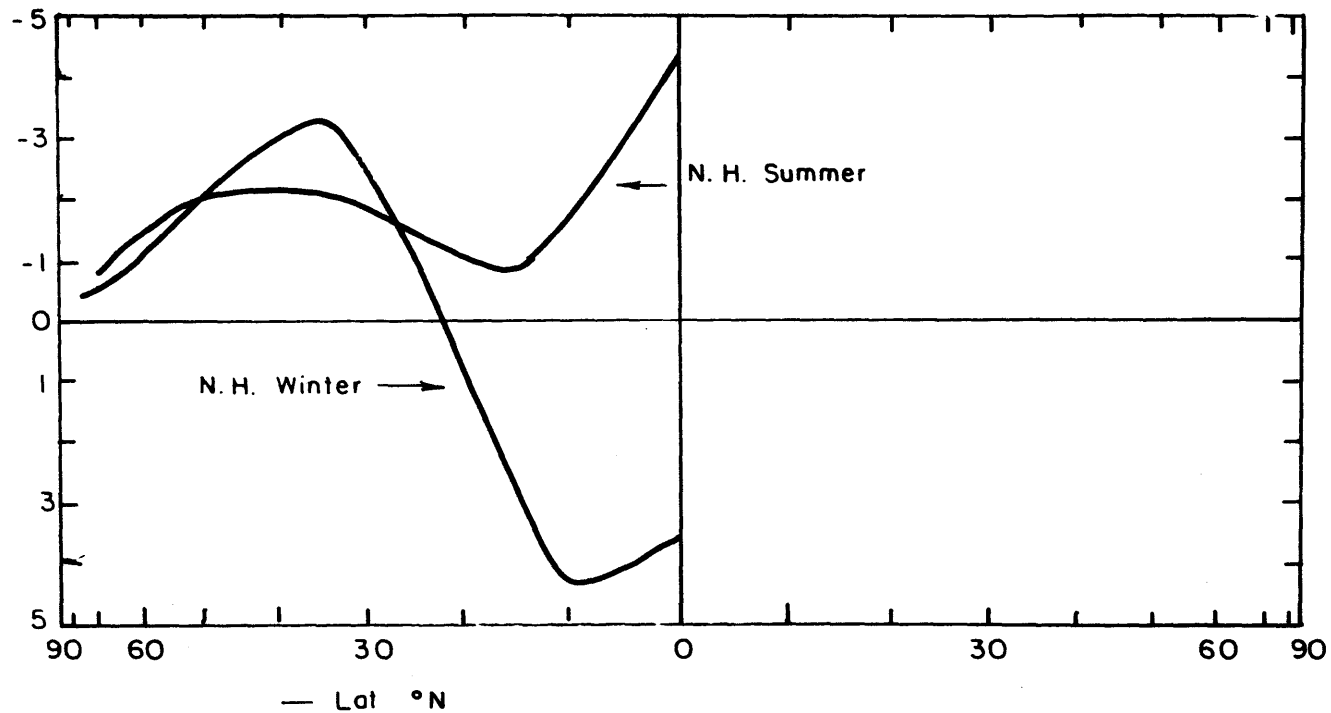


Figure 1.4. Atmospheric vertically-averaged meridional transport of water vapor ($\text{m sec}^{-1} \text{g kg}^{-1}$) for northern hemisphere winter and summer. (After Oort and Rasmusson, 1971) Absolute flux convergence is greatest during the winter in polar and middle latitudes.

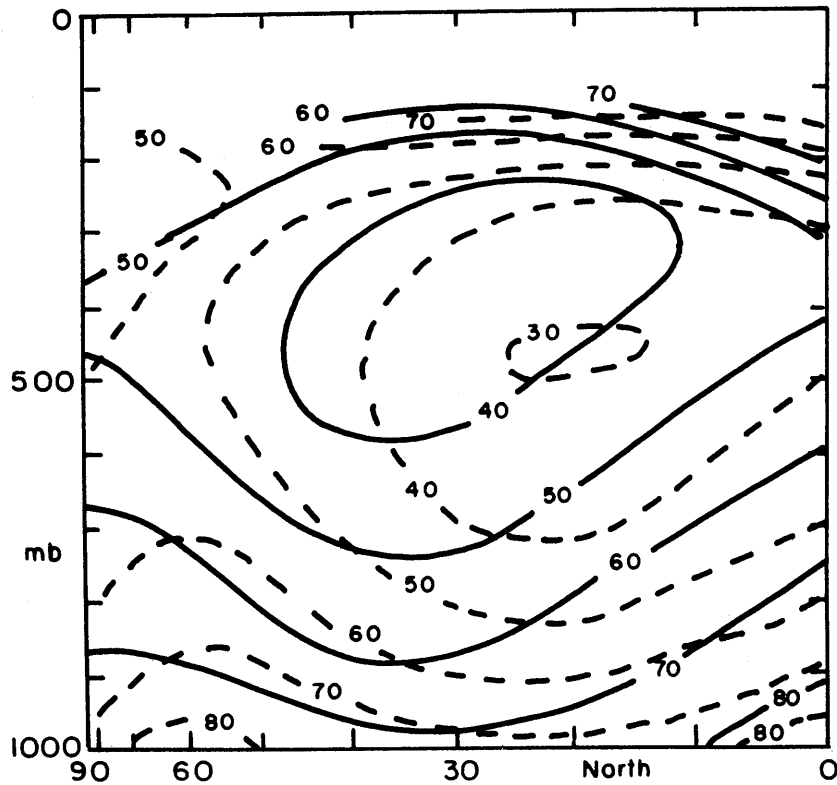


Figure 1.5. Time-and-longitude averaged relative humidity $[\bar{q}/\bar{q}^*]$ in northern summer (solid line) and winter (dashed line). (After Lorenz, 1967.) Relative humidity is greatest in middle latitudes during the winter.

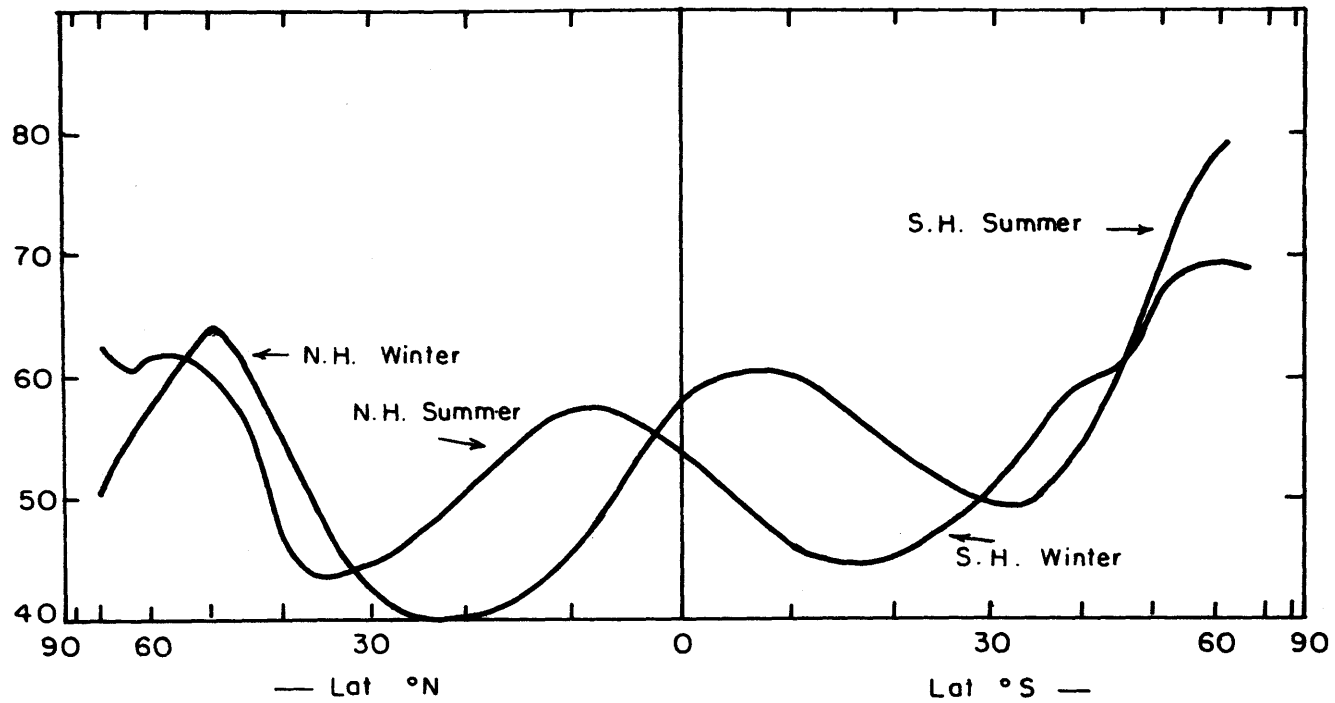


Figure 1.6a. Total zonal cloud fractional coverage (space and time) (percent) for northern and southern hemisphere winter and summer. (After Landsburg, 1945) Cloudiness is greatest during the winter in midlatitudes.

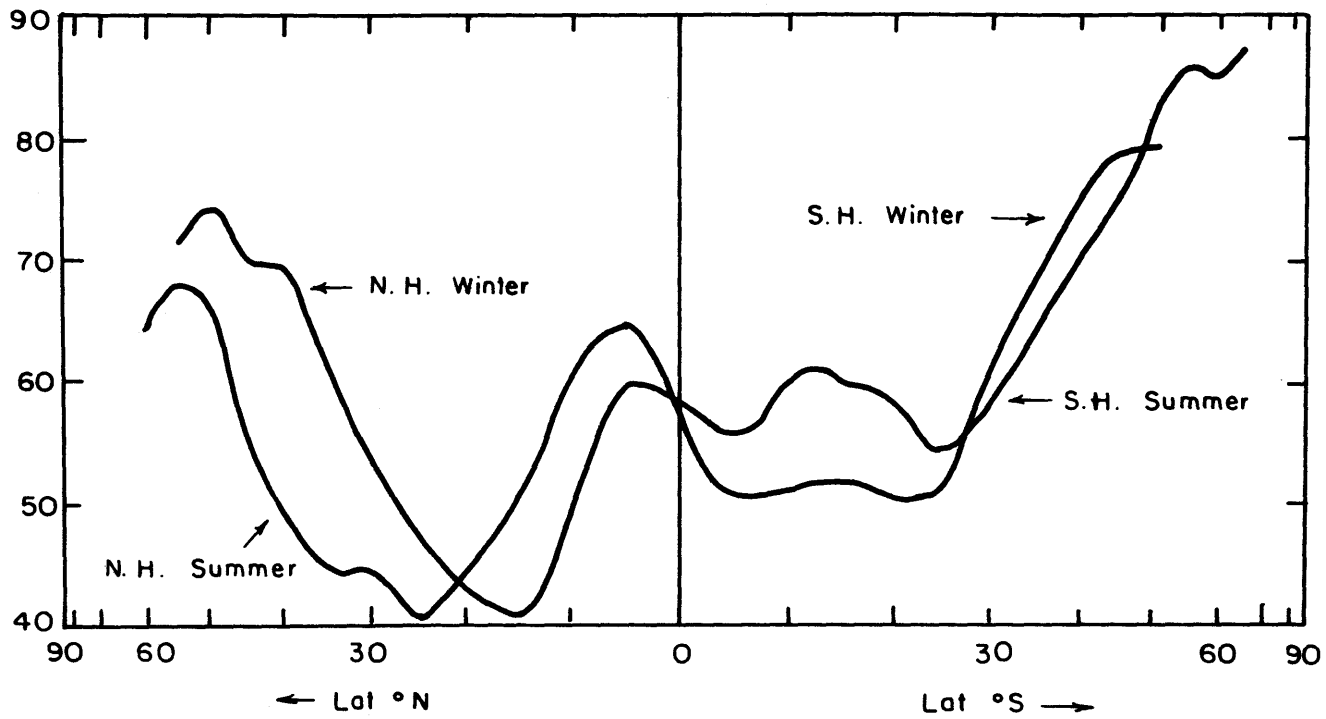


Figure 1.6b. Same as Figure 1.6a. (After Clapp, 1967)

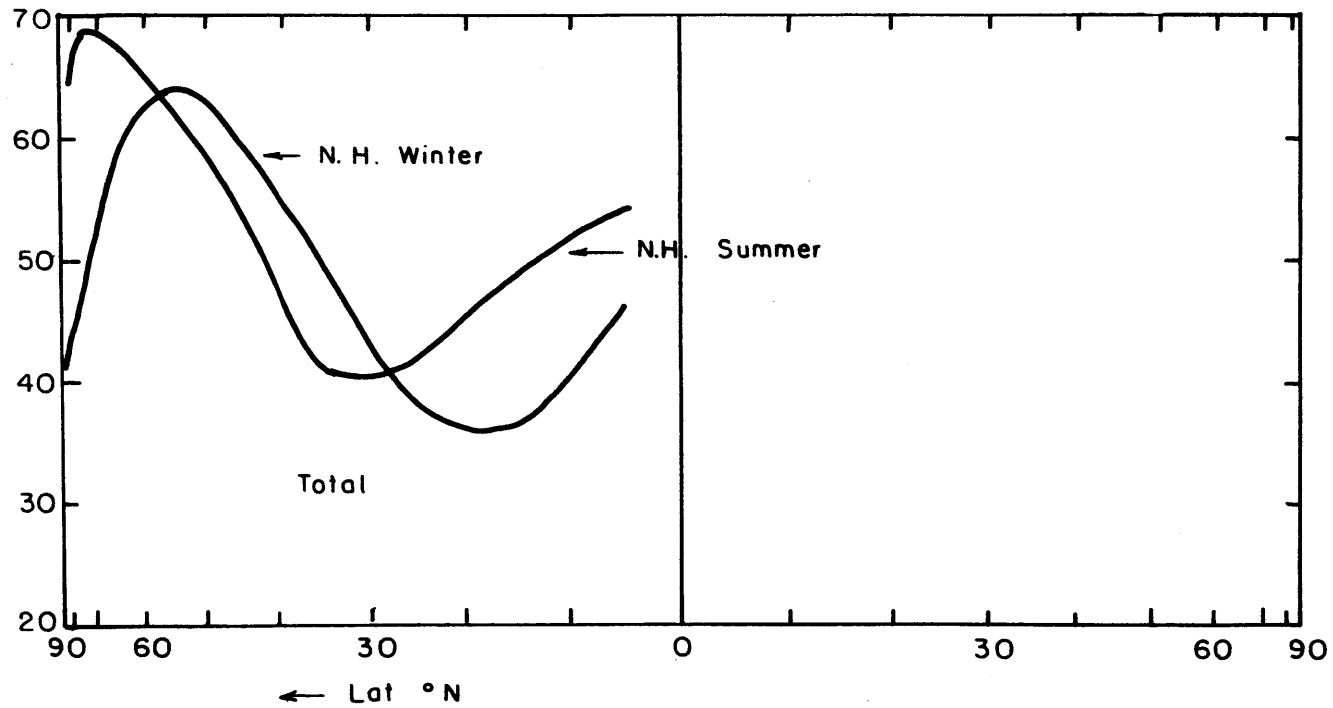


Figure 1.6c. Same as Figure 1.6a, but for northern hemisphere only. (After London, 1967)

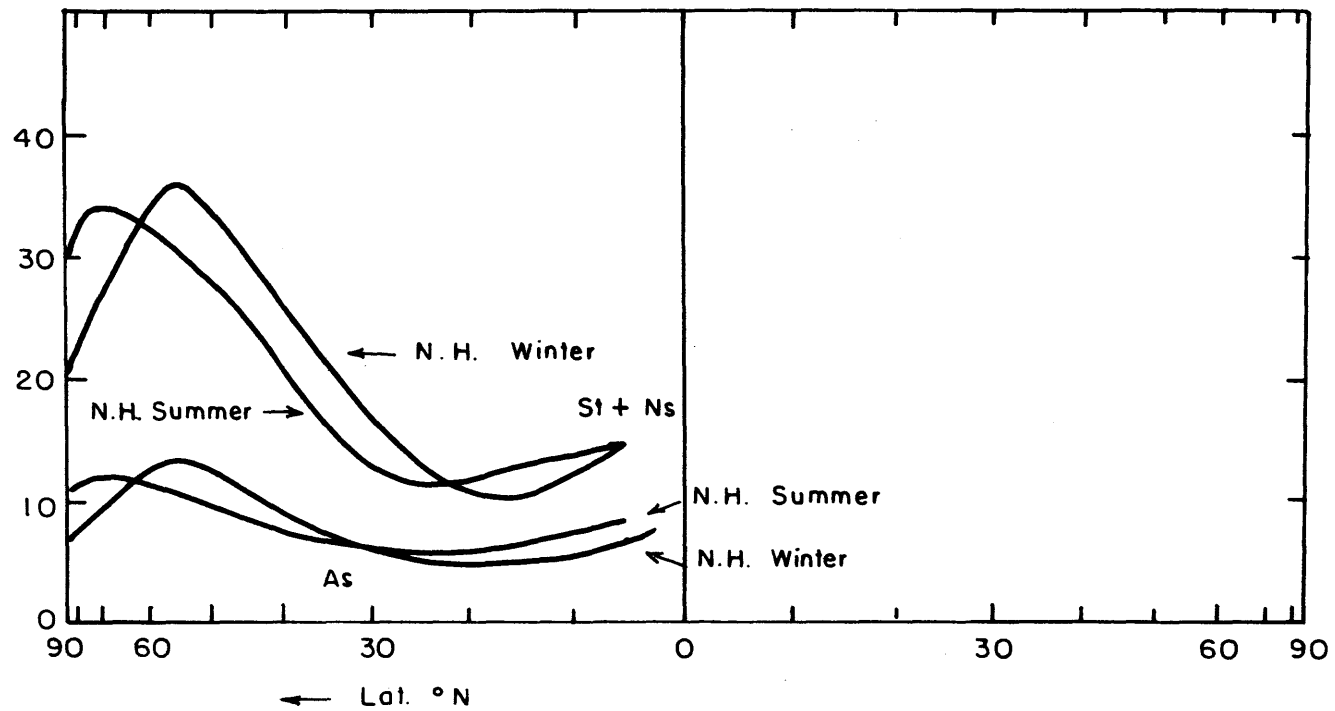


Figure 1.7a. Altostratus and Nimbostratus plus stratus zonal fractional cloud coverage for northern hemisphere winter and summer. (After London, 1957) Cloudiness is greatest during the winter in midlatitudes.

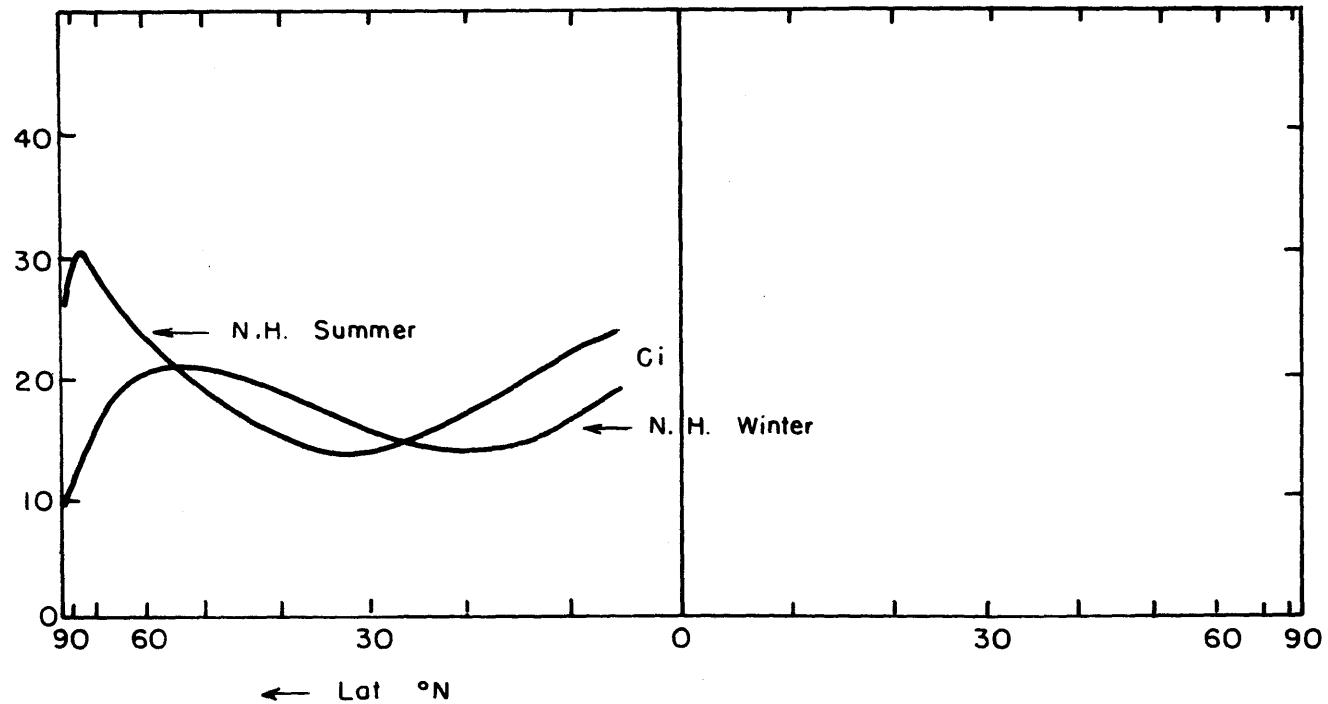


Figure 1.7b. Cirrus zonal fractional cloud cover for northern hemisphere winter and summer. (After London, 1957) Cloud cover is greatest during the winter in mid-latitudes.

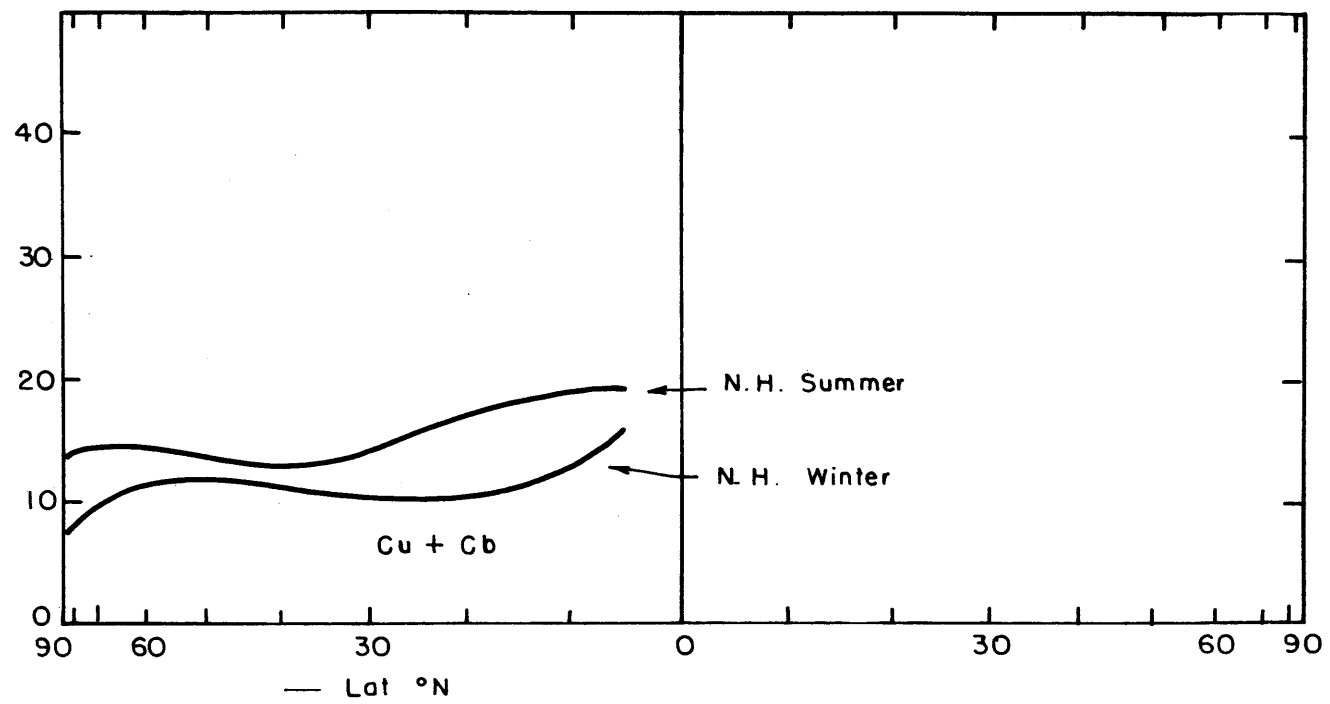


Figure 1.7c. Cumulus plus cumbulonimbus for northern hemisphere winter and summer. (After London, 1957) Cloudiness is greatest during the summer.

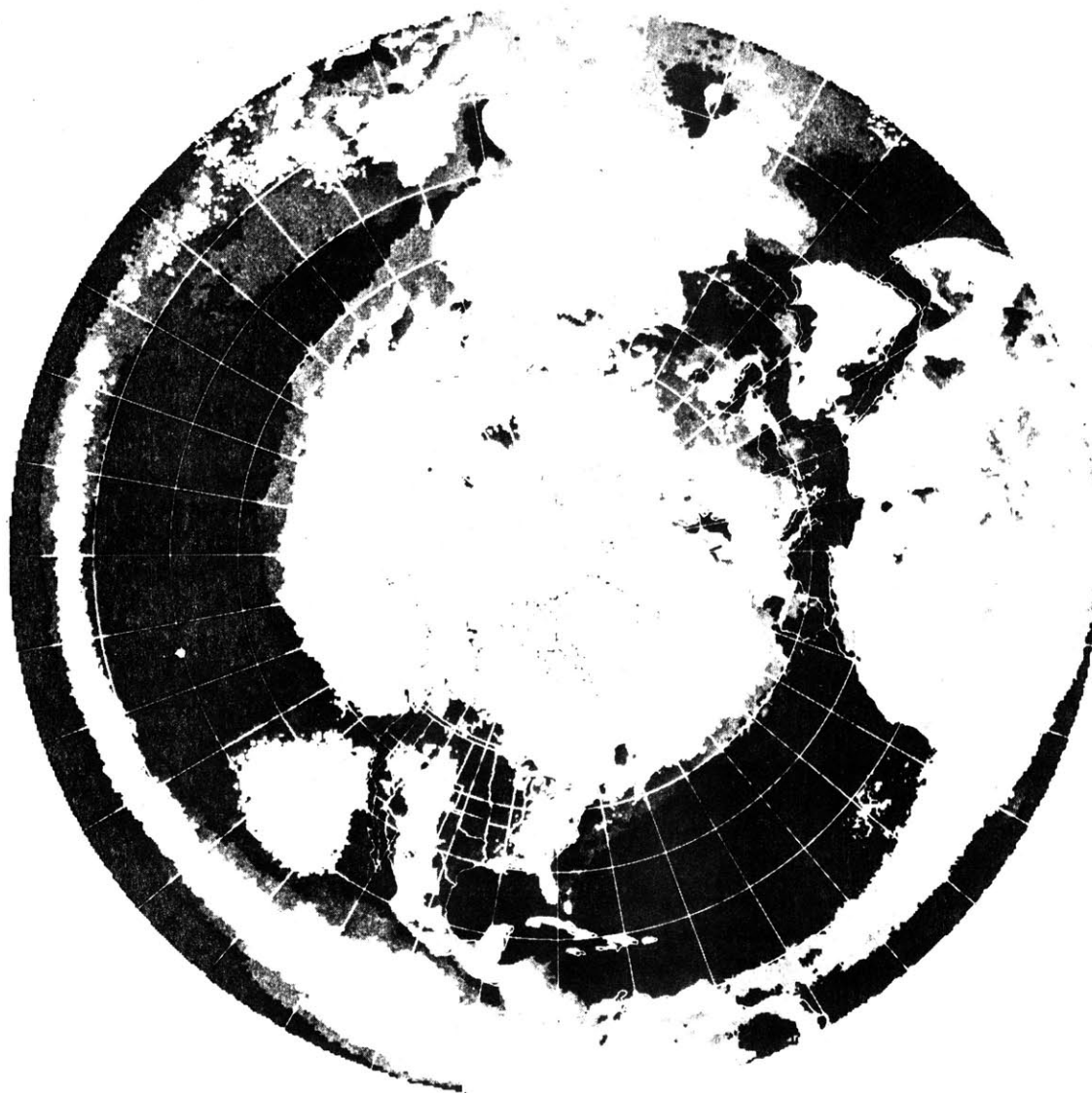


Figure 1.8a.
Polar Stereographic Satellite Relative Cloud Cover, 1400 Local, Northern Hemisphere, Mean Octas, June through August 1967-1970.
(From Miller, 1971)



2

Figure 1.8b.
Polar Stereographic Satellite Relative Cloud Cover, 1400 Local, Northern Hemisphere, Mean Octas,
December through February 1967-1970.
(From Miller, 1971)

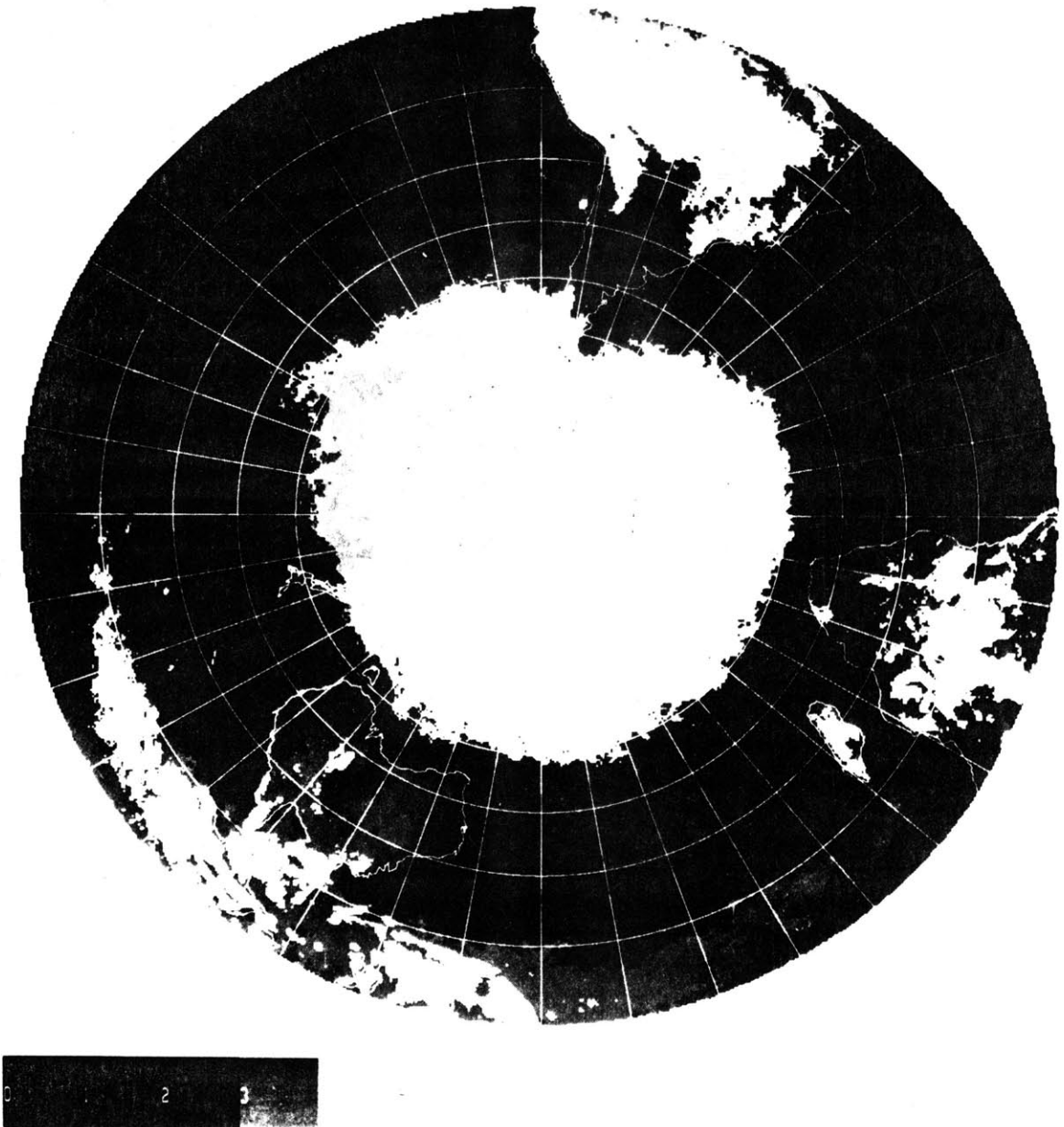


Figure 1.8c.
Polar Stereographic Satellite Relative Cloud Cover, 1400 Local, Southern Hemisphere, Mean Octas, December through February 1967-1970.
(From Miller, 1971)

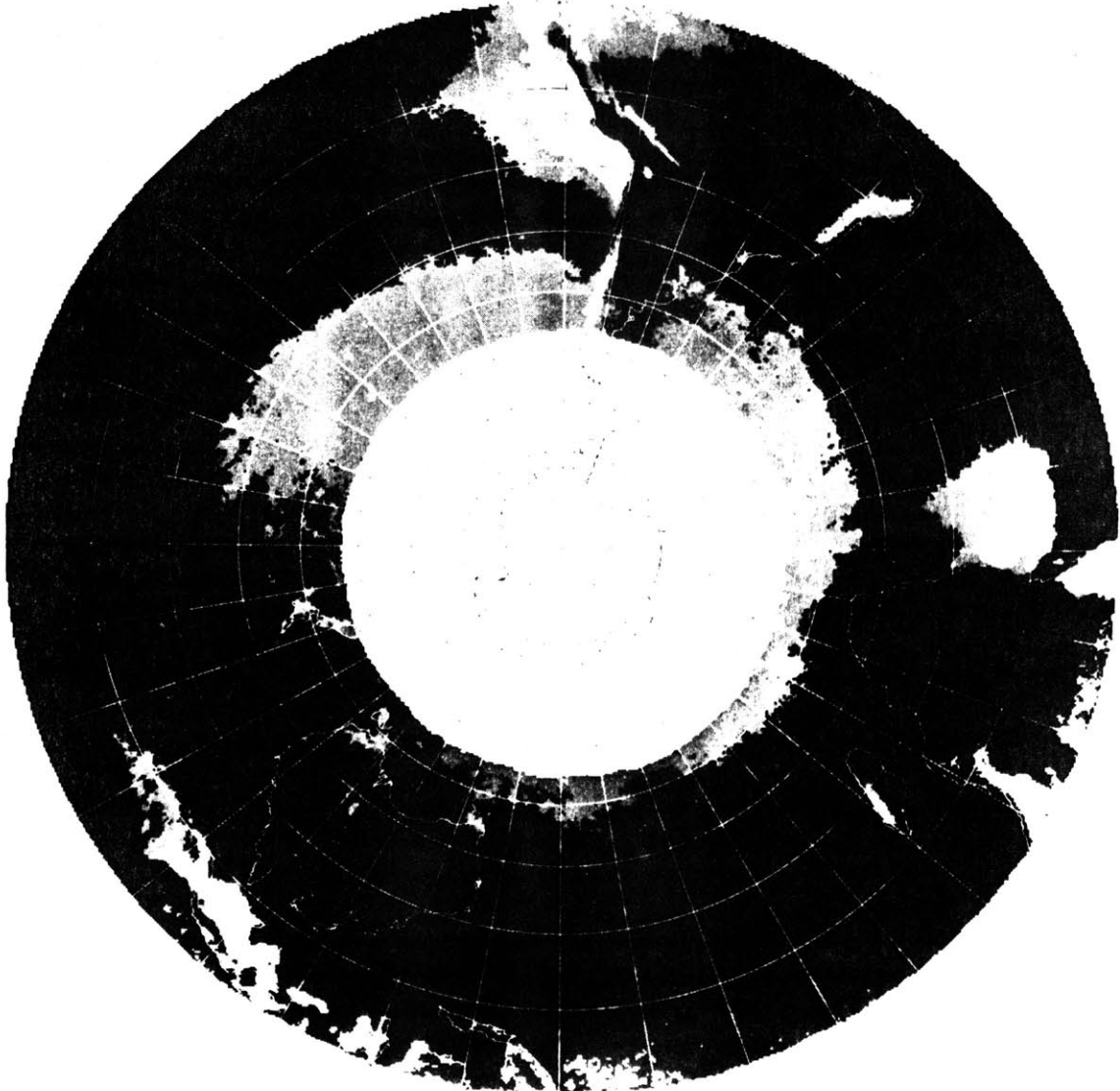


Figure 1.8d.
Polar Stereographic Satellite Relative Cloud Cover, 1400 Local, Southern Hemisphere, Mean Octas, June through August 1967-1970.
(From Miller, 1971)

2. Numerical Model

2.1 Introduction

A Newtonian heating law based upon specified radiative equilibrium temperatures and a relaxation time constant appropriate to radiative-convective heat transfer time scales is used to drive an atmospheric circulation which evaporates latent energy from a saturated surface of infinite heat capacity and specified temperature. The kinetic energy of the circulation is dissipated, mainly at the surface, by friction. We do not consider the influence of the generated clouds or the radiative exchange. The heating law determines, essentially, the average temperature and the associated gradients of temperature.

The model domain is a re-entrant channel with sigma and Cartesian coordinates. The channel is situated on a mid-latitude f plane (see figure 2.1a). The vertical extent includes the entire atmospheric mass while the horizontal extent is limited; $0 \leq x \leq X$, $0 \leq y \leq Y$ (see figure 2.1b). Two vertical levels are used for various horizontal grid sizes and resolutions.

We assume that the atmosphere is a perfect gas and assume the gas constants are those of dry air. The latent heat of vaporization and sublimation is assumed to be constant regardless of the temperature. We assume that the sigma velocity is zero at $\sigma=0$ in addition to being zero at the surface.

With the above assumptions, the basic equations for the dependent variables $(p_s, x, T, q_1, \dot{\sigma}, \omega, \phi)$ in terms of the independent variables (x, y, σ, t) * are:

* For a derivation of the basic equations in sigma coordinates, see Arakawa and Mintz (1974) or Phillips (1957).

Tendency

$$\frac{\partial p_s}{\partial t} = - \nabla \cdot p_s \int_0^1 \tilde{v} d\sigma \quad (2.1.1)$$

Continuity

$$\dot{\sigma} = (\sigma \nabla \cdot p_s \int_0^1 \tilde{v} d\sigma - \nabla \cdot p_s \int_0^{\sigma} \tilde{v} d\sigma) / p_s \quad (2.1.2)$$

ω

$$\omega = p_s \dot{\sigma} - \sigma (\nabla \cdot p_s \int_0^1 \tilde{v} d\sigma - \tilde{v} \cdot \nabla p_s) \quad (2.1.3)$$

Zonal Momentum

$$\begin{aligned} \frac{\partial p_s u}{\partial t} = & - \nabla \cdot p_s \chi u - \frac{\partial p_s}{\partial \sigma} \dot{\sigma} u + f p_s v - \\ & - R \frac{\partial p_s T}{\partial x} - \frac{\partial p_s}{\partial \sigma} \sigma \frac{\partial \Phi}{\partial x} - p_s F_x \end{aligned} \quad (2.1.4)$$

Meridional Momentum

$$\begin{aligned} \frac{\partial p_s v}{\partial t} = & - \nabla \cdot p_s \chi v - \frac{\partial p_s}{\partial \sigma} \dot{\sigma} v - f p_s u - \\ & - R \frac{\partial p_s T}{\partial y} - \frac{\partial p_s}{\partial \sigma} \sigma \frac{\partial \Phi}{\partial y} - p_s F_y \end{aligned} \quad (2.1.5)$$

Thermodynamic

$$\begin{aligned} \frac{\partial p_s T}{\partial t} = & - \nabla \cdot p_s \chi T - \frac{\partial p_s}{\partial \sigma} \dot{\sigma} T + \frac{\omega R T}{c_p \sigma} + \\ & + p_s \frac{\dot{\sigma}}{c_p} + \frac{1}{c_p} p_s \dot{c} v c \end{aligned} \quad (2.1.6)$$

Water

$$\begin{aligned} \frac{\partial p_s q_i}{\partial t} = & - \nabla \cdot p_s \chi q_i - \frac{\partial p_s}{\partial \sigma} \dot{\sigma} q_i - p_s \sum \dot{c}_{ij} + \\ & + g \frac{\partial F_{q_i}}{\partial \sigma} + g \frac{\partial}{\partial \sigma} p V_i q_i, \quad i = 1, m \end{aligned} \quad (2.1.7)$$

(See Chapter 3 for explanation of \dot{c}_{ij} and q_i)

Hydrostatic

$$\frac{\partial \phi}{\partial \sigma} = - \frac{R T}{\sigma} \quad (2.1.8)$$

The f-plane Cartesian geometry simplifies the dynamics and eventual interpretation of model results since there is no asymmetry due to differential rotation and domain shape. The only asymmetry in the model is that of the temperature structure which is described in Section 2.2. The f-plane also has the advantage of having a set of boundary conditions with simple symmetry which the beta plane would not have (see Section 2.3).

The size of the domain is chosen to allow the simulation of large scale atmospheric-like dynamical behavior. For the same external parameters, including temperature gradient, greater eddy kinetic energies were obtained for greater zonal widths. For the same external parameters, it may also be shown that the larger meridional width has a greater available potential energy. The available potential energy can be increased by increasing the meridional temperature gradient. Coarse resolution ($\Delta = 500$ km.) and fine resolution ($\Delta = 333 \frac{1}{3}$ km.) models were run to test the effect of the horizontal grid size on the results. Only slight differences were noted in most results.

2.2 Heating and Friction Parameterizations

2.2.1 Heating

The Newtonian heating parameterization is intended to simulate sensible heating by turbulent convection as well as solar and infrared heating. A dry convective adjustment described in conjunction with

the moist convection scheme is used only rarely since atmosphere is almost always statically stable, especially for a hot climate.

The radiative-convective heating term is of the form

$$\dot{Q} = C_p (T_E(y, \sigma) - T(x, y, \sigma, t)) / \tau_E. \quad (2.2.1)$$

$T_E(y, \sigma)$ is the preset equilibrium temperature and τ is the associated time constant. The atmosphere would relax to the equilibrium temperature on a time scale of τ if the other influences such as latent heating and the dynamical redistribution of heat were absent.

We ensure that these processes are present, however, by means of the imposed gradients in T_E . First, we assume that the equilibrium temperature is warmer in the southern part of the domain than the northern part (we work with a northern hemisphere model). Consideration of the boundary conditions for the model (see section 2.3) requires $\frac{\partial T_E}{\partial y} = 0$ at the lateral walls. We also require the domain to be symmetrical in the imposed surface temperature gradient - the maximum gradient is imposed in the center of the domain. We chose:

$$T_g = \llbracket T_g \rrbracket + \llbracket \frac{\partial T_g}{\partial \mu} \rrbracket \left(-\frac{Y}{2} + \frac{3\mu^2}{Y} - \frac{2\mu^3}{Y} \right), \quad (2.2.2a)$$

where

$$\frac{\partial T_g}{\partial \mu} = 6 \llbracket \frac{\partial T_g}{\partial \mu} \rrbracket \frac{\mu}{Y} \left(1 - \frac{\mu}{Y} \right). \quad (2.2.2b)$$

The atmospheric temperatures are related to this profile by specifying the static stability, $\frac{1}{C_p} \frac{\partial s_E}{\partial z}$ and solving for T_E ,

$$\frac{1}{C_p} \frac{\partial s_f}{\partial z} = \frac{g}{C_p} \left(1 - \frac{\partial T_E}{\partial \sigma} \frac{C_p \sigma}{R T_E} \right). \quad (2.2.3)$$

We specified the static stability of the boundary layer and free atmosphere separately, assuming an increase in stability with respect to latitude and

pressure. The chosen equilibrium static stability can influence the partition between stable and unstable condensation. It was decided to make the equilibrium lapse rate close to the standard -6.5×10^{-5} deg/cm. This would ensure a sufficiently stable lapse rate, even for a cold climate. Moist convection, especially for the warm climates, and the dynamics stabilized the lapse rate further. Moist convection tended to be the dominant effect. One of the experiments which will be discussed later assumed a moist-adiabatic lapse rate.

The time constant was estimated from Cunnold et al. (1971) to be 1.6 sec (~ 18.5 days). The total model heating also includes the heating that results from the moist-convective adjustment. This will be elaborated on later.

2.2.2 Friction

A surface drag law is used to transfer momentum from the surface layer to the boundary. Following Phillips (1960), the momentum in the boundary layer is taken to be a linear extrapolation of the upper-level momentum but with only 70% of the magnitude. The stress may be written in the form

$$\tau_s = \rho_s C_D |v_s| v_s. \quad (2.2.4)$$

An upper-level shear stress of the form

$$\tau_A = \rho K \frac{\partial v}{\partial z} \quad (2.2.5)$$

is also used. We assume a free-stress boundary for the domain.

Horizontal diffusion can be incorporated to represent the effects of eddies smaller than the grid point size, to eliminate computational instability due to spurious growth of short-wavelength components caused by truncation errors and nonlinear interactions, and to smooth the solution fields. Higher-order operators (see Shapiro, 1970) damp the shorter waves more selectively. We use an operator of the form

$$\dot{S}(A) = -\alpha \left(\frac{\partial^4}{\partial x^4} + \frac{\partial^4}{\partial y^4} \right) A \quad (2.2.6)$$

where the coefficient is chosen such that for a grid length of 500 kilometers and a diffusion coefficient of $K_H \sim 10^9 \text{ cm}^2 \text{ sec}^{-1}$, the damping for the KV^2 and $-\alpha$ operators is equal for two-grid-point waves. The relative damping versus grid-point wavelengths is shown in figure 2.3. We also use this operator on the surface-pressure field.

2.2.3 Summary

Radiation and Sensible Diabatic Heating

$$\dot{Q}_K = C_p (T_E(y, \sigma) - T(x, y, \sigma, t)) / \tau_E + C_p \dot{S}(T_K) \quad (2.2.7a)$$

† moist convection

$$T_g(y) = [T_g] + 6 \left[\frac{\partial T_g}{\partial y} \right] \left(-\frac{y}{2} + \frac{y^2}{2Y} - \frac{y^3}{3Y^2} \right)$$

$$T_{E,2}(y) = T_g(y) \left(-A + (A^2 + 4P_2 P_3)^{1/2} \right) / (2P_3)$$

$$T_{E,1}(y) = T_{E,2}(y) \left(-B + (B^2 + 4P_1 P_2)^{1/2} \right) / (2P_2)$$

$$\tau_E = 1.6 \times 10^6 \text{ sec} \quad (2.2.7b)$$

$$A = -\Delta p_s \left(1 - \frac{2R \left[6 \times 10^{-5} \text{ deg cm}^{-1} - \frac{(\gamma - \gamma/2)}{\gamma} 10^{-5} \right]}{g} \right)$$

$$B = -\Delta p \left(1 - \frac{2R \left[7 \times 10^{-5} \text{ deg cm}^{-1} - \frac{(\gamma - \gamma/2)}{\gamma} 10^{-5} \right]}{g} \right)$$

$$p_1 = 2.5355 \times 10^5 \text{ dynes cm}^{-2}$$

$$p_2 = 7.6125 \times 10^5 \text{ "}$$

$$\Delta p = 5.025 \times 10^5 \text{ "}$$

$$\Delta p_s = 2.5375 \times 10^5 \text{ "}$$

Friction

(2.2.8a)

$$p_s \dot{\Gamma}_1 = k_1 (\underline{v}_1 - \underline{v}_2) - p_s \dot{\Gamma} (\underline{v}_1)$$

$$p_s \dot{\Gamma}_2 = k_1 (\underline{v}_2 - \underline{v}_1) - p_s \dot{\Gamma} (\underline{v}_2) + 2p_s g C_D |\underline{v}_3| \underline{v}_3$$

$$k_1 = 2 \rho g K_a / \Delta z \approx 10^{-2} \text{ g cm}^{-1} \text{ sec}^{-3} \quad (2.2.8b)$$

$$C_D = \min \left[(1 + 7 \times 10^{-4} |\underline{v}_3|) 10^{-3}, 2.5 \times 10^{-3} \right]$$

$$\underline{v}_3 = 0.7 \left(\frac{3}{2} \underline{v}_2 - \frac{1}{2} \underline{v}_1 \right)$$

Smoothing

(2.2.9)

$$\dot{\Gamma}(A) = \frac{-\Delta^4 \left(\frac{\partial^4}{\partial x^4} + \frac{\partial^4}{\partial y^4} \right) A \delta(\text{mod. } n=0)}{280 \Delta t}$$

2.3 Horizontal Boundary Conditions

For systems of equations possessing periodicities and symmetries, one can eliminate all but a small finite part of an unbounded domain by using periodic and symmetric boundary conditions. This is advantageous since it may not be clear, otherwise, what the appropriate boundary conditions for a limited computational domain should be. For example: periodic boundary conditions in the longitudinal direction successfully simulate large scale flow with wavelengths less than the longitudinal length; mirror boundary conditions at the equator successfully simulate large scale flow resulting from hemispherically symmetric forcings.

For lateral boundaries not at the equator, one can exploit the parity (see Saxon, 1971, for a discussion of the concept of parity) relationships inherent in the equations. Any dependent variable $A(x_i)$ may be expressed as the sum of even parity, $A^+(x_i)$, and odd parity, $A^-(x_i)$, functions of the independent variables, x_i . That is, since

$$A(x_i) = \frac{1}{2} [A(x_i) + A(-x_i)] + \frac{1}{2} [A(x_i) - A(-x_i)] \quad (2.3.1)$$

we can write

$$A(x_i) = A^+(x_i) + A^-(x_i), \quad (2.3.2)$$

where

$$A^+(x_i) = \frac{1}{2} [A(x_i) + A(-x_i)] \quad (2.3.3a)$$

and

$$A^-(x_i) = \frac{1}{2} [A(x_i) - A(-x_i)]; \quad (2.3.3b)$$

such that

$$A^+(x_i) = + A^+(-x_i) \quad (2.3.4a)$$

and

$$A^-(x_i) = - A^-(-x_i). \quad (2.3.4b)$$

From 2.3.3 and 2.3.4 one can show that even and odd products of $A^+(x_i)$ and even products of $A^-(x_i)$ are even whereas odd products of $A^-(x_i)$ are odd. Even spatial derivatives of $A^+(x_i)$ and odd spatial derivatives of $A^-(x_i)$ are even whereas odd spatial derivatives of $A^+(x_i)$ and even spatial derivatives of $A^-(x_i)$ are odd.

For an elementary example consider the barotropic vorticity equation on an f plane:

$$\frac{\partial}{\partial t} \nabla^2 \psi = - \hat{k} \cdot \nabla \psi \times \nabla \nabla^2 \psi. \quad (2.3.5)$$

Examination of 2.3.5 shows that

$$\psi(x, y) = \psi^+(x, y) \quad (2.3.6)$$

is a conservative property of this system of equations if the odd parity part is equal to zero and hence the velocity components conserve odd parity. ψ^- is not conserved, even if ψ^+ is initially 0 unless ψ^- is also 0. For the more complex numerical model equations, it is shown in Appendix B that a consistent conservative system consists of even parity for all variables except for the horizontal velocity components which have odd parity. If a variable f domain were used, f would have to behave like an even function of y . If f were an odd function then mirror boundary conditions are appropriate. Symmetry boundary conditions could not be used if f were of mixed parity. Similar restrictions are required for the forcing terms.

Essentially we retain a periodic system in y but assume a solution with definite parity to eliminate one half of the north south system. We could do the same for the longitudinal direction but this would require the zonal flow equal to zero at the boundaries, which is undesirable. Therefore we assume periodicity in x and the following boundary conditions at the zonal lateral walls:

$$u(x, -\eta) = -u(-x, \eta) \quad ; \quad u(x, Y+\eta) = -u(-x, Y-\eta) \quad (2.3.7)$$

$$v(x, -\eta) = -v(-x, \eta) \quad ; \quad v(x, Y+\eta) = -v(-x, Y-\eta)$$

$$p_s(x, -\eta) = +p_s(-x, \eta) \quad ; \quad p_s(x, Y+\eta) = +p_s(-x, Y-\eta)$$

$$T(x, -\eta) = T(-x, \eta) \quad ; \quad T(x, Y+\eta) = T(-x, Y-\eta)$$

$$q_i(x, -\eta) = q_i(-x, \eta) \quad ; \quad q_i(x, Y+\eta) = +q_i(-x, Y-\eta).$$

Since the integral with respect to x at the lateral boundary vanishes for odd parity terms, we have the following average boundary conditions:

([()]) denotes a zonal average)

$$[u(0)] = 0 \quad ; \quad [u(Y)] = 0 \quad (2.3.8)$$

$$[v(0)] = 0 \quad ; \quad [v(Y)] = 0$$

$$\left[\frac{\partial p_s}{\partial \eta}(0) \right] = 0 \quad ; \quad \left[\frac{\partial p_s}{\partial \eta}(Y) \right] = 0$$

$$\left[\frac{\partial T}{\partial \eta}(0) \right] = 0 \quad ; \quad \left[\frac{\partial T}{\partial \eta}(Y) \right] = 0$$

$$\left[\frac{\partial q_i}{\partial \eta}(0) \right] = 0 \quad ; \quad \left[\frac{\partial q_i}{\partial \eta}(Y) \right] = 0$$

$$\begin{aligned}
 [p_s v(x)] &= 0 & ; & [p_s v(Y)] = 0 \\
 [p_s vT(x)] &= 0 & ; & [p_s vT(Y)] = 0 \\
 [p_s vq_i(x)] &= 0 & ; & [p_s vq_i(Y)] = 0 \\
 [p_s v\chi^2(x)] &= 0 & ; & [p_s v\chi^2(Y)] = 0 .
 \end{aligned}$$

The boundary conditions do not give $[psv] = 0$ at the boundaries and hence a momentum exchange occurs there. The parity conditions are equivalent, on the average, to the no-slip, insulating, impermeable surface whereas the mirror boundary conditions are equivalent to the free-slip, insulating, impermeable surface. The symmetry imposed on the domain by these boundary conditions is shown in figure 2.4.

2.4 Finite Differences

We use the total-energy, mass, and quadratic-conserving box finite-difference method formulated by Kurihara and Holloway (1967) for the basic equations. The scheme is of second order accuracy for a regular grid and was formulated in this form by Shuman (1962). He called it the "filtered factor form." Leapfrog time differencing with periodic application of a Euler backward step is used. Specifically, for most of the runs we integrate for 10 steps using leapfrog (the diffusion and forcing terms are evaluated at the previous time step), smooth the solution, apply the Euler backward step and continue.

The vertical and horizontal grids are shown in figure 2.5a and 2.5b. The atmosphere is divided into two layers in the vertical with ν , T, and

q_i carried at the integer levels halfway between the boundaries and the layered interface where $\dot{\sigma}$ and ϕ are carried. The horizontal outermost grid point's information is determined from the boundary conditions. A "box" surrounds one of the horizontal grid points in figure 2.3b. The average properties of the box are described by the values at the grid point.

The following finite-difference operators are defined:

Space (2.4.1a)

$$A_{\Delta}^n = A(i\Delta x, j\Delta y, \sigma_k, n\Delta t); \sigma_1 = .25, \sigma_{\frac{1}{2}} = .5, \sigma_2 = .75$$

$$\overline{A_{\Delta}^n}^S = \frac{1}{2} (A_{\Delta}^n (S + \frac{\Delta S}{2}) + A_{\Delta}^n (S - \frac{\Delta S}{2}))$$

$$\delta_S A_{\Delta}^n = \frac{1}{\Delta S} (A_{\Delta}^n (S + \frac{\Delta S}{2}) - A_{\Delta}^n (S - \frac{\Delta S}{2}))$$

$$D_{\Delta}^n(A_{\Delta}^n) = \delta_x \overline{p_s^n}^x \overline{u_{\Delta}^n}^x \overline{A_{\Delta}^n}^x + \delta_y \overline{p_s^n}^y \overline{v_{\Delta}^n}^y \overline{A_{\Delta}^n}^y + p_s^n \delta_{\sigma} \dot{\sigma} \overline{A_{\Delta}^n}^{\sigma}$$

$$H_{\Delta}^n(A_{\Delta}^n) = D_{\Delta}^n(A_{\Delta}^n) - p_s^n \delta_{\sigma} \dot{\sigma} \overline{A_{\Delta}^n}^{\sigma}$$

$$G_S^n(A_{\Delta}^n B_{\Delta}^n) = \delta_S \overline{A_{\Delta}^n}^S \overline{B_{\Delta}^n}^S$$

$$L_S^n(B_{\Delta}^n A_{\Delta}^n) = \overline{B_{\Delta}^n}^S \delta_S \overline{A_{\Delta}^n}^S;$$

Time

(2.4.1b)

The leapfrog operator is

$$\frac{\partial A^n}{\partial t} = \frac{A^{n+1} - A^{n-1}}{2\Delta t},$$

For the Euler backward step we have

$$\frac{\partial A^{\sim}}{\partial t} = \frac{A^{\sim+1} - A^{\sim*}}{\Delta t} = F(A^{\sim*}),$$

where

$$A^{\sim*} = A^{\sim} + \Delta t F(A^{\sim}).$$

This latter time step is done after the solution at time step $\text{mod}_{10} n = 0$ is smoothed according to the formulation in section 2.2.

The equations are written in finite differenced form:

Tendency

$$\frac{\partial p_s^{\sim}}{\partial t} = - \sum_{k=1}^2 H_k^{\sim}(1) \Delta \sigma_k \quad (2.4.2)$$

Continuity

$$\dot{\sigma}^{\sim} = \frac{1}{4 p_s^{\sim}} (H_2^{\sim}(1) - H_1^{\sim}(1)) \quad (2.4.3)$$

ω

$$\omega_a^{\sim} = \frac{p_s^{\sim} \dot{\sigma}^{\sim}}{\lambda} + \sigma_k \left(- \sum_{k=1}^2 H_k^{\sim}(1) \Delta \sigma_k + u_k^{\sim} G_x^{\sim}(p_s^{\sim}) + v_k^{\sim} G_y^{\sim}(p_s^{\sim}) \right) \quad (2.4.4)$$

Zonal momentum

$$\begin{aligned} \frac{\partial p_s^{\sim} u_a^{\sim}}{\partial t} = & - D_a^{\sim}(u_a^{\sim}) + p_s^{\sim} v_a^{\sim} f - R G_x^{\sim}(p_s^{\sim} T_a^{\sim}) - \\ & - \delta_{\sigma} (\sigma_k L_x^{\sim}(p_s^{\sim}, \phi_a^{\sim})) - F_{x,k}^{\sim-1} \end{aligned} \quad (2.4.5)$$

Meridional momentum

$$\begin{aligned} \frac{\partial p_s^{\sim} v_a^{\sim}}{\partial t} = & - D_a^{\sim}(v_a^{\sim}) - p_s^{\sim} u_a^{\sim} f - R G_y^{\sim}(p_s^{\sim} T_a^{\sim}) - \\ & - \delta_{\sigma} (\sigma_k L_y^{\sim}(p_s^{\sim}, \phi_a^{\sim})) - F_{y,k}^{\sim-1} \end{aligned} \quad (2.4.6)$$

Thermodynamic

$$\begin{aligned} \frac{d}{dt} p_s^m T_h^m &= - D_h^m (T_h^m) + \frac{R T_h^m \omega_h^m}{C_p \sigma_h} + \\ &+ \frac{p_s^{m-1} \dot{Q}_h^{m-1}}{C_p} + \frac{L}{C_p} p_s^{m-1} \dot{C}_{vc} \end{aligned} \quad (2.4.7)$$

Water (see section 3.1)

$$\begin{aligned} \frac{d}{dt} p_s^m q_{i,2}^m &= - H_2^m (q_{i,2}^m) + 2g F_{q_{i,2}}^{m-1} + 2g \beta_s V_i q_i \\ &- \sum C_{i,2} \end{aligned} \quad (2.4.8)$$

Geopotential

$$\phi^m = \frac{\Delta \sigma R T_2^m}{\sigma_2} \quad (2.4.9)$$

As shown by Kurihara and Holloway, the finite-difference analogues of mass and total energy are conserved for global integrals. As shown in Appendix C, total energy and mass are also conserved in our limited domain. Zonal momentum is conserved only for both our computational domain and an adjoining anti-symmetric domain; it can be transferred into and out of the domain depending on the circulation. The momentum distribution is determined consistently with the circulation rather than with some lateral walls.

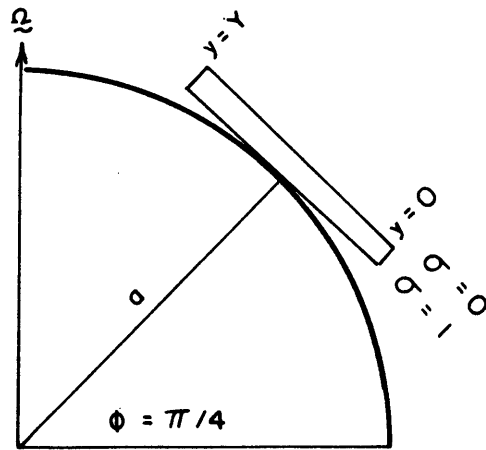


Figure 2.1a. A mid-latitude f plane channel with a vertical sigma coordinate.

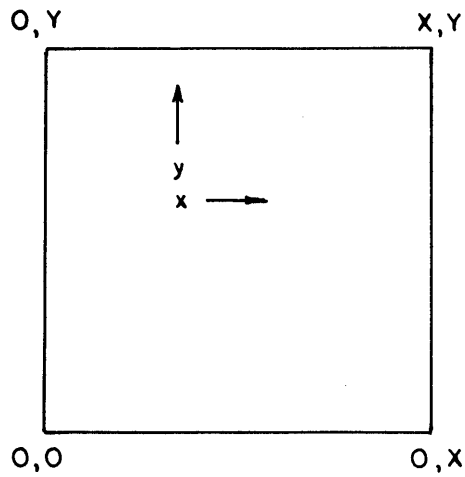


Figure 2.1b. The horizontal domain.

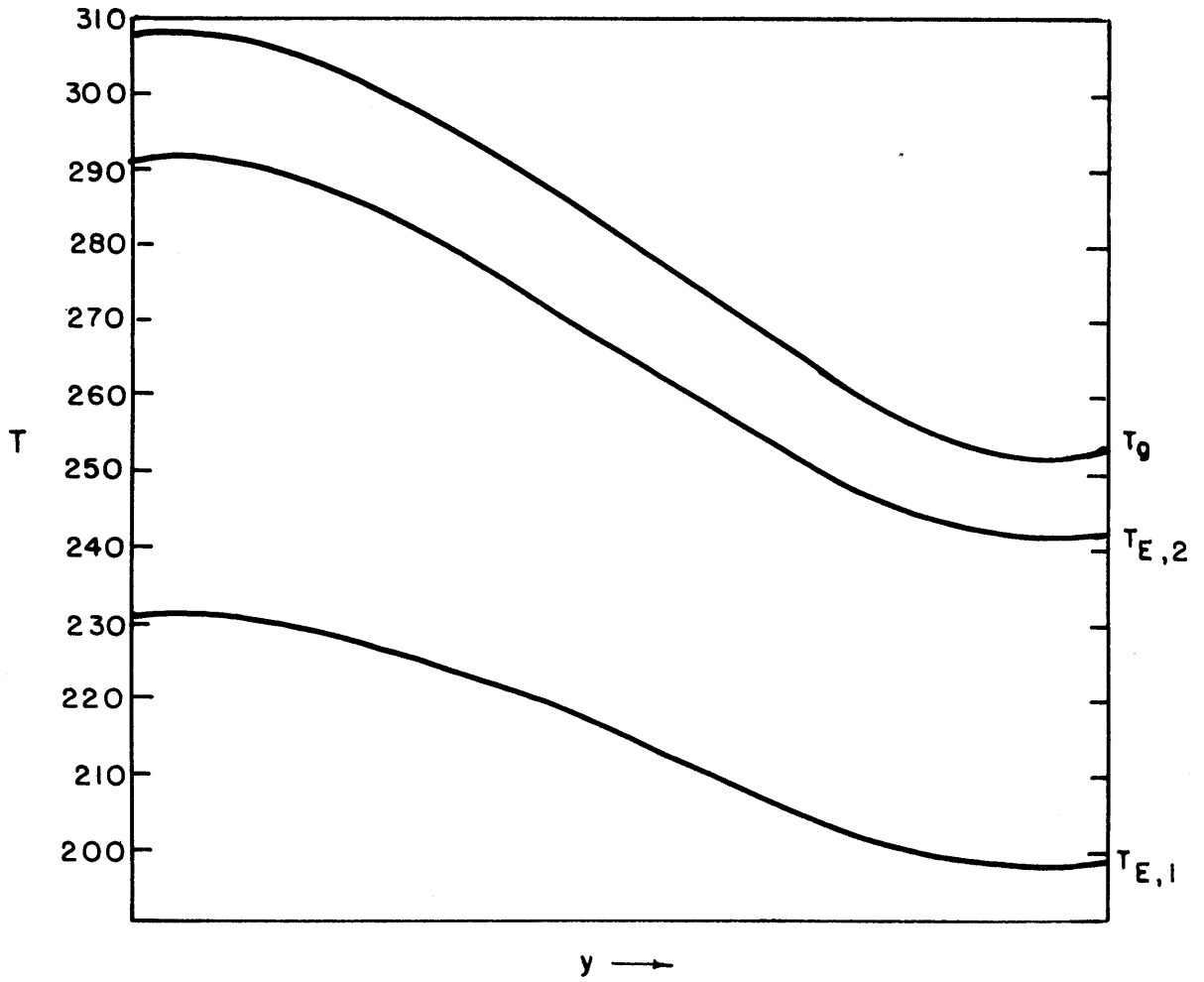


Figure 2.2a. Typical equilibrium temperature structure for the model.

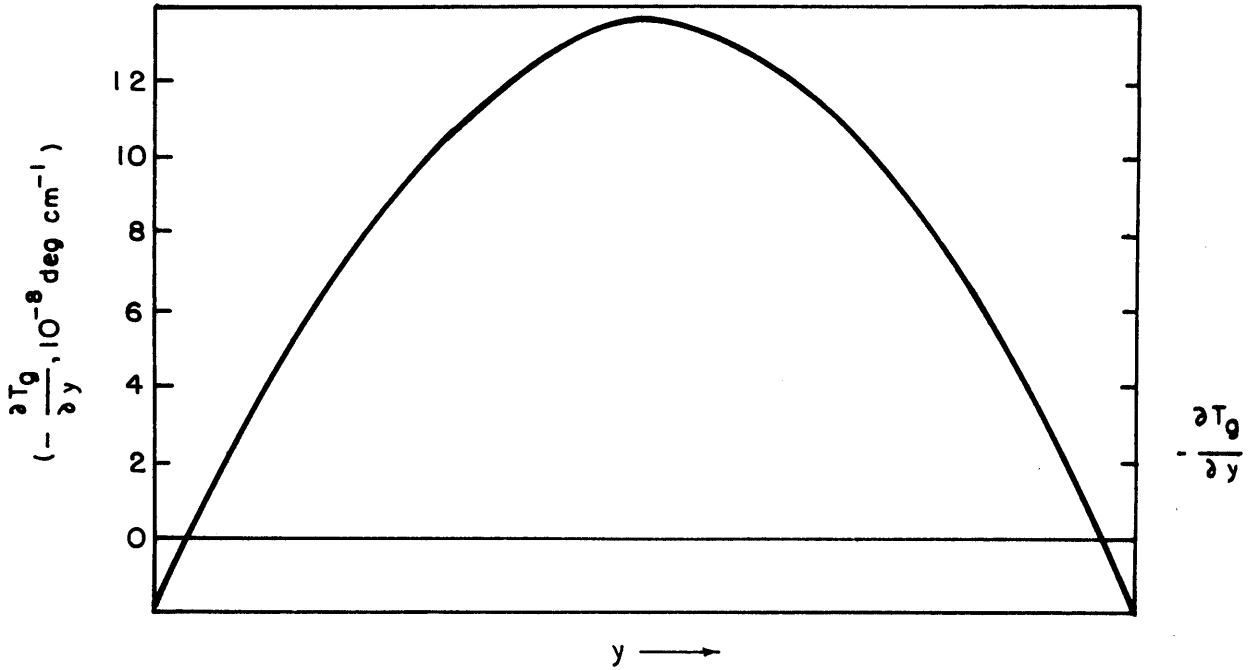


Figure 2.2b. Surface temperature gradient.

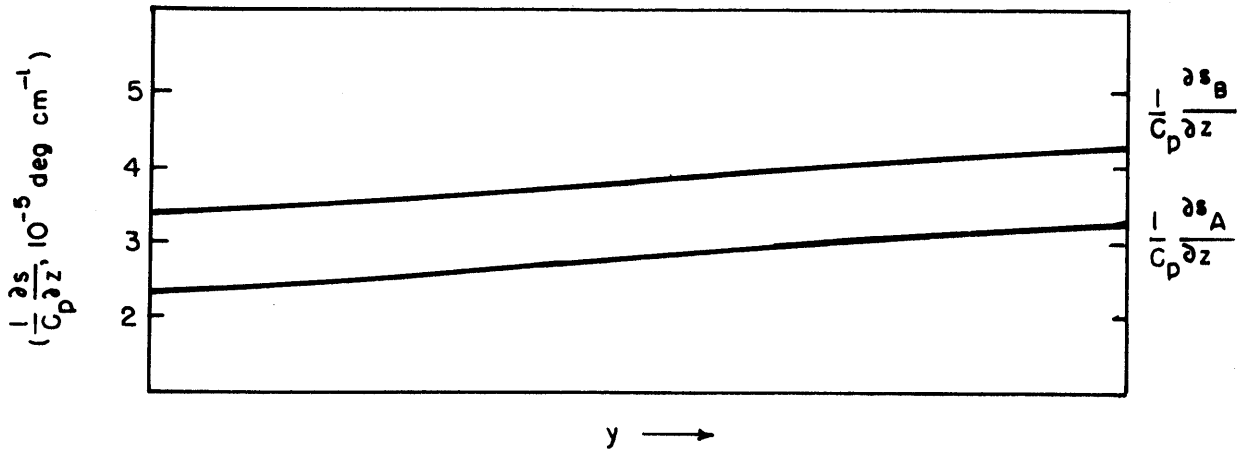


Figure 2.2c. Atmospheric and boundary-layer static stability.

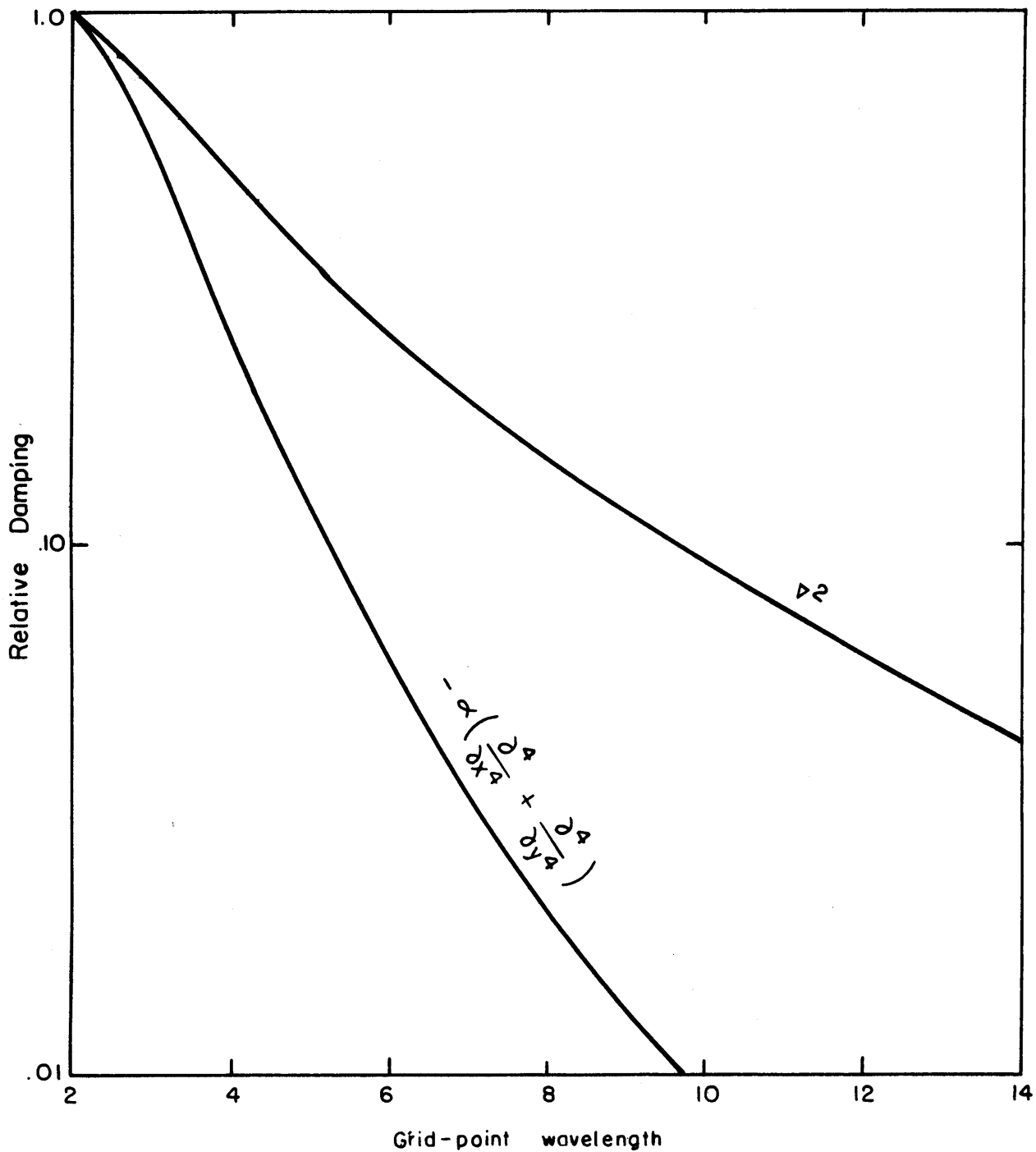


Figure 2.3. Relative damping of ∇^2 and $-\alpha$ operators versus grid-point wavelengths.

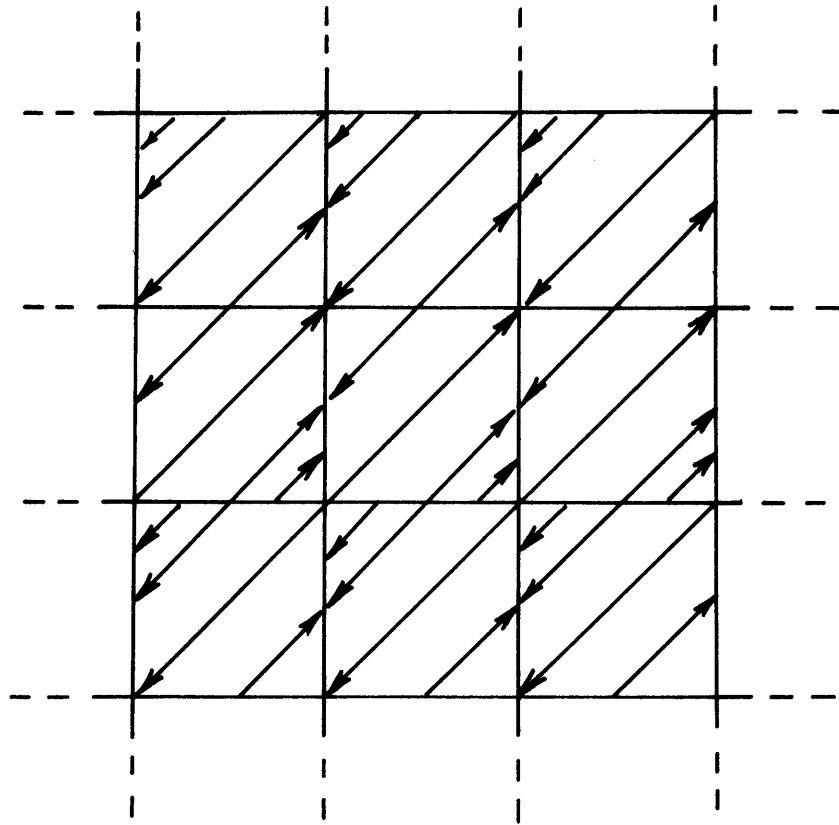


Figure 2.4. The unbounded domain and associated symmetry

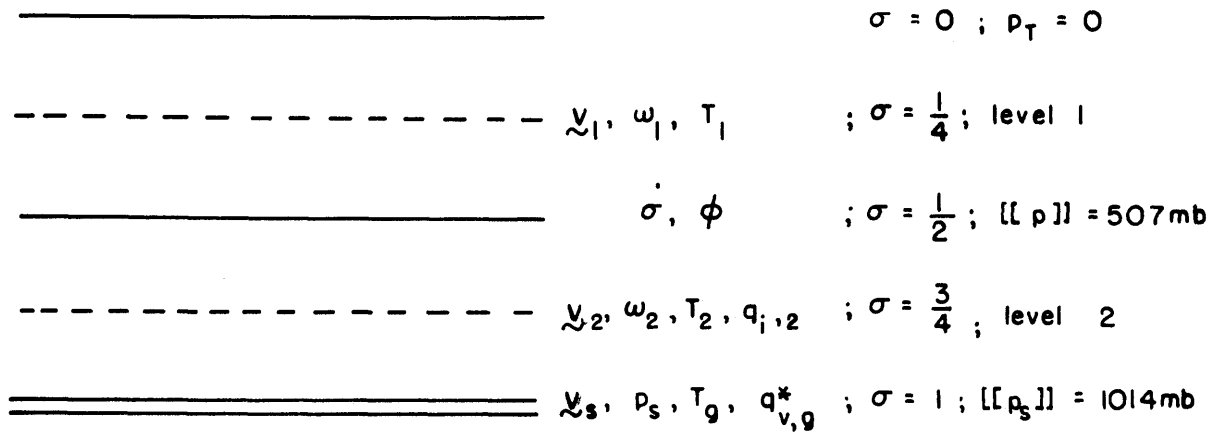


Figure 2.5a. Vertical differencing in the computational domain.

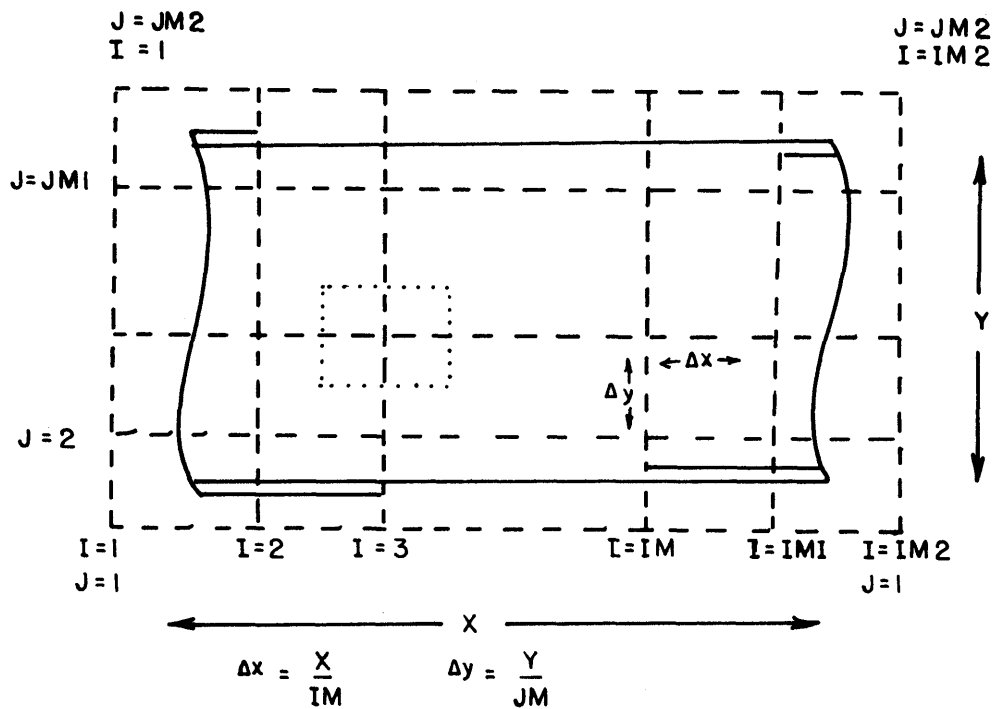


Figure 2.5b. Horizontal differencing in the computational domain.

3. Water Model

3.1 Atmospheric Water

The continuity equation for the water substance partitioned into various phases and sizes may be written

$$D'(q_i) = - p_s \sum_{j=1}^m \dot{C}_{ij} + g \frac{\partial F_{q_i}}{\partial \sigma} + g \frac{\partial}{\partial \sigma} (\rho V_i q_i). \quad (3.1.1)$$

The C_{ij} 's are the conversions from one form to another. We partition water into two phases: vapor and liquid-solid, and the liquid-solid phase into two sizes: cloud and precipitation. Explicitly:

$$D'(q_v) = - p_s \dot{C}_{vc} - p_s \dot{C}_{vp} + g \frac{\partial F_{q_v}}{\partial \sigma} \quad (3.1.2a)$$

$$D'(q_c) = p_s \dot{C}_{vc} - p_s \dot{C}_{cp} + g \frac{\partial F_{q_c}}{\partial \sigma} + g \frac{\partial}{\partial \sigma} (\rho V_c q_c) \quad (3.1.2b)$$

$$D'(q_p) = p_s \dot{C}_{vp} + p_s \dot{C}_{cp} + g \frac{\partial F_{q_p}}{\partial \sigma} + g \frac{\partial}{\partial \sigma} (\rho V_p q_p), \quad (3.1.2c)$$

where

$$D'(q_i) = \frac{\partial}{\partial t} p_s q_i + \nabla \cdot p_s \chi q_i + \frac{\partial}{\partial \sigma} p_s \sigma q_i - p_s \dot{S}(q_i). \quad (3.1.3)$$

subscript v = vapor

" c = cloud

" p = precipitation

F_q = small scale vertical turbulent flux

V_i = mass weighted sedimentation velocity, ≤ 0

C_{vc} = conversion from vapor to cloud

C_{vp} = conversion from vapor to precipitation

C_{cp} = conversion from cloud to precipitation

Since the saturation vapor pressure is related exponentially to the temperature, condensation ensures that the water vapor is an exponential function of altitude. Therefore we require that the finite difference equations conserve $\ln q$. Arakawa and Mintz (1974, eq. 111.14) have shown that this gives

$$q_{\frac{1}{2}} = \frac{\ln q_1 - \ln q_2}{\frac{1}{q_2} - \frac{1}{q_1}} \quad (3.1.4)$$

In the limit that $q_1 \rightarrow 0$ we have

$$q_{\frac{1}{2}} \rightarrow -q_1 \ln q_1 \rightarrow 0 \quad (3.1.5)$$

Since $q_{i,2} \gg q_{i,1}$ ($q_{v,2} \sim 25q_{v,1}$) we can consider the contribution by the lower level only to the atmospheric water processes. The equation for the water, then, is

$$D_t^*(q_{i,z}) = -P_s \sum_{j=1}^3 \dot{C}_{i,j,z} + \frac{1}{\Delta\sigma_z} (g F_{q_{i,s}} + f_s g V_{i,s}) \quad (3.1.6)$$

For this form of the equations, the mean water is conserved, and the observed exponential decrease of water in the atmosphere is modeled implicitly. The upper level moisture

should be included for models with more finite difference levels. The water in this form has an additional advantage for the analysis since only one vertical level has to be considered.

3.2 Surface Fluxes

At molecular distances above the sea surface in the interfacial region, the water vapor is in equilibrium with the liquid. The diffusion of water vapor away from this region would proceed slowly were it not for the turbulence generated by boundary layer eddies. This process has been parameterized by a surface bulk-evaporation formula

$$E = F_{q_{v,s}} = \rho_s C_D |V_s| (q_{v,g}^* - q_{v,s}). \quad (3.2.1)$$

C_D is determined experimentally. $q_{v,g}^*$ is the saturated mixing ratio in the inter-facial region while $q_{v,g}$ is the mixing ratio at the anemometer level. $q_{v,s}$ will increase over time to the equilibrium value of $q_{v,g}^*$ unless other processes act to decrease its value. Close to the boundary layer the only other process that can affect the surface layer mixing ratio is the turbulent transport which acts to exchange relatively moist air from below with relatively dry air from above or vice versa. Assuming an equilibrium on time scales short compared to the large scale time scales or, equivalently, a constant-flux layer, obtain

$$E = g \rho_s^2 K \frac{\partial q_v}{\partial p} \sim \rho_s^2 \frac{gK}{\Delta p} (q_{v,s} - q_{v,z}). \quad (3.2.2)$$

Solving for $q_{v,s}$ we obtain an evaporation formula applicable to our large scale model:

$$E = \rho_s C_{00} |v_s| (q_{v,g}^* - q_{v,2}), \quad (3.2.3)$$

where

$$C_{00} = \frac{C_D}{(1 + C_D |v_s| \Delta p / (\rho_s g k))} \quad (3.2.4)$$

and may be thought of as an empirical parameter applicable to the entire unresolved lower domain. When $q_{v,2} > q_{v,g}^*$ negative evaporation or net downward transport of water vapor or dew deposition occurs. This occurs only in extreme northern regions where surface inversions are likely to form in our model. For most of the domain, however, $q_{v,2} < q_{v,g}^*$ and net evaporation results. Since condensation will prohibit $q_{v,2}$ becoming greater than $q_{v,2}^*$, we see that for a reasonable boundary layer temperature differential, evaporation will continue during condensation due to turbulent diffusion. Hence turbulent diffusion can cloud the atmosphere although the process is important mainly in generating clouds with negligible precipitation. From Gates et al. (1971) we set

$$C_D = \min \left((1 + 7 \times 10^{-4} |v_s|) 10^{-3}, 2.5 \times 10^{-3} \right), \quad (3.2.5)$$

$$k = 100 |v_s| \text{ cm}^2 \text{ sec}^{-1}. \quad (3.2.6)$$

Figure 3.1 shows the evaporation formulation as a function of surface temperature for various surface wind speeds and lower-level relative humidities.

The boundary condition used for the liquid and solid particles is constant flux from the lower dynamical level of the model to the surface,

that is,

$$P_s q_{i,s} V_{i,s} = \left(P_2 V_{i,2} - \frac{P_3 \dot{\sigma}}{2g} \right) q_{i,2} \delta; \quad (3.2.7)$$

$$\delta = 1 : \left(P_2 V_{i,2} - \frac{P_3 \dot{\sigma}}{2g} \right) < 0$$

$\delta = 0$ otherwise.

The downward turbulent flux of cloud and precipitation from the upper levels as well as evaporation of sedimenting drops in the unresolved boundary layer is neglected.

3.3 Condensation

Condensation occurs instantaneously in our model, reducing the supersaturation to zero, and producing cloud particles with a size spectra. Likewise, negative condensation resulting from evaporating cloud droplets in subsaturated conditions occurs instantaneously and reduces the subsaturation condition to saturation unless sufficient cloud material is unavailable to completely saturate.

The large scale saturation limit may not be an appropriate limit. Local variations can cause clouds to occur locally even though, on the average, the large scale is unsaturated. Observable precipitation seems to be initiated at approximately 85% relative humidity. (Sanders [personal communication] and Smagorinsky [1960].)

We arbitrarily set the model limit at 100% relative humidity for clouds to condense and evaporate for most model runs. For some of the runs, however, we reduced the critical value of the relative humidity to 85%. Since the model has its own self-consistent moisture budget, the

equilibrium relative humidity obtains at a higher value in the former case. Qualitative and quantitative differences between different climates for the same critical relative humidity are similar.

Local condensation occurs such that the released latent heat warms the air isobarically, and therefore, the equilibrium humidity, cloud and temperature equations must be solved locally and simultaneously. Non-local solutions occur when the atmosphere is conditionally unstable. The moist convection scheme used is similar to Manabe et al. (1965). The scheme equilibrates the moist static energies in the vertical during condensation. Summarizing, we limit the present model to large scale supersaturation cloudiness with imbedded convective elements.

We now summarize the equations for condensation.

For

$$q_{c,2} > 0 \quad (3.3.1)$$

and

$$q_{v,2} < q_{v,2}^*$$

and

$$q_{v,2} + q_{c,2} < q_{v,2}^* - \frac{\partial q_{v,2}^*}{\partial T} \frac{L}{C_p} q_c,$$

we seek the simultaneous solution to

$$C_p \delta T + L \delta q_v = 0 \quad (3.3.2)$$

$$\delta q_v + \delta q_c = 0$$

$$\delta q_c = -q_c.$$

For

$$q_{v,z} > q_{v,z}^* \quad (3.3.3)$$

and

$$\frac{\partial h}{\partial \sigma} < 0$$

or

$$q_{c,z} > 0$$

and

$$q_{v,z} < q_{v,z}^*$$

and

$$q_{v,z} + q_{c,z} \geq q_{v,z}^* - \frac{\partial q_{v,z}^*}{\partial T} \frac{L}{C_p} q_c,$$

we seek the simultaneous solution to

$$C_p \delta T + L \delta q_v = 0 \quad (3.3.4)$$

$$\delta q_v + \delta q_c = 0$$

$$q_v + \delta q_v = q_v^*(T) + \frac{\partial q_v^*}{\partial T} \delta T.$$

For

$$q_{v,2} > q_{v,2}^* \quad (3.3.5)$$

and

$$\frac{\partial h}{\partial \sigma} \geq 0,$$

we seek the simultaneous solution to

$$\int_0^1 C_p \delta T + L \delta q_v d\sigma = 0 \quad (3.3.6)$$

$$\int \delta q_v + \delta q_c d\sigma = 0$$

$$q_v + \delta q_v = q_v^* + \frac{\partial q_v^*}{\partial T} \delta T$$

$$\frac{\partial h}{\partial \sigma} + \frac{\partial}{\partial T} \left(\frac{\partial h}{\partial \sigma} \right) \delta T + \frac{\partial}{\partial q} \left(\frac{\partial h}{\partial q} \right) \delta q = 0.$$

In particular, for the two level model, we seek the simultaneous solution to

$$C_p \delta T_1 + C_p \delta T_2 + L \delta q_{v,2} = 0 \quad (3.3.7)$$

$$\delta q_{v,2} + \delta q_{c,2} = 0$$

$$q_{v,2} + \delta q_{v,2} = q_{v,2}^* + \frac{\partial q_{v,2}^*}{\partial T} \delta T_2$$

$$\frac{\partial h}{\partial \sigma} + \frac{C_p}{\Delta \sigma} (\delta T_2 - \delta T_1) - \frac{R}{2\sigma_{3/2}} (\delta T_1 + \delta T_2) + \frac{L}{\Delta \sigma} \delta q_{v,2} = 0.$$

The various schemes can be iterated for better accuracy since we have approximated

$$q_v^*(T + \delta T) \sim q_v^*(T) + \frac{\partial q_v^*}{\partial T} \delta T \quad (3.3.8)$$

3.4 Precipitation

The conversion of cloud water to precipitation is an extremely complex process and still unknown in complete physical detail. We parameterize the conversion with an expression that depends only upon cloud water and neglect the conversion from vapor to precipitation. Since this parameterization has not yet been completely formulated for even the small scale cloudiness, we determine a parameterization for the large scale finite difference model tentatively from physical considerations. Numerical values of the parameterized conversion rate are then tested for sensitivity. We feel that the qualitative form, although perhaps not the quantitative form, of the parameterization is fairly reasonable. Various climatic and weather modification effects could be represented by changes in the parameterization.

The following processes are thought to be the dominant contributors to the conversion. Initially, small cloud droplets self-collect to form larger cloud droplets and small precipitation particles. This process is denoted autoconversion and was first parameterized by Kessler (1969) intuitively. It seemed reasonable to him from various studies that the rate of cloud autoconversion increased with cloud water content and was negligible for amounts below some arbitrary threshold. Marchuk (1974), in fact, uses autoconversion to describe the complete conversion process. Berry (cf. Simpson and Wiggert, 1969) solved the stochastic collection problem numerically and developed a parameterization in which the autoconversion process had, essentially, a cubic dependence upon the cloud water, a dependence upon the relative dispersion of the initial cloud spectrum and an inverse dependence upon the number concentration. The

Kessler and Berry parameterizations give qualitatively similar results.

The Bergeron process also contributes to the formation of small precipitation particles by augmenting ice particles at the expense of liquid water in addition to sublimating vapor. This process is not considered although Simpson and Wiggert (1969) suggest that using a faster auto-conversion time scale may implicitly model this effect. We test the sensitivity of this process later by using different autoconversion time scales.

Once small precipitation particles are formed, either by autoconversion or by the Bergeron process, they further collect small cloud droplets and continue to grow until they precipitate from the cloud. This mode is denoted as accretion and is dependent on the amount of cloud water and precipitation water. This process is thought to be the dominant contributor to atmospheric precipitation. It has been parameterized by Kessler (1969) by using a simplified model of cloud-precipitation interaction. He obtained, essentially, a first-order dependence upon cloud vapor and precipitation.

Precipitation droplets differ from cloud droplets by having between one thousand to a million times more mass per drop. Observations by Marshall and Palmer (1948) give a raindrop distribution of the form

$$\text{distribution} = N_{o,p} \exp(-\lambda_p D) \quad (3.4.1)$$

Kessler (1967) argues that $N_{o,p}$ is constant over a wide range of $\rho_{q,p}$ and hence λ_p must be a function of the precipitation water content. We also assume that the distribution of cloud particles follows a similar form but with $N_{o,c} \gg N_{o,p}$. Obviously the spectrum must evolve over time from

from $N_{o,c}$ to $N_{o,p}$. Various other types of distribution could be considered but since we are interested in mass weighted averages of various quantities, any distribution describing the observed exponential tail on the large size range would suffice. Particularly important is that this distribution gives an increase in the average drop size and variance for an increase in the water content. Solving for λ_i obtain

$$\lambda_i = \left(\frac{\rho_w \pi N_{o,i}}{\rho q_c} \right)^{1/4}, \quad (3.4.2)$$

where

$$\rho = \text{air density, g/cm}^3,$$

$$\rho_w = \text{water density, g/cm}^3.$$

The size distribution will vary depending upon the initial size distribution and time history. Quite arbitrarily - with some appeal to observation - we use Kessler's (1969) value $N_{o,p} = .1 \text{ cm}^{-4}$ for the precipitation particles and use a value of $N_{o,c} = 10^5 \text{ cm}^{-4}$ for the cloud particles.

Using this distribution, Berry's autoconversion formula is

$$\dot{A}C = \frac{8.574 \times 10^{11} (\rho q_c)^{1/4} q_c}{N_{o,c}^{3/4}} \text{ sec}^{-1} \quad (3.4.3)$$

Kessler's accretion formula is:

$$\dot{A}C_R = .619 \times 10^3 N_{o,p}^{1/8} (\rho q_p)^{7/8} \left(\frac{\rho_e}{\rho} \right)^{1/2} q_c \text{ sec}^{-1} \quad (3.4.4)$$

Using the size distribution for precipitation particles; using an empirical expression for precipitation fall speed as a function of diameter; and taking a mass-weighted average over the size distribution, Kessler (1967) obtained

$$\bar{V}_p = -2.154 \times 10^3 \left(\frac{\rho q_p}{N_{o,p}} \right)^{1/8} \left(\frac{\rho_e}{\rho} \right)^{1/2} \text{ cm sec}^{-1} \quad (3.4.5)$$

The sedimentation of cloud droplets is obtained by using Stokes Law for the small cloud droplets and taking a mass weighted average over the assumed size distribution. We obtain

$$V_c = -3.154 \times 10^6 \left(\frac{\rho q_c}{N_{0,c}} \right)^{1/2} \text{ cm sec}^{-1} \quad (3.4.6)$$

If, as precipitation is formed, the vertical fallout is sufficiently large compared to the horizontal divergence, only a negligible fraction of the precipitation is diverted from the actively converting region. Therefore, for the large scale motions, only local processes are important for precipitation. This approximation is good so long as we consider large-scale equilibrium for particles with a sufficiently large fall speed. It would not be a good approximation, for example, for the smaller scale motions involved with individual cumulus clouds (see Kessler, 1967). Neither is it a good approximation for cloud particles on the large scale. The complete continuity equation must be considered for this size range of particles.

The local time rate of change precipitation content is neglected and we can solve for the equilibrium precipitation water if we neglect the evaporation of precipitating water. Essentially we assume that the cloud extends from the middle part of the atmosphere to the surface. The equilibrium solution is therefore more applicable to total time averaged cloud water contents rather than instantaneous local quantities. Accordingly, we may expect that the mixing ratio so determined will be small locally, but the total water should be comparable to the observed.

The precipitation equation is

$$0 = P_s k_{AC} q_c^{1/4} + k_{ACR} q_p^{7/8} q_c - k_{sp} P_s q_p^{9/8}, \quad (3.4.7)$$

where

$$R_{AC} = \frac{8.574 \times 10^{11} \rho^{7/4}}{N_{0,c}^{3/4}} \sim 8.574 \times 10^2 \text{ sec}^{-1} \quad (3.4.8)$$

$$R_{ACR} = .619 \times 10^3 N_{0,p}^{1/9} \left(\frac{p_0}{p}\right)^{1/2} \rho^{7/8} \sim 1.221 \text{ sec}^{-1}$$

$$R_{sp} = 2 \times 9 \times 2.515 \times 10^3 \rho^{9/8} \frac{\left(\frac{p_0}{p}\right)^{1/2}}{N_{0,p}^{1/9} p_s} \sim 2.599 \times 10^3 \text{ sec}^{-1}$$

We have assumed that the dominant variation occurs in q_c rather than in ρ and p_s .

An asymptotic solution to 3.4.7 can be made up of two asymptotic solutions; the autoconversion limit for q_c and the accretion limit for large q_c . The autoconversion limit occurs for small q_c ; by the time a relatively sparse cloud has converted some of its smaller cloud droplets into precipitating droplets, the droplets have reached the surface without being able to collect many more droplets. In the autoconversion limit

$$q_p = \left(\frac{R_{AC}}{R_{sp}}\right)^{8/9} q_c^{22/9} \quad (3.4.9)$$

and hence, sparse clouds produce tiny precipitation particles - drizzle.

For more dense clouds, however, once the conversion of small cloud droplets to small precipitation particles has occurred, substantial growth by accretion occurs producing large precipitation particles and much precipitation. From 3.4.7 in the accretion limit,

$$q_p = \left(\frac{R_{ACR}}{R_{sp}}\right)^4 q_c^4 \quad (3.4.10)$$

The precipitation from the column is determined as a function of

cloud water to be

$$\begin{aligned}
 -\rho_s V_p q_{p,s} &= k_{sp} \left(\frac{k_{ACR}}{k_{sp}} \right)^{3/2} q_c^{3/2} \frac{\rho_s}{2g} + & (3.4.11) \\
 &+ k_{AC} q_c^{1/4} \frac{\rho_s}{2g}.
 \end{aligned}$$

We define a precipitation function to include also the sedimentation of cloud droplets from the atmosphere column. The sedimentation is

$$-\rho_s V_c q_{c,s} = k_{sc} \rho_s q_c^{3/2} \quad (3.4.12)$$

where

$$k_{sc} = \frac{3.514 \times 10^6 \rho^{3/2}}{N_{0,c}^{1/2} \rho_s} \sim 3.466 \times 10^{-7} \text{ sec}^{-1} \quad (3.4.13)$$

The precipitation function is

$$\dot{P} = \alpha_1 q_c^{3/2} + \alpha_2 q_{c,2}^{1/4} + \delta \left(\alpha_3 q_{c,2}^{3/2} + \frac{\dot{\sigma}}{2} q_c \right) \text{ sec}^{-1} \quad (3.4.14)$$

where

$$\alpha_1 = k_{sp} \left(\frac{k_{ACR}}{k_{sp}} \right)^{3/2} = 2.744 \times 10^9 \text{ sec}^{-1}, \quad (3.4.15)$$

$$\alpha_2 = k_{AC} = 8.574 \times 10^2 \text{ sec}^{-1},$$

$$\alpha_3 = 2 \times g \times k_{sc} = 6.800 \times 10^{-4} \text{ sec}^{-1},$$

$$\delta = 1 : \left(\alpha_3 q_{c,2}^{3/2} + \frac{\dot{\sigma}}{2} q_c \right) > 0,$$

$$\delta = 0 : \text{ otherwise.}$$

The number of assumptions involved in obtaining the precipitation function is quite large. We assume: a constant flux between the surface and the lowest dynamical level, size distributions approximated by

exponential laws, a precipitation time scale which is small compared to the large scale advection time scale, and that N_{0c} and $N_{0,p}$ are known constants. Various assumptions might result in quantitative differences in the precipitation function. For example: if the size distribution is neglected in deriving the accretion and precipitation sedimentation terms, a cubid dependence of precipitation on cloud water for accretion would be obtained; if the Bergeron process were included, the appropriate saturation limit would be over a combination of ice and water and the autoconversion would be increased; if more vertical levels were present to resolve cloud base, and cloud-water content would probably be increased locally in the cloud; and if evaporation of precipitation in the boundary layer were included, the initial precipitation at the surface would be negligible.

We therefore think that the precipitation parameterization is qualitatively accurate only in the sense that the precipitation time constant, $\tau_p = \frac{q_c}{P}$, is a nonlinear function of cloud-water content. Whether or not the coefficients are accurate for large scale average cloud water amounts requires much more work with models of this sort. To test the sensitivity of the precipitation function on our eventual conclusions we fit the following function

$$\dot{P}_2 = \sum_{n=1}^3 a_n q_c^n = \sum_{n=1}^3 \alpha_n q_c^{\times n} \quad (3.4.16)$$

and used a much less efficient cloud-precipitation conversion

$$\dot{P}_3 = \sum_{n=1}^3 a_n (q_c/s)^n \quad (3.4.17)$$

Use of \dot{P}_3 increased the amount of equilibrium cloud water present.

It was interesting that for cloud water contents $\sim 3 \times 10^{-2} \text{ g cm}^{-1}$ the associated time constant of \dot{P}_1 is 2×10^4 sec, which is somewhat larger than Sasamori's (1975) ($\tau_p = 10^4$ sec for $\{q_c\} = 3 \times 10^{-2}$). Sasamori used observations of cloud and precipitation to obtain his precipitation parameterization. Hence we may be underestimating the precipitation for our model cloud-water contents.

3.5 Summary

We have formulated the parameterizations involved in the simplified atmospheric hydrologic cycle. Evaporation (dew deposition) occurs if the mixing ratio decreases (increases) upward. The rate at which this proceeds is dependent upon the vertical moisture gradient and the surface wind speed.

Condensation (cloud evaporation) occurs once the atmosphere super-saturates (sub-saturates with clouds present). Condensation (cloud evaporation) can occur due to radiative and sensible cooling (heating), turbulent mixing, and adiabatic temperature changes. Condensation is local unless the atmosphere is moist-adiabatically unstable in which case the moist static energies in the vertical are equilibrated. Condensation produces clouds which then either evaporate or precipitate. Precipitation is assumed to be a nonlinear function of cloud water content. The equations are summarized below:

$$\begin{aligned} \frac{\partial p_s q_{v,2}}{\partial x} + \nabla \cdot p_s \underline{v}_2 q_{v,2} - p_s \dot{S}(q_{v,2}) &= \quad (3.5.1) \\ &= 2 p_s g C_{00} |\underline{v}_s| (q_{v,2}^* - q_{v,2}) - p_s \dot{C}_{vc,2}, \end{aligned}$$

$$\begin{aligned} \frac{d}{dt} P_s q_{c,2} + \nabla \cdot P_s v_2 q_{c,2} - P_s \dot{S}(q_{c,2}) &= & (3.5.2) \\ &= P_s \dot{C}_{vc,2} - P_s \dot{P}_1 \end{aligned}$$

$$C_{00} = \frac{C_0}{(1 + C_0 R T_s / (100 \times g \times 4))} \quad (3.5.3)$$

The precipitation function is taken to be one of the following three forms:

$$\dot{P}_1 = \sum_{n=2}^3 \alpha_n q_c^{x_n} + \delta \left(\alpha_1 q_c^{x_1} + \frac{\dot{q}}{2} q_c \right) \quad (3.5.4a)$$

$$\begin{aligned} \alpha_1 &= 6.800 \times 10^{-4} & ; & \quad x_1 = 1.5 \\ \alpha_2 &= 8.574 \times 10^2 & ; & \quad x_2 = 2.75 \\ \alpha_3 &= 2.744 \times 10^9 & ; & \quad x_3 = 4.5 \\ \delta &= 1 & : & \quad \left(\frac{\dot{q}}{2} q_c + \alpha_1 q_c^{x_1} \right) > 0 \\ \delta &= 0 & : & \quad \text{otherwise} \end{aligned}$$

$$\dot{P}_2 = \sum_{n=1}^3 a_n q_c^n \quad (3.5.4b)$$

$$\begin{aligned} a_1 &= 9.37 \times 10^{-7} \\ a_2 &= 7.28 \times 10^{-3} \\ a_3 &= 1.11 \times 10^4 \end{aligned}$$

$$\dot{P}_3 = \sum_{n=1}^3 a_n (q_c/3)^n \quad (3.5.4c)$$

The conditional quantity $\dot{C}_{vc,2}$ is

Conditions

Conversion

$$q_{c,2} > 0$$

and

$$\dot{C}_{vc,2} = \frac{-q_{c,2}}{2\Delta t}$$

(3.5.5a)

$$q_{v,2} < q_{v,2}^*$$

and

$$q_{v,2} + q_{c,2} < q_{v,2}^* - \frac{\partial q_{v,2}^*}{\partial T} \frac{L}{C_p} q_c$$

$$q_{v,2} > q_{v,2}^*$$

$$\dot{C}_{vc,2} = \frac{\Delta q}{2\Delta t}$$

(3.5.5b)

and

where

$$\frac{\partial h}{\partial \sigma} < 0$$

$$\gamma = 1 + \frac{L}{C_p} \frac{\partial q_{v,2}^*}{\partial T}$$

or

$$\Delta q = q_{v,2} - q_{v,2}^*$$

$$q_{c,2} > 0$$

and

$$q_{v,2} < q_{v,2}^*$$

and

$$q_{v,2} + q_{c,2} \geq q_{v,2}^* - \frac{\partial q_{v,2}^*}{\partial T} \frac{L}{C_p} q_c$$

Conditions

$$q_{v,2} > q_{v,2}^*$$

and

$$\frac{\partial h}{\partial \sigma} \geq 0$$

Conversion

$$\dot{C}_{v,c,2} = -\frac{\delta q_v}{2 \Delta t} \quad (3.5.5c)$$

where

$$\delta q_v = -\frac{C_p}{L} (\delta T_1 + \delta T_2)$$

$$\delta T_2 = \frac{\left(\frac{L \Delta q_v}{C_p} - \delta T_1 \right)}{\gamma}$$

$$\delta T_1 = \frac{\left(\gamma \Delta h - \frac{L R \Delta q_v}{2 C_p} \right)}{\left(2 C_p + (\gamma - 1) \left(2 C_p + \frac{R}{2} \right) \right)}$$

$$h = C_p T + g z + L q_v$$

$$\Delta h = C_p \Delta T - R T \frac{\Delta \sigma}{\sigma} + L q_{v,2}$$

$$\Delta T = T_2 - T_1$$

$$T = \frac{(T_1 + T_2)}{2}$$

$$\dot{Q}_{1,c} = \frac{C_p \delta T_1}{2 \Delta t}$$

$$\dot{Q}_{2,c} = \frac{(C_p \delta T_2 + L \delta q_v)}{2 \Delta t}$$

Condensation, precipitation, and evaporation are evaluated via a forward difference time scheme. In the leapfrog scheme they are evaluated at the previous time step. Water vapor and cloud water are not allowed to be negative. This can occur due to finite differencing. Evaporation is increased and/or precipitation is decreased at the particular grid point at which this happens during the course of the time integration.

The qualitative atmospheric hydrologic cycle is shown in figure 3.3. Note that evaporation of precipitation has not been included in this hydrologic cycle. This and other boundary layer processes need to be considered eventually, but for now the parameterizations are sufficiently simple that we can consider analytic models to determine some of the feedbacks involved in the hydrologic cycle.

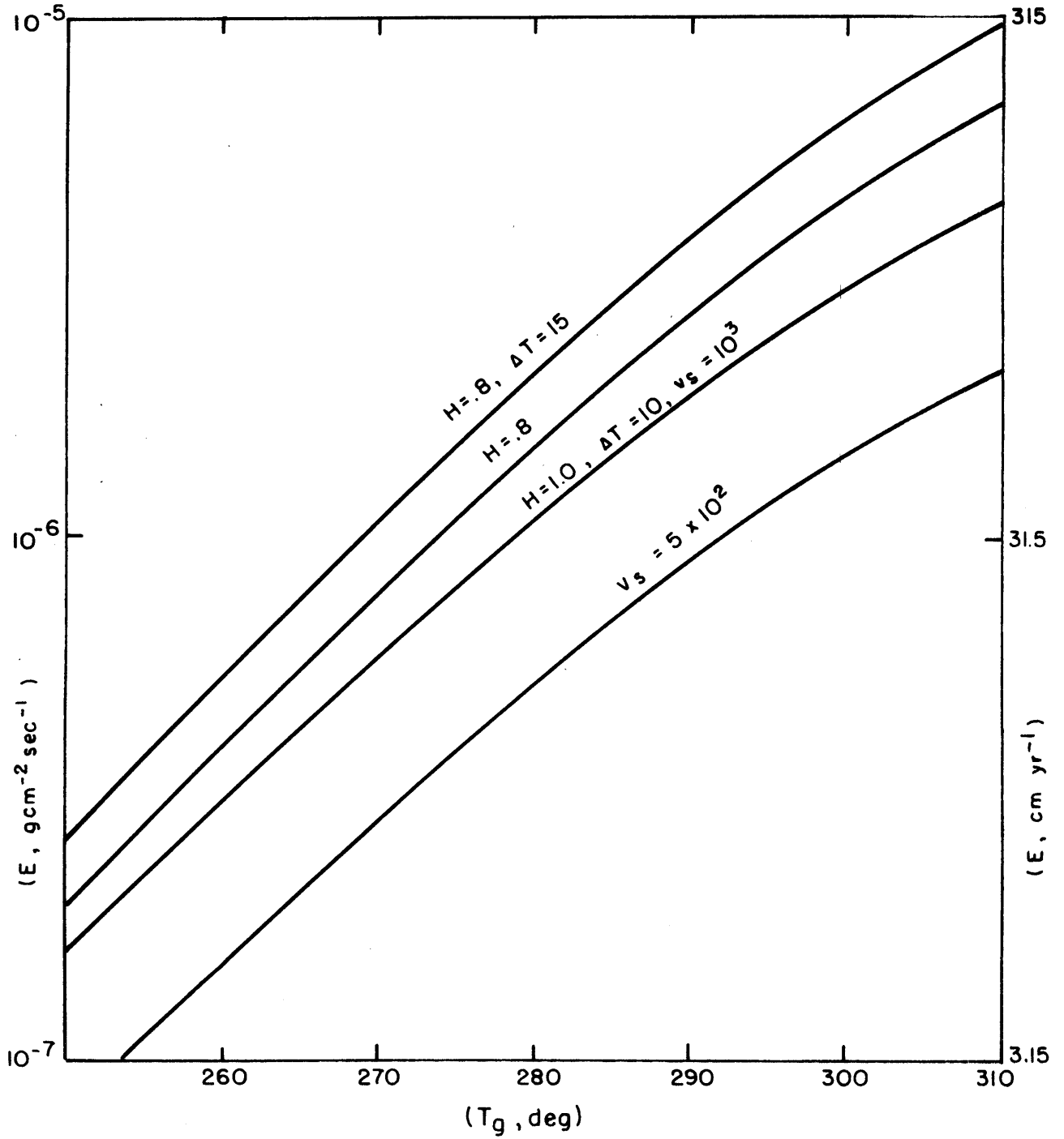


Figure 3.1. The evaporation parameterization.

$$E = \rho_s C_{DD} |\underline{v}_s| (q_{v,g}^* - Hq_{v,2}^*)$$

for various parameters

H = lower level relative humidity

ΔT = boundary-layer temperature differential

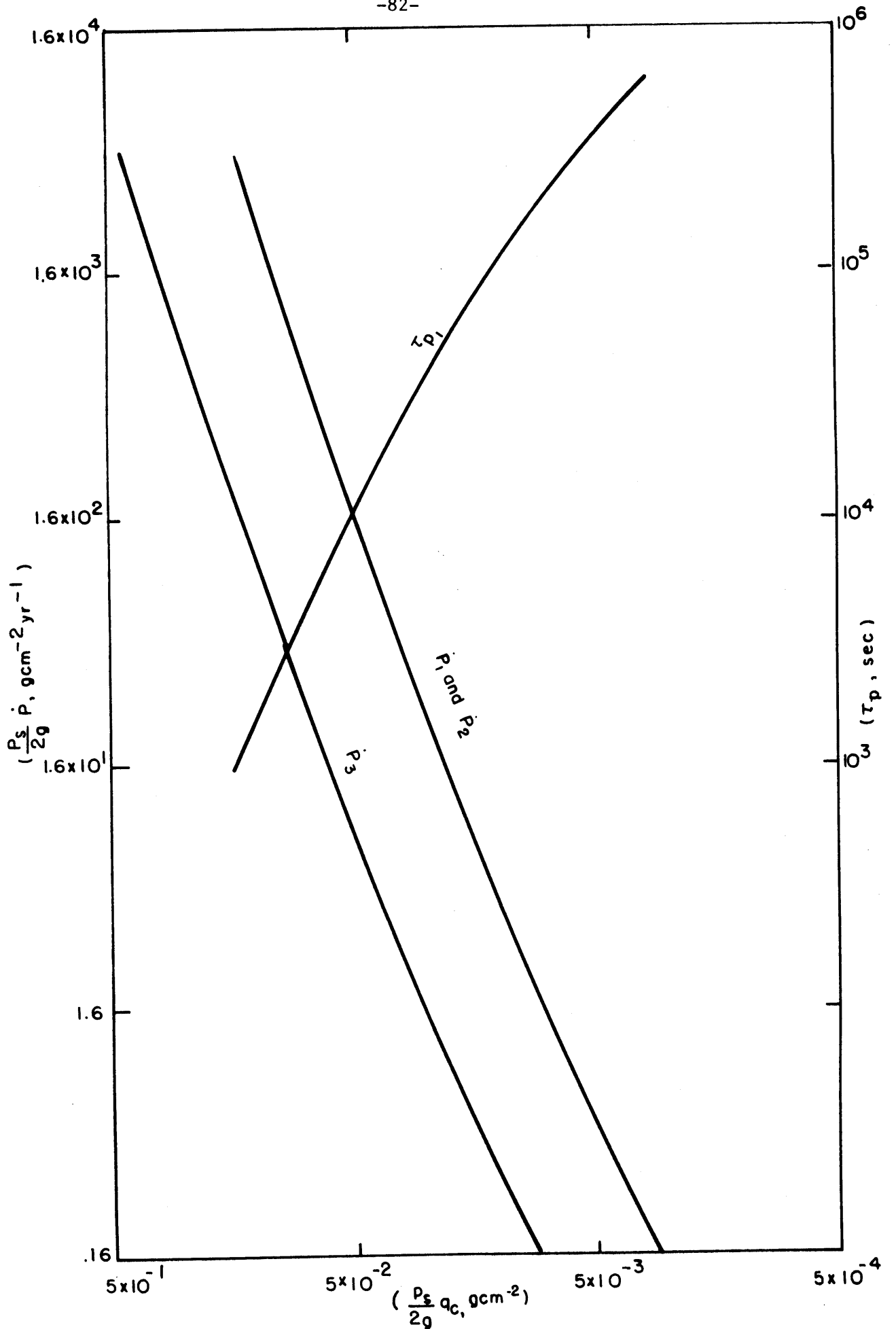


Figure 3.2. Precipitation functions and precipitation time constant.

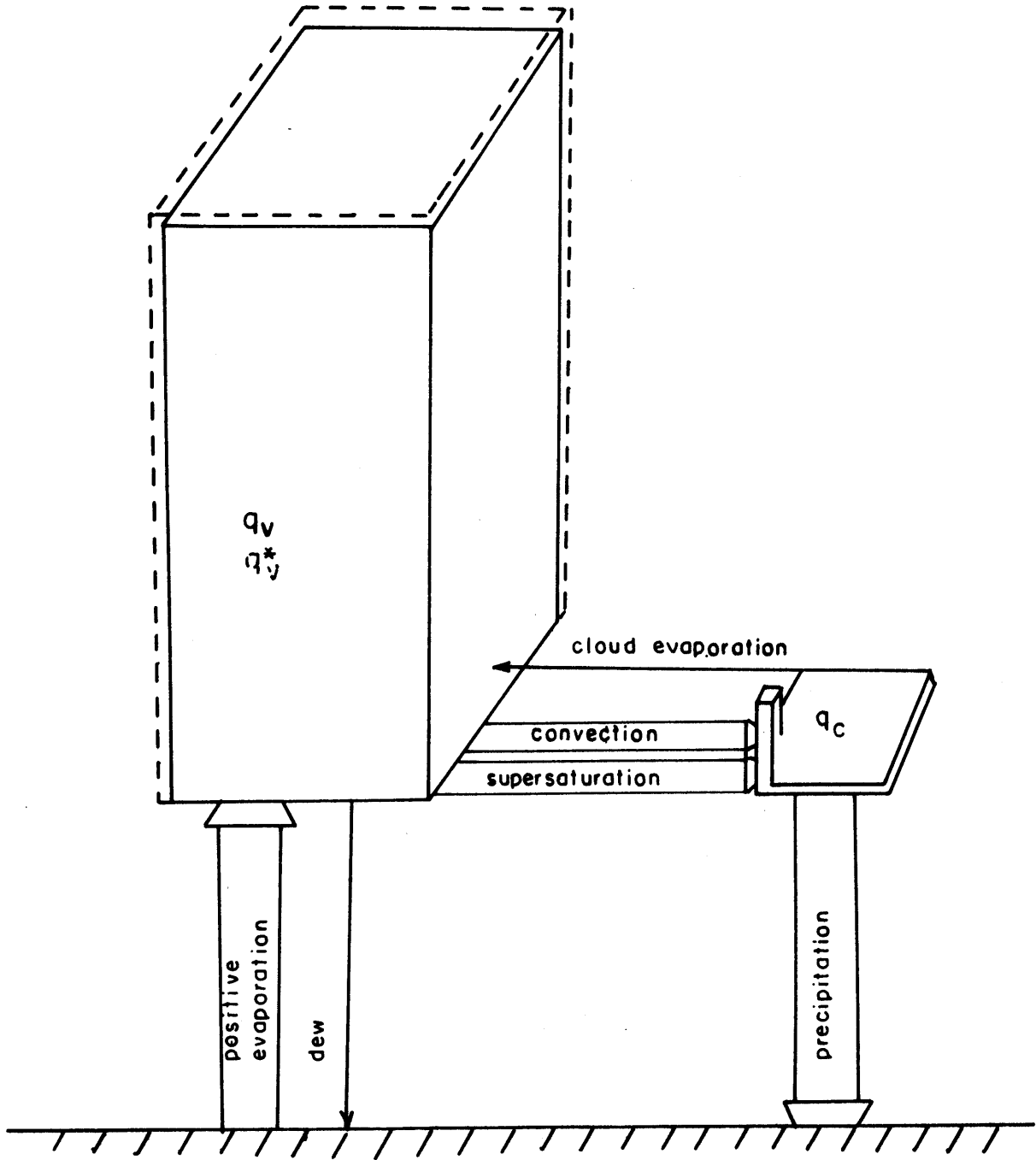


Figure 3.3. The atmospheric hydrologic cycle. Water is exchanged with the surface through evaporation, dew deposition and precipitation. Gaseous water is converted to cloud water through convective and supersaturation condensation. Some cloud water is reevaporated. Cloud water and the difference between the saturation water vapor and actual water vapor is small compared to the actual water vapor.

4. Sensitivities of the Water Distribution

4.1 Relative-Humidity Equation

Before we discuss the more complex numerical model results, we analyze the relative-humidity equation, in order to determine the dependence of the water distribution on the various parameters, and the inter-relationships between the relative-humidity, fractional coverages, and precipitation. The relative humidity equation is derived for our model from the water-vapor, cloud-water, lower level-temperature, mass-continuity and pressure-velocity equations:

$$\frac{\partial}{\partial x} p_s q_{v,2} = -\nabla \cdot p_s \underline{v}_2 q_{v,2} + 2 g p_s C_{00} |\underline{v}_s| (q_{v,1g}^* - q_{v,2}) - p_s \dot{C}_{vc,2} \quad (4.1.1)$$

$$\frac{\partial}{\partial x} p_s q_{c,2} = -\nabla \cdot p_s \underline{v}_2 q_{c,2} + p_s \dot{C}_{vc,2} - p_s \dot{P} \quad (4.1.2)$$

$$p_s \left(\frac{\partial T_2}{\partial x} \right) = - p_s \underline{v}_2 \cdot \nabla T_2 + p_s \dot{\sigma} (p_s S) + \frac{L}{C_p} p_s \dot{C}_{vc,2} + \frac{\dot{Q}_2 p_s}{C_p} + (w_2 - p_s \dot{\sigma} / 2) \frac{RT_2}{2C_p \sigma_2} \quad (4.1.3a)$$

where

$$S = \frac{(T_1 - T_2)}{2 \Delta \sigma p_s} + \frac{RT_2}{2C_p p_2} \quad (4.1.3b)$$

$$\frac{\partial p_s}{\partial t} = -\nabla \cdot p_s \underline{v}_2 + \frac{p_s \dot{\sigma}}{\Delta \sigma} \quad (4.1.4)$$

$$\omega_2 = \frac{p_s \dot{\sigma}}{2} + \sigma_2 \left(\frac{\partial p_s}{\partial t} + \underline{v}_2 \cdot \nabla p_s \right). \quad (4.1.5)$$

The appropriate* relative humidity for our model is

$$H = q_{v,2} / q_{v,2}^*. \quad (4.1.6)$$

The relative-humidity equation is

$$\begin{aligned} \frac{\partial}{\partial t} p_s q_{v,2}^* H = & -\nabla \cdot p_s \underline{v}_2 q_{v,2}^* H + 2 g p_s C_{00} |\underline{v}_s| (q_{v,2}^* - H q_{v,2}^*) - \\ & - p_s \dot{C}_{vc,2}. \end{aligned} \quad (4.1.7)$$

With the continuity equation 4.1.4, the omega equation 4.1.5, and the functional relationship

$$q_{v,2}^* = q_{v,2}^*(T, p), \quad (4.1.8)$$

the relative-humidity equation, 4.1.7, becomes

$$\begin{aligned} p_s q_{v,2}^* \left(\frac{\partial H}{\partial t} \right) = & - p_s q_{v,2}^* \underline{v}_2 \cdot \nabla H - \frac{p_s \dot{\sigma}}{\Delta \sigma} q_{v,2}^* H - \\ & - p_s H \frac{\partial q_{v,2}^*}{\partial T} \left(\frac{\partial T_2}{\partial t} + \underline{v}_2 \cdot \nabla T_2 \right) - p_s H \frac{\partial q_{v,2}^*}{\partial p} \left(\omega_2 - \frac{p_s \dot{\sigma}}{2} \right) + 2 p_s g C_{00} |\underline{v}_s| (q_{v,2}^* - q_{v,2}^* H) - \\ & - p_s \dot{C}_{vc,2}. \end{aligned} \quad (4.1.9)$$

* The exact relative humidity, e/e^* , is approximated very well by $\frac{e}{e^*} \frac{(p-e^*)}{(p-e)}$ since $p \gg e^*$.

Substituting 4.1.3 into 4.1.9, we obtain

$$\begin{aligned}
 p_s q_{v,2}^* \frac{\partial H}{\partial x} = & - p_s q_{v,2}^* v_2 \cdot \nabla H - \frac{p_s \dot{\sigma}}{\partial \sigma} q_{v,2}^* H - \\
 & - p_s H \frac{\partial q_{v,2}^*}{\partial T} \left(p_s \dot{\sigma} S + \frac{L}{C_p} p_s \dot{C}_{vc,2} + \dot{Q}_2 \frac{p_s}{C_p} \right) + \\
 & + 2 p_s g C_{00} |v_3| (q_{v,2}^* - q_{v,2}^* H) \\
 & - p_s \dot{C}_{vc,2} \\
 & - \left(\omega_2 - \frac{p_s \dot{\sigma}}{2} \right) p_s H \left(\frac{\partial q_{v,2}^*}{\partial T} \frac{RT_2}{2C_p p_2} + \frac{\partial q_{v,2}^*}{\partial p} \right).
 \end{aligned} \tag{4.1.10}$$

Dividing 4.1.10 by $p_s q_{v,2}^*$ and combining certain terms, we

$$\begin{aligned}
 \frac{\partial H}{\partial x} = & - v_2 \cdot \nabla H \\
 & + \left(2gC_{00}|v_3| \left(\frac{q_{v,2}^*}{q_{v,2}^*} - H \right) - H \frac{\dot{Q}_2}{C_p} \frac{\partial \ln q_{v,2}^*}{\partial T} \right) - \\
 & - H p_s \dot{\sigma} \left(\frac{1}{\Delta p} + \frac{\partial \ln q_{v,2}^*}{\partial T} S \right) - \\
 & - \dot{C}_{vc,2} \left(\frac{1}{q_{v,2}^*} + \frac{L}{C_p} H \frac{\partial \ln q_{v,2}^*}{\partial T} \right) + \\
 & + H \left(\omega_2 - \frac{p_s \dot{\sigma}}{2} \right) \left(\frac{\partial \ln q_{v,2}^*}{\partial p} + \frac{\partial \ln q_{v,2}^*}{\partial T} \frac{RT_2}{2C_p p_2} \right).
 \end{aligned} \tag{4.1.11}$$

The relative-humidity equation is similar to the one obtained by Smagorinsky (1960) except for the second term on the right - which represents the evaporation and radiative-sensible heating.

The relative humidity can be increased by advection of relative humidity, by evaporation, by radiative and sensible cooling, by

rising motion, and by negative condensation (cloud evaporation). The sixth term on the right hand side of 4.1.11 is the correction for motion not occurring at constant pressure. This equation is to be used in two different ways. We solve for the relative humidity only if the initial relative humidity is less than one. If the relative humidity becomes greater than one, the equation can be used to solve for the positive condensation by setting the relative humidity to one. This positive condensation produces cloud water which has the equation (substituting $\dot{C}_{vc,2}$ from 4.1.2)

$$\begin{aligned}
 & \left(\frac{1}{q_{v,2}^*} + \frac{L}{C_p} H \frac{\partial \ln q_{v,2}^*}{\partial T} \right) \left(\frac{\partial q_c}{\partial t} + \underline{v}_z \cdot \nabla q_c + p_s \frac{\dot{\sigma} q_c}{\Delta p} + \right. \\
 & \left. + \dot{P} \right) = - \left(\frac{\partial H}{\partial t} + \underline{v}_z \cdot \nabla H \right) + \\
 & + \left(\frac{2gC_{pd}}{RT_s} |\underline{v}_z| \left(\frac{q_{v,g}^*}{q_{v,2}^*} - H \right) - H \frac{\dot{Q}_z}{C_p} \frac{\partial \ln q_{v,2}^*}{\partial T} \right) - \\
 & - H p_s \dot{\sigma} \left(\frac{1}{\Delta p} + \int \frac{\partial \ln q_{v,2}^*}{\partial T} \right) + \\
 & + H (w_z - p_s \dot{\sigma} / 2) \left(\frac{\partial \ln q_{v,2}^*}{\partial p} + \frac{\partial (\ln q_{v,2}^*)}{\partial T} \frac{RT_2}{2C_p p_z} \right).
 \end{aligned} \tag{4.1.12}$$

The cloud water can be dispersed to other regions in space and/or time where the atmospheric conditions may cause the cloud water to evaporate. Equation 4.1.12 is also conditional and is solved for the cloud water only if the initial cloud water is greater than 0 by setting the relative humidity equal to one. If the cloud water becomes less than 0 then the equation can be used to solve for the relative humidity. Note that the negative condensation can be obtained from 4.1.2 and must be such that upon substituting it into 4.1.11, the relative humidity is equal to one.

Because of the conditional nature of these equations we define the fractional coverage to be that fraction of a region in which a quantity is present or certain conditions of the equations are satisfied.

Different measures of cloud fractional coverage are used. A traditional approximation is that cloudiness occurs in regions of ascending motion and no cloudiness occurs in descending regions. The correct relationship, however, also involves evaporation, heating, entrainment and detrainment, in addition to the vertical velocity. This will be discussed later. We use the following two measures: the fractional part of space and time in which positive condensation occurs, and the fractional part of space and time in which cloud water is present. The first measure is being used by the UCLA, Rand, and GISS models. They presumably under-predict cloud water fractional coverage. A schematic diagram is shown in figure 4.1.

We define the following parameters:

$$q_{\alpha} = \frac{\partial \ln q_{v,2}^*}{\partial T} \quad (4.1.13)$$

$$q_{\beta} = \left(\frac{L}{\Delta p} + \int q_{\alpha} \right)$$

$$q_{\gamma} = q_{v,2}^* / q_{v,2}^*$$

$$q_{\delta} = \left(\frac{L}{q_{v,2}^*} + \frac{L}{C_p} H q_{\alpha} \right)$$

$$q_{\epsilon} = \frac{\partial \ln q_{v,2}^*}{\partial p} + q_{\alpha} \frac{RT_2}{2C_p}$$

$$Q = \dot{Q}_2 / C_P$$

$$C_{PDD} = \frac{2 f_s g C_{DD} |v_s|}{P_s}$$

$$\omega = P_s \dot{\sigma}$$

$$\omega_2 = \omega_2.$$

We determine the fractional coverages by solving for the boundaries of the positive condensation and cloudy regions. From 4.1.11 the implicit equation for the boundary of the positive condensation region is found by setting $\dot{C}_{vc,2} = 0$ and $H=1$.

$$\begin{aligned} 0 = & - \left(\frac{\partial H}{\partial t} + \underline{v}_2 \cdot \nabla H \right) \\ & + \left(C_{DD} (q_\gamma - 1) - Q q_\alpha \right) - \\ & - \omega q_\beta + \\ & + (\omega_2 - \omega/2) q_\epsilon. \end{aligned} \tag{4.1.14}$$

At the cloud boundary, the first term on the right represents entrainment of dry air into the positive condensation region (detrainment of moist air has a negligible effect on the cloud boundaries since $H = 1$ in positive condensation regions). (See Stommel, 1947, for a discussion of entrainment for a cumulus cloud.)

From 4.1.12, the implicit equation for the cloud region is found by setting $q_c = 0$ and $H = 1$. We obtain

$$\begin{aligned}
 q_s \left(\frac{\partial q_e}{\partial t} + \underline{v}_2 \cdot \nabla q_c \right) = & - \left(\frac{\partial H}{\partial t} + \underline{v}_2 \cdot \nabla H \right) + \quad (4.1.15) \\
 & + \left(C_{000}(q_s - 1) - Q q_a \right) - \\
 & - \omega q_\beta \\
 & + (\omega_2 - \omega/2) q_e.
 \end{aligned}$$

The term on the left represents detrainment of cloud water from the region of positive condensation. The detrainment term is the only difference between 4.1.15 and 4.1.14. The entrainment and detrainment terms are discussed further in Section 4.3.

We tabulated eddy quantities and mean quantities in Table 4.1 for the hot climate (see Chapter 5). For this climate and also for other climates, the mean terms are larger than the eddy terms - except for the vertical velocities which have a much larger eddy term than a mean term. Table 4.1b tabulates the values for the appropriate combinations of the various terms. It shows that the fractional coverage is determined mainly by the interaction of the eddy vertical-velocity field with the mean evaporation, mean radiative and sensible heating, mean vertical velocity, and entrainment

or advection of relative humidity.

The eddy variations in the saturation moisture terms and static stability tend to be much smaller than the mean terms and hence we shall use only the mean values for these terms. We probably should also use q_{β}^* with ω^* but we shall assume that $q_{\beta}^* = 0$ for simplicity; in other words, the static stability is assumed to be a function of latitude only - it is the variation in S that causes the largest variation in q_{β}^* . We shall also neglect the term which gives the contribution from the eddy motion not on a constant pressure level. This term would automatically be eliminated from a model with constant surface pressure.

Since entrainment effects are important mainly when large gradients occur in the relative humidity field, we shall first investigate the solution when entrainment is neglected. We shall call this approximation the principal approximation to the equation for the cloud fractional coverage. We have at the cloud boundary,

$$0 = -(\omega^* + [\bar{\omega}]) q_{\beta} - Q q_{\alpha} + C_{000} (q_{\gamma} - 1). \quad (4.1.16)$$

The equation for the precipitation is (neglecting $(\omega^* + [\omega]) q_c q_{\delta}$)

$$q_{\delta} \dot{P} = -(\omega^* + [\bar{\omega}]) q_{\beta} - Q q_{\alpha} + C_{000} (q_{\gamma} - 1). \quad (4.1.17)$$

In the clear region the equation for the relative humidity is

$$0 = -(\omega^* + [\bar{\omega}]) q_{\beta} H - Q q_{\alpha} H + C_{000} (q_{\gamma} - H). \quad (4.1.18)$$

Equations 4.1.16 - 4.1.18 are a set of consistent equations that give the relative humidity, the precipitation, and the cloud fractional coverage. The solution to these equations for a simple model is given in section 4.2.

The entrainment and detrainment terms are included in the equations in sections 4.3. In this case the equation for the fractional coverage of positive condensation is

$$\frac{\partial H}{\partial t} + \underline{v}_z \cdot \nabla H = -(\omega^* + [\bar{\omega}])q_\beta - Qq_\alpha + C_{000}(q_\gamma - 1), \quad (4.1.19)$$

and the equation for the fraction coverage of total cloudiness is

$$q_\delta \left(\frac{\partial q_c}{\partial t} + \underline{v}_z \cdot \nabla q_c \right) = -(\omega^* + [\bar{\omega}])q_\beta - Qq_\alpha + C_{000}(q_\gamma - 1). \quad (4.1.20)$$

The equation for the precipitation is

$$q_\delta \left(\frac{\partial q_c}{\partial t} + \underline{v}_z \cdot \nabla q_c \right) = -(\omega^* + [\bar{\omega}])q_\beta + q_c q_\delta + C_{000}(q_\gamma - 1) - q_\delta \dot{P}. \quad (4.1.21)$$

And, in the clear region, the equation for the relative humidity is

$$\frac{\partial H}{\partial t} + \underline{v}_z \cdot \nabla H = -(\omega^* + [\bar{\omega}])q_\beta H - Qq_\alpha H + C_{000}(q_\gamma - H). \quad (4.1.22)$$

4.2 Principal Approximation to the Relative-Humidity Equation

4.2.1 Fractional Coverage

The approximate implicit equation for the cloud boundary is

$$0 = -(\omega^* + [\bar{\omega}])q_\beta - Qq_\alpha + C_{000}(q_\gamma - 1). \quad (4.2.1)$$

Solving for the eddy vertical velocity

$$\omega^* = B, \quad (4.2.2)$$

where

$$B = \frac{C_{000} (q_{\gamma} - 1) - Q q_{\alpha}}{q_{\beta}} - [\bar{\omega}] \quad (4.2.3)$$

B is the term representing all mean quantities except the eddy velocity. For regions in which $q_{\gamma} > 1$, Q and $[\bar{\omega}] = 0$, the balance is obtained for $\omega^* > 0$ - regions of subsidence. In regions of mean descending motion $[\bar{\omega}] > 0$ and sensible and radiative heating, $Q > 0$, ω^* needn't be as strongly positive in order for the balance to be obtained.

This qualitative behavior can be elucidated further by a simple model for the eddy vertical velocity - a finite amplitude wave with phase speed \hat{s} in the zonal direction:

$$w^* = W \cos \hat{k} (x - \hat{s} \tau) \quad (4.2.4)$$

We transform to a scaled coordinate moving with the wave,

$$\theta = \hat{k} (x - \hat{s} \tau) \quad (4.2.5)$$

Figure 4.2 shows the qualitative behavior of the vertical velocity wave interacting with the mean field, B. A greater fractional coverage occurs when the balance between the mean field and wave field is obtained at a greater subsidence velocity. Increasing W for the same B will reduce the fractional coverage while increasing B for the same W will increase the fractional coverage. Hence, the relevant parameter for sensitivity studies of the cloud field is the ratio B/W. Substituting 4.2.4 into 4.2.2 we obtain at the cloud boundary

$$\cos \theta = \frac{B}{W} \quad (4.2.6)$$

Cloudiness occurs where the right hand side of 4.2.6 is greater than the left hand side.

That is, since

$$|0| < \left| \cos^{-1} \left(\frac{B}{W} \right) \right| \quad (4.2.7)$$

is the clear region, the cloudy region fractional coverage is

$$C = 1 - \frac{2 \cos^{-1} \frac{B}{W}}{2\pi} \quad (4.2.8)$$

for

$$-1 \leq \frac{B}{W} \leq 1.$$

For B/W greater (less) than 1(-1) the fractional coverage is 1(0), the solution to 4.2.8 is irrelevant, and we must set $H=1$ ($\dot{C}_{vc,2}=0$) and solve for $\dot{C}_{vc,2}(H)$.

Figure 4.3 shows the fractional cloud cover as a function of B and W. For $B>0$ an increasing W will decrease C to 50%. For $B<0$ an increasing W will increase C to 50%. For the same W, C increases with increasing B.

The climatic sensitivities can be discussed in terms of the factor B. From 4.1.15 this can be expanded to

$$B = \frac{2g}{RT_s} C_{opp} |X_s| \left(\frac{q_{v,2}^* - 1}{q_{v,2}} \right) - \left(\frac{1}{\Delta p} + \int \frac{\partial \ln q_{v,2}^*}{\partial T} \right) \quad (4.2.9)$$

$$- \frac{\dot{Q}_2}{C_p} \frac{\frac{\partial \ln q_{v,2}^*}{\partial T}}{\left(\frac{1}{\Delta p} + \int \frac{\partial \ln q_{v,2}^*}{\partial T} \right)} - [\bar{w}].$$

As mentioned previously B and hence C increases with increasing radiative and sensible cooling and rising motion. The temperature effect - which is subtle - depends upon the ratios

$$q_a = \frac{\left(\frac{q_{v,g}^*}{q_{v,2}^*} - 1 \right)}{\left(\frac{1}{\Delta p} + \int \frac{\partial \ln q_{v,2}^*}{\partial T} \right)} \quad (4.2.10a)$$

and

$$q_b = \frac{\frac{\partial \ln q_{v,2}^*}{\partial T}}{\left(\frac{1}{\Delta p} + \int \frac{\partial \ln q_{v,2}^*}{\partial T} \right)} \quad (4.2.10b)$$

Figure 4.4a shows that q_a decreases with increasing temperature with the strongest relative decrease occurring for the smallest static stabilities and coldest temperatures. This is dependent upon the boundary-layer temperature difference being great enough so that $q_{v,g}^* > q_{v,2}^*$; q_a increases with increasing temperature if $q_{v,g}^* < q_{v,2}^*$. Figure 4.4b shows that q_b decreases with increasing temperatures, with the strongest relative decrease occurring for the smallest static stabilities and lowest temperatures. Hence for $q_{v,g}^* > q_{v,2}^*$ and $Q < 0$, B decreases with increasing temperature.

Although evaporation increases with increasing temperature, it does not lead to increased cloudiness because of the concomitant increase in the atmospheric transport and dynamical heating effects. Evaporation can be increased, however, by an increase in the surface wind speed $|\bar{v}_s|$, which influences the intensity of the turbulent transport. In this case cloudiness will increase.

Finally, from examination of equation 4.2.9 we find that an increase in the static stability will decrease cloudiness if $B + [\bar{\omega}] > 0$. This is

because the static stability determines the dynamical heating and cooling effect of atmospheric motions and hence moistening and drying ability of the atmosphere. Therefore clouds tend to become associated with ascending regions only.

Summarizing, for increased static stability, increased eddy velocities, and increased temperatures the fractional coverage tends toward 50%. For increased radiative and sensible cooling, increased mean rising motion and (if $q_{v,g}^* > q_{v,2}^*$) increased surface wind speed, the fractional coverage tends toward 100%. For increased radiative and sensible heating, increased mean subsidence, and (if $q_{v,g}^* > q_{v,2}^*$) increased surface wind speed, the fractional coverage tends toward 0%. It is the relative increase or decrease in these variables that determines the response of the cloud coverage.

4.2.2 Relative Humidity

In the cloud-free region of the wave, the relative humidity is

$$H = \frac{C_{000} q_r}{W \cos(\theta) q_\beta + [\bar{\omega}] q_\beta + Q q_\alpha + C_{000}} \quad (4.2.11)$$

Substituting 4.2.3 into 4.2.11 and simplifying, obtain

$$H = \frac{C_{000} q_r}{W q_\beta} \quad (4.2.12)$$

$$\cos \theta - \frac{\beta}{W} + \frac{C_{000} q_r}{W q_\beta}$$

Hence, in addition to B/W, the relative humidity is affected by the parameter,

$$\eta = \frac{C D P D q_s}{W q_B}, \quad (4.2.13)$$

which gives a measure of the ratio of the surface turbulent transport to the atmospheric transport and dynamical heating. From 4.2.8 we obtain

$$\frac{B}{W} = \cos \pi (1-C) = -\cos \pi C, \quad (4.2.14)$$

if

$$-1 \leq \frac{B}{W} \leq 1. \quad (4.2.15)$$

Hence

$$H = \frac{\eta}{\cos \theta + \cos \pi C + \eta} \quad (4.2.16)$$

in the cloud free portion of the wave. For

$$\frac{B}{W} > 1, \quad H = 1. \quad (4.2.17a)$$

For

$$\frac{B}{W} < 1, \quad H = \frac{\eta}{\cos \theta - \frac{B}{W} + \eta}. \quad (4.2.17b)$$

We average H over the wave in order to relate the average relative humidity to the fractional coverage.

$$[H] = C + \frac{1}{2\pi} \int_{-\pi(1-C)}^{\pi(1-C)} \frac{\eta}{\cos \theta + \cos \pi C + \eta} d\theta \quad (4.2.18)$$

The first term on the right hand side is that portion contributed by the saturated portion of the wave, where $H=1$. The second part is the contribution from the dry region. The limits of the integration are obtained from 4.2.6 and 4.2.14.

Integrating, we obtain ($a=\eta+\cos\pi C$)

$$\begin{aligned}
 [H] &= C + & (4.2.19) \\
 &+ \frac{2\eta}{\pi\sqrt{a^2-1}} \tan^{-1} \left(\frac{a \tan\left(\frac{\pi}{2}(1-C)\right)}{\sqrt{a^2-1}} \right) & : a^2 > 1 \\
 &+ \frac{\eta}{\pi\sqrt{1-a^2}} \ln \left| \frac{\tan\left(\frac{\pi}{2}(1-C)\right) + \sqrt{\frac{1+a}{1-a}}}{\tan\left(\frac{\pi}{2}(1-C)\right) - \sqrt{\frac{1+a}{1-a}}} \right| & : a^2 < 1 \\
 &+ \frac{\eta}{\pi} \tan\left(\frac{\pi}{2}(1-C)\right) & : a^2 = 1.
 \end{aligned}$$

For the asymptotic limit

$$\eta \rightarrow 0, \quad (4.2.20a)$$

$$[H] \rightarrow C. \quad (4.2.20b)$$

That is, as the ratio of the vertical velocity to the turbulent source term becomes large, the relative humidity approaches zero in the cloud-free region and identically 1 in the cloudy region. For

$$\eta \rightarrow \infty, \quad (4.2.21a)$$

$$[H] \rightarrow 1. \quad (4.2.21b)$$

That is, as the turbulent source term becomes large relative to the atmospheric ω term, the relative humidity must approach 1 since the descending atmospheric motions have little drying effect. For

$$C \rightarrow 1, \quad (4.2.22a)$$

$$[H] \rightarrow 1. \quad (4.2.22b)$$

That is, the relative humidity becomes very closely related to the fractional cloud cover as the cloud cover almost covers the zone. For

$$C \rightarrow 0, \quad (4.2.23a)$$

$$[H] \rightarrow \frac{\eta}{\sqrt{\eta^2 + 2\eta}}. \quad (4.2.23b)$$

This is the 0-line intercept of figure 4.5a. Figure 4.5a shows that C is an increasing function of [H] and η and is fairly linear for η very large or η very small.

Except for the asymptotic limits the solution itself is rather obtuse; we found it more convenient to deal with the inverse of the relative humidity,

$$[H^{-1}] = C + \frac{1}{2\pi} \int_{-\pi(1-C)}^{\pi(1-C)} \left(1 + \frac{1}{\eta} (\cos \theta + \cos \pi C) \right) d\theta. \quad (4.2.24)$$

Integrating, obtain

$$[H^{-1}]^{-1} = \left(1 + \frac{1}{\eta} \left(\frac{\sin \pi C}{\pi} + (1-C) \cos \pi C \right) \right)^{-1}. \quad (4.2.25)$$

The previous asymptotic relations

$$\eta \rightarrow \infty \Rightarrow [H^{-1}]^{-1} \rightarrow 1 \quad (4.2.26a)$$

and

$$C \rightarrow 1 \Rightarrow [H^{-1}]^{-1} \rightarrow 1 \quad (4.2.26b)$$

are satisfied and the asymptotic limit

$$C \rightarrow 0 \Rightarrow \quad (4.2.27a)$$

$$[H^{-1}]^{-1} \rightarrow \frac{\eta}{1+\eta} \quad (4.2.27b)$$

is the 0-line intercept of figure 4.5b. This also shows that C is an increasing function of $[H^{-1}]^{-1}$ and has a functional relation much like that

shown in figure 4.5a. In fact, the relationship between the zonally averaged inverse relative humidity is shown in figure 4.5c to have a simple relationship as a function of C and η ; hence one may use either figure 4.5a or 4.5b to discuss the relationship between the relative humidity and fractional cloud cover.

Figure 4.5 may be relevant to Smagorinsky's (1960) curves (figure 1.1), but we cannot discuss this adequately without doing the calculations for a model with more vertical resolution.

4.2.3 Average Precipitation

In the cloudy region the equation for the precipitation is

$$q_s \dot{P} = C_{000} (q_\gamma - 1) - Qq_\alpha - Wq_\beta \cos\theta - [\bar{w}]q_\beta. \quad (4.2.28)$$

From 4.2.2 this may be written

$$\dot{P} = \left(\frac{B}{W} - \cos\theta \right) \frac{Wq_\beta}{q_s}. \quad (4.2.29)$$

Using 4.2.8,

$$\dot{P} = \left(-\cos\pi C - \cos\theta \right) \frac{Wq_\beta}{q_s}. \quad (4.2.30)$$

Integrating 4.2.30 over the cloudy region, $[\pi - \pi C < \theta < (2\pi - \pi + \pi C)]$

$$[\dot{P}] = \left(\frac{\sin\pi C}{\pi} - C \cos\pi C \right) \frac{Wq_\beta}{q_s}. \quad (4.2.31)$$

The average normalized precipitation in the cloud region is obtained by dividing 4.2.31 by C . We obtain

$$\varepsilon \dot{P} \beta = \left(\frac{\sin\pi C}{\pi C} - \cos\pi C \right) \frac{Wq_\beta}{q_s}. \quad (4.2.32)$$

The normalized zonally averaged and cloud averaged (i.e. averaged over the cloudy longitudes) precipitation as a function of cloud cover are shown in figure 4.6. Both increase with increasing fractional cloud cover.

The cloud water content, however, is dependent upon the characteristic time scale for precipitation which may be non-linearly related to the precipitation. For example, from figure 3, we may choose the approximate relationship

$$\dot{p} \sim a q_c^3. \quad (4.2.33)$$

If as an approximation the cloud properties are taken to be uniform over the cloud, we obtain

$$\epsilon q_c^3 \sim \left(\left(\frac{\sin \pi C}{\pi C} - \cos \pi C \right) \frac{W q_\beta}{a q_\delta} \right)^{1/3}, \quad (4.2.34)$$

which indicates that the cloud water content is a weak function of cloud cover, C , and climate characteristics, $\frac{W q_\beta}{q_\delta a}$ - at least for our model.

4.2.4 Cloud Formulae

We have obtained solutions for the average relative humidity and precipitation in terms of the fractional cloud cover. We can use these relationships to solve, in turn, for the fractional cloud cover. For example, substituting 4.2.26 into 4.2.31 and solving for C , we obtain

$$C = \frac{\cos^{-1}}{\pi} \left(\frac{[CH^{-1}] (1 - [CH^{-1}]^{-1}) C_{\infty} q_\gamma - \dot{p} q_\delta}{W q_\beta} \right). \quad (4.2.35)$$

As $W q_\beta$ becomes very large the fractional cloud cover tends toward 50%. This is a traditional approximation - complete cloudiness in regions

of ascending motion and completely clear skies in regions of subsidence. As the relative humidity decreases, fractional cloud cover decreases to zero - another traditional approximation. As the turbulent transports increase in intensity without a compensating increase in relative humidity and precipitation, the fractional cloud cover decreases. Finally, as \dot{P} increases without a decrease in relative humidity or increase in evaporation, the fractional coverage of the region increases. These latter behaviors can be discussed more easily if we eliminate the vertical velocity from 4.2.25. From 4.2.19, we obtain

$$Wq_{\beta} = \frac{([H^{-1}] - 1) C_{000} q_{\gamma}}{\left(\frac{\sin \pi C}{\pi} + (1-C) \cos \pi C\right)} \quad (4.2.36)$$

From 4.2.31

$$Wq_{\beta} = \frac{q_{\delta} \dot{P}}{\left(\frac{\sin \pi C}{\pi} - C \cos \pi C\right)} \quad (4.2.37)$$

Eliminating Wq_{β} from 4.2.36 and 4.2.37, we obtain

$$\frac{q_{\delta} \dot{P}}{C_{000} q_{\gamma} [H^{-1}] (1 - [H^{-1}]^{-1})} = \left(\frac{\frac{\sin \pi C}{\pi} - C \cos \pi C}{\frac{\sin \pi C}{\pi} + (1-C) \cos \pi C} \right) \quad (4.2.38)$$

Figure 4.7 shows the solution to 4.2.38 for C.

The cloud cover in our numerical model is fairly large.

Solving 4.2.38 near $C \approx 1$, we obtain

$$C_E \sim 1 - \left(\frac{3 C_{000} q_{\gamma} (1 - [H^{-1}]^{-1})}{[H^{-1}]^{-1} q_{\delta} \pi^2 \dot{P}} \right)^{1/3} \quad (4.2.39)$$

This may be compared to Sellers' (1976) cloud formula

$$C_S = \left(.75 + .25 \frac{(P_c - E)}{(P_c + E)} \right) H, \quad (4.2.40)$$

which shows similar behavior; for increased E relative to P_c, C_s decreases, and for increased H, C_s increases.

It is important to remember that H, P_c and E are implicitly related to the vertical velocity, which must be calculated explicitly or implicitly in order to use these formulae.

4.3 Entrainment and Detrainment

4.3.1 Entrainment

Entrainment of dry air into a particular region will inhibit the formation of cloudiness by preventing saturation from occurring. For the entrainment term, $\frac{\partial H}{\partial t} + \underline{v}_2 \cdot \nabla H$, we transform into a coordinate system moving with the vertical-velocity phase speed \hat{s} (i.e., the speed of the waves in the vertical velocity field). Letting $t, y, [\hat{k}(x-\hat{s}t)]$ be the independent variable, we have

$$\frac{\partial H}{\partial x} + \frac{d\theta}{dt} \frac{\partial H}{\partial \theta} + v \frac{\partial H}{\partial y} = \frac{\partial H}{\partial x} + \hat{k}(u-\hat{s}) \frac{\partial H}{\partial \theta} + v \frac{\partial H}{\partial y}. \quad (4.3.1)$$

We examine the two-dimensional steady state solution where

$$\frac{\partial H}{\partial x} + \underline{v}_2 \cdot \nabla H = \hat{k}(u-\hat{s}) \frac{\partial H}{\partial \theta}. \quad (4.3.2)$$

We now have an explicit dependence on the scale of the wave. Entrainment has the largest effect for small wavelengths; the effect is also dependent upon the difference between the mean zonal wind and the phase speed of the vertical velocity waves; essentially the effect is largest for waves with a small period or large frequency.

The equation for the relative humidity in the dry region is

$$\hat{k}(u-\hat{s}) \frac{\partial H}{\partial \theta} = - (W \cos \theta - \underline{c} \bar{\omega}) q_{\beta} H - Q q_{\alpha} H + C_{000} (q_{\gamma} - H). \quad (4.3.3)$$

From 4.2.3,

$$\frac{\hat{k}(u-\hat{s})}{Wq_B} \frac{\partial H}{\partial \theta} = \frac{\beta}{W} - \cos \theta + (1-H) \frac{C_{DDD} q_r}{Wq_p}. \quad (4.3.4)$$

From 4.2.14 and 4.2.13,

$$\epsilon \frac{\partial H}{\partial \theta} = (-\cos \pi C - \cos \theta) H + (1-H) \eta, \quad (4.3.5)$$

where

$$\epsilon = \frac{\hat{k}(u-\hat{s})}{Wq_B}. \quad (4.3.6)$$

ϵ is essentially a measure of the time it takes a region of air to reach saturation or dry out by vertical motions to the time it takes for dry or moist air to be entrained into the region. A similar parameter was discussed by Shukla (1976). He suggested that when latent heat effects are important, the dominant unstable waves would be those with a large ratio of $\frac{c_i}{c_r}$ where c_i is the imaginary part (growth rate) and c_r is the real part of the complex phase speed of the wave. For our case a large $\frac{c_i}{c_r}$ corresponds to a small ϵ .

At the cloud boundary, $H=1$ and

$$\epsilon \frac{\partial H}{\partial \theta} = -\cos \pi C - \cos \theta, \quad (4.3.7)$$

and within the cloud, condensation operates such that

$$H=1, \quad (4.3.8a)$$

$$\frac{\partial H}{\partial \theta} = 0, \quad (4.3.8b)$$

and (neglecting cloud water transports)

$$\frac{q_s \dot{P}}{W q_p} = -\cos \pi C - \cos \theta. \quad (4.3.8c)$$

Consider figure 4.2. For

$$-\pi(1-C) \geq \theta \geq \pi(1-C), \quad (4.3.9a)$$

then

$$-\cos \pi C - \cos \theta \geq 0, \quad (4.3.9b)$$

which from 4.3.8c means condensation can occur only within this region.

For

$$-\pi(1-C) < \theta < \pi(1-C), \quad (4.3.10a)$$

then

$$-\cos \pi C - \cos \theta < 0, \quad (4.3.10b)$$

and hence

$$e \frac{\partial H}{\partial \theta} < 0 \text{ if } H \sim 1. \quad (4.3.11)$$

That is, the relative humidity becomes less than one for increasing θ in this latter region. As the relative humidity is reduced to a small value, however, then (from 4.3.5) $e \frac{\partial H}{\partial \theta}$ can increase again due to the evaporation term, $(1-H)\eta$, which becomes important for $H \rightarrow 0$ and is dominant near $H=0$; H reaches a smallest value, dependent on η , at which point it begins to increase again because of the rising motion and eventually can reach a point where it once again becomes saturated.

The saturation region is the cloud region. In this region, the relative humidity is equal to one because of the condensation. At the edge of the cloud at θ_1 ($-\pi + \pi C$), negligible relative humidity is detrained and the value of unity for H is consistent with 4.3.5 since

$$-\cos \pi C - \cos \theta_1 = 0 \Rightarrow \frac{\partial H}{\partial \theta} = 0. \quad (4.3.12)$$

The western side of the cloudy region however has dry air entrained into it since the relative humidity must be increasing at this point (see figure 4.8). If θ_2 is the boundary of the cloudy region that occurs when $\epsilon=0$, that is when the vertical velocity phase speed is equal to the zonal velocity, the effect of an increasing ϵ will be to shift the western cloud boundary further to the east - from θ_2 to θ_{2N} since θ_{2N} must be greater than θ_2 in order that $-\cos \pi C - \cos \theta$ be much greater than zero, that is, in order that the vertical-velocity moistening effect overcome the horizontal-advection drying effect.

We note that if $\epsilon < 0$, the dry air would be entrained on the eastern side of the system and negligible relative humidity would be detrained on the western side. That is, if $u < \hat{s}$ the vertical velocity wave is moving into a dryer region; as mentioned previously, if $u > \hat{s}$ or $\epsilon > 0$, the drier regions are moving into the vertical velocity wave. For convenience we assume $\epsilon > 0$ recognizing that different portions of the cloudy system may have different sides on which entrainment of dry air is occurring.

We may write the exact solution to 4.3.5 with some arbitrary initial condition, $H_1(\theta_1)$, as

$$H(\theta) = H_1(\theta_1) e^{(\eta + \cos \pi C) \frac{(\theta_1 - \theta)}{\epsilon} + \frac{(\sin \theta_1 - \sin \theta)}{\epsilon}} + \int_{\theta_1}^{\theta} \frac{\eta}{\epsilon} e^{(\eta + \cos \pi C) \frac{(\theta' - \theta)}{\epsilon} + \frac{(\sin \theta' - \sin \theta)}{\epsilon}} d\theta' \quad (4.3.13)$$

Consider first the case

$$\eta + \cos \pi C < 0. \quad (4.3.14)$$

Since the second part of 4.3.13 is positive for increasing θ , we have

$$H(\theta) > H_1(\theta_1) e^{(\eta + \cos \pi C) \frac{(\theta_1 - \theta)}{\epsilon} + \frac{(\sin \theta_1 - \sin \theta)}{\epsilon}} \quad (4.3.15)$$

and

$$H(\theta) \rightarrow 1 \text{ as } \theta \rightarrow \infty \quad (4.3.16)$$

regardless of the initial condition. Once $H(\theta) = 1$, we find from 4.3.7 and 4.3.8 that it must remain equal to 1 until

$$\theta = 2\pi m - \pi(1-C) \quad ; \quad m = 1, 2, 3, \dots, \quad (4.3.17)$$

at which point, 4.3.13 becomes the valid solution again. Using 4.3.13 with $(\eta + \cos \pi C) \geq 0$ and $H_1(\theta_1) = 1$ we obtain from 4.3.15

$$H(2\pi(m+1) - \pi(1-C)) > 1 \quad (4.3.18)$$

and somewhere before this point (at θ_{2N}), H must be equal to unity. From θ_{2N} and onward, 4.3.13 is invalid and 4.3.8 is the valid solution until

$$\theta = 2\pi(m+1) - \pi(1-C). \quad (4.3.19)$$

At this θ , 4.3.13 is valid once more and the procedure outlined above is continually repeated.

Summarizing, since equations 4.3.8 and 4.3.13 have periodic initial conditions and periodic coefficients, every solution will be periodic with

$$H=1 \quad ; \theta_{2N} \leq \theta \leq 2\pi + \theta_1 \quad (4.3.20a)$$

and

$$\epsilon \frac{\partial H}{\partial \theta} = -(\cos \pi C + \cos \theta) H + (1-H) \eta \quad ; \theta_1 \leq \theta \leq \theta_{2N}, \quad (4.3.20b)$$

where

$$\theta_1 = 2\pi m - \pi(1-C) \quad ; m = 0, 1, 2, 3, \dots \quad (4.3.20c)$$

and

$$\theta_{2N} = 2\pi m + \theta_{2N} \quad ; m = 0, 1, 2, 3, \dots \quad (4.3.20d)$$

Consider now the case,

$$\eta + \cos \pi C > 0, \quad (4.3.21)$$

and let us neglect condensation for now. Then $\theta \rightarrow \infty$; that is, for a region relatively far away from the initial point, the first part of 4.3.13 becomes negligible and

$$H(\theta) \rightarrow \int_{\theta_1}^{\theta} \frac{\eta}{\epsilon} e^{(\eta + \cos \pi C)(\theta' - \theta)} + \frac{(\sin \theta' - \sin \theta)}{\epsilon} d\theta' \quad (4.3.22)$$

This integral is evaluated by using the series expansion in Bessel functions (cf. 9.1.42 and 9.1.43 of Abramowitz & Stegun)

$$\begin{aligned}
 e^{\frac{a \sin \theta}{\epsilon}} &= e^{i(-\frac{i}{\epsilon}) \sin \theta} && (4.3.23) \\
 &= \cos\left(-\frac{i}{\epsilon} \sin \theta\right) + i \sin\left(-\frac{i}{\epsilon} \sin \theta\right) \\
 &= J_0\left(-\frac{i}{\epsilon}\right) + \\
 &\quad + 2 \sum_{k=1}^{\infty} J_{2k}\left(-\frac{i}{\epsilon}\right) \cos 2k\theta + \\
 &\quad + 2i \sum_{k=0}^{\infty} J_{2k+1}\left(-\frac{i}{\epsilon}\right) \sin\{(2k+1)\theta\}
 \end{aligned}$$

The integral becomes

$$\begin{aligned}
 \int e^{a\theta + \frac{a \sin \theta}{\epsilon}} d\theta &= \frac{J_0}{a} \left(-\frac{i}{\epsilon}\right) e^{a\theta} + && (4.3.24a) \\
 &\quad + 2e^{a\theta} \sum J_{2k}\left(-\frac{i}{\epsilon}\right) \frac{(2k \sin 2k\theta + a \cos 2k\theta)}{(a^2 + 4k^2)} \\
 &\quad + 2ie^{a\theta} \sum J_{2k+1}\left(-\frac{i}{\epsilon}\right) (a \sin\{(2k+1)\theta\} - (2k+1) \times \\
 &\quad \quad \times \cos\{(2k+1)\theta\}) / [a^2 + (2k+1)^2],
 \end{aligned}$$

where

$$a = \eta + \cos \pi C. \quad (4.3.24b)$$

Hence

$$H(\theta) \rightarrow \frac{\eta}{\eta + \cos \pi C} J_0\left(-\frac{i}{\epsilon}\right) e^{-\frac{\sin \theta}{\epsilon}} \quad (4.3.25)$$

$$+ \frac{2\eta}{\epsilon} e^{-\frac{\sin \theta}{\epsilon}} \sum_{k=1}^{\infty} J_{2k}\left(-\frac{i}{\epsilon}\right) (2k \sin 2k\theta + a \cos 2k\theta) / (a^2 + 4k^2) +$$

$$+ \frac{2i\eta}{\epsilon} e^{-\frac{\sin \theta}{\epsilon}} \sum_{k=0}^{\infty} J_{2k+1}\left(-\frac{i}{\epsilon}\right) (a \sin \{(2k+1)\theta\} -$$

Note that as $\epsilon \rightarrow \infty$

$$- (2k+1) \cos \{(2k+1)\theta\} / [a^2 + (2k+1)^2] .$$

$$H(\theta) \rightarrow \frac{\eta}{\eta + \cos \pi C} \quad (4.3.26)$$

Because the large entrainment rate is limiting the variation with respect to θ , H approaches a constant value less than 1 if the equilibrium cloud cover without entrainment is less than $\frac{1}{2}$.

In fact, since the solution to 4.3.25 has an asymptotic periodic solution of period 1, or smaller, we may take an average over a 2π interval

$$[H(\theta)] \rightarrow \frac{\eta}{\eta + \cos \pi C} J_0^2\left(\frac{i}{\epsilon}\right) = \quad (4.3.27)$$

$$= \frac{\eta}{\eta + \cos \pi C} \sum_{l, k=0}^{\infty} \frac{\left(\frac{i}{\epsilon}\right)^{2k+2l}}{4^{2k+2l} (k!)^2 (l!)^2} .$$

Note that

$$[H(\theta)] \geq \frac{\eta}{\eta + \cos \pi C} \quad (4.3.28)$$

$[H(\theta)]$ approaches, from above, a constant value greater than 1 for $C > \frac{1}{2}$. Our

solution is no longer valid for this case since we haven't included condensation.

In this case we must use the condition of 4.3.20 to solve the equation. That is, if any saturation at all is allowed then 4.3.20 is the valid procedure.

The final case to be considered is

$$\eta + \cos \pi C = 0, \quad (4.3.29)$$

From 4.3.23 and 4.3.24 we know that $H(\theta) \rightarrow 1$ linearly and from then on 4.3.18 shows that some saturation must occur within a 2π interval and hence 4.3.20 is the valid procedure.

While equation 4.3.5 would be solved analytically, we found it much more convenient to integrate forward in θ numerically (fourth order Runge-Kutta) from $H_1(\theta_1)=1$ until $H=1$ again - which is at an angle θ_{2N} somewhat greater than θ_2 because of the entrainment of dry air. At this point H will remain 1, because of condensation, until $\theta > \theta_1$ (plus some multiple of 2π) unless, as noted previously, entrainment prevents cloudiness from occurring at all. This can happen because the entrainment is tending to limit the variation of H with θ by entraining drier air from the dry portions of the wave to the moist portions and entraining moist air from the moist portions to the dry portions. (This will prevent total cloudiness only if $C < .5$ and $\epsilon \rightarrow \infty$; for $C > .5$ some cloudiness must occur since $[H(\theta)] \geq 1$.) If the new state has no saturation then we have no periodic solution for the $0 \rightarrow 2\pi$ interval; since we are interested only in the asymptotic periodic solution we continue the integration of 4.3.5 until the solution over a

2π length of 2π converges, regardless of the initial condition. We know that it must asymptotically approach a periodic state, because if no saturation occurs then $C < .5$ (hence $\eta + \cos\pi C < 0$) and 4.3.25 is the valid solution.

Figure 4.9a shows that if the atmosphere barely becomes saturated for a stationary wave then the presence of entrainment prevents saturation. The largest entrainment rates allow the least area of saturation and show the smallest variation in H with respect to θ . The maximum is shifted to the right as $\epsilon \rightarrow \infty$. Iterations (we iterate until $|H'(\theta + 2\pi) - H'(\theta)| \leq 10^{-5}$) were required for some of the ϵ since the initial condition on the initial point was not a valid asymptotic solution. In figure 4.9a $H \rightarrow .503$ as $\epsilon \rightarrow \infty$. In figure 4.9b, $H \rightarrow .764$ as $\epsilon \rightarrow \infty$. In this latter figure the mean state is coming closer to saturation. Note that an increase in entrainment can increase the relative humidity and decrease the fractional cloud cover. Figure 4.9c shows the effect of decreasing η on the solution. In this case $H \rightarrow .288$ as $\epsilon \rightarrow \infty$. η is a measure of the mean field source intensity versus the intensity of the atmospheric up and down motions - and concomitant transport and dynamical heating. Because of increased entrainment of dry air into the cloudy region, decreasing η decreases the fractional coverage. This is illustrated in figure 4.9d which shows the effect of decreasing η for ϵ equal to 1.

From numerical solutions to these equations we can graph the change in cloud cover when entrainment is present. Figures 4.9e and f show that cloud cover is decreased with increasing entrainment and decreasing η . Hence, if either the vertical velocities are increased relative to the

surface evaporation, and if the relative entrainment $\hat{k}(u-\bar{s})/Wq_{\beta}$ remains constant, the fractional cloud cover is decreased; or if the vertical velocities are decreased relative to the horizontal velocities, but η remains constant, then the cloud cover is also decreased.

Figure 4.9g shows the equilibrium cloud cover as a function of the zonally averaged relative humidity is decreased with increasing η .

Figure 4.9h shows that the equilibrium cloud cover - as a function of the zonally averaged relative humidity is decreased with increasing entrainment. Figure 4.9i shows that if we write

$$\epsilon = \eta \epsilon', \quad (4.3.30a)$$

where

$$\epsilon' = \frac{\hat{k}(u-\bar{s})}{C_{000}q_{\beta}}, \quad (4.3.30b)$$

then for an increase in the atmospheric horizontal advection relative to the surface turbulent transports, the cloud cover is decreased and the relative humidity is increased.

In summary, we have found the solution applicable when entrainment is present. For large entrainment rates the relative humidity approaches a constant less than 1 if the mean state is unsaturated. This means that if the fractional coverage is less than .5 without entrainment, large entrainment would reduce it to zero. A wave stationary with respect to the zonal flow will have the largest cloud cover and smallest relative humidity. The effect of entrainment is to reduce the efficiency of the vertical motions in moistening and drying the atmosphere (suggested by

Shukla [1976]). If the mean state produces a completely saturated state - even in the presence of subsidence - entrainment will have no effect on the relative humidity. However, there will be a rearrangement of cloud water.

4.3.2 Detrainment

The detrainment in the coordinate system traveling with the vertical velocity wave is

$$q_s \left(\frac{\partial q_c}{\partial \tau} + \underline{v} \cdot \nabla q_c \right) = \hat{h} (u - \hat{s}) q_s \frac{\partial q_c}{\partial \theta}, \quad (4.3.31)$$

and the equation for the precipitation is

$$\begin{aligned} q_s \hat{h} (u - \hat{s}) \frac{\partial q_c}{\partial \theta} = & - (W \cos \theta + [\bar{w}]) (q_0 + q_c q_s) - \\ & - Q q_\alpha + C_{\text{DD}} (q_\gamma - 1) - \\ & - \dot{p} q_s . \end{aligned} \quad (4.3.32)$$

Using the following parameters

$$q_{cc} = q_s q_c, \quad (4.3.33)$$

$$\delta = \frac{a_3}{W q_0 q_s^2},$$

$$\dot{p} = \delta q_{cc}^3,$$

$$\chi = \frac{1}{\Delta P q_0} ,$$

$$\psi = \frac{[\bar{\omega}]}{W} ,$$

and using equation 4.3.8, 4.3.32 can be rewritten as

$$\begin{aligned} \epsilon \frac{\partial q_{cc}}{\partial \theta} = & -\cos \pi C - \cos \theta - \delta q_{cc}^3 - \\ & - \cos \theta \chi q_{cc} - \chi \psi q_{cc}. \end{aligned} \quad (4.3.34)$$

At the cloud boundaries $q_{cc}=0$ and the implicit equation for the total fractional cloud cover is

$$\epsilon \frac{\partial q_{cc}}{\partial \theta} = -\cos \pi C - \cos \theta - \epsilon \frac{\partial H}{\partial \theta}. \quad (4.3.35)$$

This equation can be solved only in conjunction with 4.3.5. At θ_{2N} for $\epsilon > 0$, $\frac{\partial q_{cc}}{\partial \theta} = 0$ since $q_{cc} = 0$ to the immediate left. At θ_1 , however, $\frac{\partial q_{cc}}{\partial \theta} \neq 0$ since q_{cc} must be greater than zero in the cloudy region and hence $\theta_{1N} > \theta_1$ because of the extension of the cloud boundary by zonal advectations of cloud water.

We solved 4.3.34 by solving 4.3.5 in the cloudy region assuming $H=1$ at θ_1 and integrating forward until saturation is reached at which point H was set equal to 1 and $\frac{\partial H}{\partial \theta}$ was set equal to zero; we then integrated 4.3.34 until $q_{cc} \leq 0$ at which point the relative humidity was again integrated. This procedure was continued until the solutions converged (we iterate until either $|H'(\theta + 2\pi) - H(\theta)| \leq 10^{-5}$ or $|q'_{cc}(\theta + 2\pi) - q_{cc}(\theta)| \leq 10^{-7}$). For typical values of the parameters:

$$\delta = 3 \times 10^4, \quad (4.3.36)$$

$$\psi = .1,$$

$$\chi = \frac{2}{3},$$

we found results typical of those shown in figure 4.10a.

For small fractional coverages, the entrainment effects dominated; for large fractional coverage, detrainment became almost as important as entrainment although both effects were very small. The change in cloud cover resulting from the addition of detrainment is shown in figure 4.10b and c to not be much different from figures 4.9e and f - which give the effects when only entrainment is occurring.

This is because the cloud water contents were so much smaller than the relative dryness of the air that they had little moistening effect. Also, since $\frac{\epsilon \partial q_{cc}}{\partial \theta}$ was so much smaller than $\cos \theta$, the transport of moisture away from the condensing region was negligible compared to the production and precipitation. This could be altered if δ was chosen to be much smaller; however, δ was chosen to represent the typical conditions of our model.

4.3.3 Summary

Entrainment had much larger effects than detrainment for small fractional coverages while for large fractional coverages entrainment and detrainment tended to be comparable but small. The entrainment effects

can be sufficiently large to prevent saturation occurring at all for conditions where no entrainment would give some cloudiness. The entrainment effects are largest for: (1) large ε , $\frac{\hat{k}(u-\hat{s})}{Wq_{\beta}}$, because of the resultant decrease in the amplitude of the relative-humidity wave; and (2) for small η because of a decrease of relative humidity in the dry region and concomitant increase in dry air entrainment.

One aspect not investigated was the variation - because of instabilities - with time of the various amplitudes. Another aspect not investigated was the meridional advection of cloud water. For example, if a certain latitude band had more cloudiness than another band, then the meridional advection of cloud water into the deficient region would increase the cloudiness there. This may even act contrary to the total transport of cloud water if the transports are particularly strong within the cloud. This could be compensated for by the meridional advection of relative humidity and subsequent entrainment. Without having an appropriate analytic dynamical model of the system we cannot discuss these aspects further.

What we can do is examine some of the climatic variables describing the distribution in a numerical model that has atmospheric-like behavior to see if the appropriate sensitivities and interrelationships described by the simple models are correct and what corrections should be made to deal with the approximations in this chapter. More importantly, we have, perhaps, a better understanding of sensitivity results from more complex models. And, most importantly, we will have more confidence in numerical results if they are consistent with these simpler results.

Table 4.1a. Magnitudes of parameters in the relative-humidity equation for the hot climate.

	units	mean	eddy
C_{DDD}	sec^{-1}	5.3×10^{-7}	2.5×10^{-7}
Q^{\dagger}	degsec^{-1}	4.1×10^{-6}	1.5×10^{-6}
ω^{\dagger}	$\text{g cm}^{-1} \text{sec}^{-1}$	9.2×10^{-2}	5.1×10^{-1}
$(\omega_2 - \omega/2)$	$\text{g cm}^{-1} \text{sec}^{-1}$	3.2×10^{-3}	1.0×10^{-1}
q_{α}	deg^{-1}	6.8×10^{-2}	9.8×10^{-4}
q_{β}	$\text{g}^{-1} \text{cmsec}$	3.0×10^{-6}	2.1×10^{-7}
q_{γ}	-	1.8	0.3
q_{δ}	-	2.7×10^2	1.9×10^1
q_{ϵ}	$\text{g}^{-1} \text{cmsec}$	2.4×10^{-6}	2.9×10^{-8}

[†] The vertical-velocity mean and radiative and sensible-heating mean are standard deviations of the zonal means about the areal means - which are approximately zero.

Table 4.1b. Magnitudes of coefficients in the relative-humidity equations (hot climate).

	$[\overline{C_{DDD}}]([\overline{q_\gamma}]-1)$	4×10^{-7}	sec^{-1}
	$[\overline{Q}][\overline{q_\beta}]$	3×10^{-7}	sec^{-1}
	$\omega^*[\overline{q_\beta}]$	2×10^{-6}	sec^{-1}
	$[\overline{\omega}][\overline{q_\beta}]$	3×10^{-7}	sec^{-1}
	$(\omega - \omega/2)^*[\overline{q_\epsilon}]$	2×10^{-7}	sec^{-1}
1	$\omega^* \frac{q_c}{\Delta p}$	1×10^{-8}	sec^{-1}
2	Entrainment	2×10^{-6}	sec^{-1}
3	Detrainment	2×10^{-8}	sec^{-1}
1	$q_c \sim 10^{-4} \text{g/g}$		
2	Entrainment $\sim \frac{(u-\hat{s})}{x}$ (H) $\sim \frac{10^3 \times 1}{5 \times 10^8}$		
3	Detrainment $\sim \frac{(u-\hat{s})}{x}$ ($q_c q_\delta$) $\sim \frac{10^2 \times 10^{-3}}{5 \times 10^8}$		

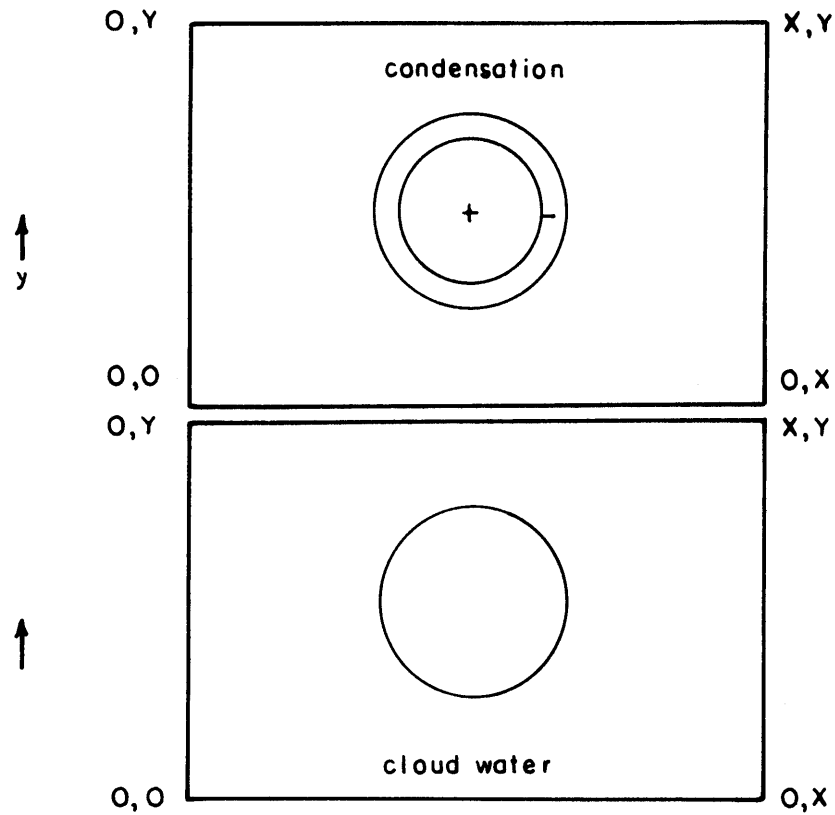


Figure 4.1. An idealized condensation field and cloud water field at a particular time, t_0 , in the model domain.

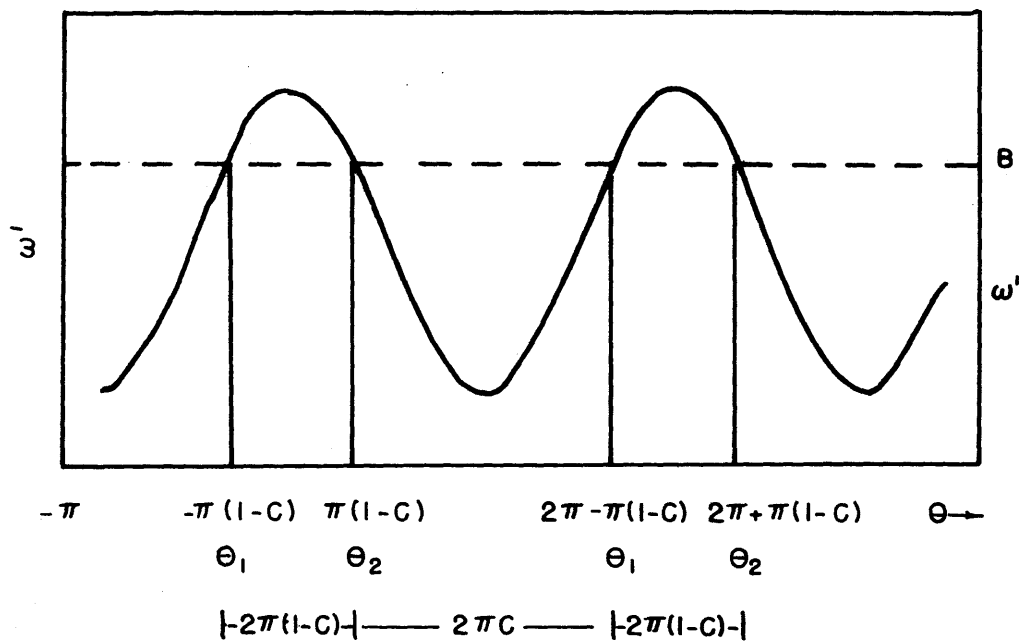


Figure 4.2. Interaction of the eddy vertical velocity with the mean field terms. Regions of clear sky occur where $\omega' > B$. Cloudy regions occur when $\omega' < B$.

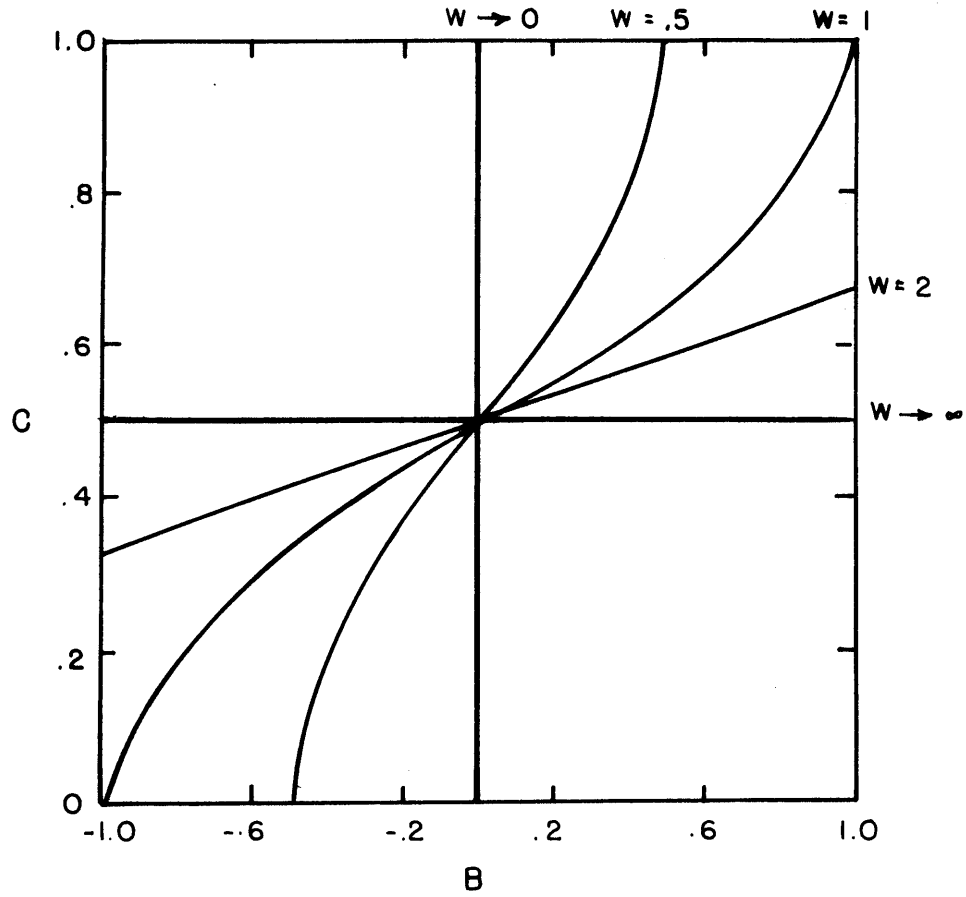


Figure 4.3. Fractional cloud cover, C , versus the factor B - which includes the evaporation, sensible and radiative heating and mean field transports, for various vertical velocities, W .

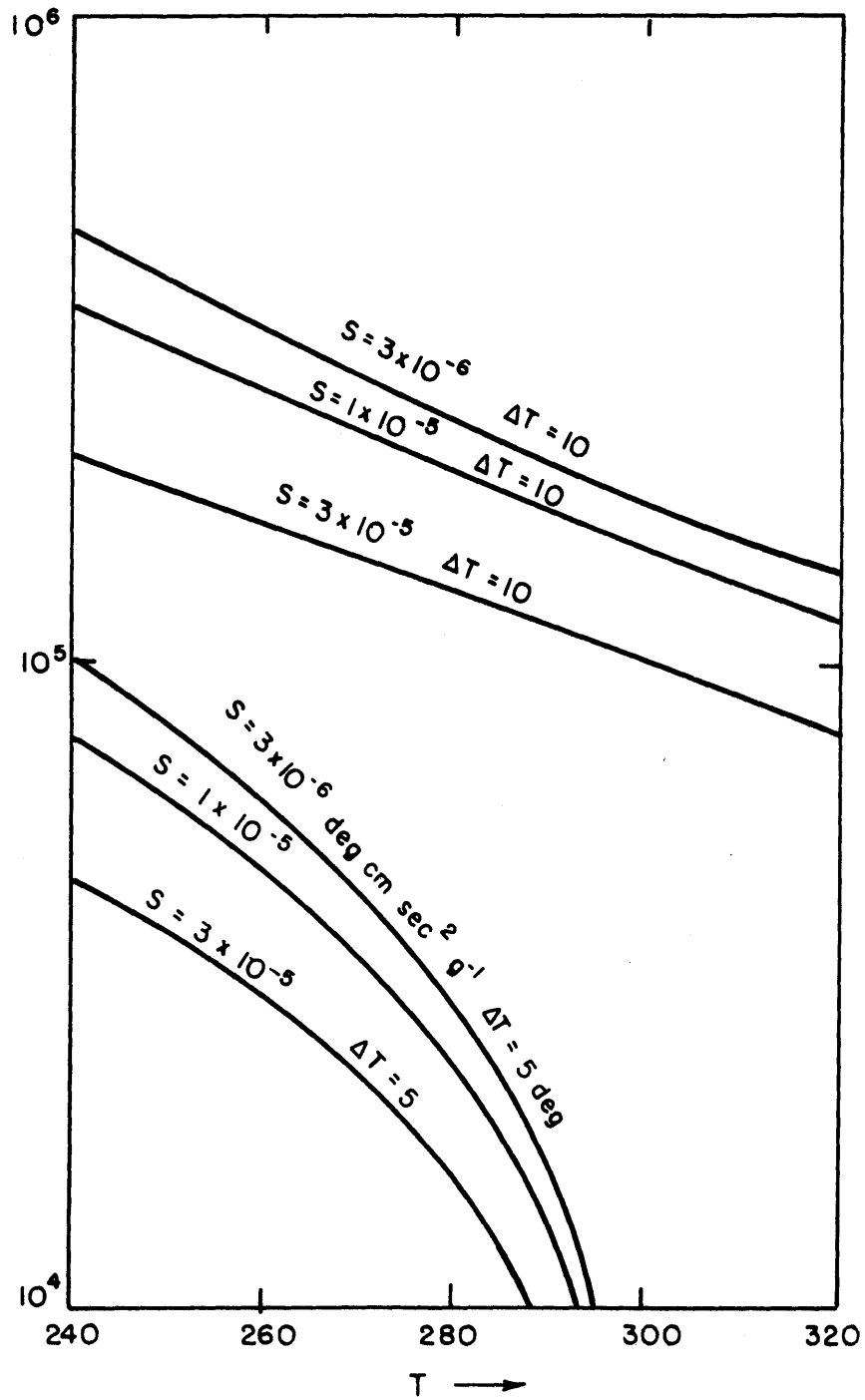


Figure 4.4a. The decrease in q_a with temperature is plotted for various boundary-layer temperature differences, ΔT , and static stabilities, S .

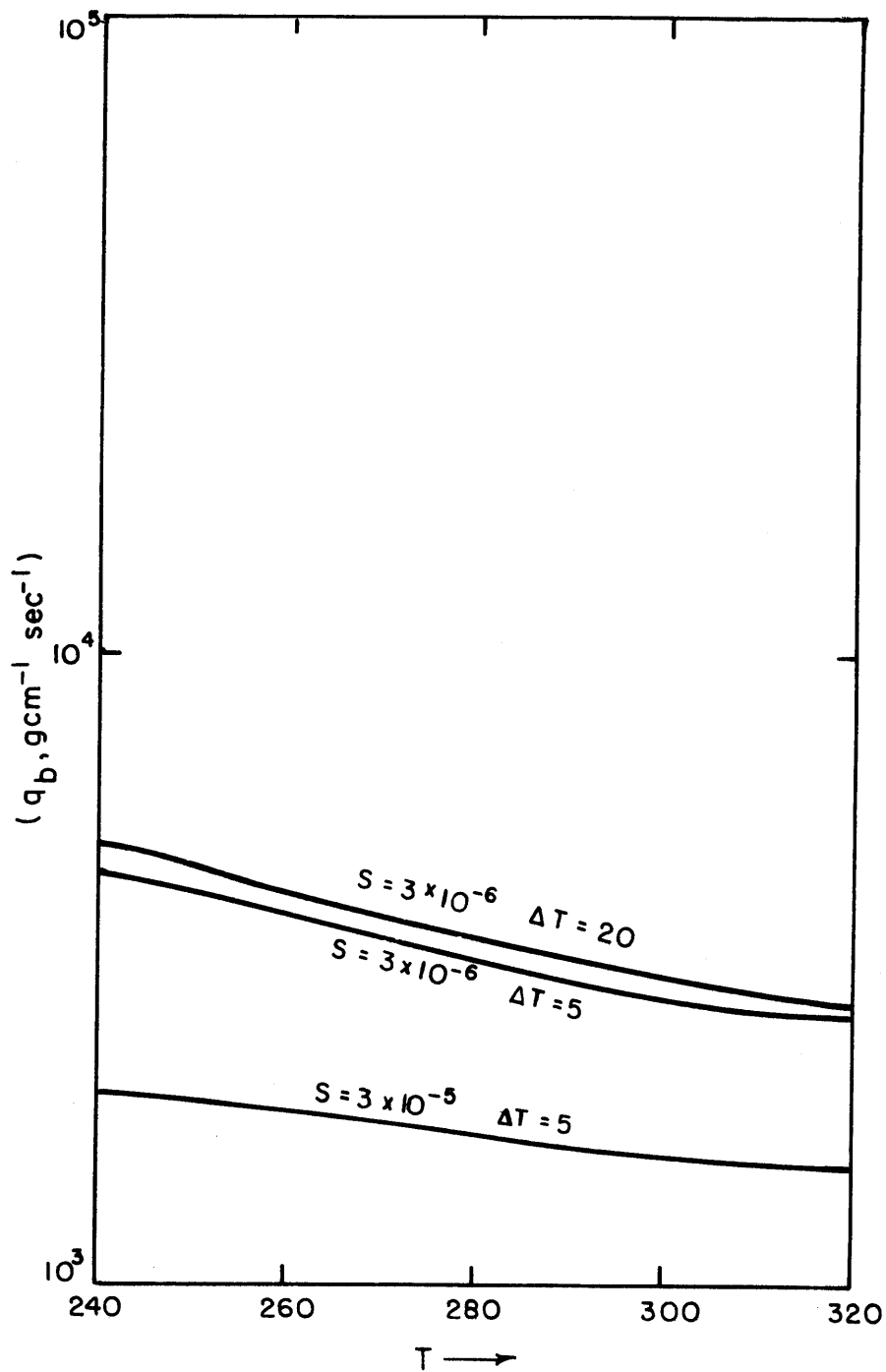


Figure 4.4b. The decrease in q_b with temperature is plotted for various boundary-layer temperature difference, ΔT , and static stabilities, S .

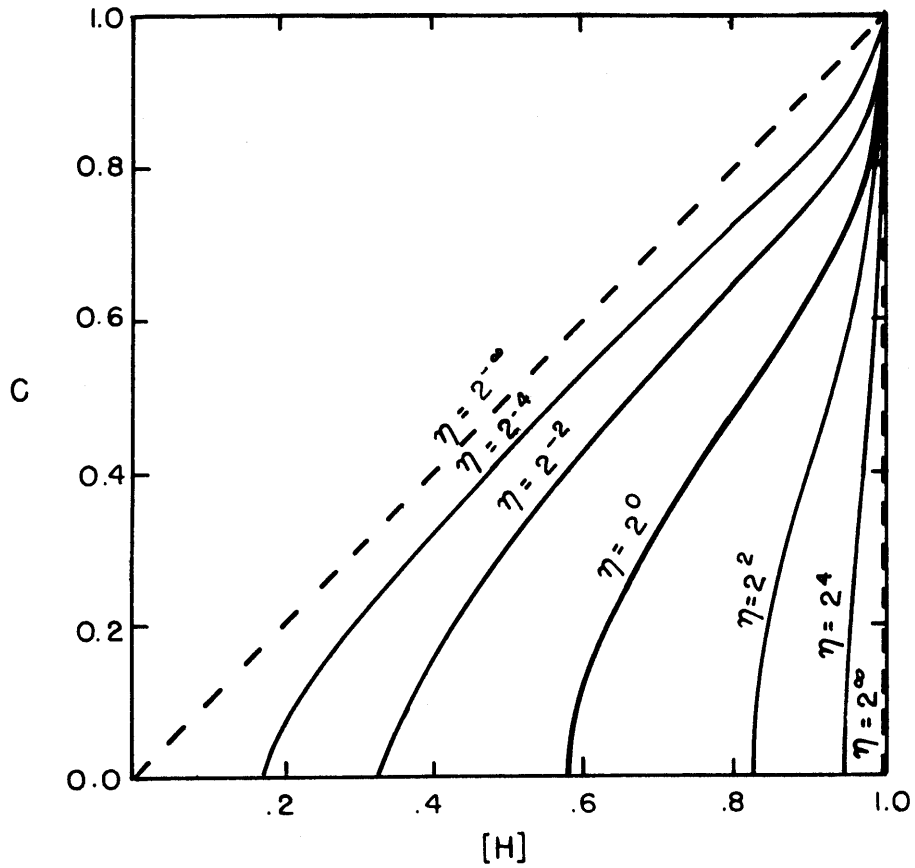


Figure 4.5a. Fractional cloud cover C, versus the zonal relative humidity for various ratios of a measure of the surface turbulent transport, to a measure of the free atmosphere water vapor transport and dynamical heating η .

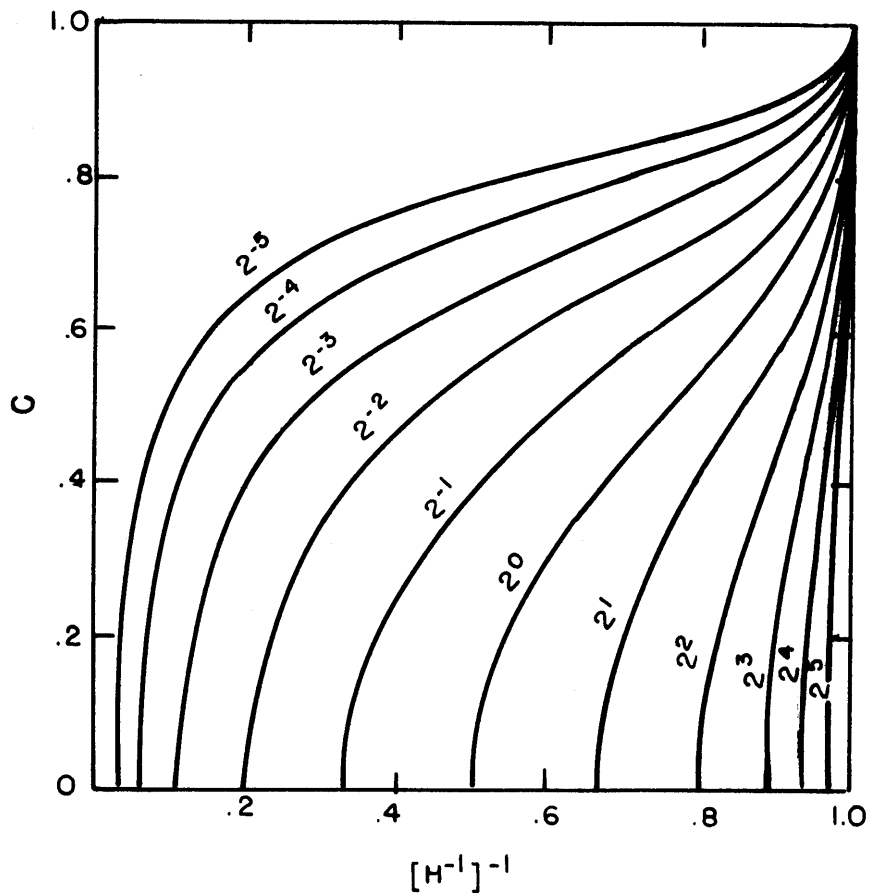


Figure 4.5b. Fractional cloud cover, C , versus the inverse of the zonal average of the inverse relative humidity for various η .

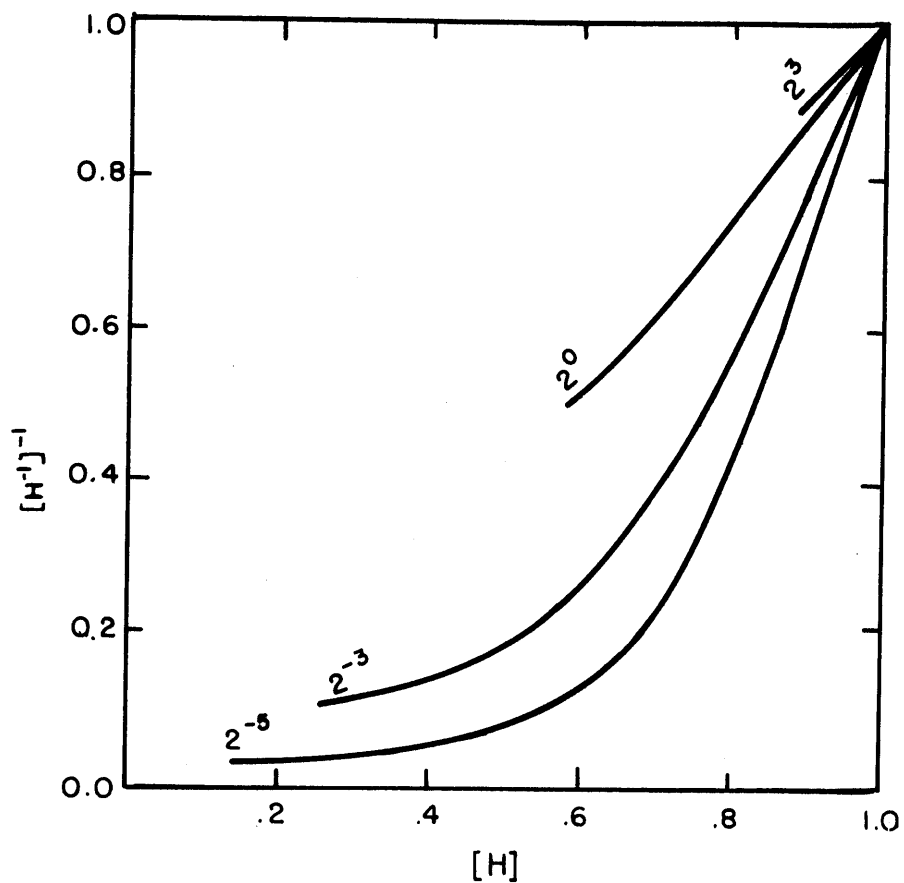


Figure 4.5c. The relationship between the inverse of the zonally averaged inverse relative humidity and the zonally averaged relative humidity is different for the various η .

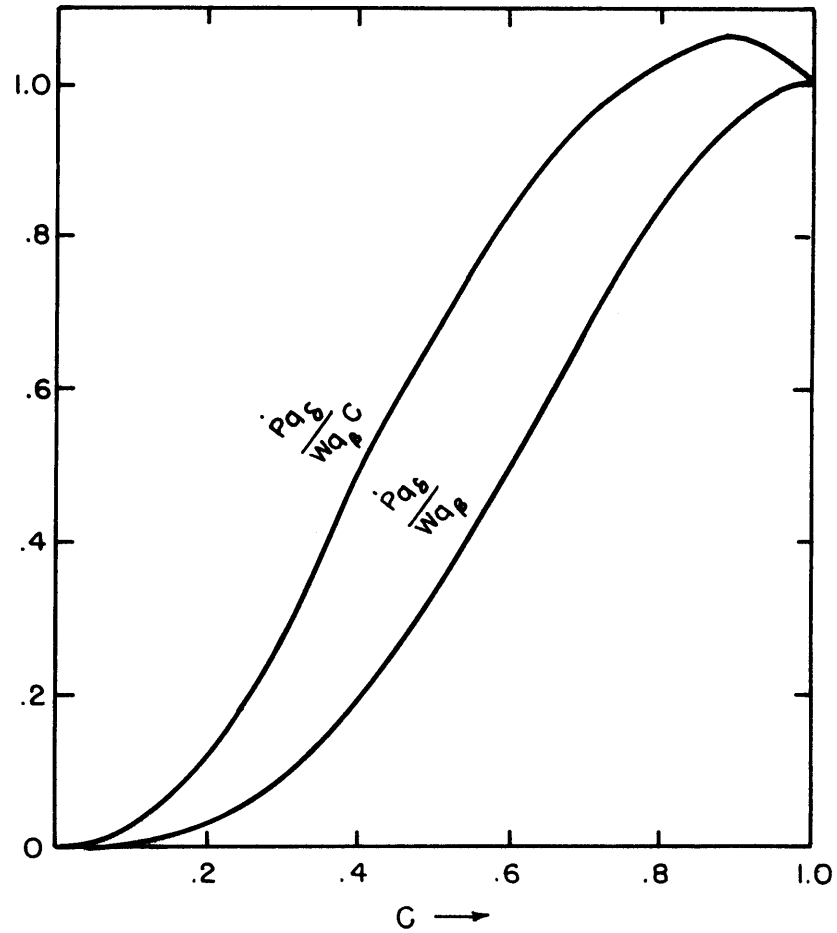


Figure 4.6. Ratio of the average precipitation versus fractional cloud cover, C .

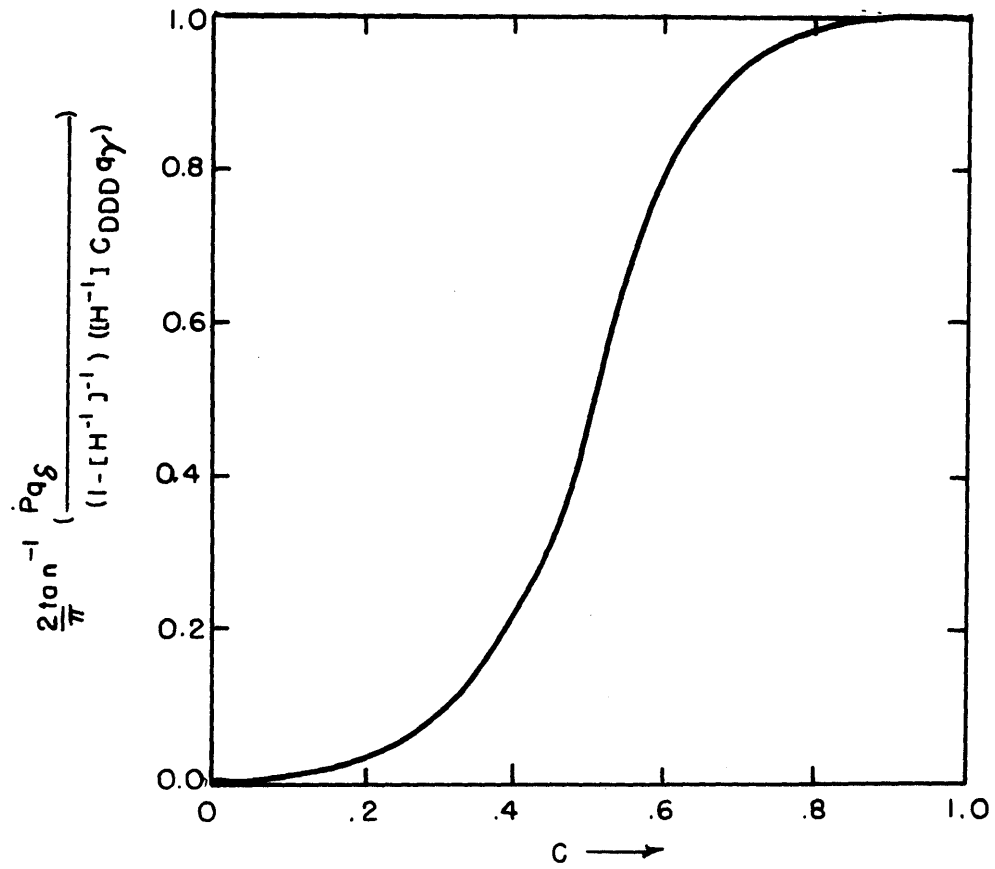


Figure 4.7. Relation between the precipitation, relative humidity and surface turbulent transports as a function of cloud cover, C.

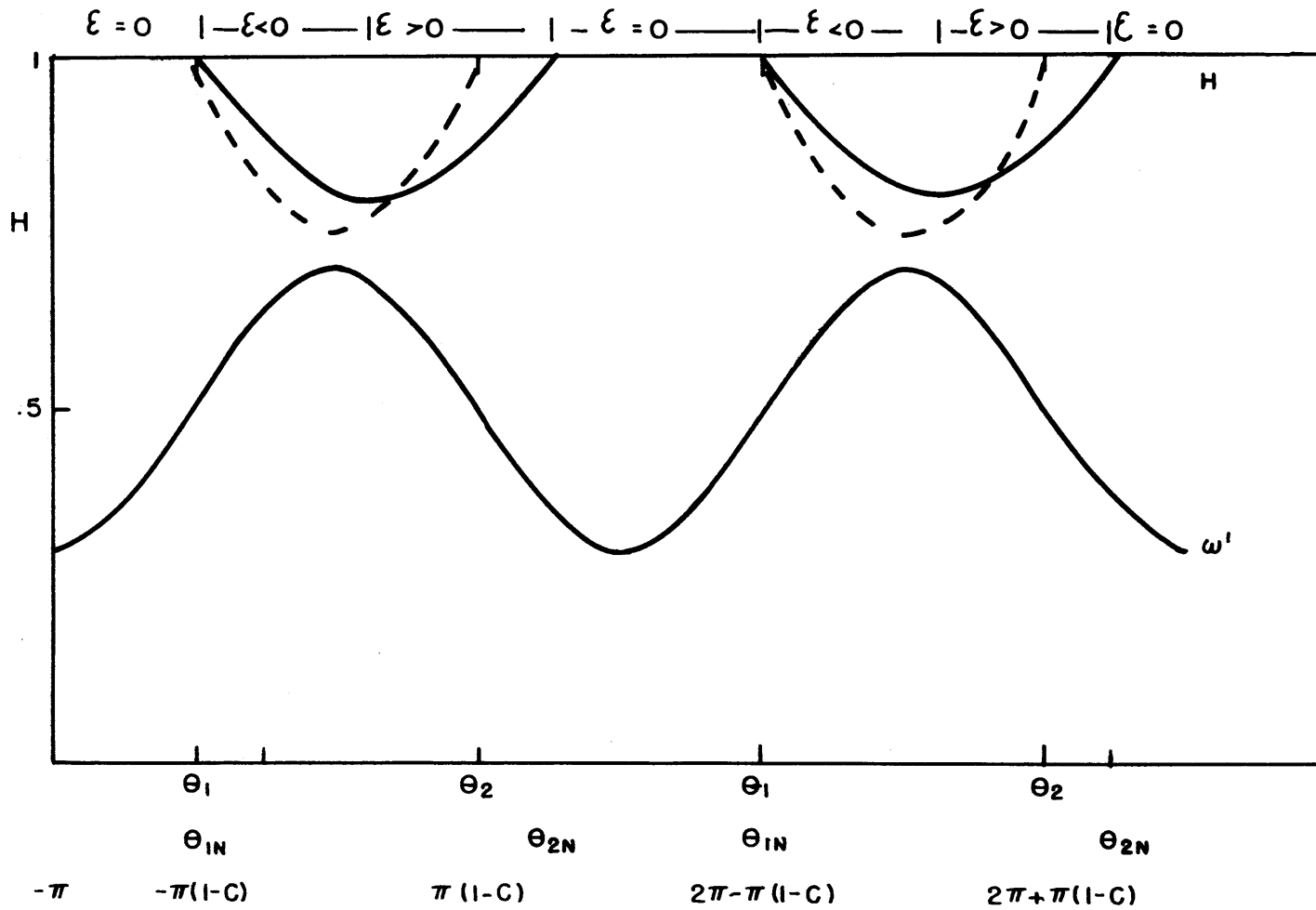


Figure 4.8. Relative humidity when entrainment is present. The dashed line is the solution of the relative humidity for no entrainment effects.

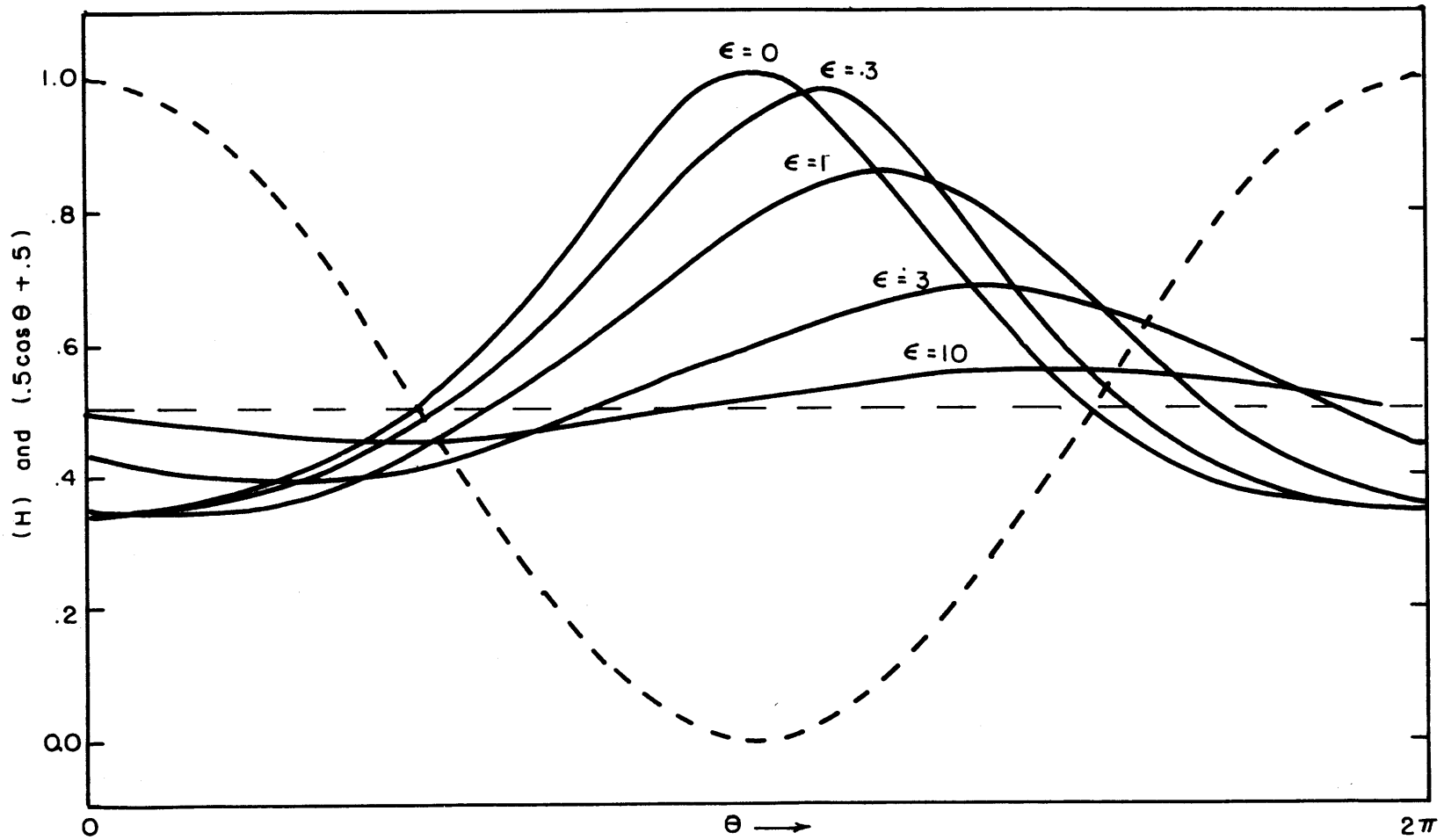


Figure 4.9a. For $C=.05$ and $\eta=1.0$, H - as a function of θ - is shown for various ϵ . The dashed line is the scaled sigma velocity.

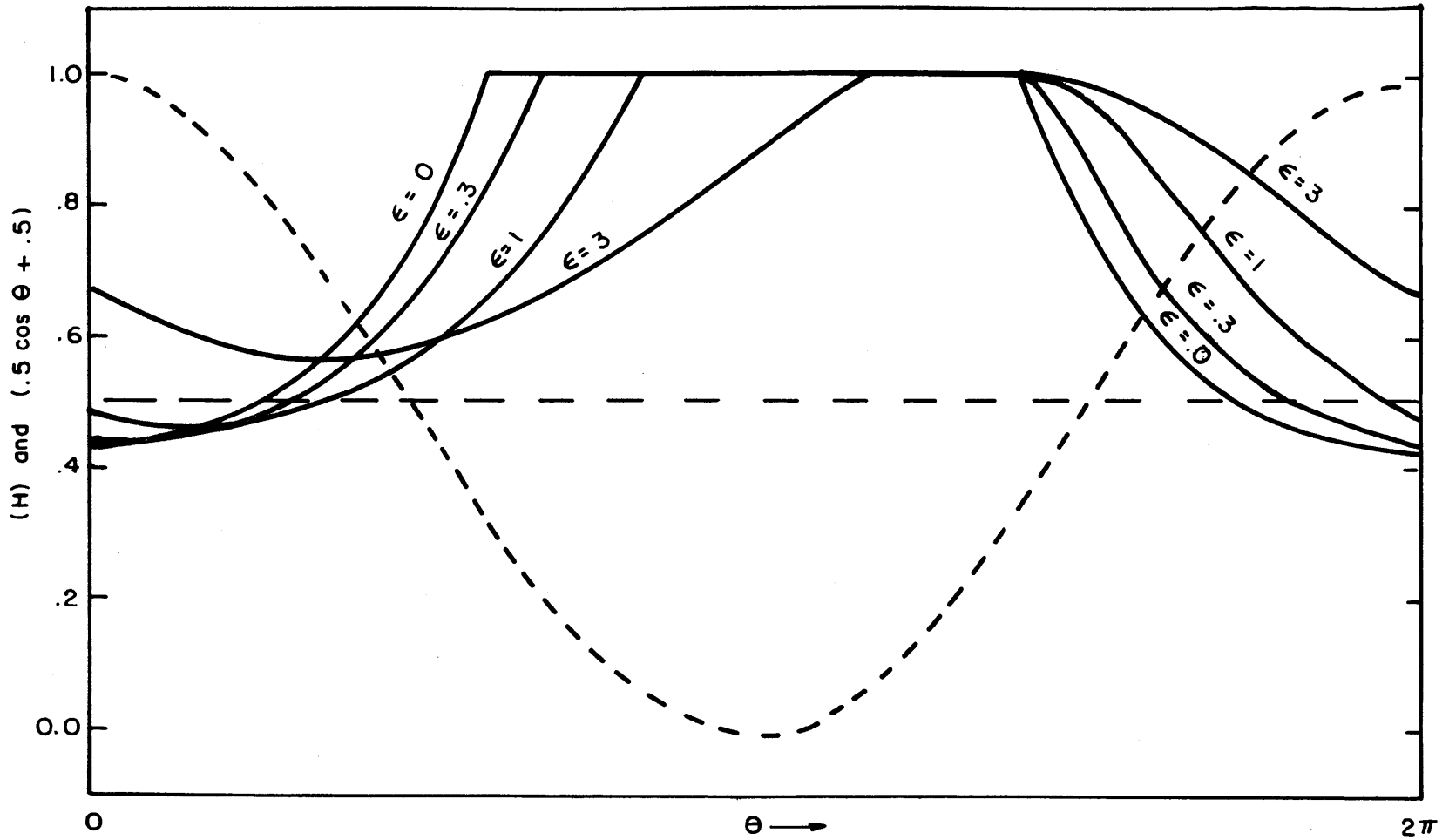


Figure 4.9b. For $C=.4$ and $\eta=1$, H - as a function of θ - is shown for various ϵ . The dashed line is the scaled sigma velocity.

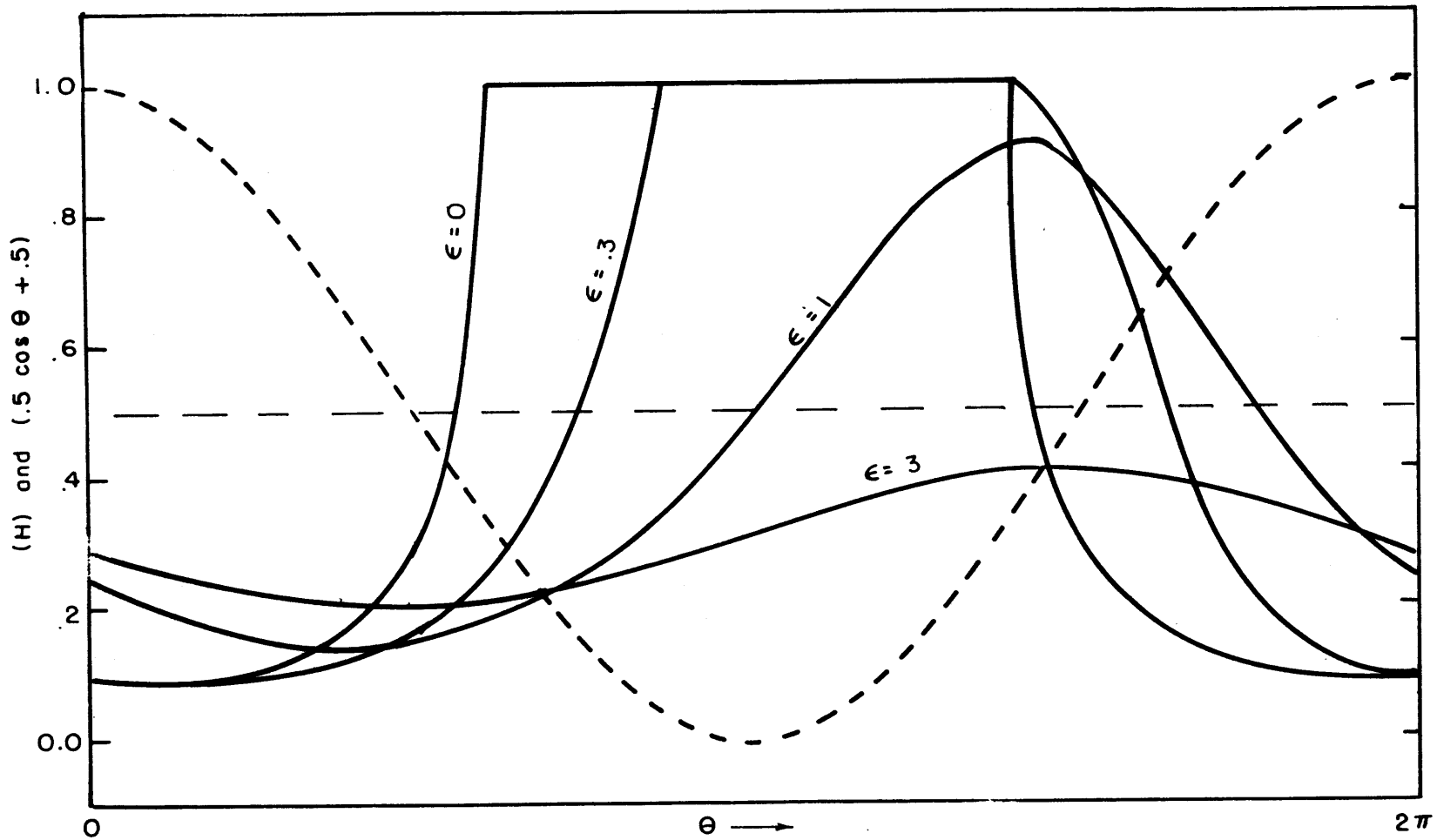


Figure 4.9c. For $C=.4$ and $\eta=.125$, H - as a function of θ - is shown for various ϵ . The dashed line is the scaled sigma velocity.

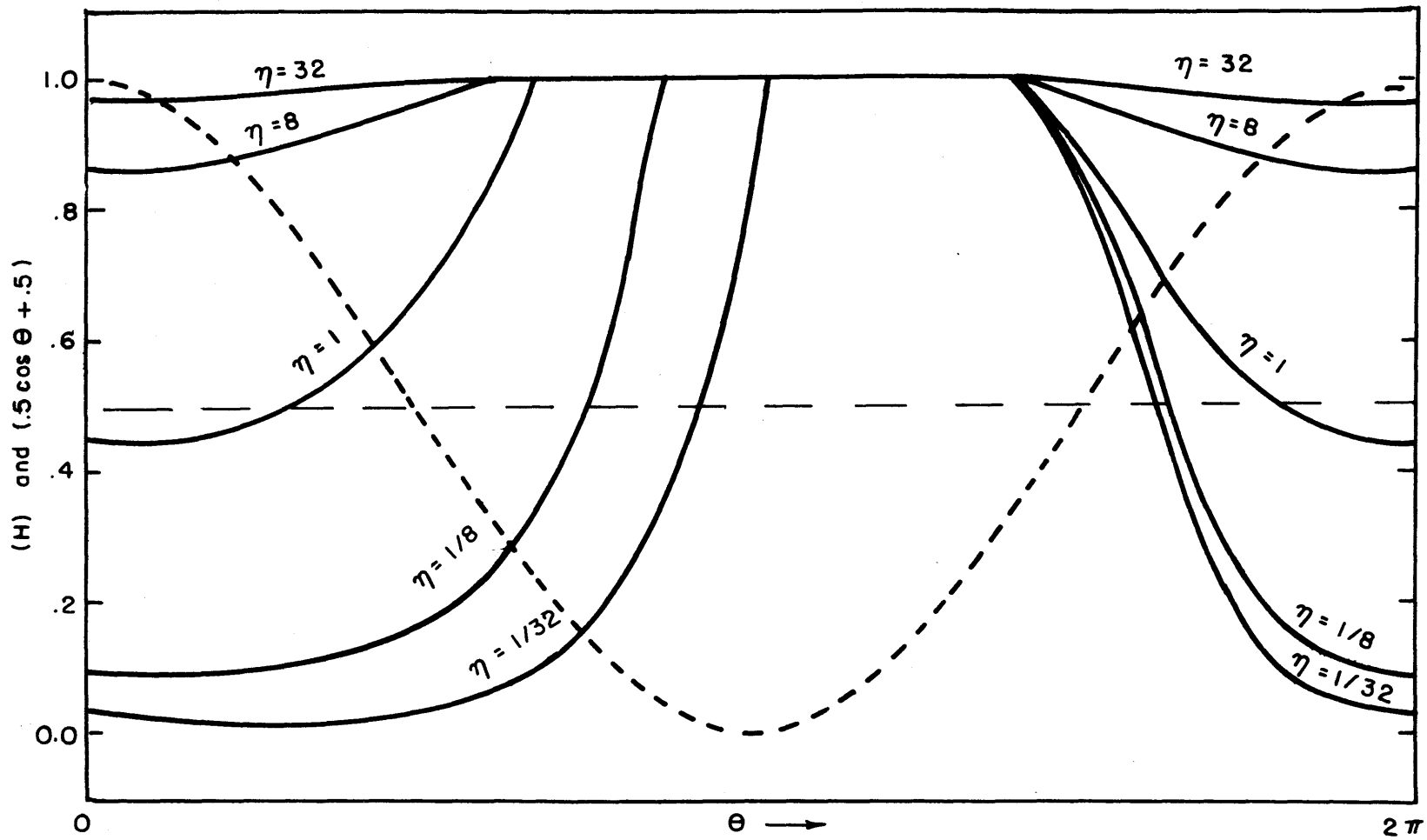


Figure 4.9d. For $C=.4$ and $\epsilon=.3$, H - as a function of θ - is shown for various η . The dashed line is the scaled sigma velocity.

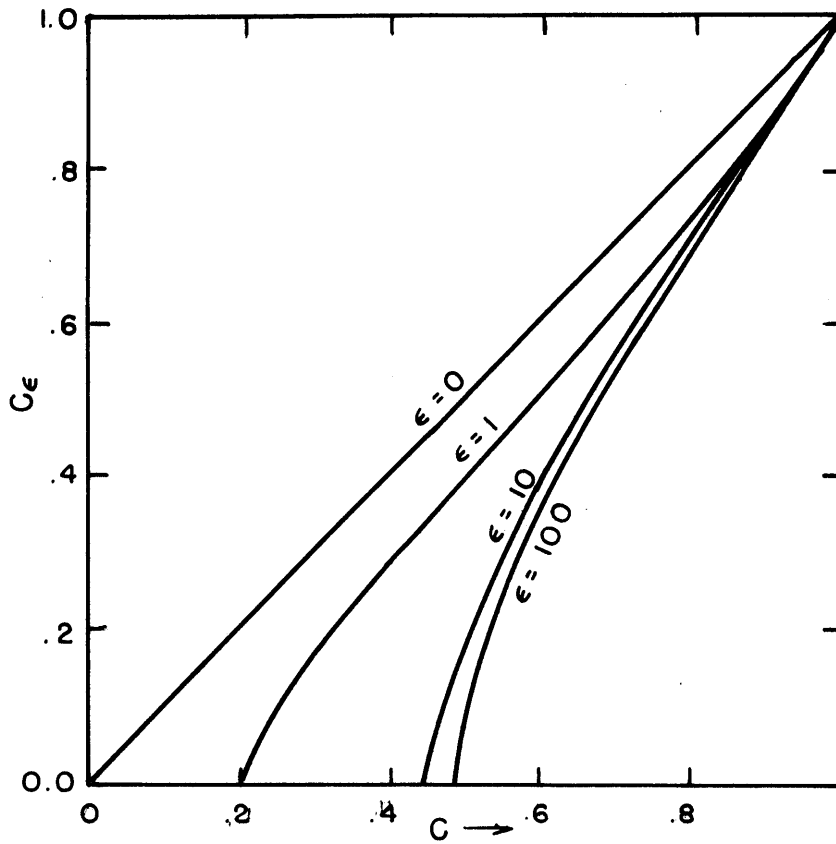


Figure 4.9e. The cloud cover C_ϵ - resulting from entrainment - is plotted as a function of the cloud cover which would result if no entrainment were present - for various entrainment rates, ϵ . $\eta=1$.

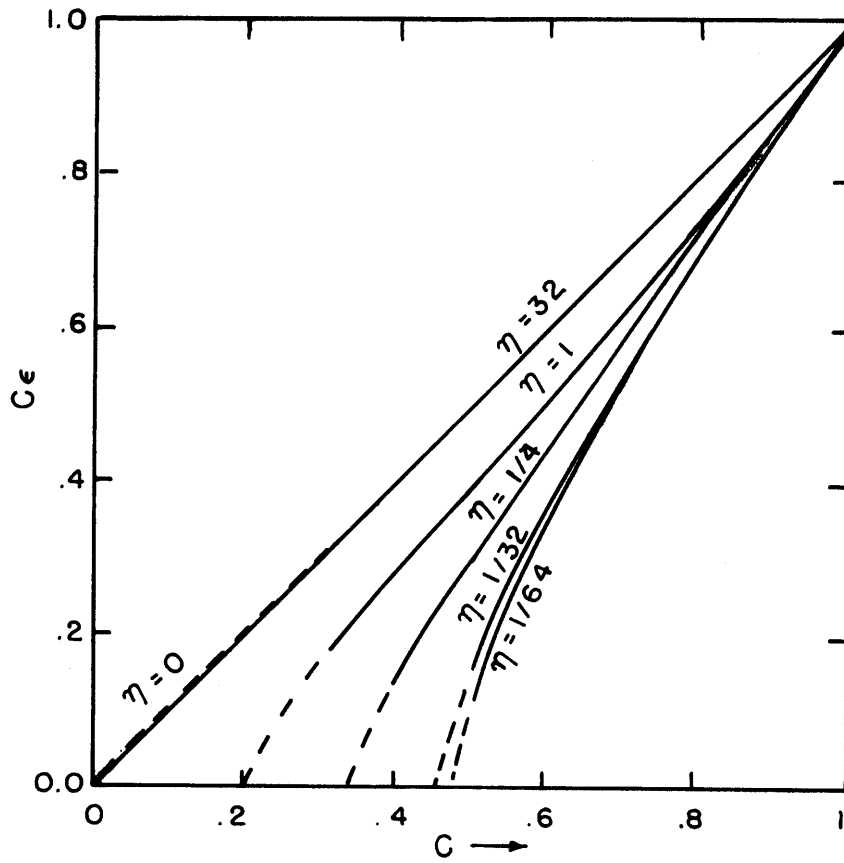


Figure 4.9f. The cloud cover resulting from entrainment is plotted as a function of the cloud cover - which would result if no entrainment were present - for various η . $\epsilon=1$.

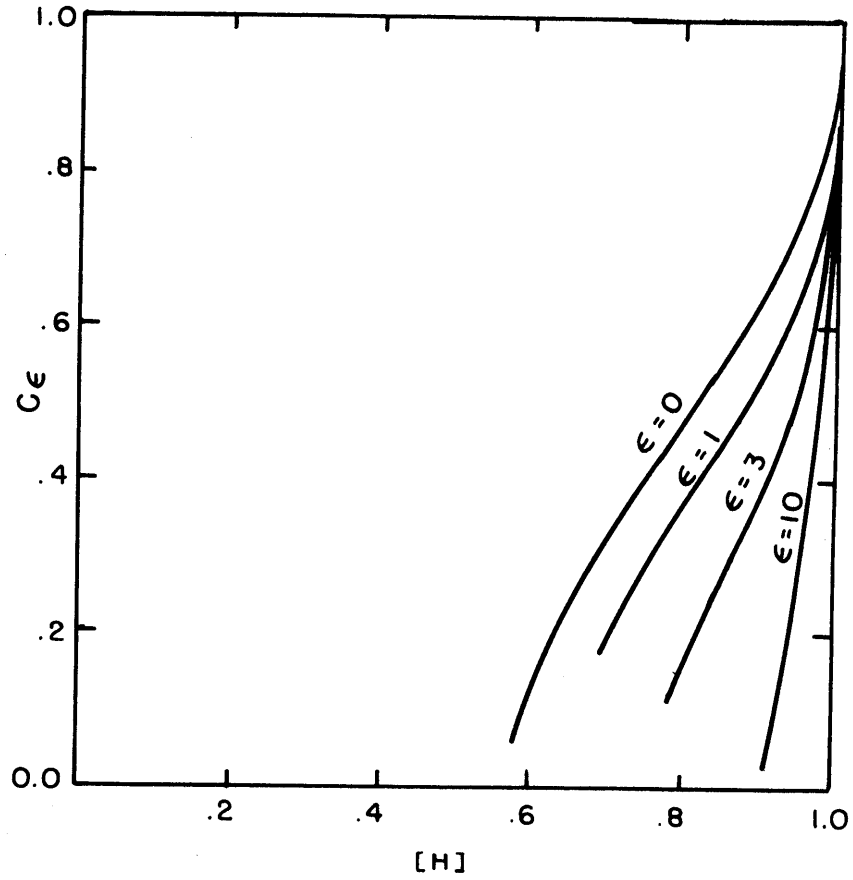


Figure 4.9g. Equilibrium fractional cloud cover - as a function of zonally averaged relative humidity - for $n=1$ and various ϵ .

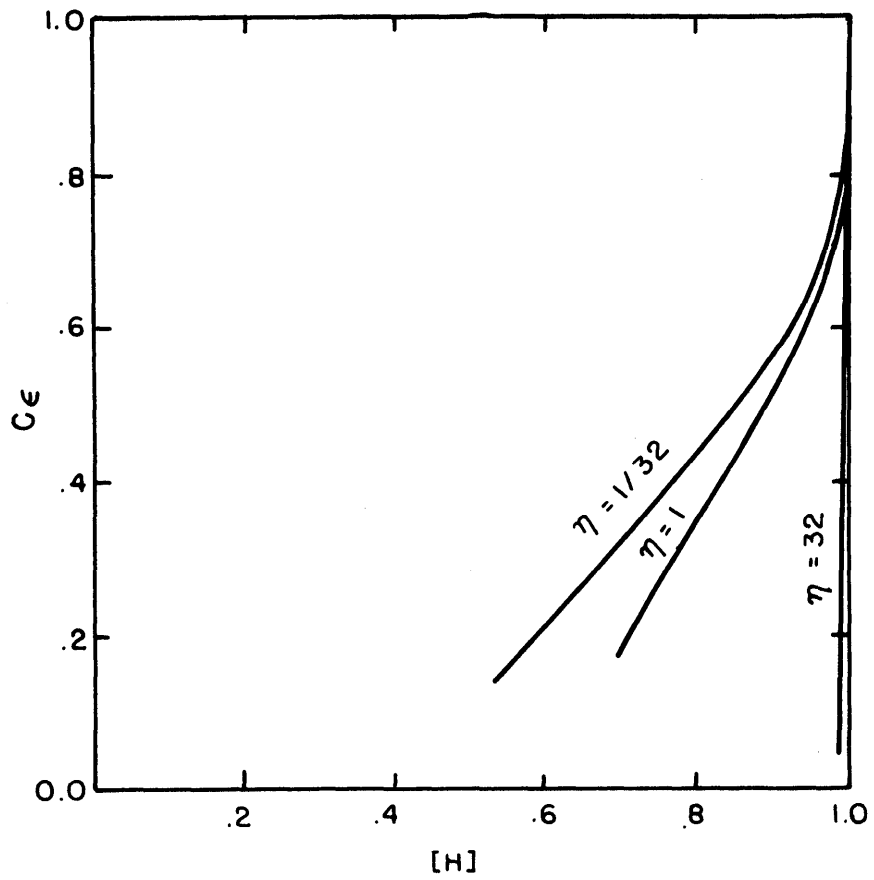


Figure 4.9h. Equilibrium fractional cloud cover - as a function of zonally averaged relative humidity - for $\epsilon=1$ and various η .

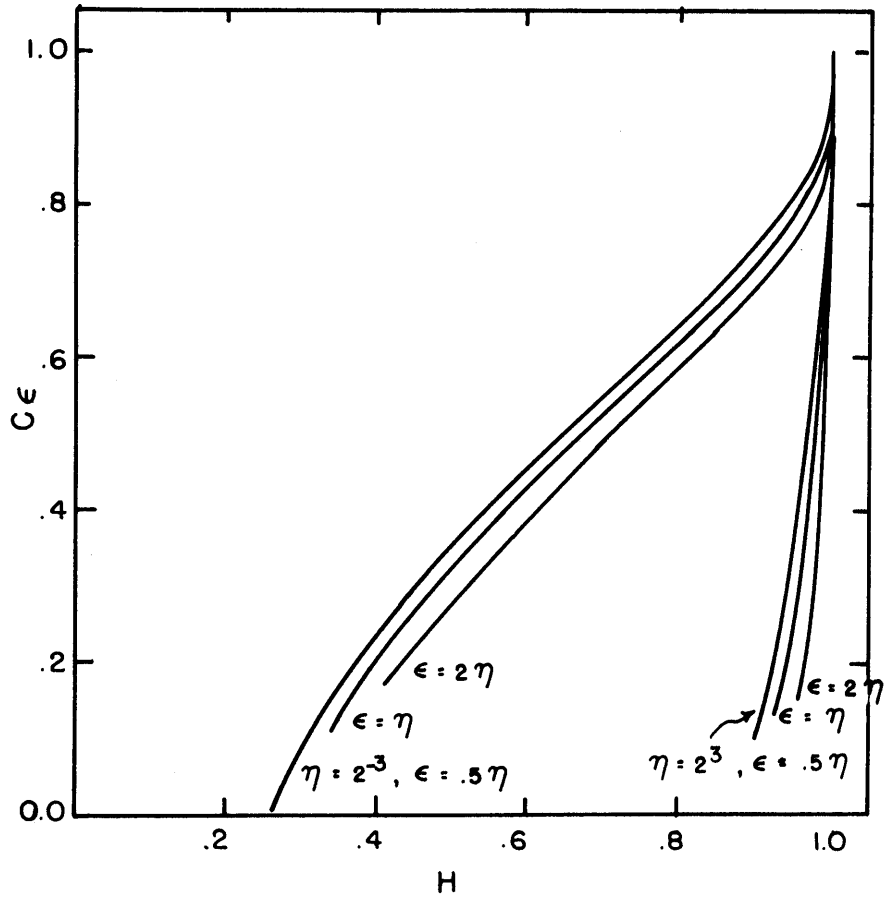
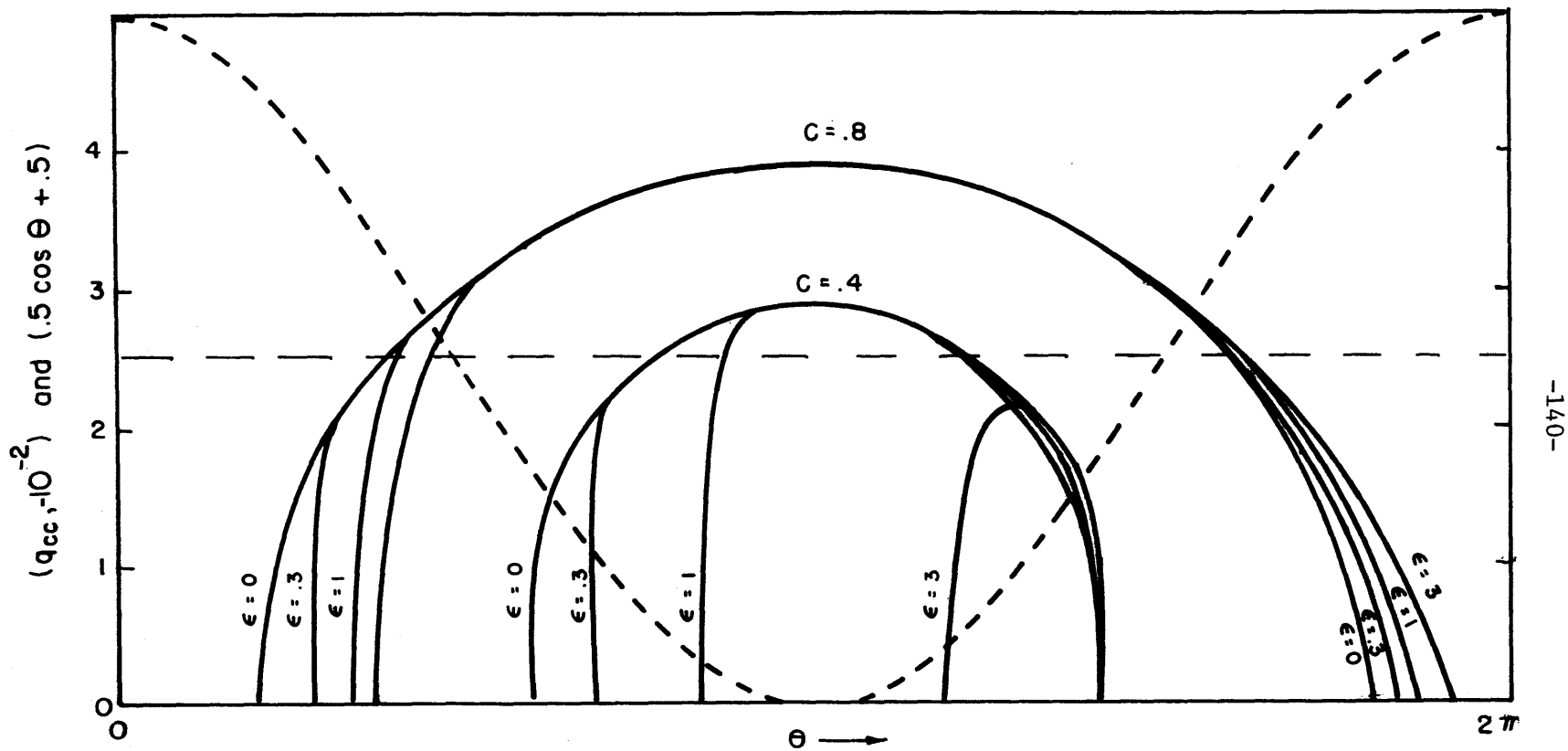


Figure 4.9i. Fractional cloud cover, C , as a function of the relative humidity for various η and ϵ .



-140-

Figure 4.10a. For $\delta=3 \times 10^{-2}$, $\chi=2/3$, $\psi=.1$, $\eta=1$, q_{cc} - as a function of θ - is shown for various C and ϵ .

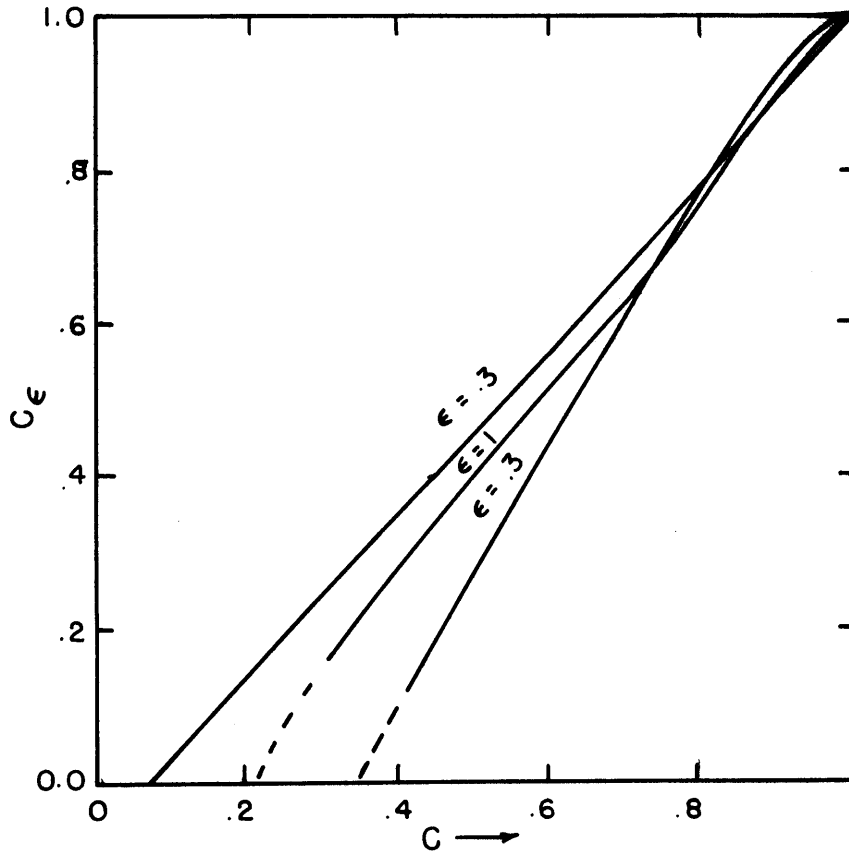


Figure 4.10b. The cloud cover, C_ϵ - resulting from entrainment and detrainment - is plotted as a function of the cloud cover which would result if $\epsilon=0$ for various ϵ . $\delta=3 \times 10^4$, $\chi=2/3$, $\psi=.1$, and $\eta=1$.

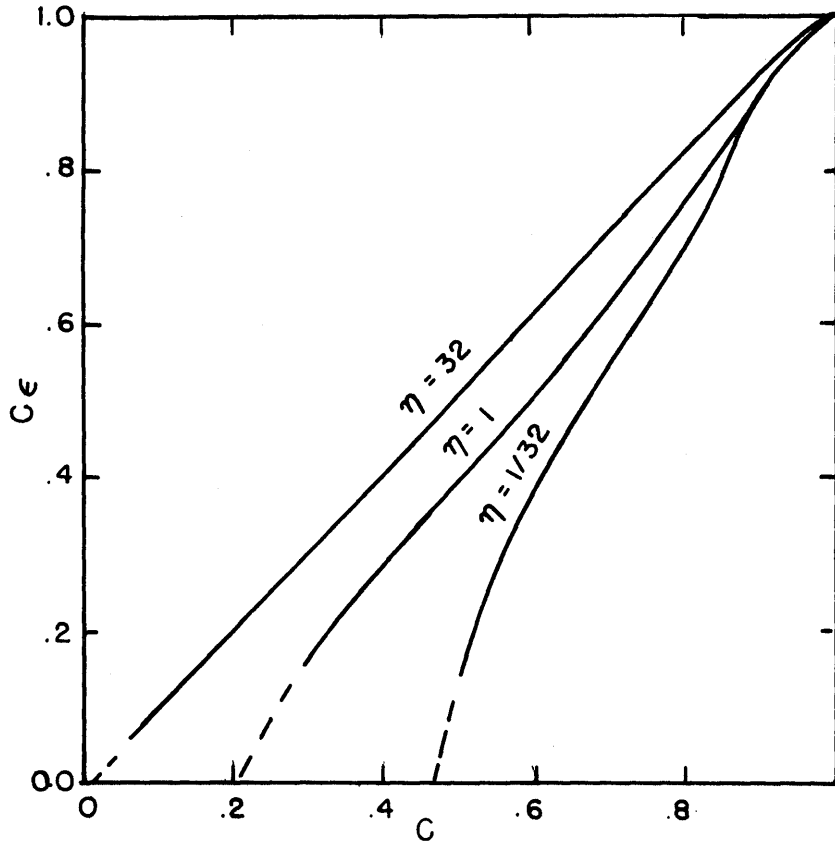


Figure 4.10c. The cloud cover, C - resulting from entrainment and detrainment - is plotted as a function of the cloud cover which would result if $\epsilon=0$ for various η . $\epsilon=1$.

5. Description of Experiments

5.1 Time Series

Starting at the same initial point (the initial point was taken as soon as the model was assumed error free), the average equilibrium temperature (T_E) was specified for one experiment to be 15° warmer than the T_E of the normal climate ($[T_g]=280$) experiment and was specified to be 15° colder in a third experiment. These experiments are hereafter denoted the hot (H), normal (N), and cold (C) climates respectively. Another set of experiments specified the equilibrium absolute meridional temperature gradient ($AMTG_E$) to either be larger by 3×10^{-8} deg cm^{-1} or smaller by 3×10^{-8} deg cm^{-1} than the N climate which had an $AMTG_E$ at the surface of 6×10^{-8} deg cm^{-1} . These latter experiments are hereafter denoted the 9 and 3 climates, respectively. The variations in the imposed experimental forcings were rather large in order that we would not have to integrate for long periods in order to obtain statistically significant results. By forcing these large differences, however, we had to integrate for long enough periods to ensure that the time averages are statistically independent of the initial state. (See the discussion by Chervin and Schneider, 1976.)

The free atmosphere average equilibrium static stability of 2.85×10^{-5} deg cm^{-1} varied linearly from 2.35×10^{-5} deg cm^{-1} at the southern boundary to 3.35×10^{-5} deg cm^{-1} at the northern boundary and the boundary layer average equilibrium static stability of 3.85×10^{-5} deg cm^{-1} ($\Delta T \approx 14.5$ deg) varied linearly from 3.35×10^{-5} deg cm^{-1} ($\Delta T \approx 16.6$) at the southern boundary

to 4.35×10^{-5} deg cm^{-1} ($\Delta T \approx 12.4$ deg). See Chapter 2 for a description of the imposed temperature gradients.

The average surface pressure was initially specified to be 1015.0mb; a certain amount of mass was lost over time due to truncation and smoothing; since the loss was small no correction was made. Other general circulation modelling groups usually add a small amount every day.

The basic model parameters are tabulated in table 5.1. Various other experiments to test some of the effects of these model parameterizations and scales are discussed in section 6.3 - after the basic experiments' temperature sensitivity is discussed.

Time series of TPE and TKE for the various experiments are shown in figures 5.2 and 5.3. By plotting the time series of variables such as these we are able to determine qualitatively when a particular experiment has reached statistical equilibrium. We then can proceed to time average over the remainder of the series. The averaging periods are indicated on the figures. The type of climate is denoted on the right hand side of the series.

From the initial starting point, the TPE of the hot and cold climates reached statistical equilibrium after about 100 days - see figure 5.2a. Since the hot climate's TPE increased relatively more than the cold climate's, the relative time for TPE to reach statistical equilibrium is actually much less for warm climates. This has been discussed by Wetherald and Manabe (1975) for their general circulation model.

The climate for a small AMTG_E started at a much higher relative value than the climate with a large AMTG_E and hence took a longer time to reach statistical equilibrium - although the time was still on the order of a

hundred days (figure 5.3a). Less drastic changes require less time to reach statistical equilibrium - as may be seen from examination of other time series. For example, the kinetic energy for the cold climate was relatively unchanged from that of the normal climate and hence statistical equilibrium was reached almost immediately. Examination of a particular time series is required if great confidence is needed that a particular model average of a time series is taken when the time series is stationary.

Once statistical equilibrium has been reached, the time variations or standard deviations of various time series depend upon the particular model variable and the particular climate. Time variations in TPE increase with an increasing T_E (figure 5.2a) and an increasing $AMTG_E$ (figure 5.3a). Time variations in TKE increase with an increasing $AMTG_E$ (figure 5.3b) and increase greatly for the hot climate (figure 5.2b) but no distinct difference between the normal and cold climates was obtained. The variations of TPE and TKE tend to correspond to their respective magnitudes.

5.2 Synoptic Examples

Since climatic results are time averages of many weather events, we present some typical weather from the hot and cold climates in the small domain ($0 \leq x \leq 9 \times 10^3$ km, $0 \leq y \leq 6 \times 10^3$ km). We discuss briefly the non-divergent component of the horizontal wind field, the sigma velocities, the cloud water, and the relative humidity.

The nondivergent component of the horizontal wind field is presented in terms of the horizontal stream function, Ψ ; we define

$$\frac{p_s v_k}{2g} = \frac{\partial \Psi_k}{\partial x} \quad (5.2.1)$$

and

$$\frac{p_s u_k}{2g} = -\frac{\partial \Psi_k}{\partial y}$$

From model results we obtain u_k , v_k , and p_k ; Ψ is obtained from

$$(\delta_x^2 + \delta_y^2) \Psi_k = \frac{1}{2g} (\delta_x \overline{p_s^x} \overline{v_k^x} - \delta_y \overline{p_s^y} \overline{u_k^y}) \quad (5.2.2)$$

by relaxation.

Figure 5.4a shows the horizontal mass stream function at the upper level for the hot climate at day 447.5; numbered contours are placed every 5.0×10^{13} g/sec with small numbers corresponding to cyclonic circulation and large numbers to anticyclonic circulations. There is a predominantly cyclonic circulation in the northern part and a predominantly anticyclonic circulation in the southern part. The strongest winds are zonal and occur in the center of the domain (the zonal jet). Figure 5.4b shows the horizontal mass stream function at the lower level. Although the patterns are qualitatively similar, the winds are much weaker.

Figure 5.4c shows the vertical velocity field for the hot climate. Upward velocities less than $-2 \text{gcm}^{-1} \text{sec}^{-3}$ are exceeded in several parts of the domain whereas downward velocities greater than $2 \text{gcm}^{-1} \text{sec}^{-3}$ are never exceeded. This indicates that the non-linear process of condensation is distorting the vertical velocities into small areas of intense upward motion, large areas of weak upward motion, and large areas of weak downward motion.

The cloud-water field is shown in figure 5.4d. The blank regions represent clear skies ($0 \leq \{q_c\} < 5 \times 10^{-3} \text{ gcm}^{-1}$) while the larger numbers indicate that large amounts of cloud water are present. By comparing figure 5.4d with figure 5.4c we find that the largest cloud amounts are associated with upward velocities stronger than $-2.0 \text{ gcm}^{-1} \text{ sec}^{-3}$. Clear regions are associated with downward velocities.

The relative-humidity field is shown in figure 5.4e. The smallest relative humidities are associated with the largest downward velocities, and the relative humidities greater than 95% (denoted by plus signs) are mainly associated with upward velocities.

Figures 5.4f, 5.4g, 5.4h, 5.4i, and 5.4j show the same variables 3.75 days later. The systems have all been translated eastward with considerable distortion. Essentially, the storm on the western and central part of the domain has been translated to the central and eastern part of the domain.

The variables for the hot climate are to be compared with figure 5.5 which shows the variables for the cold climate. For the cold climate the winds are much weaker, vertical velocities are much smaller, clouds have much less water content in the vertical but are spread over larger horizontal areas, and the relative humidities are much larger in the fewer clear regions. Since we are comparing different synoptic situations, it is perhaps not fair to make conclusions about climatic differences. Nevertheless, as shown in Chapter 6, these conclusions are supported by the time averages.

5.3 Statistics of Time Averages

When comparing the time averages from different model runs, it is necessary to know whether the results are statistically significant or whether we were lucky in obtaining the desired result. Various statistical tests require a knowledge of the standard deviation of the fluctuations; the differences in the averages must be much greater than the standard deviations for us to have great confidence that they really are different. If the data from a particular series were statistically independent, then the standard deviation, $\bar{\sigma}$, of a particular model average is

$$\bar{\sigma} = \sigma / \sqrt{N}, \quad (5.3.1)$$

the standard deviation, σ , of the series divided by the square root of the number of observations. Larger sample averages for a stationary series will have smaller standard deviations. Unfortunately, much larger samples are needed for meteorological time-series data since most meteorological variables are serially correlated; the effective N for meteorological time samples is the effective number of independent events within the sample.

Leith (1973) suggested a method for determining the number of independent events. For a stationary time series, $\psi(t)$, with a mean, μ , and random fluctuations, $\phi(t)$;

$$\Psi(\tau) = \mu + \Phi(\tau). \quad (5.3.2)$$

the ratio of the variance of the time average, $\bar{\sigma}^2$, to the variance, σ^2 , of the series is

$$\frac{\bar{\sigma}^2}{\sigma^2} = \frac{2}{T} \int_0^T \left(1 - \frac{\tau}{T}\right) R(\tau) d\tau, \quad (5.3.3)$$

where

$$R(\tau) = \frac{\int_0^T \phi(x) \phi(x+\tau) dx}{\int_0^T \phi(x) \phi(x) dx} \quad (5.3.4)$$

is the ensemble lag-time correlation.

The lag-time correlations can be estimated from the series and then substituted into 5.3.3 to obtain an estimate of $\bar{\sigma}^2$ - as was done by Shukla (1975), or, following Leith, a simple model for $R(\tau)$ can be used to integrate 5.3.3 analytically.

For this reason, various lag-time correlations were plotted. Figure 5.6 shows the lag correlations for meridional and areal averages for T_1 , T_2 , and U_1 . Leith suggested that a first-order autoregressive process was an appropriate approximation for meteorological series. The lag-time correlation is given by

$$R(\tau) = e^{-\nu|\tau|}. \quad (5.3.5)$$

Substituting 5.3.5 into 5.3.3 Leith obtained

$$\frac{\bar{\sigma}^2}{\sigma^2} = \frac{2}{\nu T} \left(1 - \frac{1}{\nu T} (1 - \exp(-\nu T))\right) \quad (5.3.6)$$

and

$$\frac{\bar{\sigma}^2}{\sigma^2} \leq \frac{2}{\nu T} = \frac{T_0}{T} \quad ,$$

where T_0 is Leith's estimate of the characteristic time between independent events. The effective number of independent events is

$$N = T/T_0. \quad (5.3.7)$$

For simplicity T_0 is estimated by

$$T_0 = -\frac{2}{\ln R_1}, \quad (5.3.8)$$

where

$$R_1 = \frac{\sum_{i=1}^{T-1} \phi_i \phi_{i+1}}{\sum_{i=1}^T \phi_i \phi_i} \quad (5.3.9)$$

and

$$1 \leq T_0 \leq T. \quad (5.3.10)$$

The standard deviation of the time averages is

$$\bar{\sigma} = \sigma \sqrt{\frac{T_0}{T}}. \quad (5.3.11)$$

Areal averages tend to have a larger T_0 than zonal averages, which tend to have a larger T_0 than meridional averages; temperatures, horizontal velocities and evaporation tend to have a larger T_0 than vertical velocities, condensation, precipitation, and cloud fractional coverage; T_0 varies from less than a day to greater than 150 days depending on the variable and type of average; and T_0 tends to decrease with an increasing $AMTG_E$.

Summarizing, our statistical procedure is as follows: the effective T_0 for a particular time series is estimated from the auto-correlation at one lag; the standard deviation of the average is estimated; if the

model average for a particular variable is much different for different climates, the resulting difference is designated statistically significant - the statistical significance is in the eyes of the beholder. One pleasing result was that various bumps and irregularities in the variables - plotted with respect to y - were within the standard deviations. For most model variables the statistical procedure tends to over-estimate the integrand $(1 - \frac{\tau}{T})R(\tau)$ and, consequently, under-estimate the statistical significance of the results.

Table 5.1. Basic sensitivity tests' parameterizations and model scales

1. $[[T_g]] = 280$
2. $\frac{1}{C_p} [[\frac{\partial s_E}{\partial z}]] = 2.85 \times 10^{-5} \text{ deg cm}^{-1}$
3. $[[\frac{\partial T_g}{\partial y}]] = 6 \times 10^{-8} \text{ deg cm}^{-1}$
4. $\tau = 1.6 \times 10^6 \text{ sec}$
5. $H_c = 1.0$
6. $\dot{P} = \dot{P}_1$
7. $X = 9 \times 10^8 \text{ cm}$
8. $Y = 6 \times 10^8 \text{ cm}$
9. $IM = 18$
10. $JM = 12$
11. $\Delta = 5 \times 10^7 \text{ cm}$
12. $\Delta t = 900 \text{ sec}$

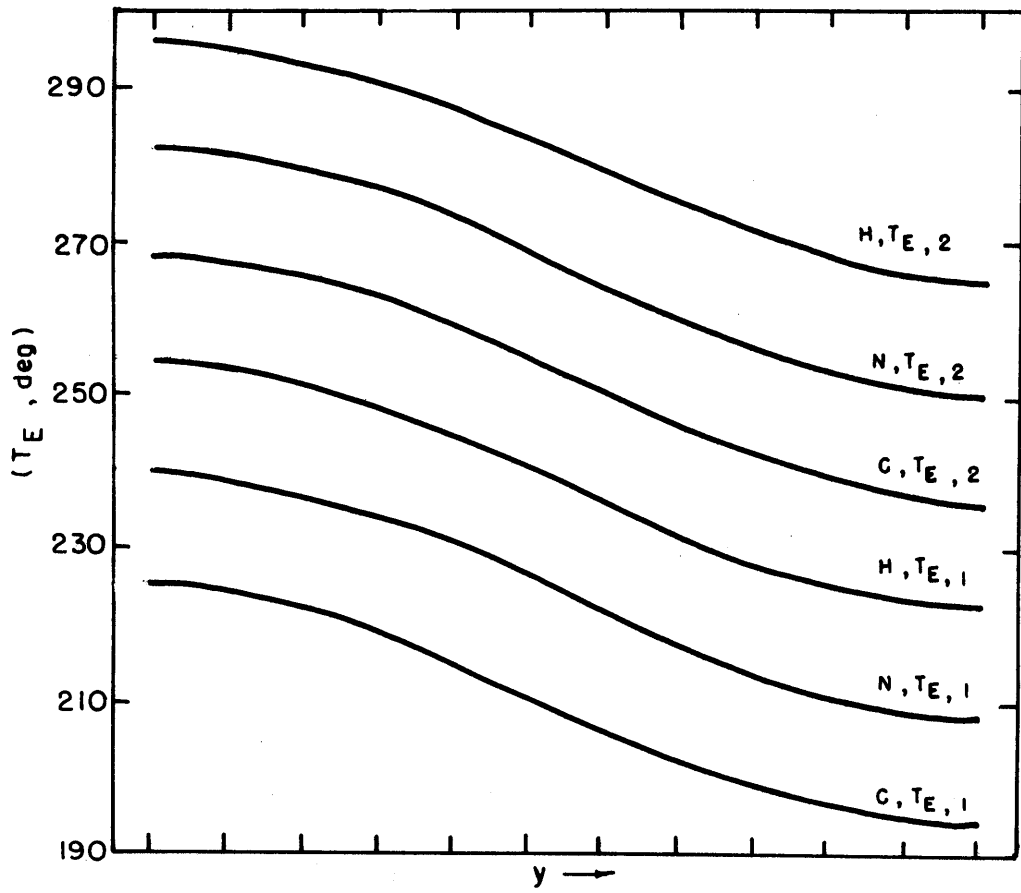


Figure 5.1a. Equilibrium temperature (T_E) at the upper (1) and lower levels (2) as a function of y are shown for the hot (H), normal (N), and cold (C) climates.

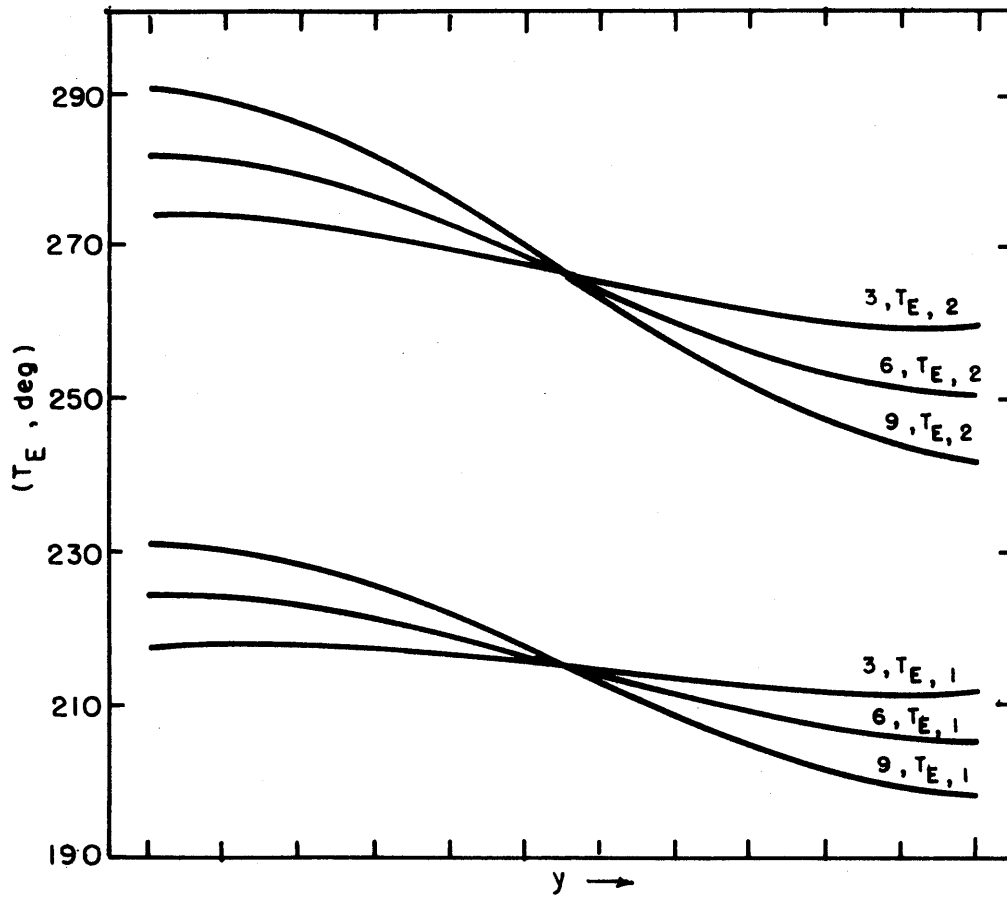


Figure 5.1b. Equilibrium temperatures as a function of y are shown for the climates with a large AMTG (9), normal AMTG (6), and a small AMTG (3).

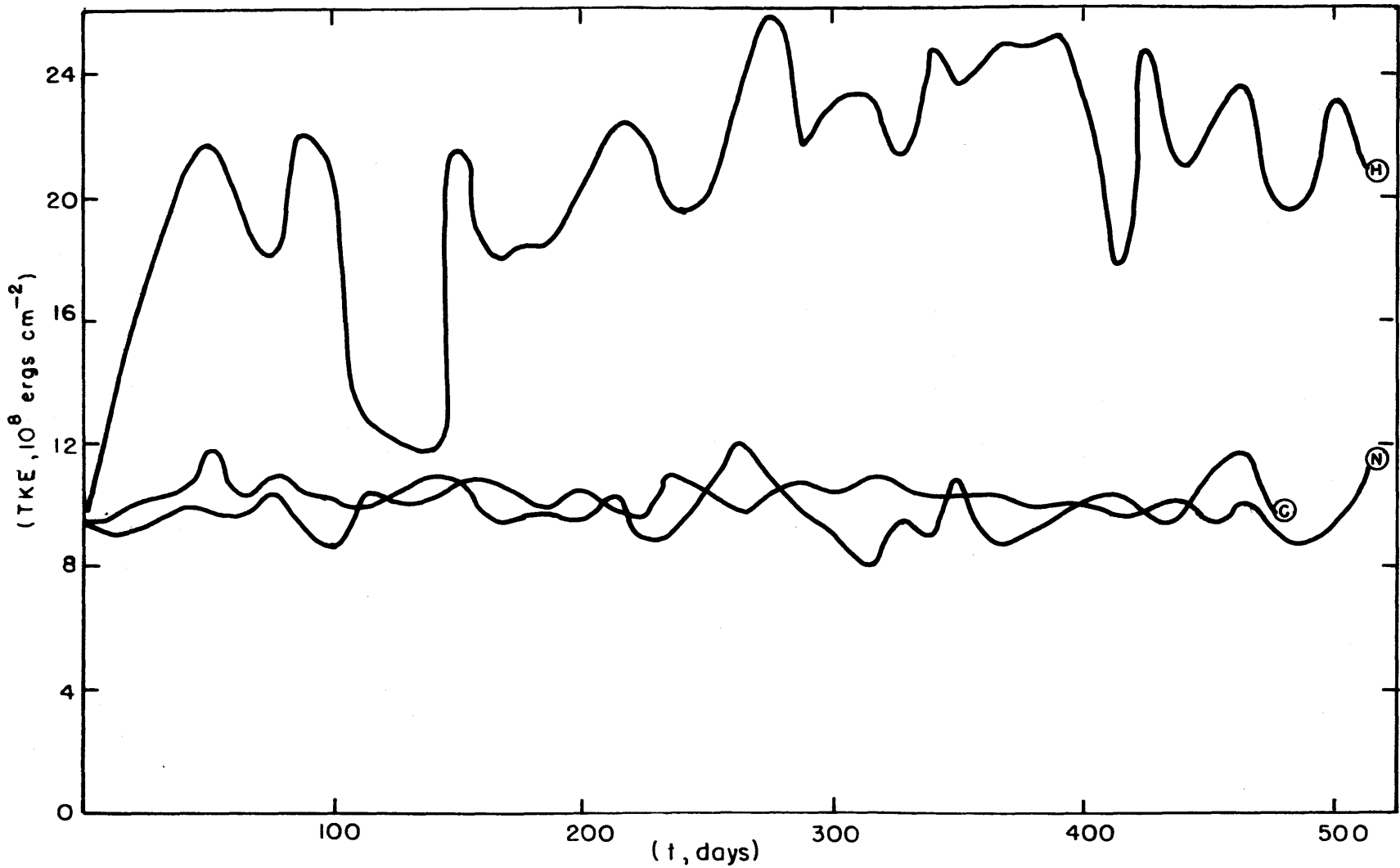


Figure 5.2a. Model TPE as a function of time for the hot, normal, and cold climates. Curves plotted from points 12.5 days apart. Dashed lines indicate the averaging period and the numbers refer to the experiment numbers. See Table 5.1.

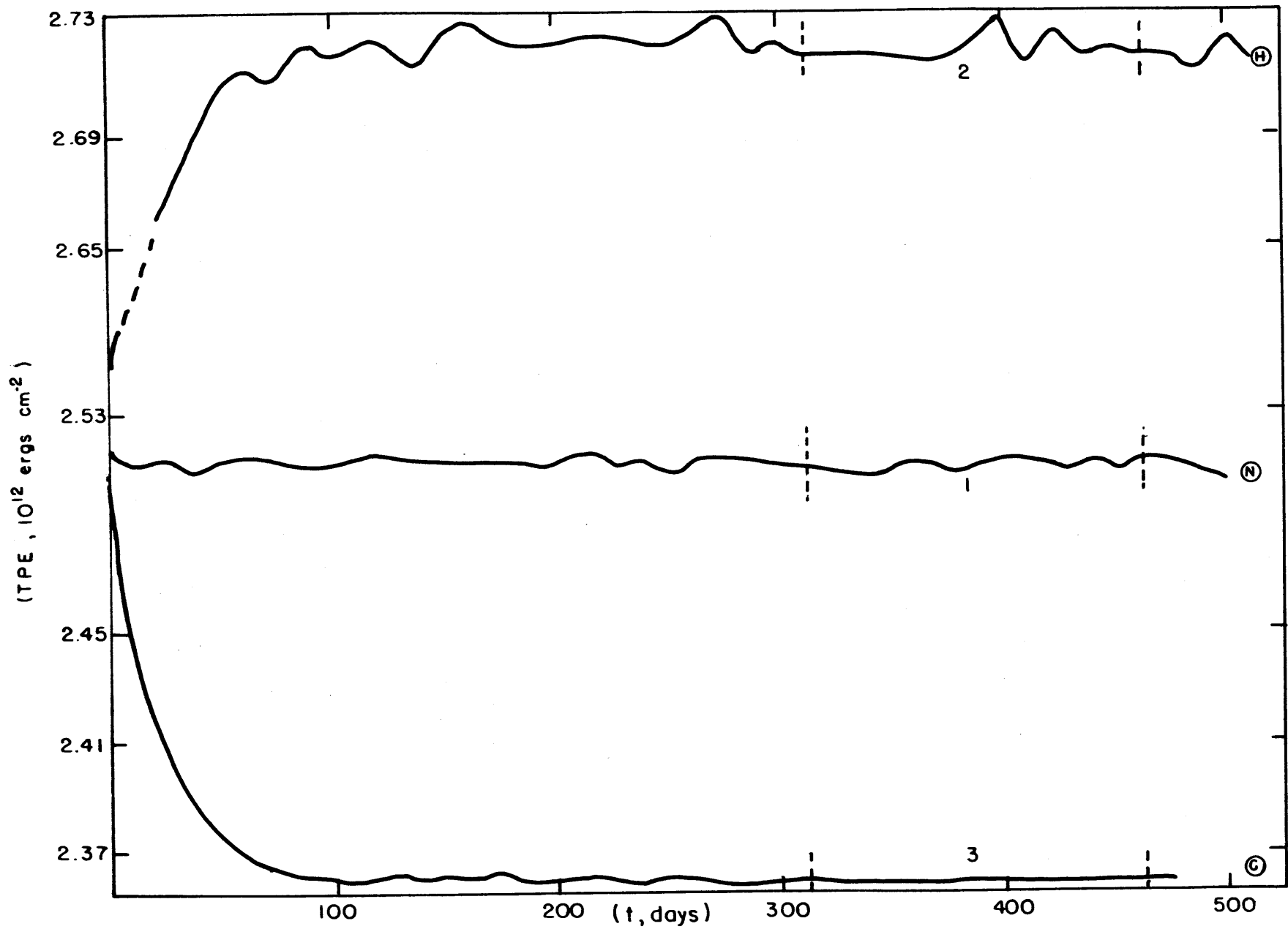


Figure 5.2b. Model TKE as a function of time for the hot, normal, and cold climates.

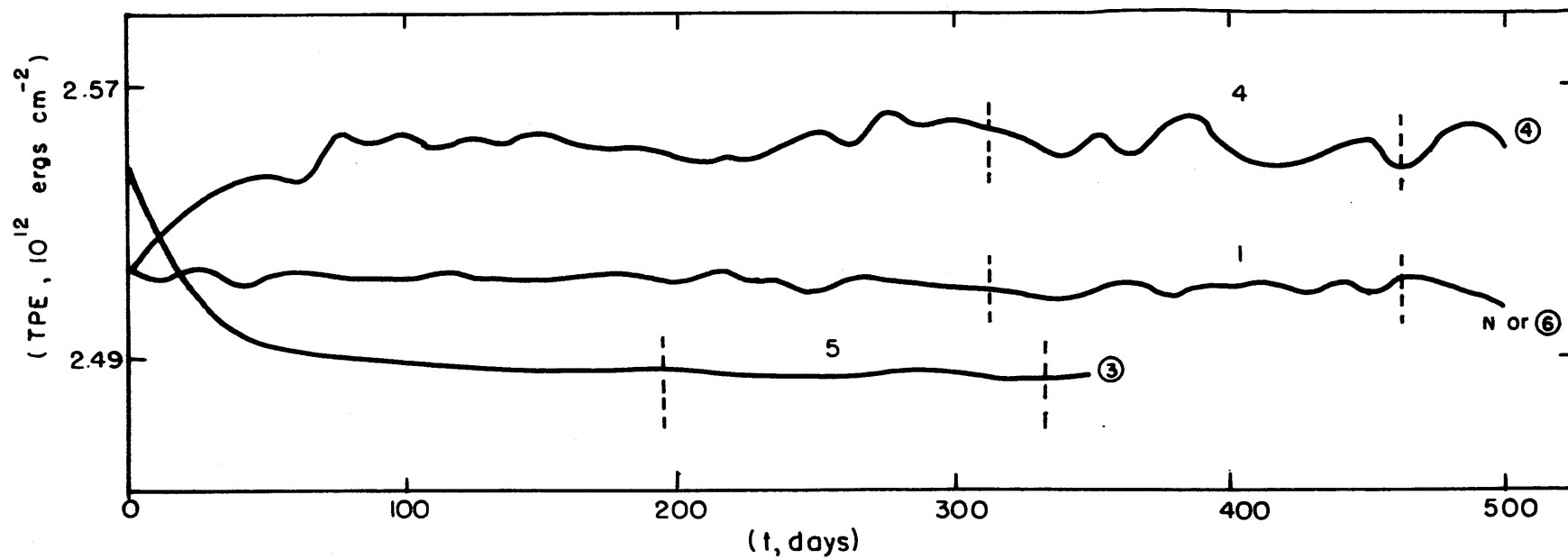


Figure 5.3a. Model TPE as a function of time for the climates with a large, normal, and small AMTG.

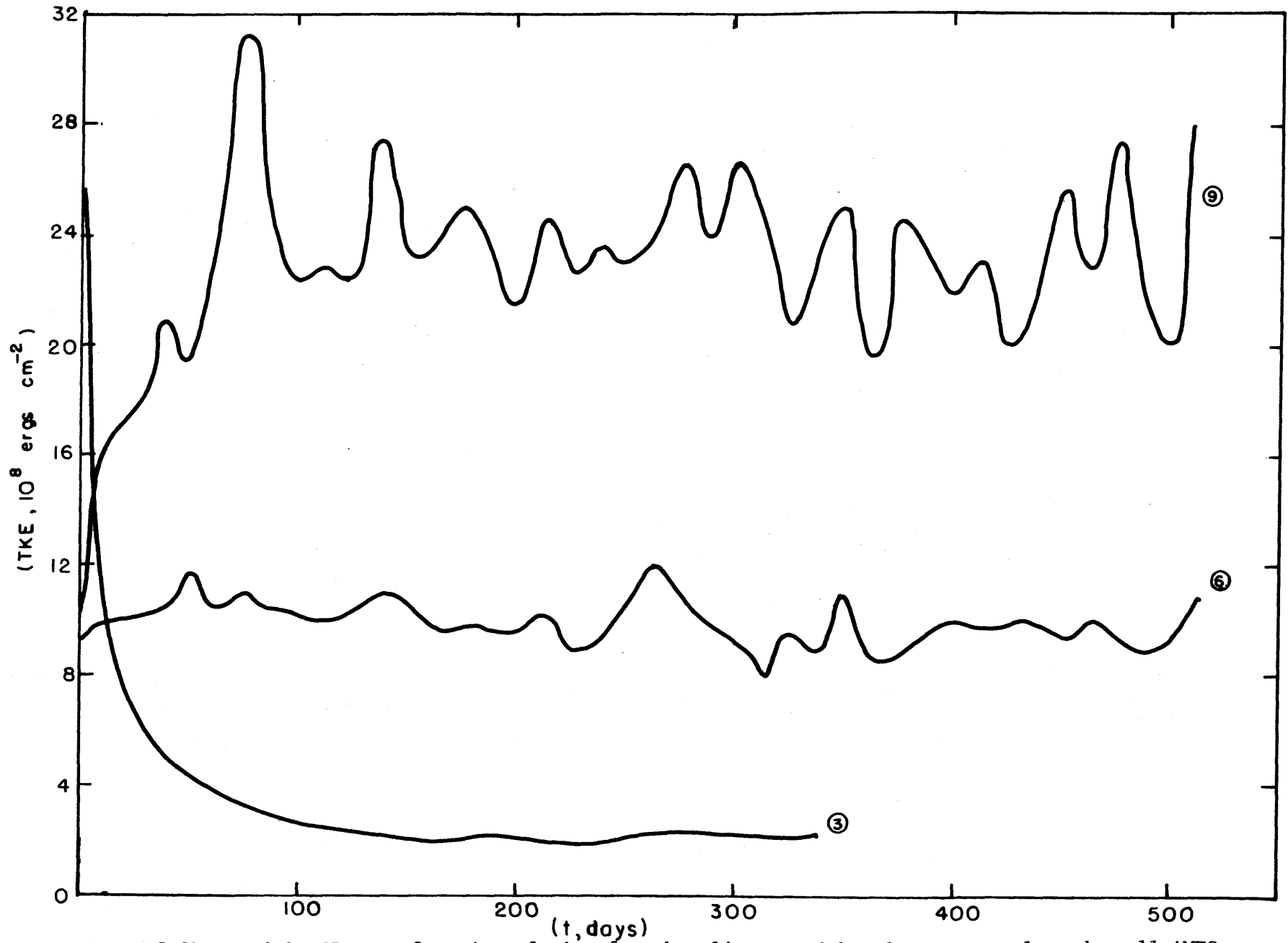


Figure 5.3b. Model TKE as a function of time for the climates with a large, normal, and small AMTG.

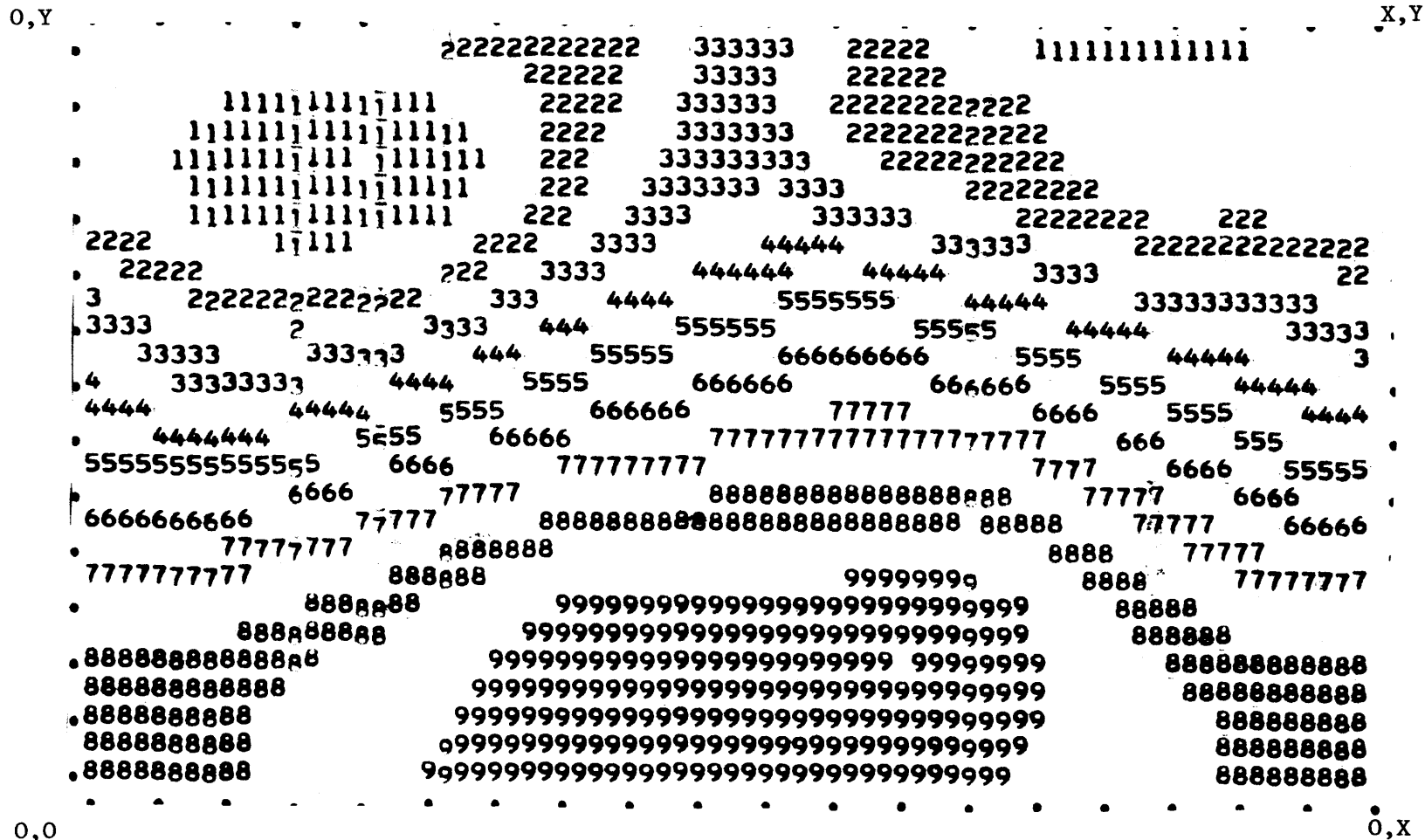


Figure 5.4a. Ψ_1 at day 447.5 for the hot climate (tape I.D. - 0335,1473/272267,272627/);
 1 => $-25. \leq \Psi_1 < -22.5$, 2 => $-20 \leq \Psi_1 < -17.5$, ..., 9 => $17.5 \leq \Psi_1 < 20$ g sec⁻¹. Numbers 1-5
 represent the cyclonic circulation whereas 6-9 represent the anti-cyclonic circulation.

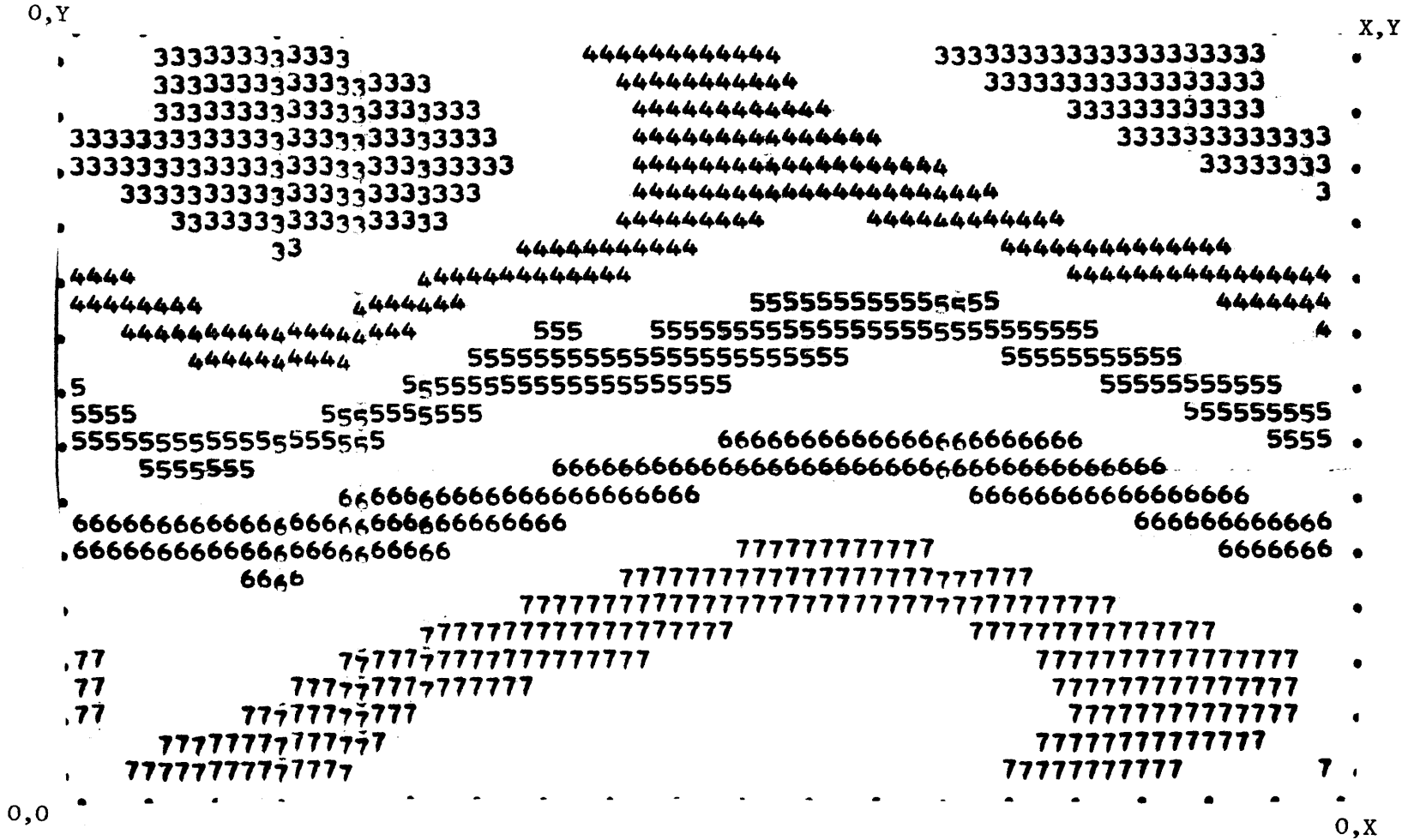


Figure 5.4b. Ψ_2 at day 447.5 for the hot climate.

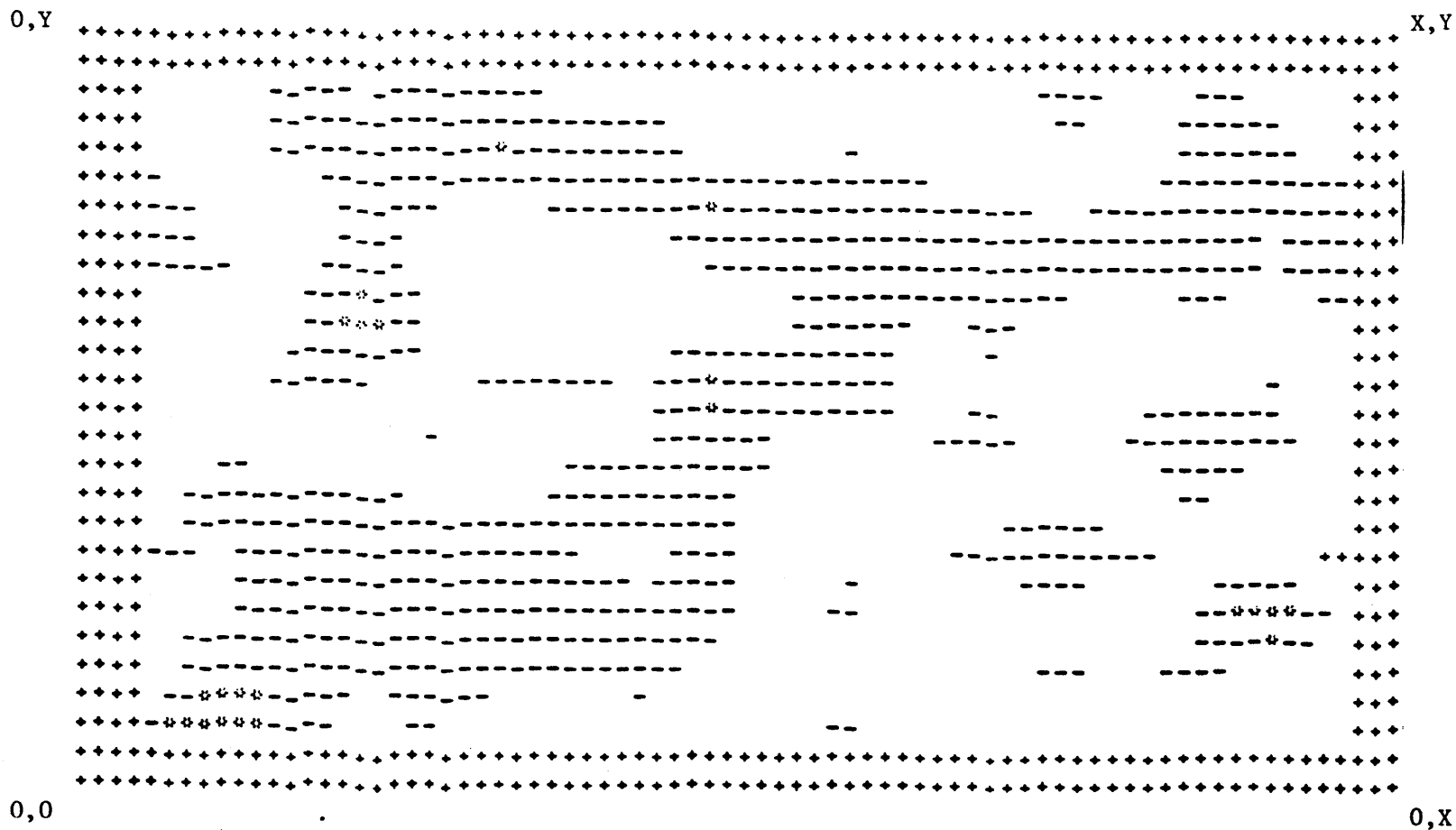


Figure 5.4c. $p_s \sigma$ at day 447.5 for the hot climate (tape I.D.-0335,1473/272267/) minus signs denote upward motion, asterisks denote regions where the upward vertical sigma velocities exceed $-2 \text{gcm}^{-1} \text{sec}^{-3}$, blank regions denote regions of subsidence. Unlike the upward motions, downward motions never exceeded $2 \text{gcm}^{-1} \text{sec}^{-3}$

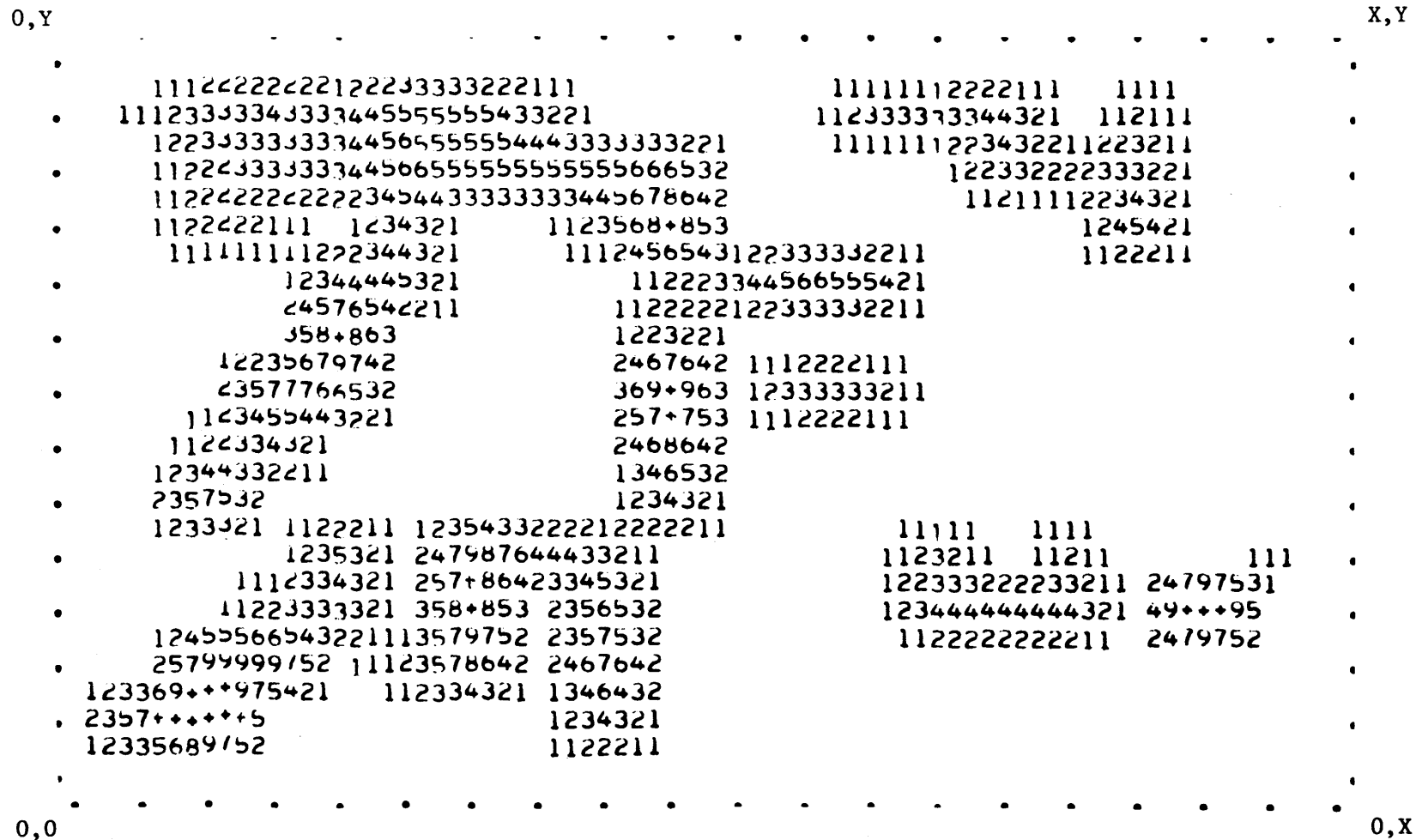
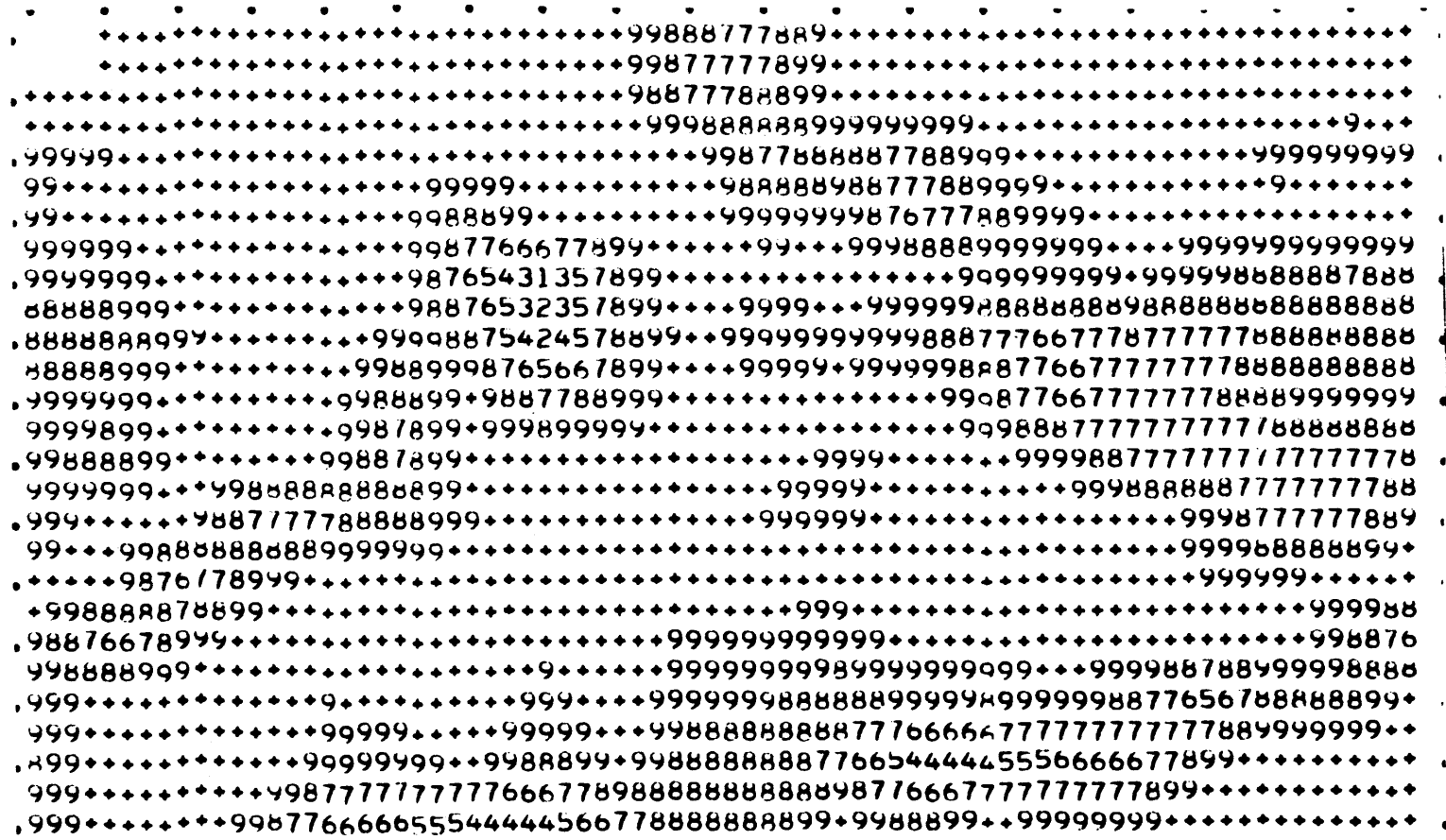


Figure 5.4d. $\{q_c\}$ at day 447.5 for the hot climate, blank \Rightarrow 0. $< \{q_c\} < 5 \times 10^{-2}$, 1 $\Rightarrow 5 \times 10^{-2}$
 $\leq \{q_c\} \leq 1.5 \times 10^{-2}$, ..., 9 $\Rightarrow 8.5 \leq \{q_c\} < 9.5 \times 10^{-2}$, + $\Rightarrow 9.5 \times 10^{-2} \leq \{q_c\} \text{ g cm}^{-2}$

0,Y

X,Y



0,0

0,X

Figure 5.4e. H at day 447.5 for the hot climate, blank => $0 \leq H < .05$, 1 => $.05 \leq H < .15$, ..., 9 => $.85 \leq H < .95$, + => $.95 \leq H$.

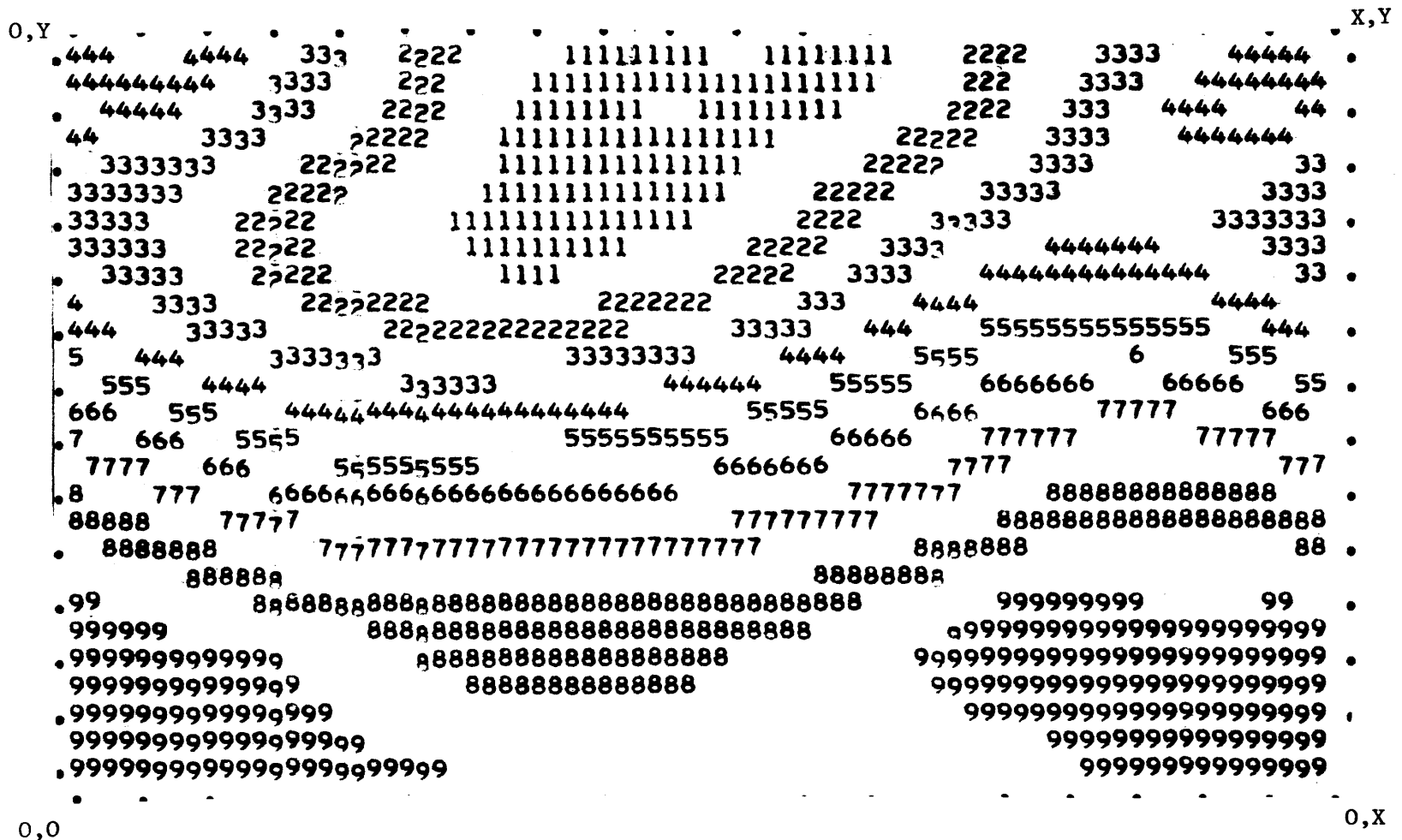


Figure 5.4f. Ψ_1 at day 451.25 for the hot climate.

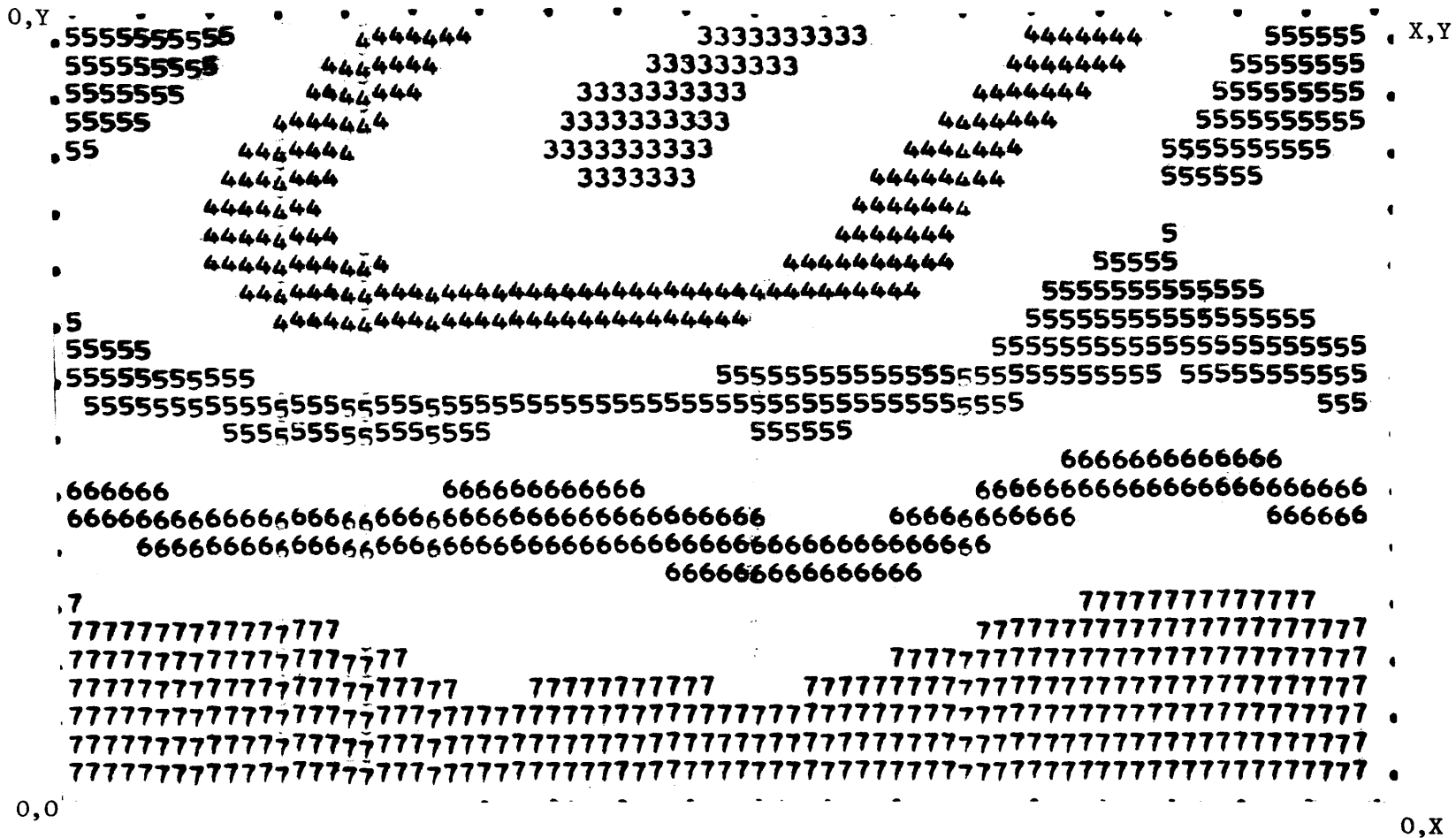
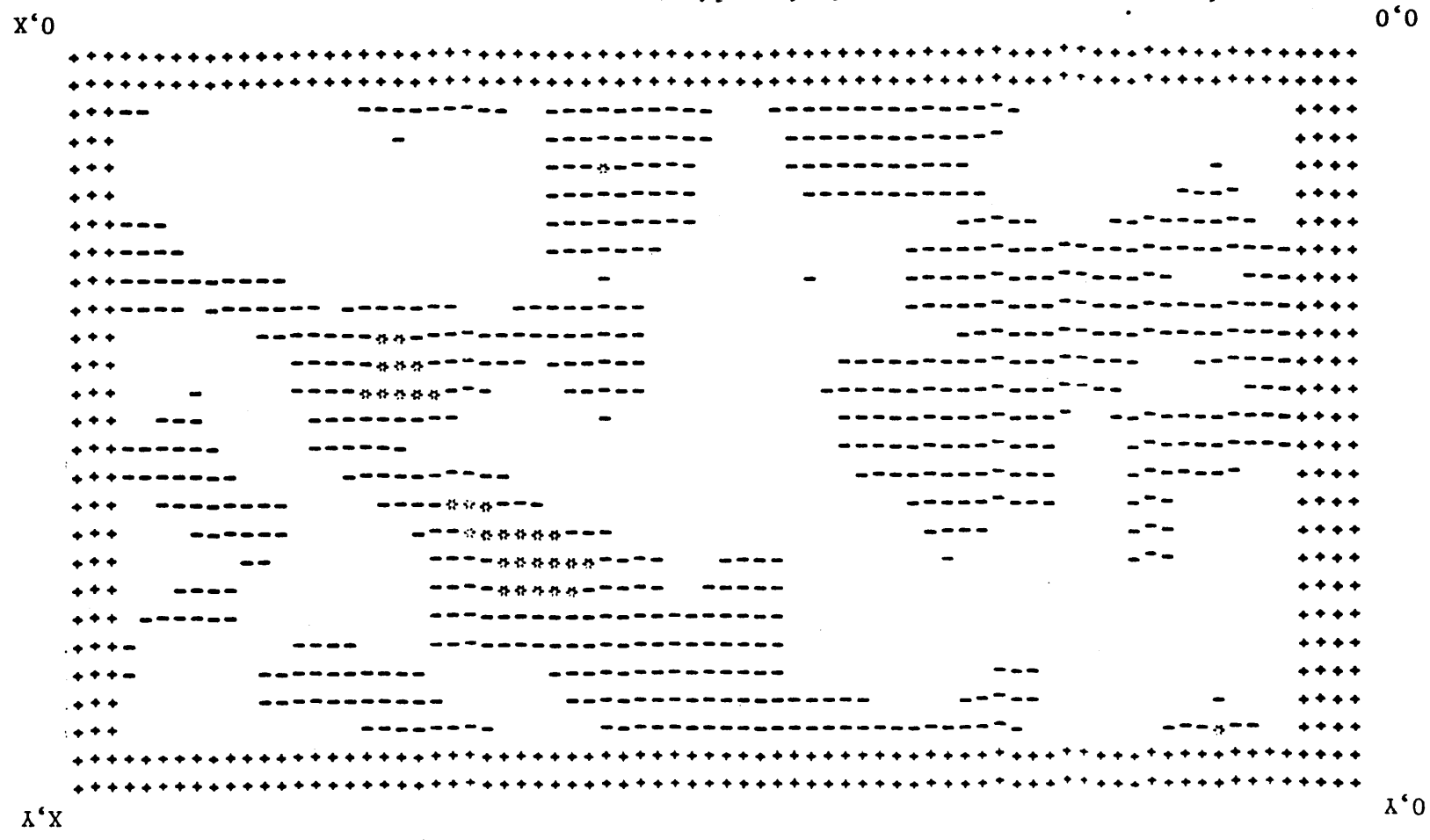


Figure 5.4g. Ψ_2 at day 451.25 for the hot climate.

Figure 5.4h. p_{50} at day 451.25 for the hot climate.



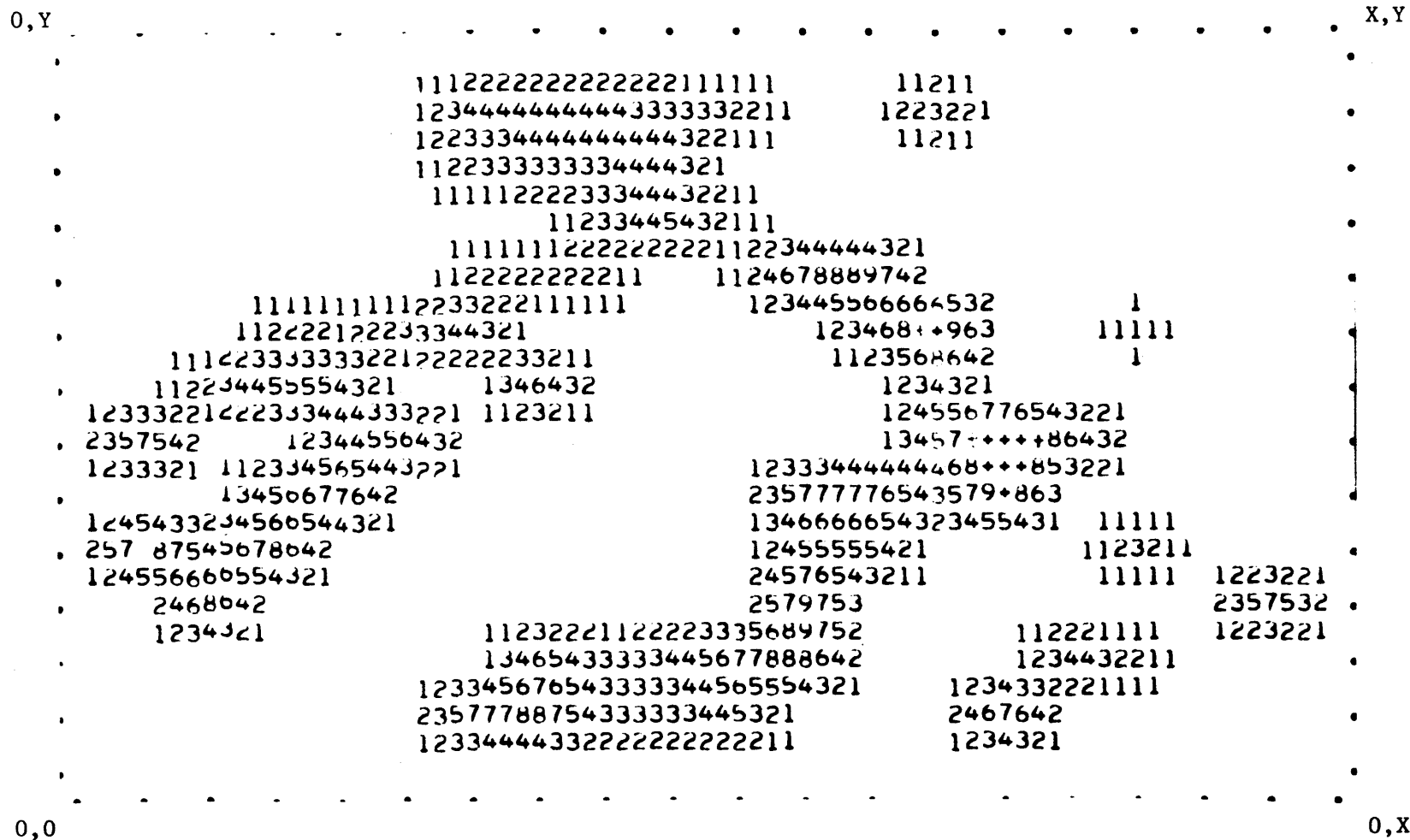


Figure 5.4i. $\{q_c\}$ at day 451.25 for the hot climate.

0,Y

X,Y



0,0

0,X

Figure 5.4j. H at day 451.25 for the hot climate.

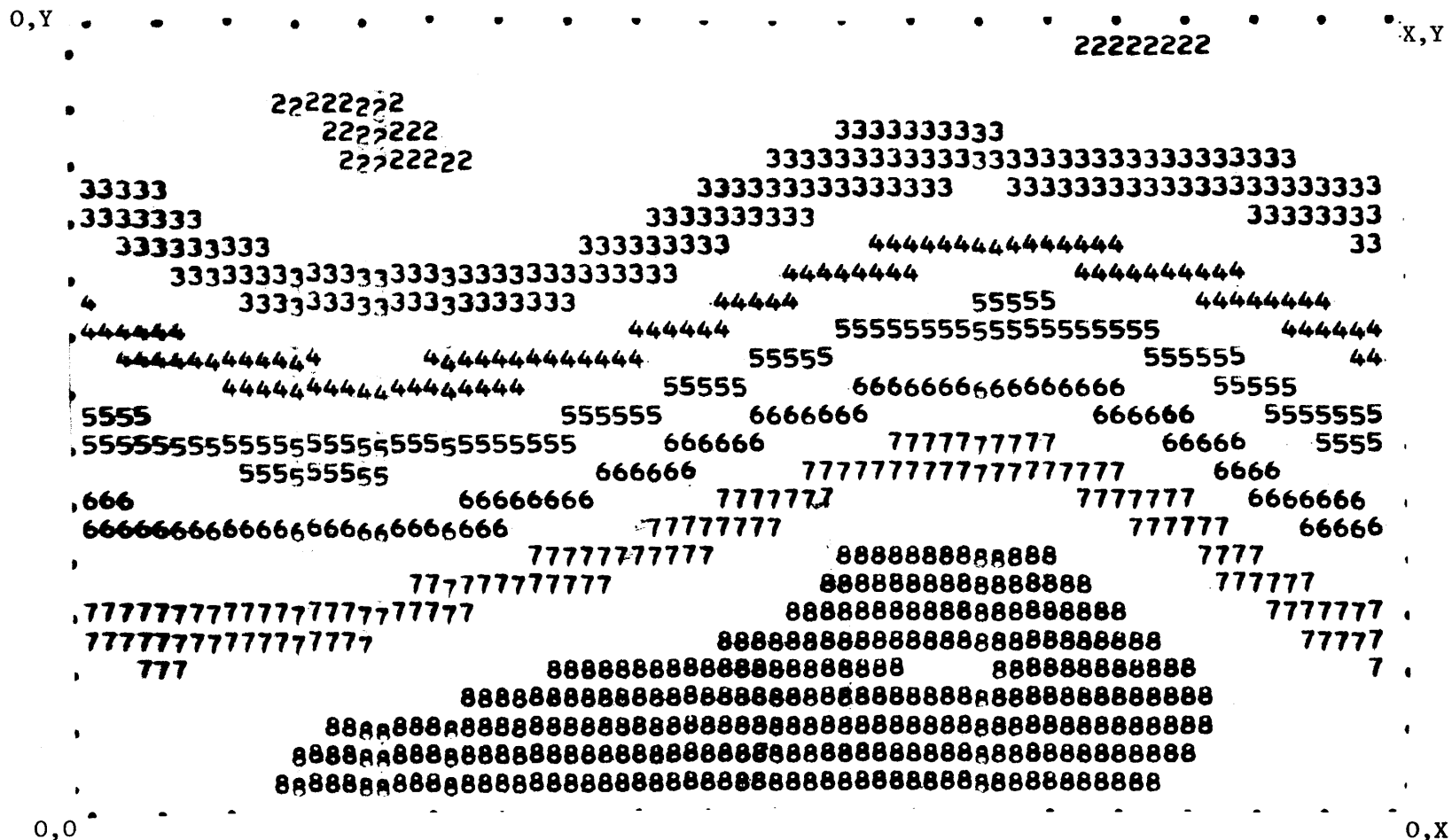
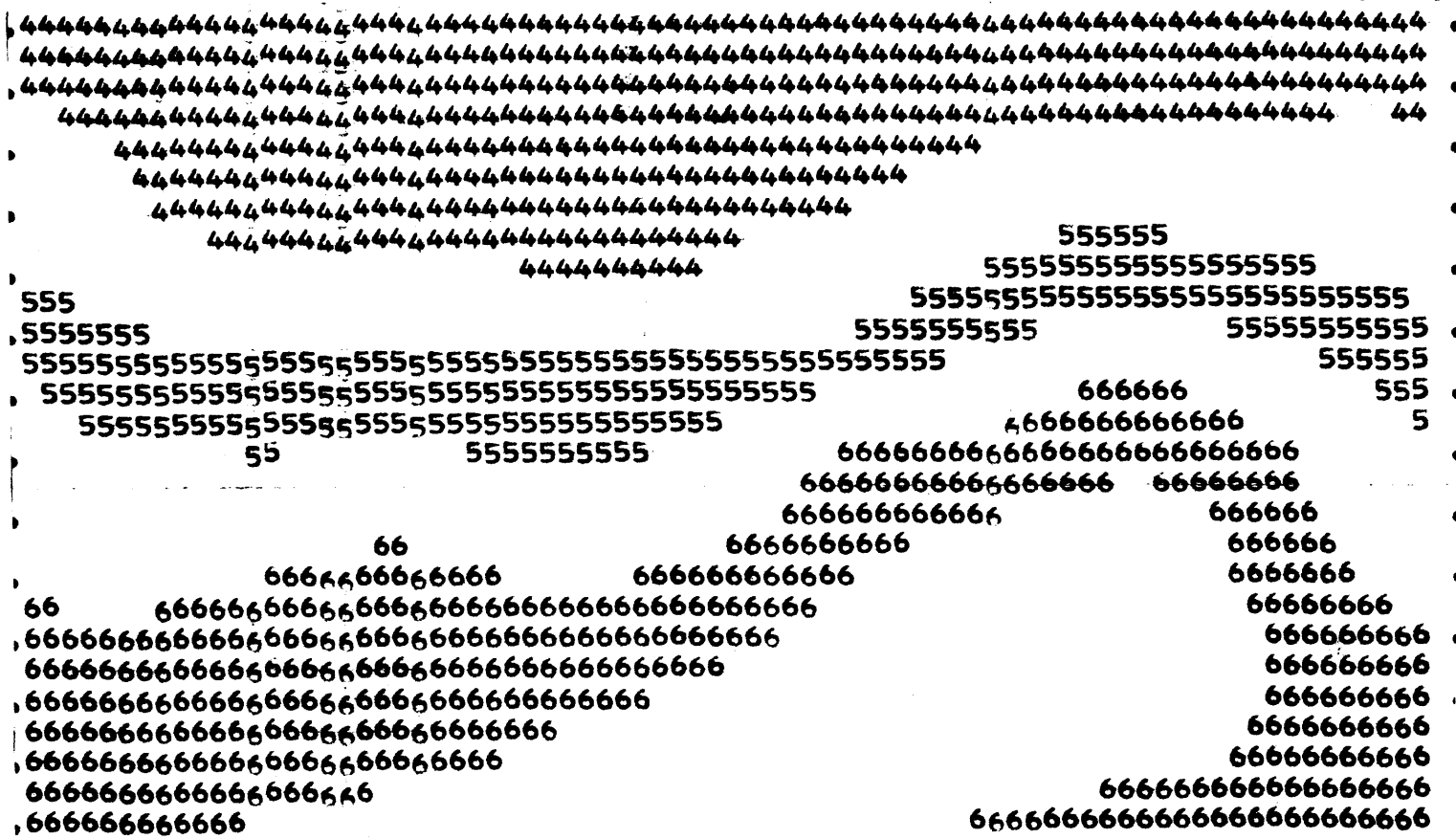


Figure 5.5a. Ψ_1 at day 447.5 for the cold climate (tape I.D. - 0845,6044/272267-272627/)

0,Y

X,Y



0,0

0,X

Figure 5.5b. Ψ_2 at day 447.5 for the cold climate.

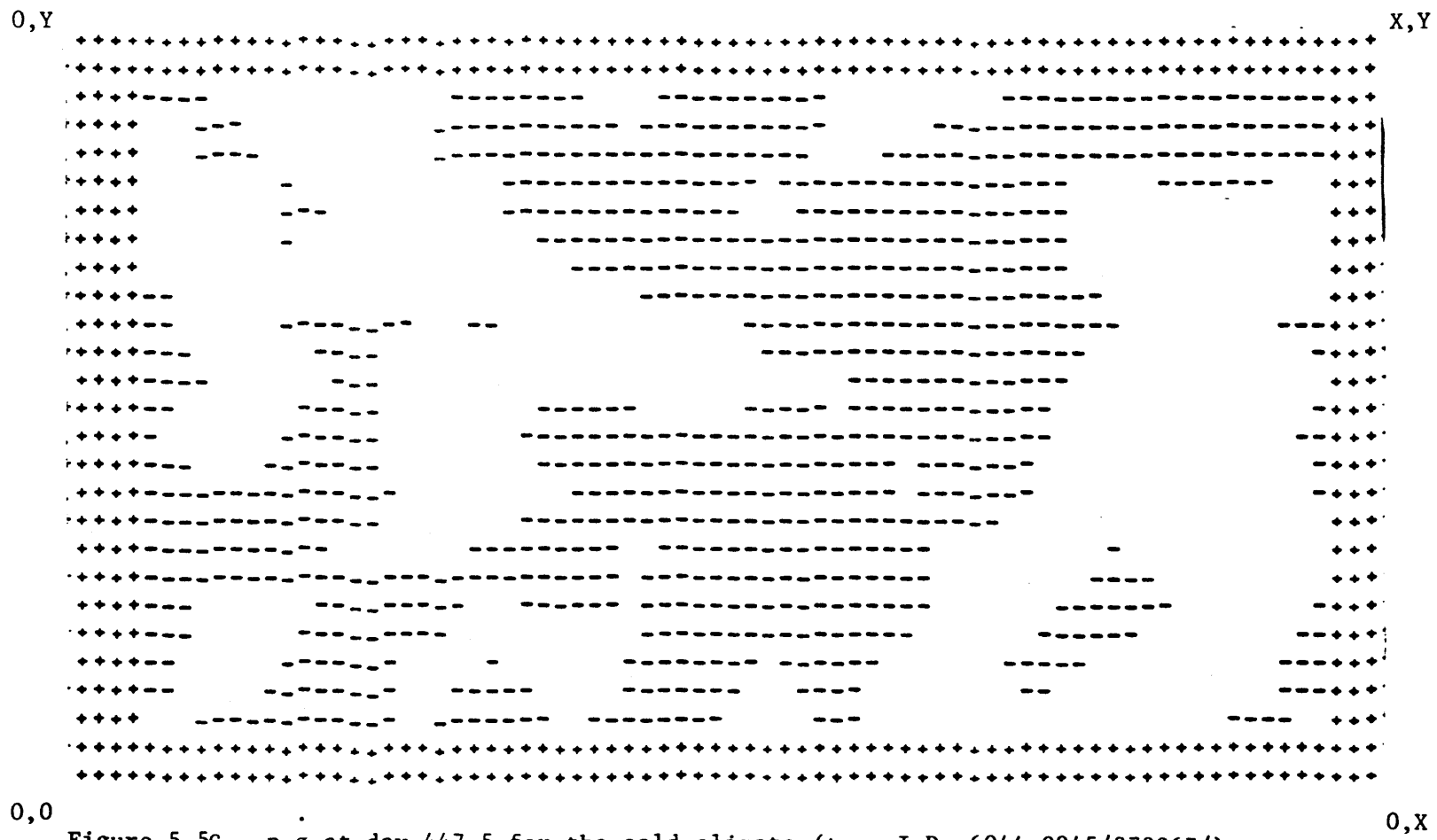


Figure 5.5c. $p_s \sigma$ at day 447.5 for the cold climate. (tape I.D.-6044,0845/272267/)

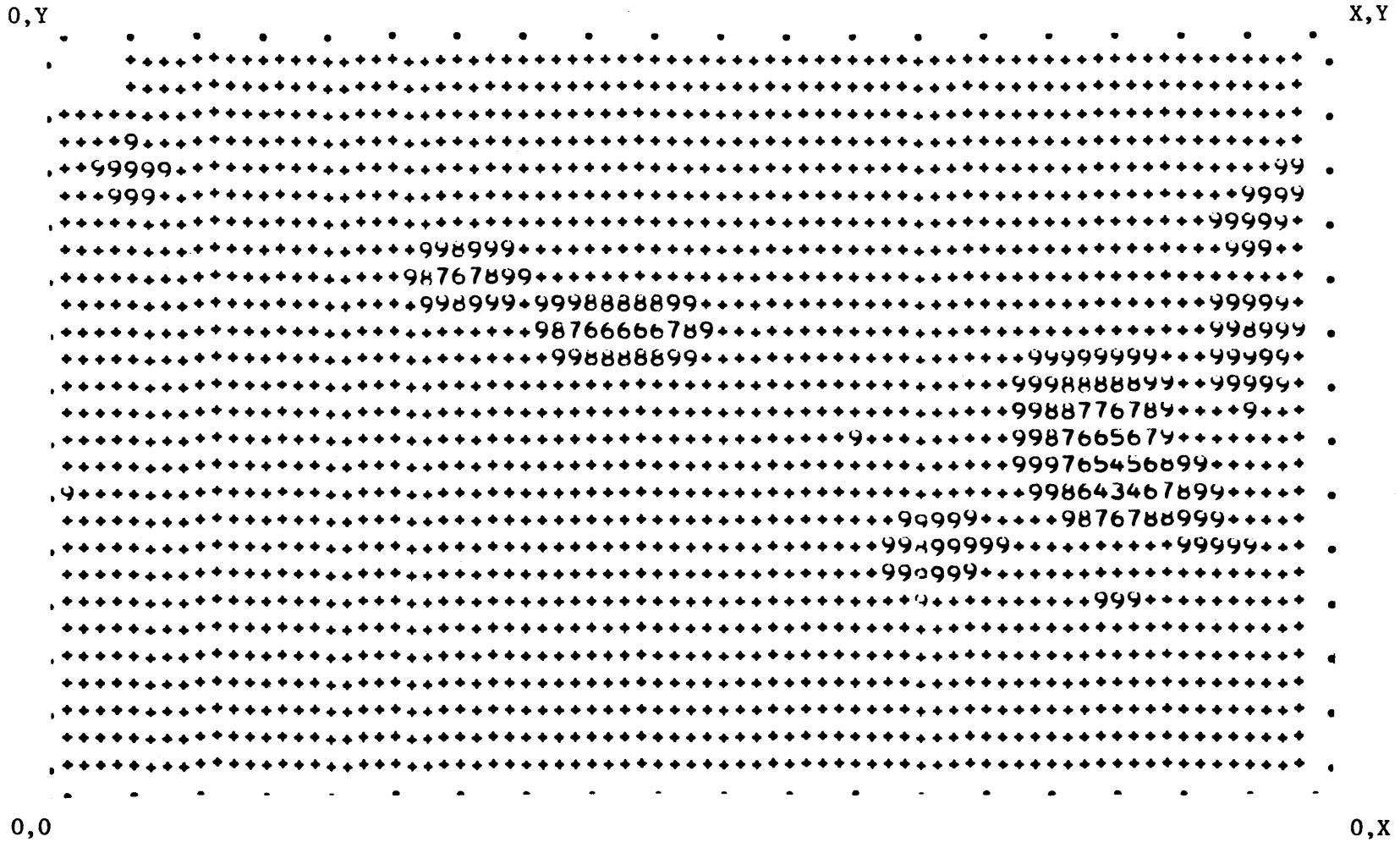


Figure 5.5e. H at day 447.5 for the cold climate.

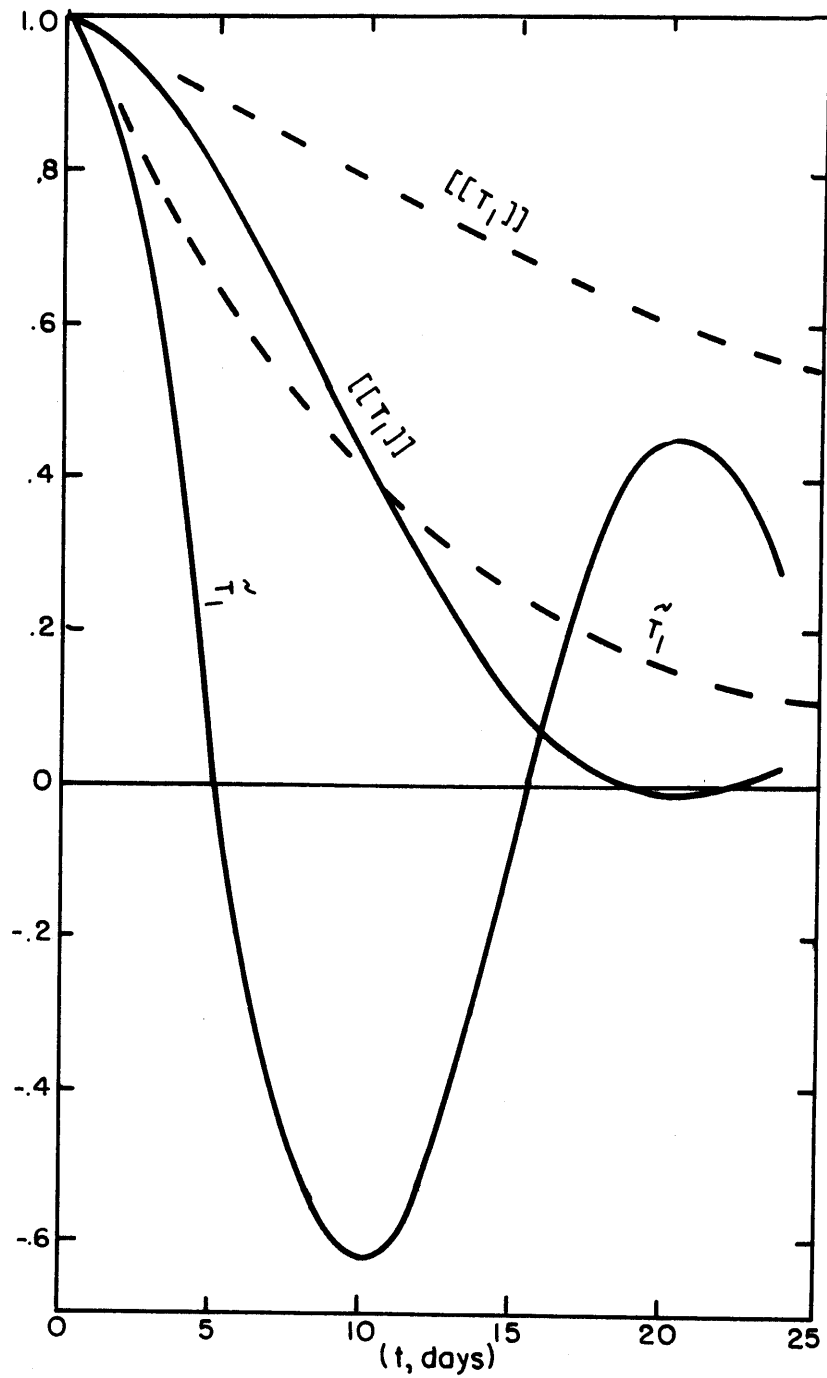


Figure 5.6a. Lag-time correlation for the upper level areally-averaged and meridionally-averaged temperatures for the normal climate. Solid lines are model values and dashed lines are estimated from $R(\tau) = e^{-\nu\tau}$.

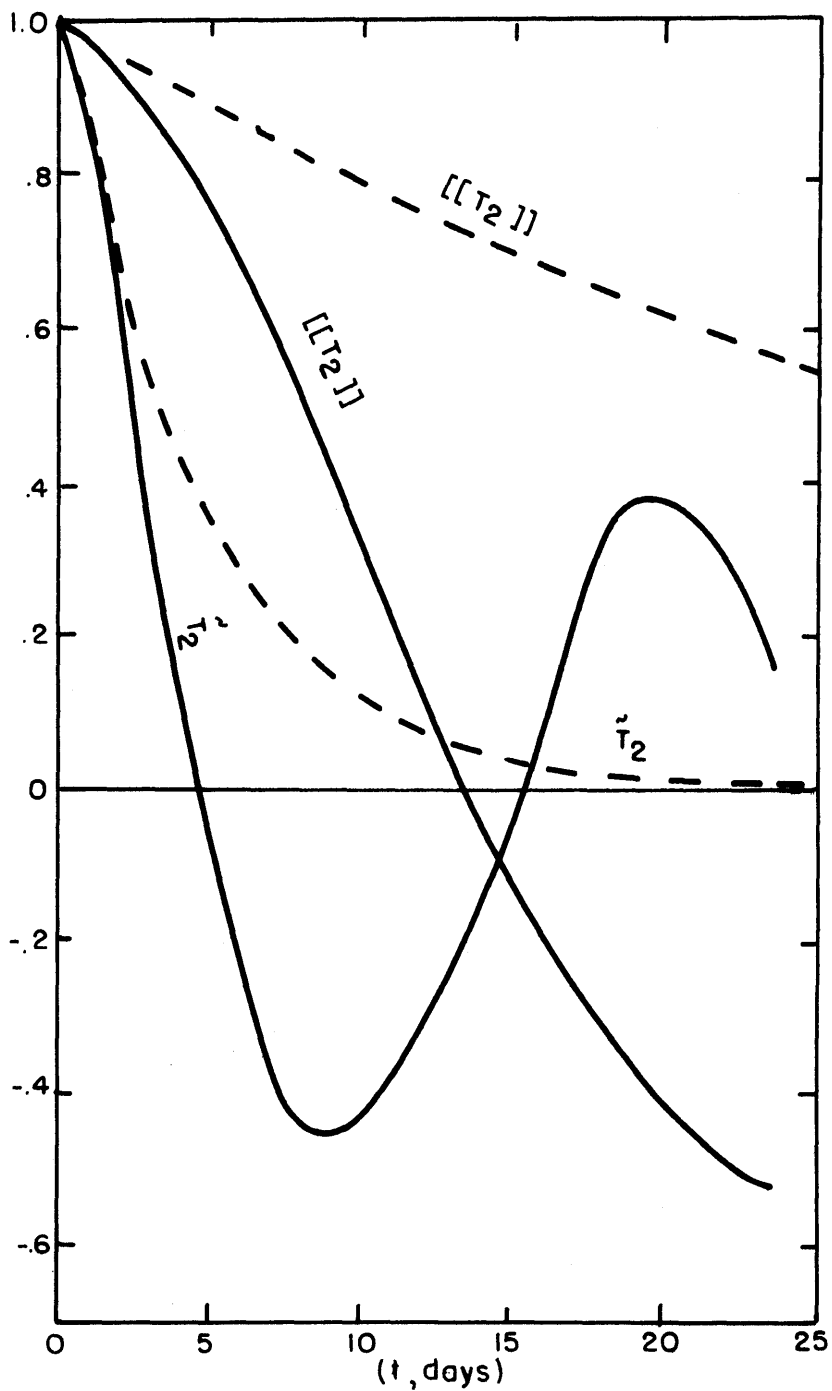


Figure 5.6b. Lag-time correlations for the areally-averaged and meridionally averaged lower-level temperatures for the normal climate. Solid lines are model values and dashed lines are estimated from $R(\tau) = e^{-\nu\tau}$.

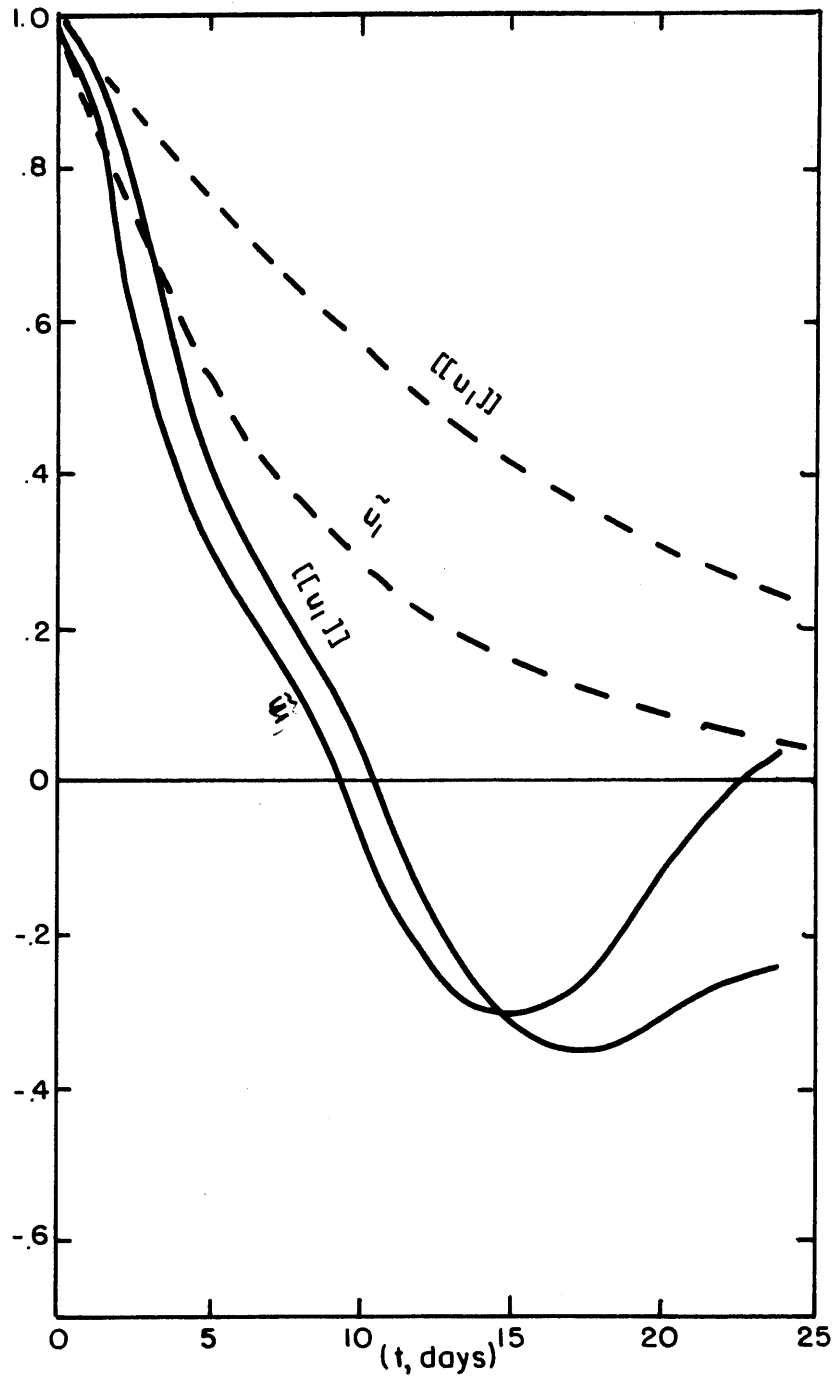


Figure 5.6c. Lag-time correlations for the areally-averaged and meridionally-averaged upper-level zonal momentum for the normal climate. Solid lines are model values and dashed lines are estimated from $R(\tau) = e^{v\tau}$.

6. Sensitivities of the Numerical Model

6.1 Sensitivities of the Zonal Temperatures and Zonal Winds

6.1.1 Evaporation

One important aspect of the thermodynamic properties of the water substance - which is described by the Clausius-Clapeyron equation - is that the difference in the saturation mixing ratio, between the surface and lower model level, increases non-linearly with increasing temperature. Since this is the dominant effect among many factors, evaporation increases non-linearly with increasing T_E (figure 6.1a) and with increasing $AMTG_E$ (figure 6.1b). The increase in surface wind speed with increasing T_E and increasing $AMTG_E$ (figure 6.3) and the decrease in relative humidity with increasing T_E and increasing $AMTG_E$ (figure 6.18) also contribute. And, evaporation is increased even more with increasing $AMTG_E$ (figure 6.1b) because of an increase in the boundary layer temperature difference, ΔT (figure 6.4b) in the hot southern region where the bulk of the evaporation occurs. The northward decrease in ΔT (figure 6.4) and in T_g , for all experiments, combine to give a fairly monotonic northward decrease in evaporation even though $|v_s^v|$ (figure 6.3) is greatest in the central portions of the domain.

Since the surface temperature is fixed, horizontal heat transports in the lower layer can destabilize the boundary layer in the southern regions and stabilize the northern regions. The strongest destabilization and stabilization occurs for the climate with the large $AMTG_E$.

Negative evaporation (dew deposition) occurs in the northern regions of our model in conjunction with the boundary layer inversion since the transport of water vapor (figure 6.8) and cloud evaporation (figure 6.7) are larger than the positive condensation (figure 6.6). Although dew

deposition increases with increasing T_E (figure 6.2a) and with increasing $AMTG_E$ (figure 6.2b) the areally averaged dew deposition is at least an order of magnitude less than the positive evaporation and hence the areally averaged evaporation increases with an increasing T_E and $AMTG_E$.

6.1.2 Average Temperature

Were it not for the eventual release of the latent heat of evaporation into the free atmosphere, the average model temperature would be almost equal to the average pre-specified radiative and sensible heating equilibrium temperatures (since the dissipation is a relatively small term). The average model temperatures are greater than the average equilibrium temperatures by .4 deg ($4 \times 10^5 \text{ deg g cm}^{-1} \text{ sec}^{-2}$) per $10^{-7} \text{ g cm}^{-2} \text{ sec}^{-1}$ ($3.16 \text{ g cm}^{-2} \text{ yr}^{-1}$) of evaporated water vapor since the Newtonian cooling relaxation time constant is $1.6 \times 10^6 \text{ sec}$ ($\sim 18.5 \text{ days}$). Hence the difference between the preset equilibrium temperature increases with increasing T_E (figure 6.4a) and with increasing $AMTG_E$ (figure 6.4b).

The meridional temperature gradient is also determined indirectly by the amount of latent heat of evaporation since latent heat of condensation released in southern regions will maintain the temperature differential between the northern and southern regions which the heat transports decrease.

6.1.3 Condensation

Condensation increases with increasing T_E (figure 6.6a) and with increasing $AMTG_E$ (figure 6.6b) since it must balance evaporation over long time periods. And although the latent heat of condensation is

spread throughout the domain more evenly than the latent heat of evaporation because of latent heat transports, condensation can help to maintain the AMTG - that dry energy transports destroy - by releasing more latent heat in southern regions than in northern regions. For the normal climate and the 3 climate (figure 6.6b) however, condensation is greatest near the central portions of the domain and for these climates the AMTG is decreased in the southern regions and increased in the northern regions. All other climates' condensation is greatest in the southern regions; hence their AMTG is increased in the south, central and northern regions.

Cloud evaporation, which increases with increasing T_E (figure 6.7a) and with increasing $AMTG_E$ (figure 6.7b) is greatest toward the center of the domain for all climates and acts to increase the AMTG in the southern regions and decrease it in the northern regions. Since cloud evaporation is much smaller than the positive condensation, however, the total latent heat of condensation effects are determined mainly by the positive condensation.

6.1.4 Absolute Meridional Temperature Gradient

Latent-heat transports increase with increasing T_E (figure 6.8a) and increasing $AMTG_E$ (figure 6.8b) and act to decrease the effect on the AMTG that latent heat would have if evaporation were balanced locally by condensation. Total transport of energy increases with increasing T_E (figure 6.9a) and increasing $AMTG_E$ (figure 6.9b) and also acts to decrease the $AMTG_E$. As was shown previously by Wetherald and Manabe (1976) and which is also obtained for these model results, the dry energy transports

actually decrease with an increasing T_E - but for our model the total transport increases because of an increasing latent heat transport.

Both the latent-heat transports and dry energy transports increase with an increasing $AMTG_E$. It is the balance between the latent heat of evaporation and total flux divergence that determines the magnitude of the difference between the preset radiative and sensible equilibrium temperature gradients. That is, neglecting the small frictional dissipation term, the gradient of the total energy equation is

$$\left[\left| \frac{\partial}{\partial y} \{ \bar{T} \} - \frac{\partial}{\partial y} \{ T_E \} \right| \right] \cong \frac{\bar{z}_E}{C_p} \left[\left| \frac{\partial^2}{\partial y^2} \nu_{TOT} - L \frac{\partial E}{\partial y} \right| \right], \quad (6.1.1)$$

where

$$\nu_{TOT} = \left[\left\{ \nu \left(C_p T + g z + L q_v + \frac{u^2 + v^2}{2} \right) \right\} \right]. \quad (6.1.2)$$

For the derivation of the total energy balance, see Lorenz (1967) and Newell et al. (1974).

As may be deduced from figure 6.5 or calculated from figures 6.1 and 6.9 the evaporation gradient exceeds the gradient in the total flux divergence for only the hot climate - all other climates' differential flux divergence exceeds the meridional gradient in the evaporation and hence their $AMTG$ is less than the $AMTG_E$.

6.1.5 Zonal Winds

Since departures from geostrophy are small, figure 6.10 shows that the zonal winds are large for the hot climate and increase in magnitude and shear with increasing $AMTG_E$ (figure 6.10b). The cold climate's zonal

winds and shear are larger than the normal climate's in the southern region of the domain. While the difference in zonal winds between the normal and cold climates is not too significant, it is at least consistent with figure 6.6 - which shows that relative to the central and northern part of the domain, more condensation is released in the southern region for the cold climate than for the normal climate.

The surface zonal wind, which is obtained by extrapolation of the upper level wind to the surface, loses momentum by surface friction, and gains momentum by upper level convergence of momentum. That is,

$$\frac{\partial}{\partial y} [\{ \overline{vu} \}] = - [\{ \overline{F_x} \}] \sim - [\frac{\overline{F_{x2}}}{2g}] . \quad (6.1.3)$$

The surface westerlies shown in figures 6.3a and 6.3b for the various climates are balanced by the convergence of westerly momentum (figure 6.11) from the antisymmetric domain. A notable feature of the momentum transport is that momentum is transported into the zonal jet. The transport is greater from the northern regions than from the southern regions of the domain.

The surface zonal winds and the surface wind speed (which includes also the contribution from the eddy motion) increase with increasing T_E (figure 6.3a) and with increasing $AMTG_E$ (figure 6.3b). The temperature sensitivities of the surface winds follow the sensitivities of the free atmosphere zonal winds.

Along with the surface westerlies, we find that a Ferrel circulation - with sinking motion in the southern part of the domain and rising motion in the northern part of the domain - is also present. The intensity of the Ferrel circulation increases with an increasing $AMTG_E$

(figure 6.11d) and is large for the hot climate compared to the normal and small climates (figure 6.11c). Qualitatively, we note that the mean meridional momentum is balanced by the meridional advection of zonal momentum in the upper layer and by surface friction from the lower level. The lower-level meridional advection of zonal momentum, the vertical advection of zonal momentum, and the upper level friction tend to be smaller contributors to the balance.

6.1.6 Summary

Kraus (1973) proposed that because of increased evaporation the free atmosphere AMTG would increase with increasing T_E and hence geostrophically increase the zonal winds and shear even if the surface temperature gradient were slightly decreased. Since it is the condensation rather than the surface evaporation that directly heats the atmosphere, both the evaporation and water-vapor transports must be considered. For example, in the cold climate, condensation was largest near the southern region whereas in the normal climate condensation was largest near the center of the domain. Consistently, the zonal winds were stronger in the southern region for the cold climate than for the normal climate whereas the zonal winds were slightly stronger in the northern region for the normal climate than for the cold climate. (These differences are not very statistically significant.) As the T_E was increased further, however, condensation increased in the southern regions and the zonal winds and wind shear increased substantially for the hot climate.

While the effect of surface temperature may be a monotonic function for a domain that also contains the Hadley regime - as in the real

atmosphere - the transports of moisture must be considered in addition to evaporation. Also, excepting the hot climate, evaporation would be unable to maintain the imposed equilibrium temperature gradient which is maintained in the real atmosphere by solar radiation - the ultimate driving force of the general circulation.

6.2 Sensitivities of the Cloud and Relative-Humidity Fields

6.2.1 Cloud Water

Cloud water produced in the positive-condensation regions increases with increasing T_E (figure 6.12a) and with increasing $AMTG_E$ (figure 6.12b) in order that precipitation balance the increasing condensation which balances the increasing surface evaporation. Because of subsequent precipitation, transport, and evaporation of condensed cloud water, cloud water averaged over the cloudy regions corresponds less with the positive condensation than does cloud water averaged over positive-condensation regions. Cloud water averaged over the cloudy regions has the same climatic sensitivities - increasing with increasing T_E (figure 6.13a) and increasing $AMTG_E$ (figure 6.13b) - but, the climatic states are less distinct. Since the average cloud properties for this model show relatively little variation with latitude and climate, the radiative properties of individual clouds may be relatively unchanged for different climates; this is unknown, however, until an investigation of the radiative properties is made.

6.2.2 Precipitation and Cloud Water Transports

Because of the non-linear precipitation time constant, $\sim 10^4$ sec for 5×10^{-2} g cm $^{-2}$ of cloud water, the large cloud water amounts condensed in positive condensation regions are mainly precipitated locally. Consistent with the evaporation and condensation, precipitation increases with increasing T_E (figure 14a) and with increasing $AMTG_E$ (figure 6.14b). Zonal differences between the precipitation and positive condensation are minor and due to cloud evaporation and cloud transports.

Because of the increase of cloud water in cloudy regions, the transport of cloud water is northward and increases with an increasing T_E (figure 6.15a) and with an increasing $AMTG_E$ (figure 6.15b). Hence precipitation tends to be slightly greater in the northern regions than total condensation. It is interesting to note that the northern regions receive net water from both precipitation and dew deposition.

6.2.3 Fractional Coverages and Relative Humidity

In addition to the magnitude of the cloud-water content, the fractional part of space and time which is occupied by clouds has a strong influence on the radiation field. And, contrary to the increase in cloud water content which must occur in order that precipitation balance condensation which balances surface evaporation which increases with an increasing T_E and $AMTG_E$, the fractional coverage of the region of positive condensation decreases everywhere with an increasing T_E (figure 6.16a) and with an increasing $AMTG_E$ (figure 6.16b). We note that the zonal fractional coverage is not uniquely related to either the evaporation or the precipitation.

Corresponding to the fractional coverage of positive condensation, total cloud fractional coverage decreases with an increasing T_E (figure 6.17a) and with an increasing $AMTG_E$ (figure 6.17b). The magnitude of the total cloud fractional coverage is larger because of horizontal transports of cloud water and local time oscillations in the condensation field result in part of the cloud being in a region where atmospheric conditions are more appropriate to cloud evaporation. Total cloud fractional coverage also has much less variation with respect to latitude; however, the variations follow, qualitatively, the variations in the positive condensation.

The sensitivity of the relative humidity follows closely the sensitivities of the fractional coverage. H decreases with an increasing T_E (figure 6.18a) and with an increasing $AMTG_E$ (figure 6.18b). Moreover, the variation with respect to latitude is qualitatively the same although figure 6.7b indicates that the variation of the relative humidity with respect to fractional cloud cover is not a linear relationship and might in fact be weakly influenced by various other model parameters.

Summarizing: fractional cloud cover and relative humidity decrease with increasing T_E and $AMTG_E$ even though evaporation and the concomitant precipitation increase. The reasons for this antithesis can be attributed to several causes and are discussed in the remainder of this section.

6.2.4 Vertical Velocities

The model eddy vertical velocity increases with an increasing T_E (figure 6.19a) and with an increasing $AMTG_E$ (figure 6.19b) and is largest

toward the center of the domain. An increase in the vertical velocity amplitude (of a linear wave) makes the fractional cloud cover and zonally averaged relative humidity tend toward 50%. This is because an increase in the eddy vertical velocity corresponds to an increase in the atmosphere's transport of water vapor away from subsident or divergent regions into ascension or convergent regions. Also, an increase in the vertical velocity increases the rate of adiabatic warming and hence drying in regions of subsidence and cooling and hence moistening in regions of ascension. The atmosphere is becoming a more efficient condensor and dryer with an increase in the eddy vertical velocity.

6.2.5 Static Stabilities

The amount of adiabatic warming and cooling is directly proportional to the static stability - which increases with an increasing T_E (figure 6.20a) and with an increasing $AMTG_E$ (figure 6.20b). It is well known that the horizontal advections of sensible heat stabilize and destabilize portions of the atmosphere and that vertical advections stabilize the atmosphere on the average. For example, figure 6.21 shows the resultant model temperatures at the upper and lower levels compared to the radiative and sensible equilibrium temperatures. While the lower-level temperatures are warmer than the equilibrium temperatures in the northern regions, they are colder in the southern regions since the heat transports are attempting to remove the temperature gradient. The lower-level temperatures tend to be warmer on the average than the equilibrium temperature because of the latent heat of condensation. The upper-level

average temperature is even warmer than the equilibrium average temperatures because of vertical heat transports and because of moist convection - which increases with an increasing T_E (figure 6.22a) and with an increasing $AMTG_E$ (figure 6.22b). This is because, with an increasing moisture content, moist convection attempts to obtain conditional stability by increasing the static stability. Positive condensation is dominated by the convective condensation for the hot climate and by supersaturation condensation for the other climates. It is interesting to note that the convective condensation is largest where the positive condensation is largest rather than occurring predominantly in the southern regions.

6.2.6 Calculated Fractional Cloud Cover

In addition to the vertical velocity and static stabilities and concomitant transport and adiabatic warming and cooling - which increase with an increasing T_E and $AMTG_E$ - the cloud coverage is influenced by the mean field turbulent transports. As shown in Chapter 4, an increase in evaporation due to the nonlinear relationship between the saturation vapor pressure and temperature actually results in clouds tending toward regions of ascending motion. This is because the ratio of the saturation atmospheric water vapor mixing ratio to the surface water vapor mixing ratio increases with an increasing temperature if the free atmosphere is colder than the surface layer. The evaporation increases even more, however, due to an increase in the surface wind speed. And although the average boundary-layer temperature difference decreases due to increased latent heat at the lower levels, the boundary-layer temperature difference

is increased in the southern regions - where the bulk of the evaporation is occurring - with an increasing $AMTG_E$. The average radiative and sensible cooling resulting from the necessity to balance the increased condensation also helps to increase the fractional cloud cover. And, the mean vertical motion increases the cloud cover in regions of ascension and decreases the cloud cover in regions of subsidence.

Recalling figure 4.3, it is the sensitivity of the ratio of the mean terms to the eddy vertical velocity that determines the fractional coverage.

From 4.2.8

$$\begin{aligned}
 C &= 1 - \frac{\cos^{-1} \frac{B}{W}}{\pi} & : -1 \leq \frac{B}{W} \leq 1 & \quad (6.2.1) \\
 &= 0 & : \frac{B}{W} < -1 \\
 &= 1 & : \frac{B}{W} > 1 .
 \end{aligned}$$

We calculate C by letting

$$W = \sqrt{2} [(\overline{p_s \dot{\sigma}})^*{}^2]^{1/2} \quad (6.2.2a)$$

$$\begin{aligned}
 B &= \frac{2g}{RT_s} [\overline{C_{p0}}] [|\overline{v_s}|] \left(\frac{q_{vA}^*}{q_{v,2}^*} - 1 \right) - & (6.2.2b) \\
 & \quad \frac{(\frac{1}{\Delta p} + \int \frac{\partial \ln q_{v,2}^*}{\partial T})}{\overline{[Q_2]} \frac{\partial \ln q_{v,2}^*}{\partial T}} \\
 & - \frac{c_p (\frac{1}{\Delta p} + \int \frac{\partial \ln q_{v,2}^*}{\partial T})}{\overline{[p_s \dot{\sigma}]}} ,
 \end{aligned}$$

where the saturation moisture terms are calculated from the time and zonal-mean temperatures and pressures.

C decreases with an increasing T_E (figure 6.23a) and an increasing $AMTG_E$ (figure 6.23b) since relative to the increased surface wind speed and radiative and sensible cooling, the vertical velocity and static stability increase even more. C is consistent qualitatively with the model's fractional cloud covers (figures 6.16 and 6.17) but shows more variation for the normal and cold climate and less variation for the hot and small and large $AMTG_E$ climates. This could be due to the neglect of horizontal advectons.

6.2.7 Calculated Relative Humidity

As previously shown in section 4.2, the relative humidity is related to the fraction cloud cover and the parameter η through the relationship

$$H = 1 \quad ; \quad \pi(1-C) \leq \theta \leq -\pi(1-C) \quad (6.2.3a)$$

and

$$H = \frac{\eta}{\eta + \cos \pi C + \cos \theta} \quad ; \quad -\pi(1-C) < \theta < \pi(1-C), \quad (6.2.3b)$$

where

$$\eta = \frac{2g f_s [\overline{C_{DD}}] [\overline{|V_s|}] q_{v,1g}^*}{p_s W \left(\frac{q_{v,12}^*}{\Delta p} + \int \frac{\partial q_{v,12}^*}{\partial T} \right)} \quad (6.2.3c)$$

We found that for the same fractional cloud cover, [H] increased with increasing η ; for the same [H], C decreased with decreasing η . Figure

6.24 shows that η decreases with respect to latitude - mainly because the boundary layer temperature difference decreases with respect to latitude (figure 6.4) - and with increasing T_E (figure 6.24a) and increasing $AMTG_E$ (figure 6.24b). The reasons for these latter changes have been discussed previously in the previous subsection.

The relative humidity was shown in section 4.2 to be related to the fractional cloud cover by the relationship

$$[H^{-1}]^{-1} = \left(1 + \frac{1}{\eta} \left(\frac{\sin \pi C}{\pi} + (1-C) \cos \pi C \right) \right)^{-1}. \quad (6.2.3d)$$

Using the calculated C , the calculated relative humidities did not correspond very well with the observed relative humidity although their qualitative sensitivities followed the sensitivities of the model relative humidities. Therefore we used the observed total fractional cloud cover. The derived inverse average relative humidity inverse is shown to correspond qualitatively with the model's relative humidity - decreasing with an increasing T_E (figure 6.25a) and an increasing $AMTG_E$ (figure 6.25b). The variations are much greater, however, for the hot and large $AMTG_E$ climates than for the cold and small $AMTG_E$ climates - probably due to the neglect of advections. However, the normal climate's calculated H tends to correspond fairly well with the model's H .

6.2.8 Calculated Precipitation

As shown in section 4.2, the precipitation is related to the fractional cloud cover by the relationship

$$P_c = \frac{P_0}{2g} \left(\frac{\Delta \sin \pi C}{\pi} - C \cos \pi C \right) \times \quad (6.2.4)$$

$$\times W \left(\frac{1}{\Delta p} + S \frac{\partial \ln q_{v,2}^*}{\partial T} \right) / \left(\frac{1}{q_{v,2}^*} + \frac{L}{C_p} \frac{\partial \ln q_{v,2}^*}{\partial T} \right) .$$

Using the model relationships for the right hand side, a good correspondence was obtained for all climates excepting the hot climate, which had too little precipitation in the hot southern region (although still more than the normal or cold climates). A better relationship was found by using the derived fractional cloud covers shown in figure 6.23. With this relationship, figure 6.26 shows that good correspondence between the theoretically calculated precipitation and the observed precipitation (figure 6.14) was obtained. This may indicate that the horizontal advections are less important for obtaining the correct precipitation.

6.2.9 Entrainment Parameter

As the preceding formulas have indicated, the qualitative sensitivities of the model correspond qualitatively with the sensitivities of the simpler models developed in Chapter 4. There are important quantitative differences which may be due in part to the neglect of horizontal advections. In an effort to qualitatively include their effect, we studied in section 4.3 the inclusion of large scale entrainment - which was denoted this because it acted to entrain dry air into a potentially saturated region and hence reduced the potential cloudiness. It also entrained moist air from part of the wave to the dryer part and consequently reduced the variation in the relative humidity field that would be present if the zonal wind were equal to the phase velocity of the vertical motion. The effects of the entrainment are measured by the factor ϵ , where

$$\epsilon = \frac{\hat{k} (u - \hat{s})}{W \left(\frac{1}{\sigma p} + \int \frac{\partial \ln q_{v,2}^*}{\partial T} \right)} \quad (6.2.5)$$

We estimate ϵ by letting

$$u - \hat{s} = \left| \frac{[u_2] - [u_1]}{2} \right|, \quad (6.2.6)$$

$$\hat{k} = \frac{1}{T} \int_0^T \frac{2\pi}{X} \frac{\sum_{l=1}^{IM/2} l [W(l)]^2 dx}{\sum_{l=0}^{IM/2} [W(l)]^2} \quad (6.2.7a)$$

where

$$[W(l)] = \frac{2}{X} \int_0^X (p_s \dot{\sigma}) \left(\cos l \frac{2\pi x}{X} + i \sin l \frac{2\pi x}{X} \right) dx, \quad (6.2.7b)$$

$$[W(0)] = \frac{1}{X} \int_0^X (p_s \dot{\sigma}) dx, \quad (6.2.7c)$$

and

$$[W(IM/2)] = \frac{1}{X} \int_0^X (p_s \dot{\sigma}) \cos IM \frac{\pi x}{X} dx. \quad (6.2.7d)$$

Essentially the entrainment constant is a ratio of the time it takes a region to reach saturation by vertical motion to the time it takes the zonal advectants to bring dry air into it. As was shown in Chapter 4, the greatest fractional coverages and smallest relative humidities are associated with the smallest entrainment rates. As shown in figure 6.27 the entrainment constant, ϵ , is fairly large - varying between 6 and 20. ϵ also tends to be largest toward the center of the domain. This is only a qualitative assessment, however, since the model does not have a finite-

amplitude two-dimensional wave at each latitude belt giving rise to clouds and relative humidities. In fact, if $u\hat{s}$ is postulated to have instead the form $[u_2] - \left[\frac{u_1 + u_2}{2}\right]$ to take into account the fact that the vertical velocities are part of one large scale system, then ϵ would be smallest in the center of the domain. Nevertheless, the average value for the entrainment parameter does indicate that because of the large entrainment rate, the large relative humidities of the model are consistent with the model's fractional cloud cover. The entrainment constant decreases with increasing T_E (figure 6.27a) and with increasing $AMTG_E$ (figure 6.27d) but not as fast as the parameter η is decreasing (compare figures 6.24 and 6.27); hence the relative entrainment increase helps to decrease the fractional cover still further. The decreasing entrainment rate indicates, however, that the cloud field in our model is becoming more closely associated with regions of ascending motion regardless of the horizontal flow fields.

6.2.10 Cloud Formulae

As the preceding sections have shown, the theoretical cloud covers and relative humidities tend to have a different variation with respect to latitude than is present in the numerical model. This is thought to be due to the neglect of the horizontal advectons. Facets of the simpler theory may be applicable, however, to the numerical model. For example, in section 4.2, explicit reference to the vertical velocity in the cloud formula was eliminated and the approximate formula

$$C_E \sim 1 - \left(\frac{3 [C_{DDO}] [|\chi_s|] q_{v,1}^* (1 - [H']^4)}{\pi^2 [\bar{p}_c] [H']^4 \left(1 + \frac{L}{c_p} \frac{\partial q_{v,2}^*}{\partial T}\right)} \right) \quad (6.2.8)$$

for C_E was obtained. Only the dependence on the boundary-layer turbulent transport, precipitation and relative humidity is present. C_E decreases with increasing T_E (figure 6.28b) and increasing $AMTG_E$ (figure 6.28b). The variations are not as strong as in figure 6.23 and in fact are not even as strong as those in figure 6.17.

Sellers (1976) proposed the following cloud formula

$$C_s = \left(0.75 + .25 \left(\frac{p_c - E}{p_c + E} \right) \right) H. \quad (6.2.9)$$

While we did not find very good agreement by the use of this formulation, we did find an appropriate modification by using E_N ,

$$E_N = p_s C_D |\chi_s| q_{v,1}^* (1 - H), \quad (6.2.10a)$$

in place of E ,

$$E = p_s C_D |\chi_s| (q_{v,1}^* - H q_{v,2}^*), \quad (6.2.10b)$$

since this former formula is more like Sellers' evaporation formula.

Figures 6.29a and 6.29b may be compared to figures 6.17a and 6.17b; they show reasonably close agreement.

The reasons for this qualitatively better agreement for both formulae can probably be attributed to the relative humidity which - like the fractional cloud cover - is affected by the horizontal advection. In fact, the use of the relative humidity alone gives a fairly good cloud

formula. This was also suggested in figure 1.1. However, the relative humidity alone may not be sufficient to describe stratus and convective clouds under different climatic conditions and the additional variables may be needed. For example, the cloud formulae indicate that if the evaporation is large compared to the precipitation in one particular region and that if the precipitation is large compared to the evaporation in another region then even though the relative humidities may be the same the cloud cover will be less in the former case than in the latter.

6.2.11 Summary

Although the evaporation and consequently condensation and precipitation increased with an increasing T_E and $AMTG_E$, the fractional cloud covers and the relative humidity decreased. Chapter 4 showed that, other things remaining the same, an increase in temperature would increase the efficiency of the transports in moistening and drying the atmosphere, and hence decrease the cloudiness toward regions of ascent only and decrease the relative humidity in regions of descent. However, the surface wind and radiative and sensible cooling increased with an increasing T_E and could have counteracted this temperature effect were it not for the increase in the atmospheric static stabilities, vertical velocities, and relative entrainment, which also increased with an increasing $AMTG_E$. Due to the neglect of large scale entrainment and detrainment, the simpler model formulae did not correspond too well quantitatively with the numerical model's cloud cover and relative humidity. By eliminating explicit reference to the vertical velocity field and substituting variables affected by the advections, better formulae were obtained.

We have therefore gained confidence that the model's sensitivities are internally consistent. Whether or not the model accurately represents climatic change is unresolved, however, because of the many parameterizations incorporated into the model.

6.3 Sensitivity of Model Results to Various Parameterizations and Model Scales

Extensive testing of various model parameterizations and scales was done to determine what effect they might have on our eventual conclusions; none altered the qualitative answers obtained from the basic sensitivity experiments. We discuss briefly some of the most important quantitative differences.

6.3.1 Domain Size

Since the meridional scale that was chosen for the basic experiments was smaller than the earth's meridional scale, the meridional width was increased to 9,000 km. Evaporation and hence condensation, precipitation, and cloud water content increased mainly because of an increase of temperature in the hot southern region where most of the evaporation takes place. For the same average temperature the evaporation increased to $23 \times 10^{-7} \text{ g cm}^{-2} \text{ sec}^{-1}$ from $10 \times 10^{-7} \text{ g cm}^{-2} \text{ sec}^{-1}$. Corresponding to the increase in the intensity of the hydrologic cycle, the fractional coverages decreased by .20 and the relative humidity decreased by .05 - which were statistically significant changes. This was consistent with an increase of the eddy vertical velocity and atmospheric static stability.

When the average temperature of the large domain was increased to 287.5 deg., the intensity of the hydrologic cycle increased still further and the concomitant cloud and relative fields decreased still further. The average sensitivities of the large domain are therefore similar to the sensitivities for the small domain.

6.3.2 Horizontal Grid Resolution

Decreasing the grid size to 333.3 km., we found that the eddy vertical velocities increased, relative humidity decreased and fractional cloud cover decreased. The differences were slight, however, and differences between a hot and cold climate for a high resolution model were comparable to the differences found in a lower resolution model. This indicates that even though absolute magnitudes may change, the large scale climate sensitivities in the moisture field may be relatively insensitive to horizontal grid resolution. The effect of the vertical resolution was not tested.

6.3.3 Precipitation Function

Since the parameterization for conversion of cloud water to precipitation is arbitrary to a certain extent, the efficiency was decreased by using the precipitation parameterization \dot{P}_3 - which is shown in figure 3.2. Using this parameterization for a hot climate, the fractional coverages increased by $\sim .12$ and the relative humidities by $.03$. Cloud evaporation more than doubled and the conversion efficiency $(\frac{\dot{C}^+}{\dot{C}^+ + \dot{C}^-})$ decreased from 95% to 87%. It was interesting to note that even though

the cloud-water contents in cloudy regions for the hot climate increased from 2×10^{-2} g cm⁻² to 7.1×10^{-2} g cm⁻², total precipitation remained fairly constant since the evaporation was relatively unchanged by the small changes in relative humidity. The evaporation could be considerably changed, however, if radiative feedbacks had been included in the model.

6.3.4 Critical Relative Humidity

Since the real atmosphere has significant cloudiness occurring even when the relative humidity averaged over one grid interval is unsaturated, some general circulation models have condensation occurring when the relative humidity reaches a lower optimum value - usually 85%. Use of this criterion in our model increased the fractional coverage of positive condensation and total cloudiness and also increased the intensity of the hydrologic cycle. However, the sensitivity of the model with this new condensation parameterization to the equilibrium temperature remained unchanged. For an increase in the average temperature, the evaporation, condensation, and precipitation increased while the relative humidity and fractional coverages decreased.

6.3.5 Newtonian Time Constant

Although the Newtonian time constant was fairly small for the upper troposphere, it was large for the lower atmospheric layer which, in addition to radiation, includes sensible heat transfer from the lower layer to turbulent eddies; hence we decreased the time constant from

$\tau_2 = 1.6 \times 10^6 \text{sec}$ to $\tau_2 = 5 \times 10^5 \text{sec}$ in the lower layer. This had the effect of reducing the temperature difference between the resultant model temperature and the equilibrium temperature at the lower levels. The boundary-layer temperature difference was considerably reduced in the southern regions and the inversion wasn't as strong in the northern regions; the most outstanding change, however, was in the cloud field shown in figure 6.30.

The cloud cover became much more like that observed in mid-latitudes on the earth. Whether or not this is just coincidental is not important. What is important is that a radiative and sensible heating scheme that interacts with the cloud field may give a cloud field with a radically different coverage. Hence, the ultimate determination of cloud sensitivities must come from a more sophisticated model which includes all relevant feedbacks. We think, however, that the qualitative average sensitivities discussed in Section 6.2 will be unchanged.

6.3.6 Summary

Whether or not climatic changes entail changes in the basic parameterizations which the model assumes are unchanging is unknown. Also unknown are the validity of the various parameterizations being used in the model. Only by use of models such as the one described in this thesis can we determine what important feedbacks are present and how they relate to each other. We can then effect large changes in a particular parameterization to see how our basic conclusions might be altered. The testing will continue so long as people have differing opinions on the validity of the various parameterizations.

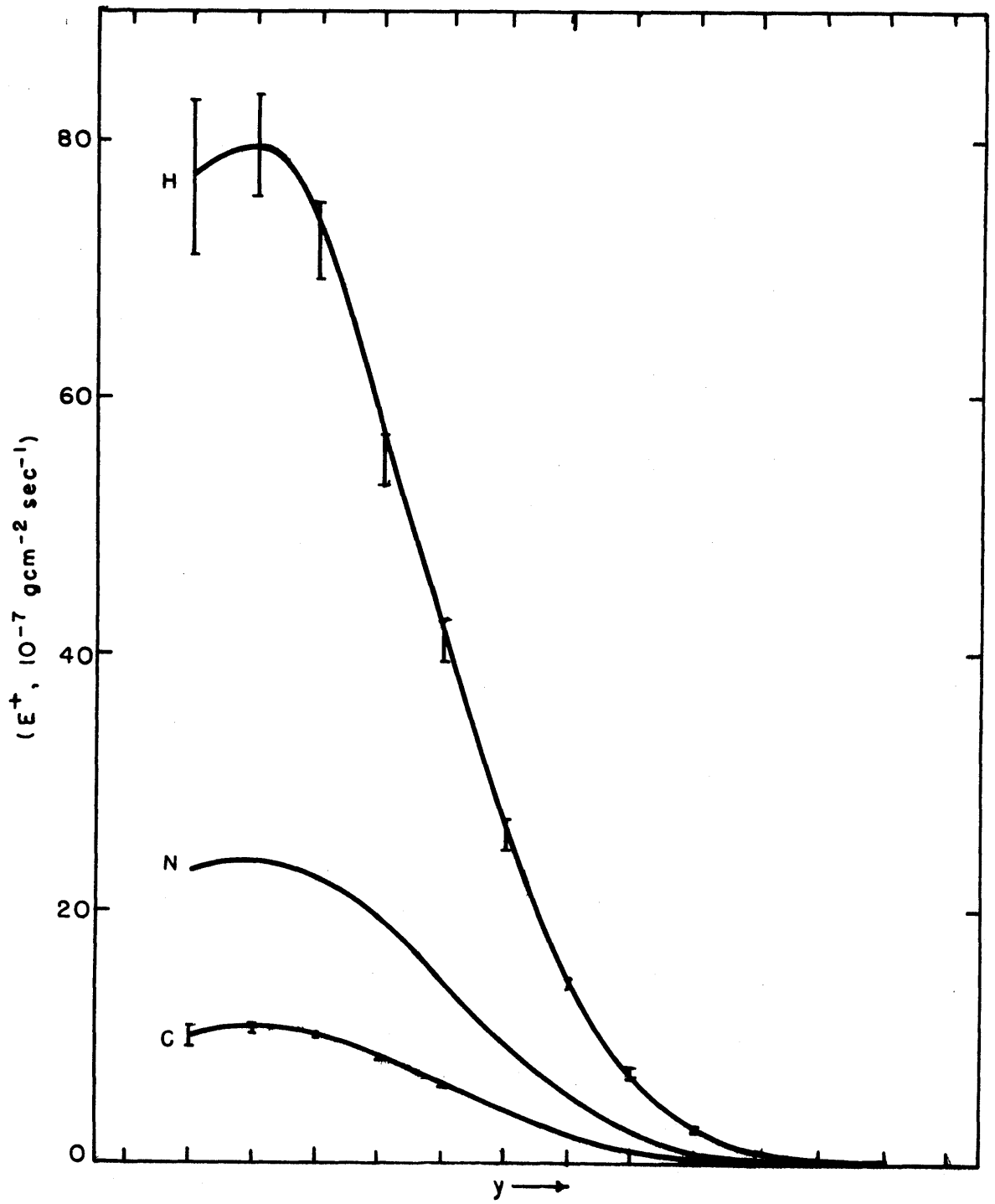


Figure 6.1a. Sensitivity of the positive evaporation to the equilibrium temperature.

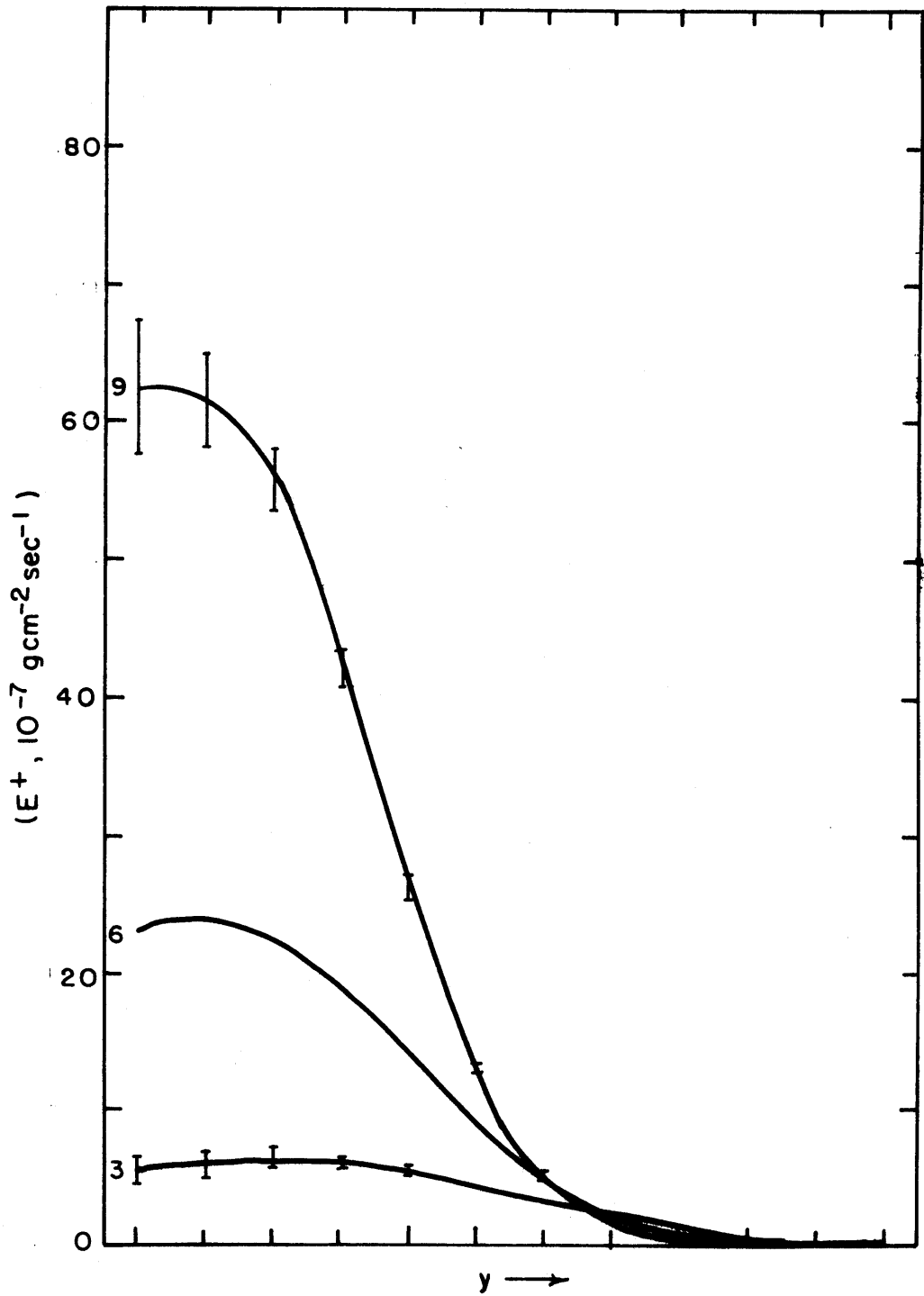


Figure 6.lb. Sensitivity of the positive evaporation to the equilibrium absolute meridional temperature gradient.

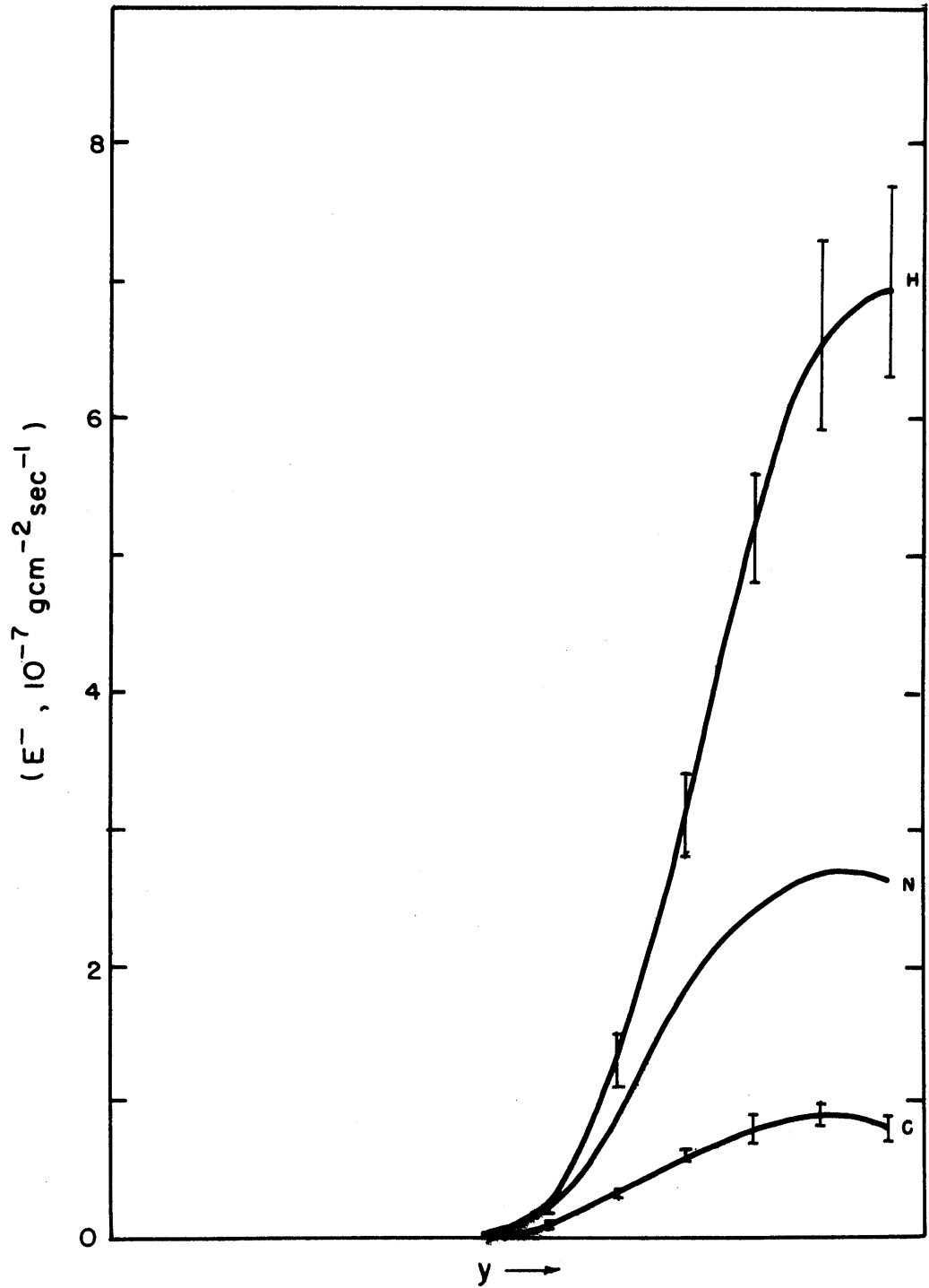


Figure 6.2a. Sensitivity of dew deposition to equilibrium temperature.

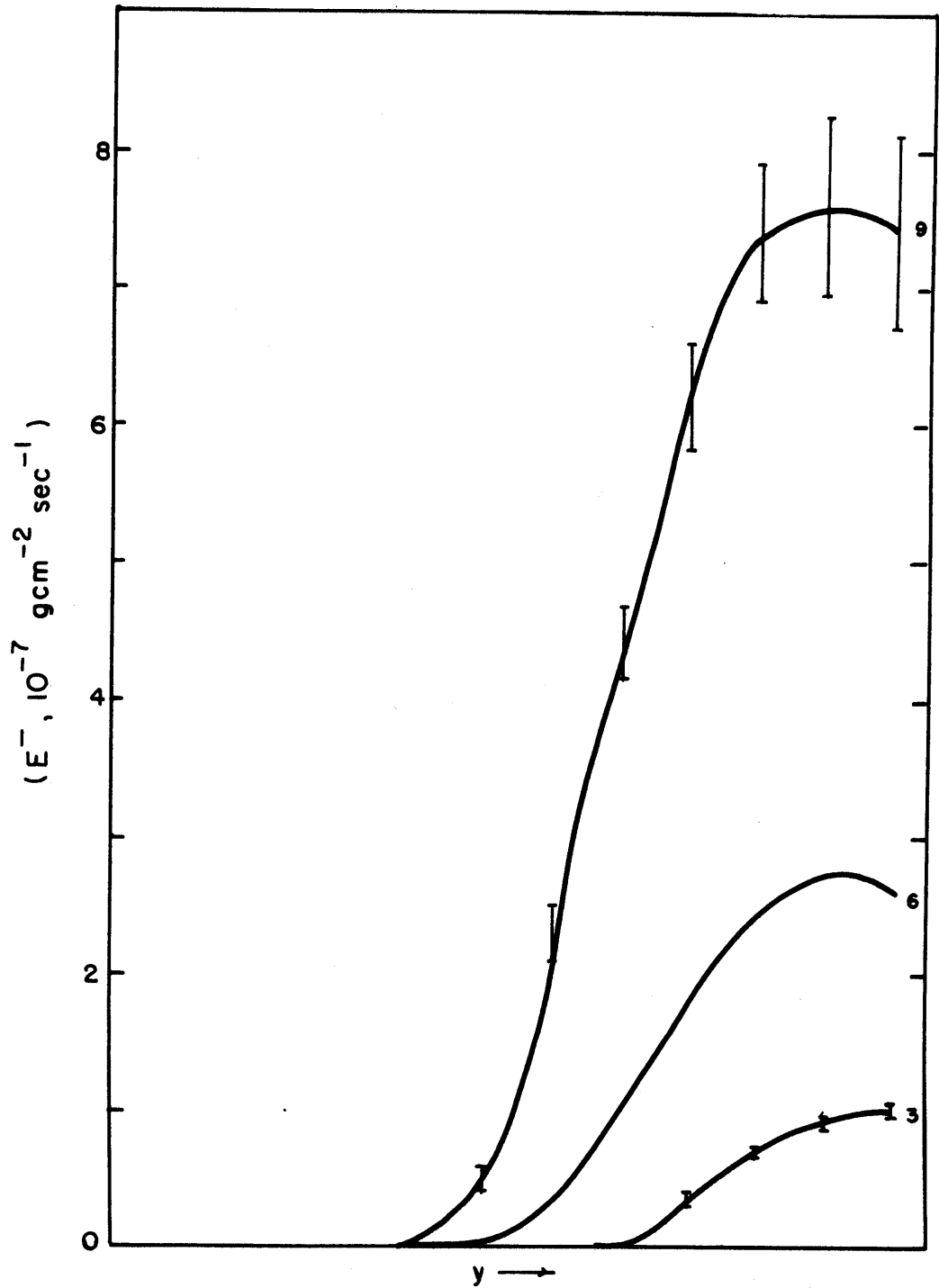


Figure 6.2b. Sensitivity of dew deposition to the equilibrium absolute meridional temperature gradient.

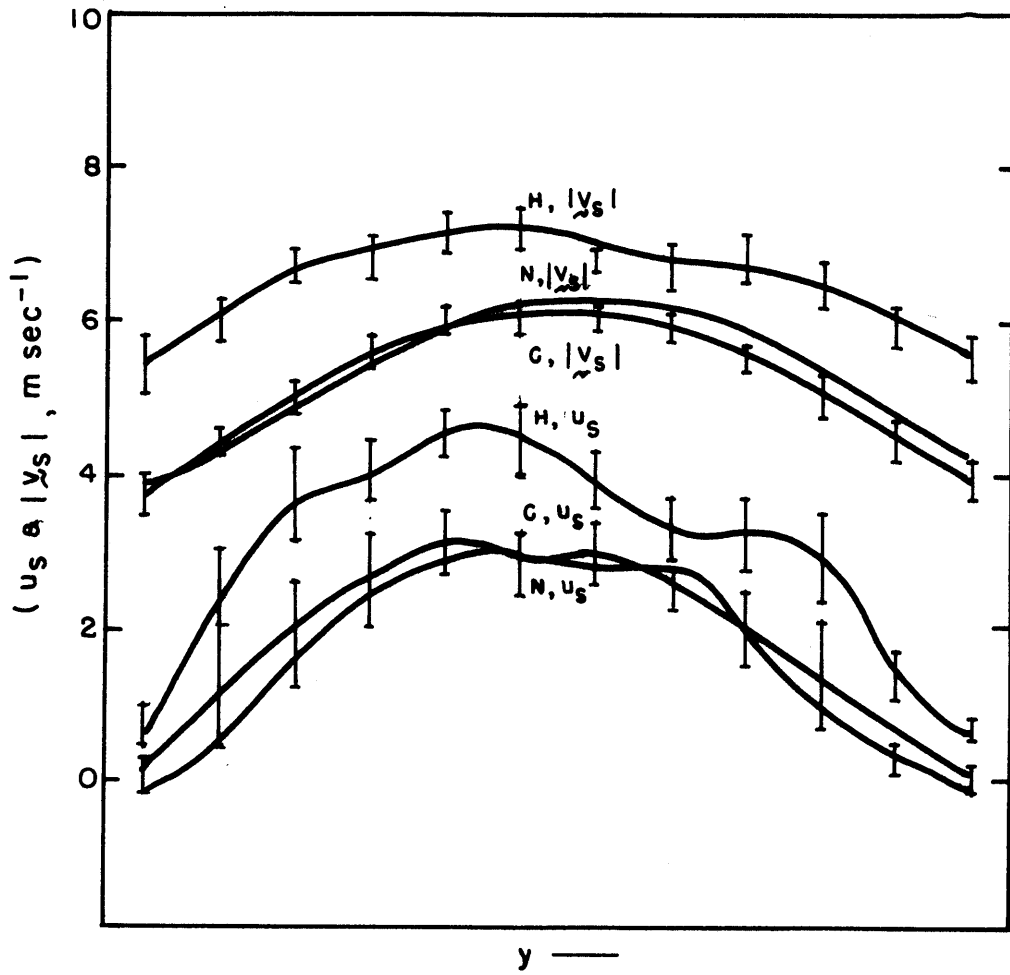


Figure 6.3a. Sensitivity of the surface wind speed and zonal wind to the equilibrium temperature.

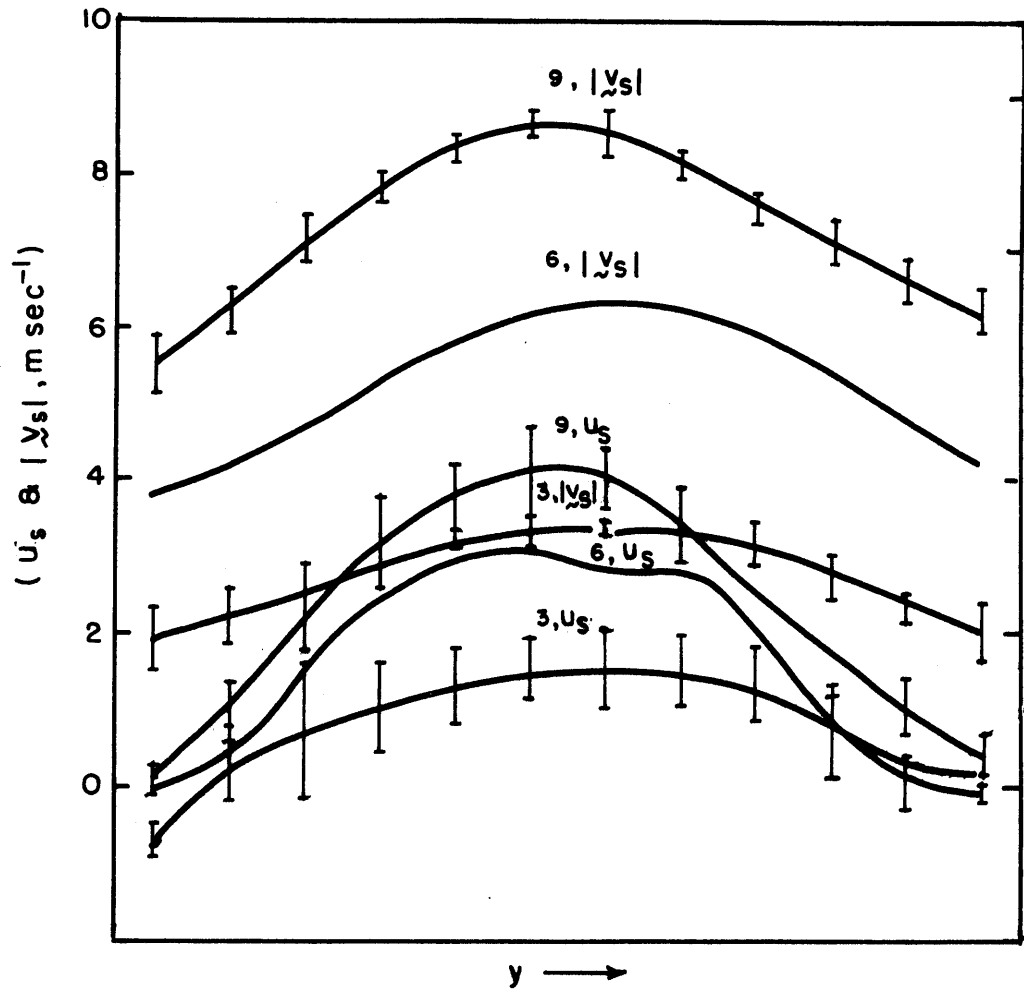


Figure 6.3b. Sensitivity of the surface wind speed and zonal wind to the equilibrium absolute meridional temperature gradient.

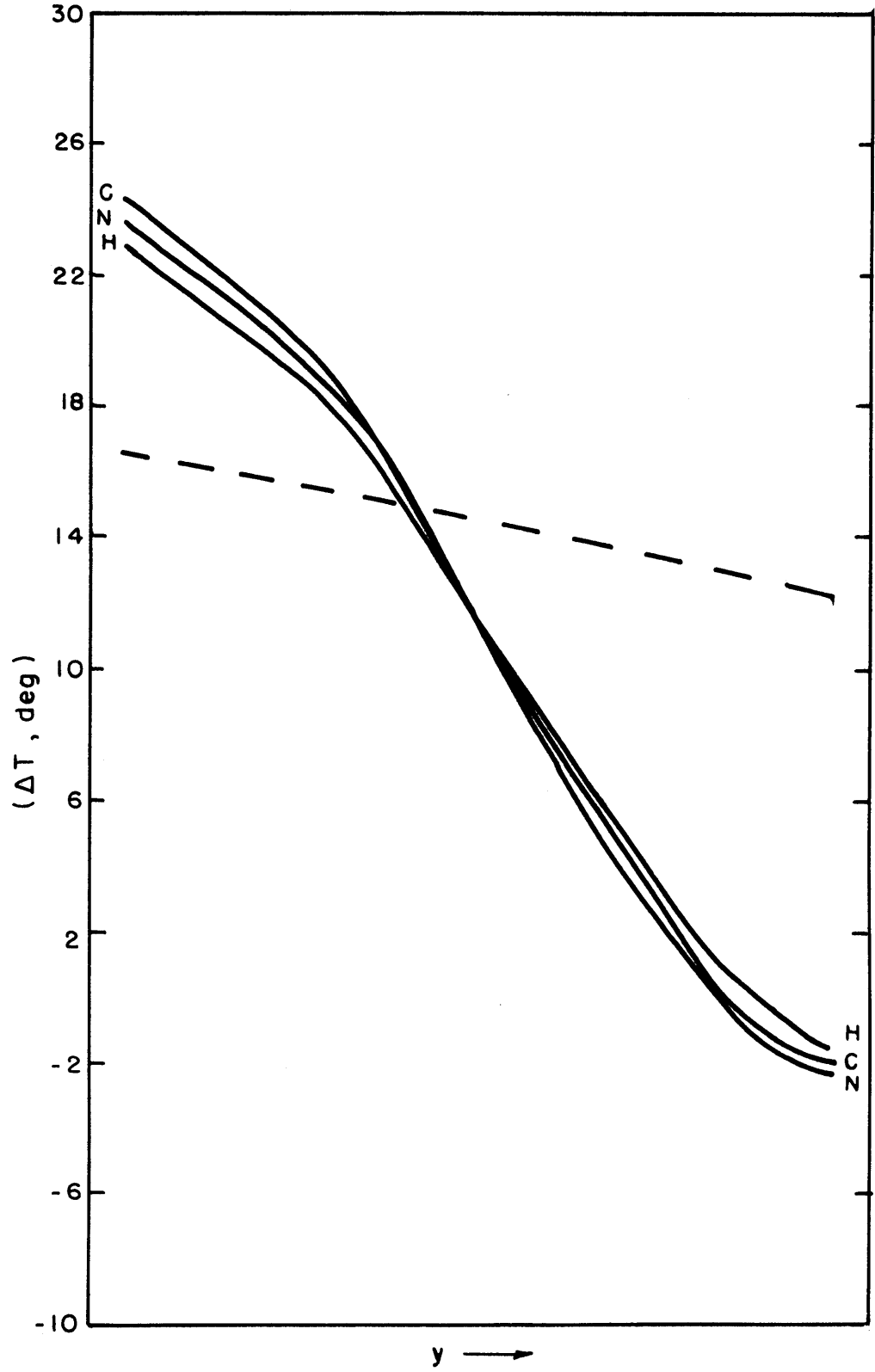


Figure 6.4a. Sensitivity of boundary-layer temperature difference $(T_g - T_2)$ to the equilibrium temperature. Dashed line is the ΔT of the imposed equilibrium temperature.

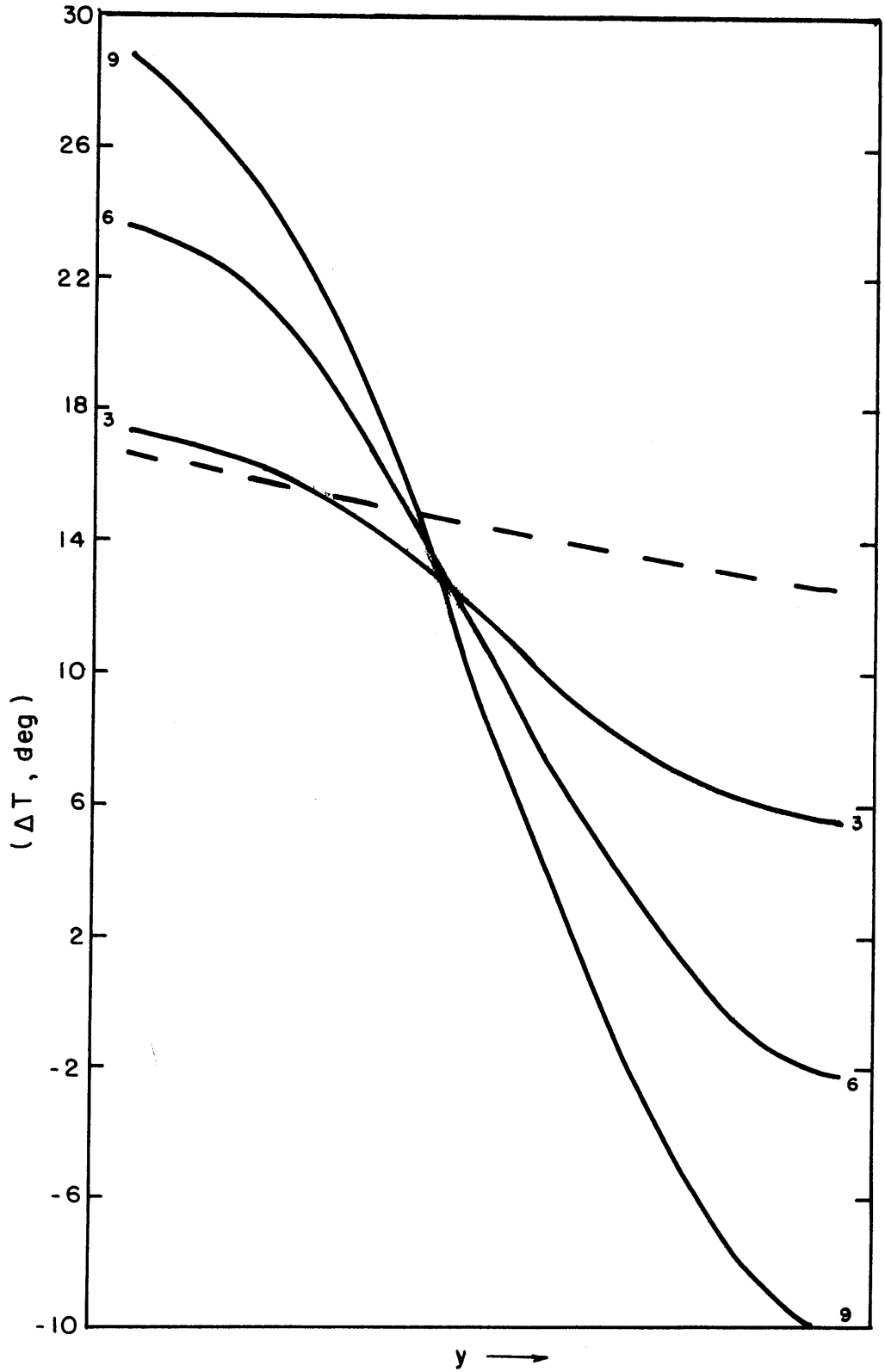


Figure 6.4b. Sensitivity of the boundary-layer temperature difference to the equilibrium absolute meridional temperature gradient. Dashed line is the ΔT of the imposed equilibrium temperature.

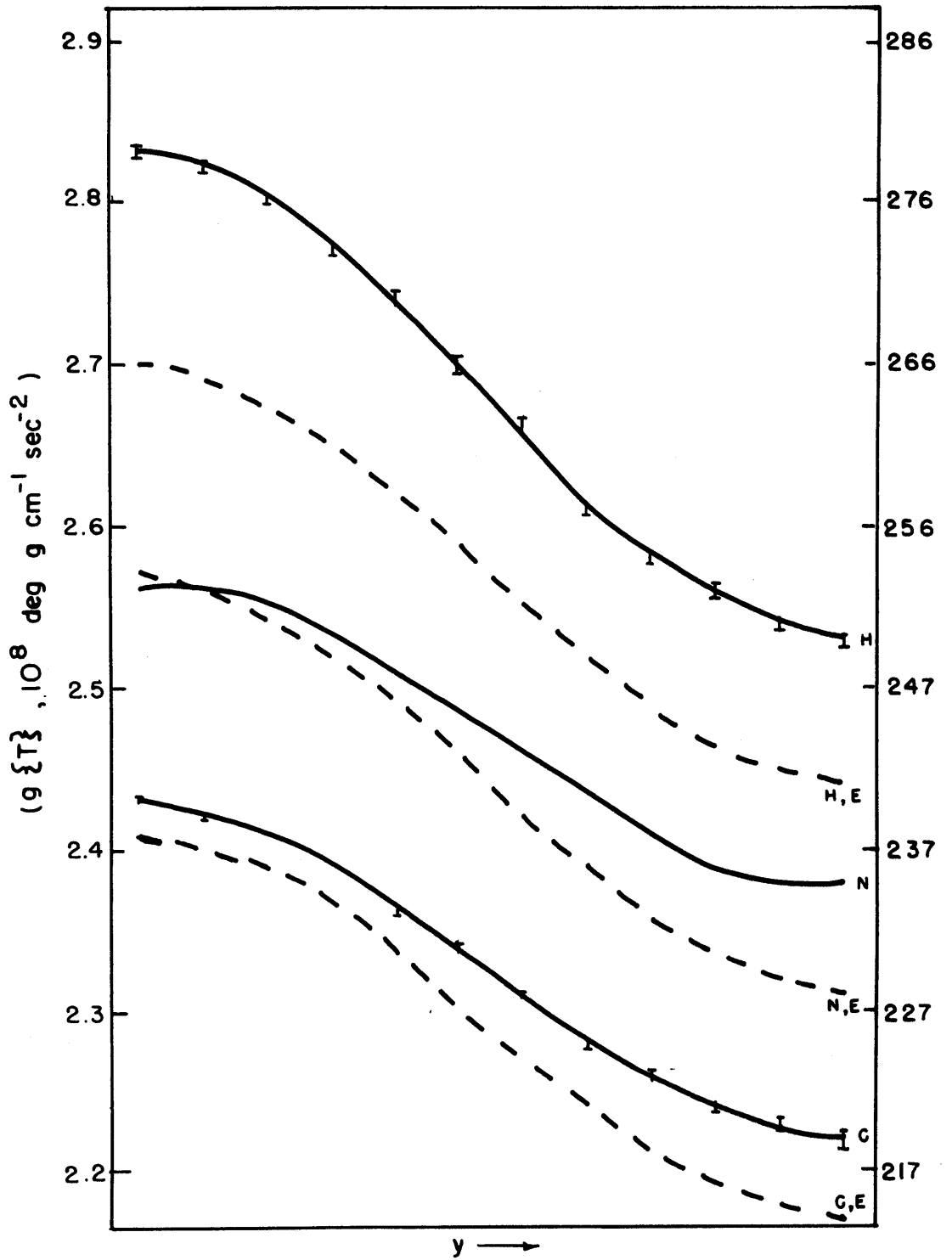


Figure 6.5a. Sensitivity of the integrated temperature to the equilibrium temperature. Dashed lines are the imposed equilibrium temperatures.

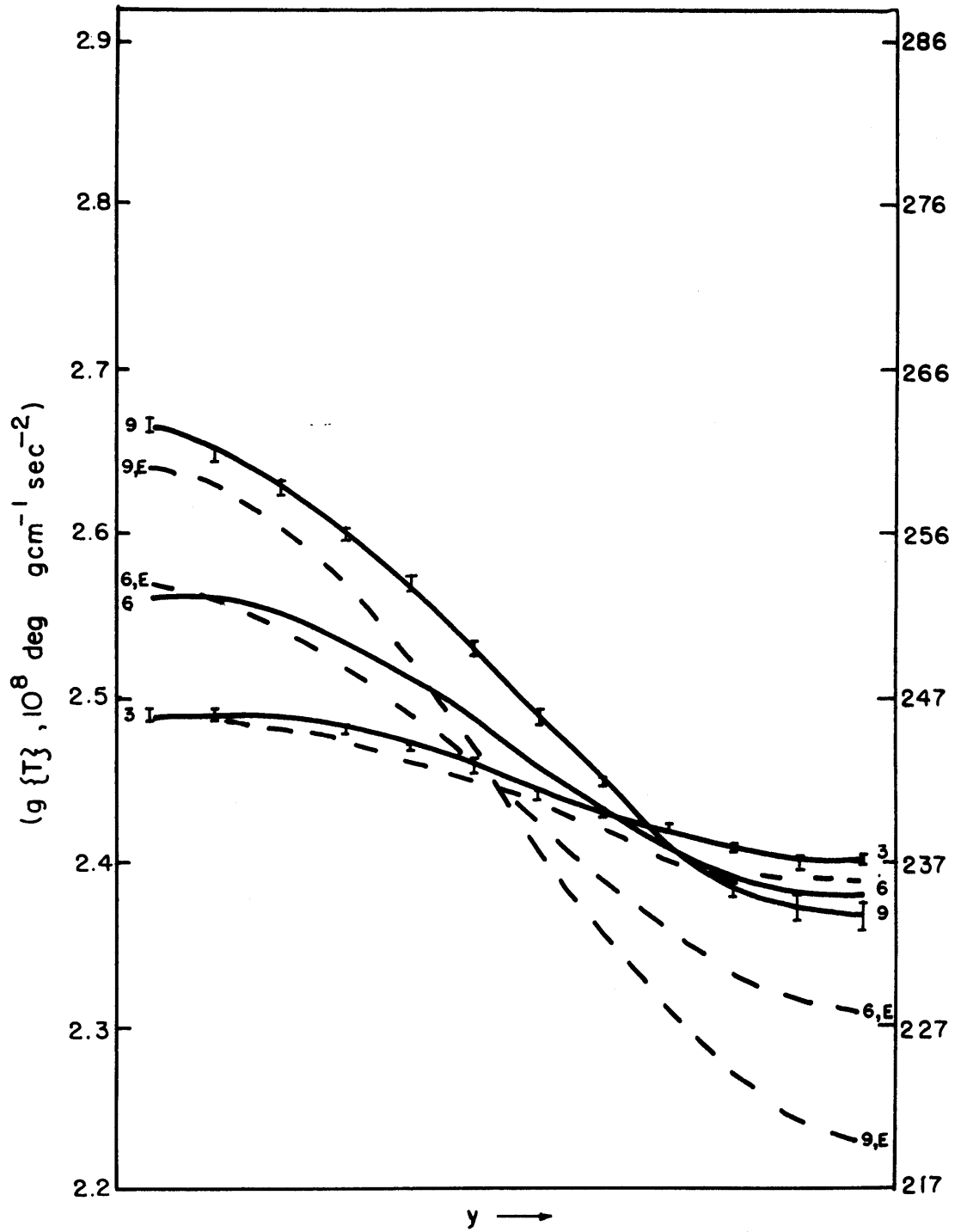


Figure 6.5b. Sensitivity of the integrated temperature to the equilibrium absolute meridional temperature gradient. Dashed lines are the imposed equilibrium temperatures.

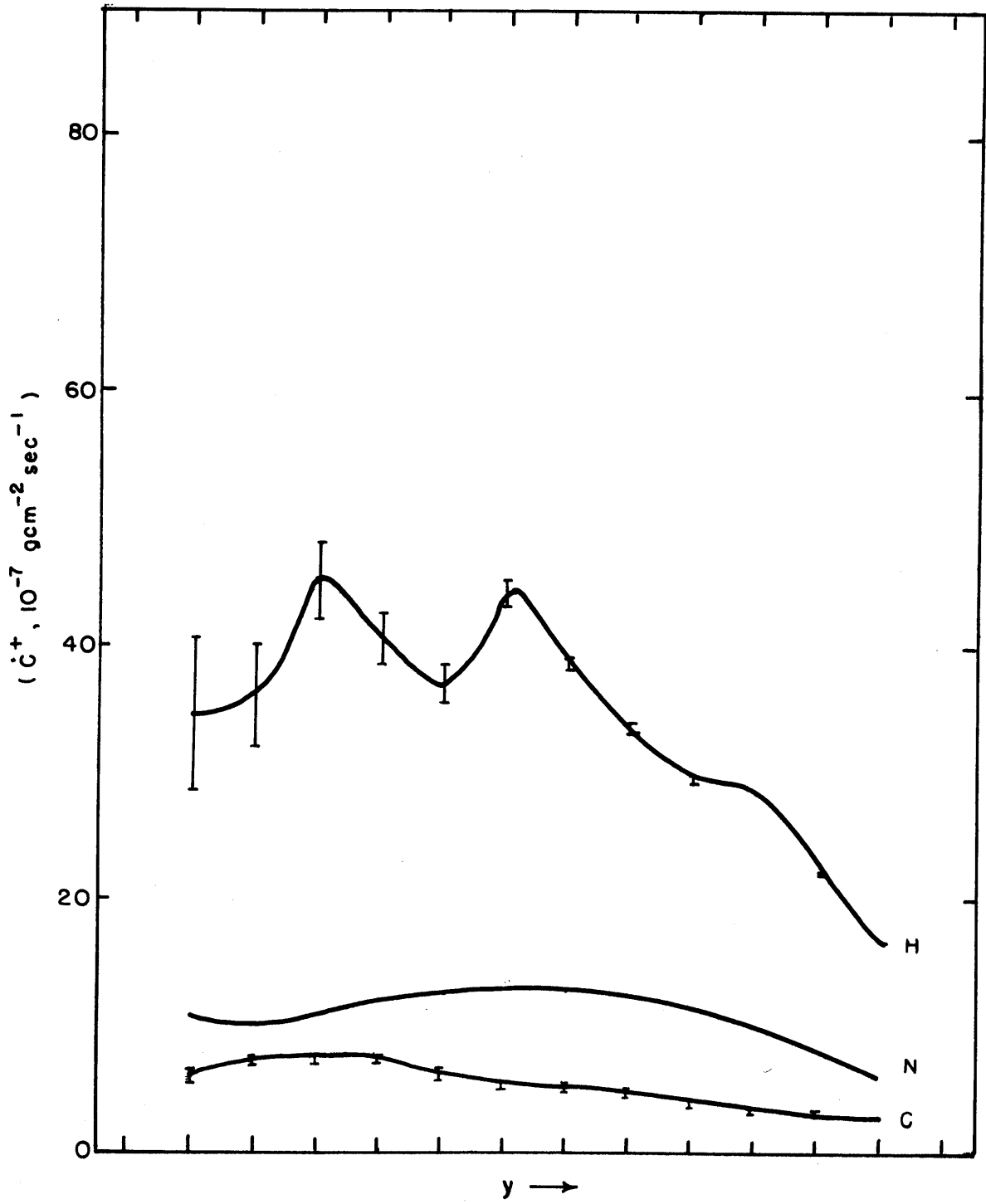


Figure 6.6a. Sensitivity of positive condensation to the equilibrium temperature.

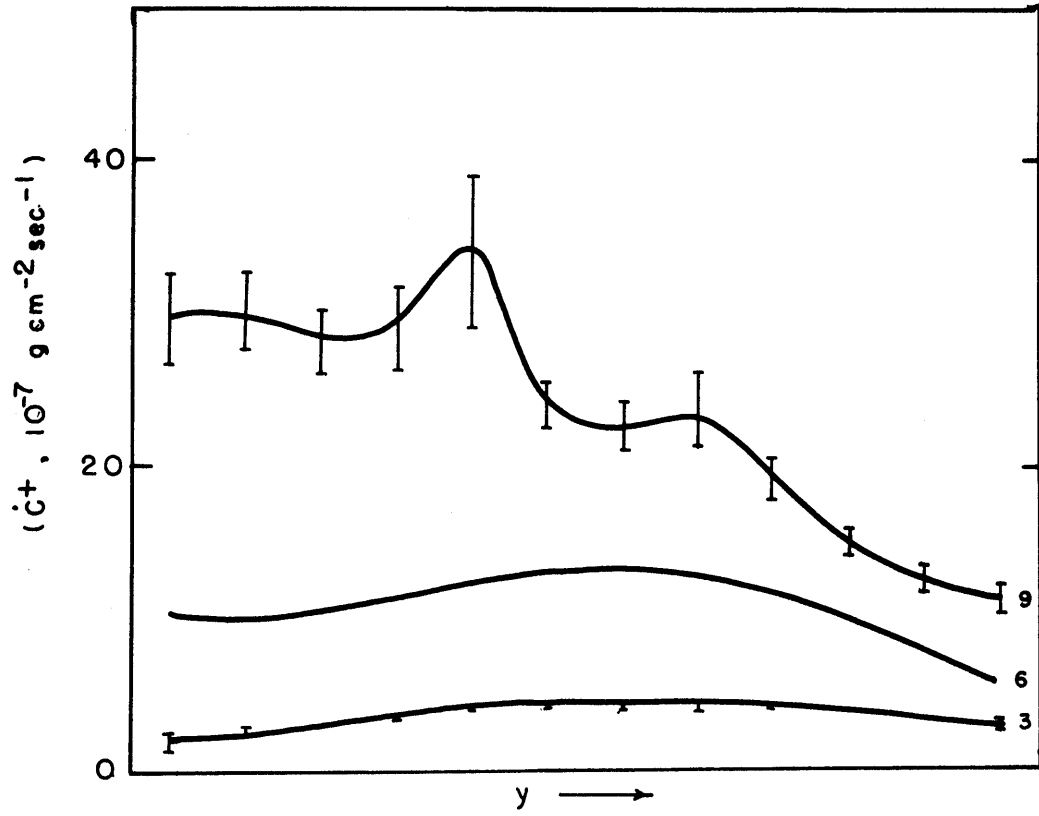


Figure 6.6b. Sensitivity of the positive condensation to the equilibrium absolute meridional temperature gradient.

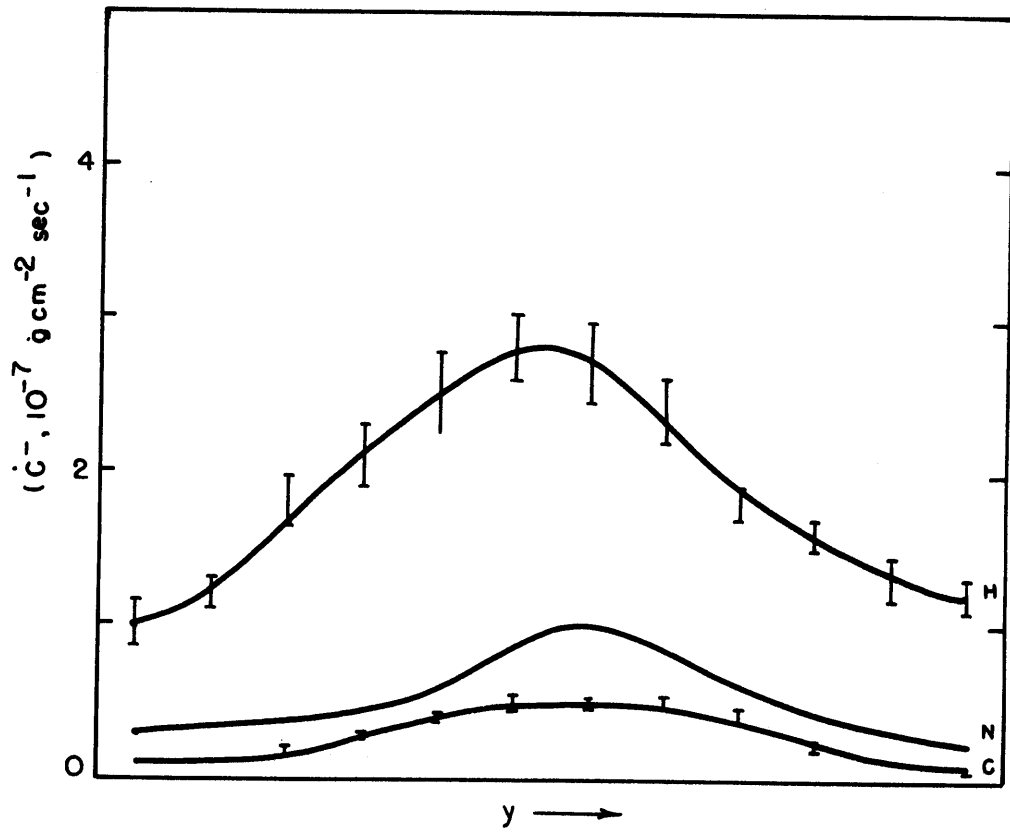


Figure 6.7a. Sensitivity of the cloud evaporation to the equilibrium temperature.

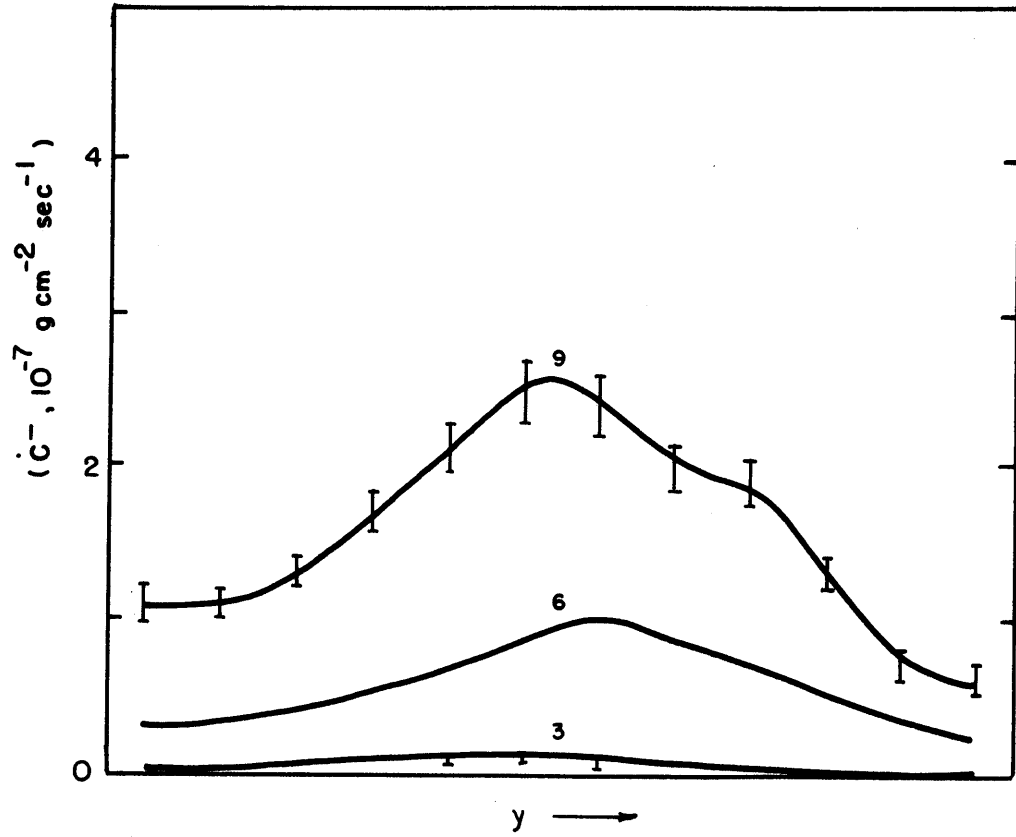


Figure 6.7b. Sensitivity of the cloud evaporation to the equilibrium absolute meridional temperature gradient.

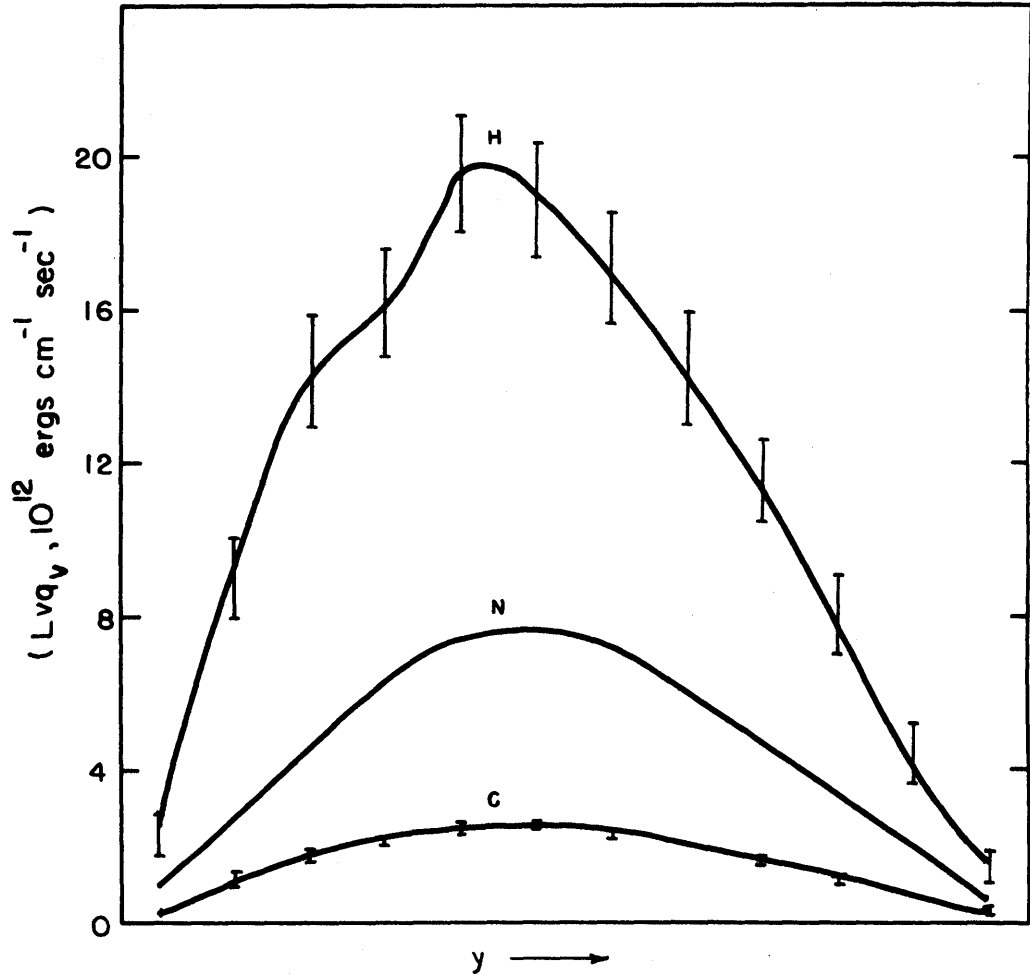


Figure 6.8a. Sensitivity of the meridional transport of latent heat to the equilibrium temperature.

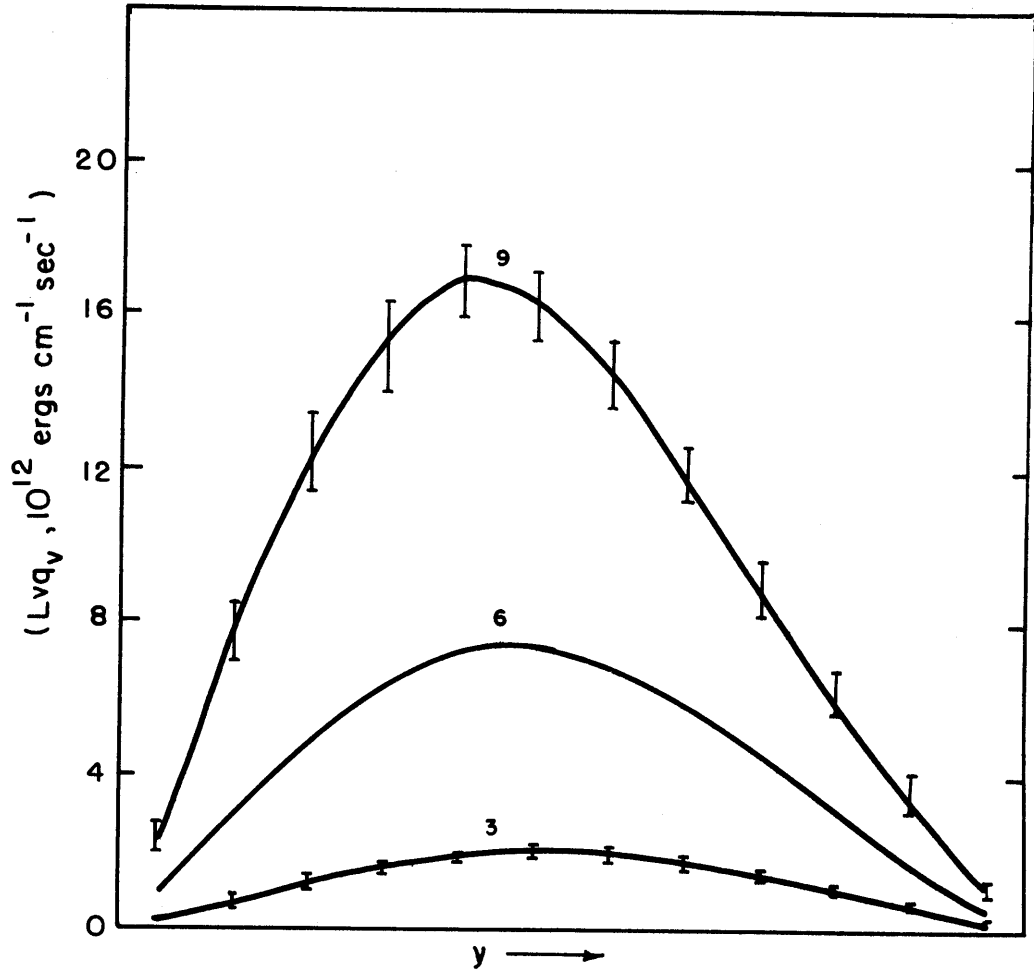


Figure 6.8b. Sensitivity of the meridional transport of latent heat to the equilibrium absolute meridional temperature gradient.

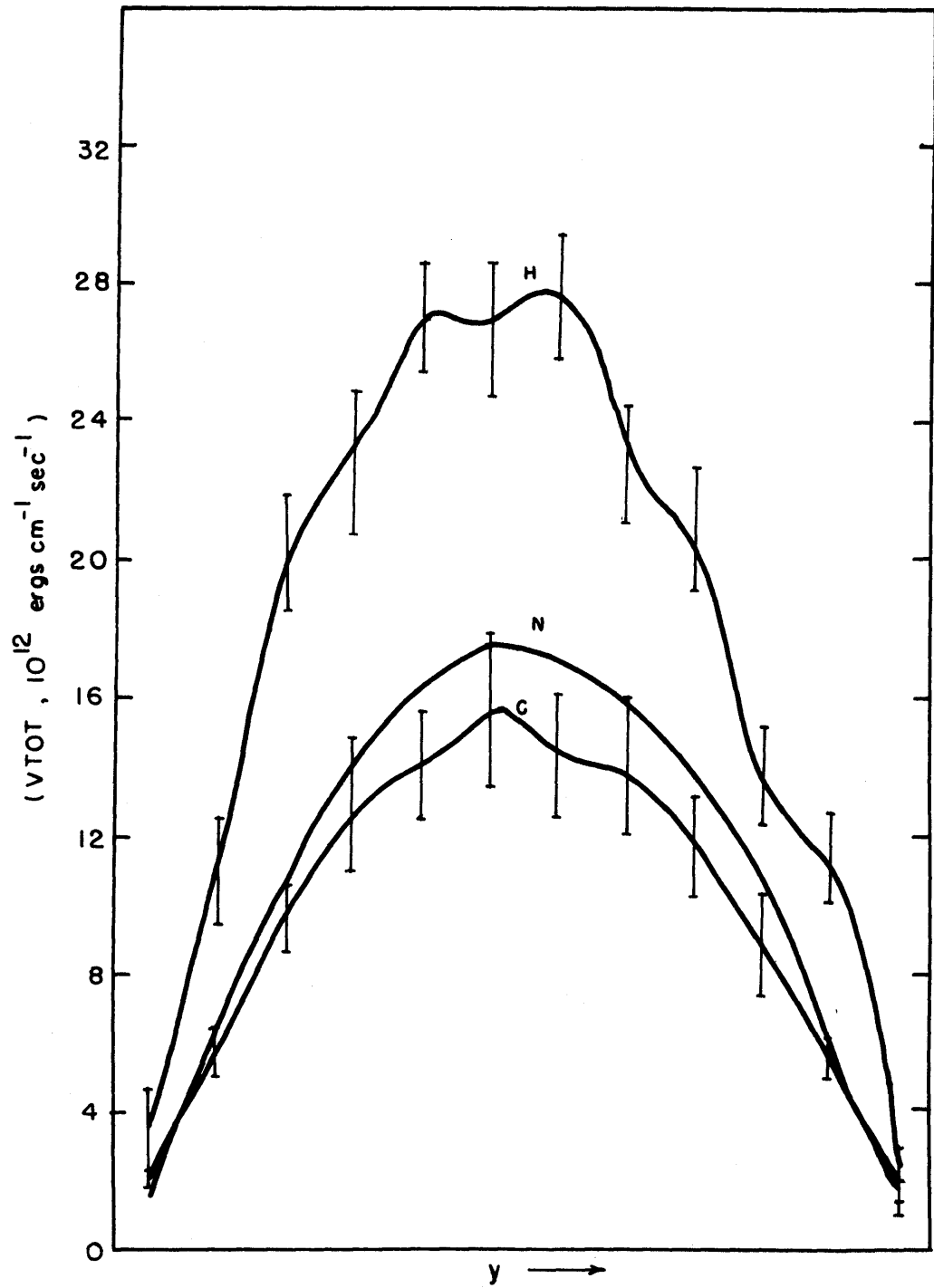


Figure 6.9a. Sensitivity of the total energy transport to the equilibrium temperature.

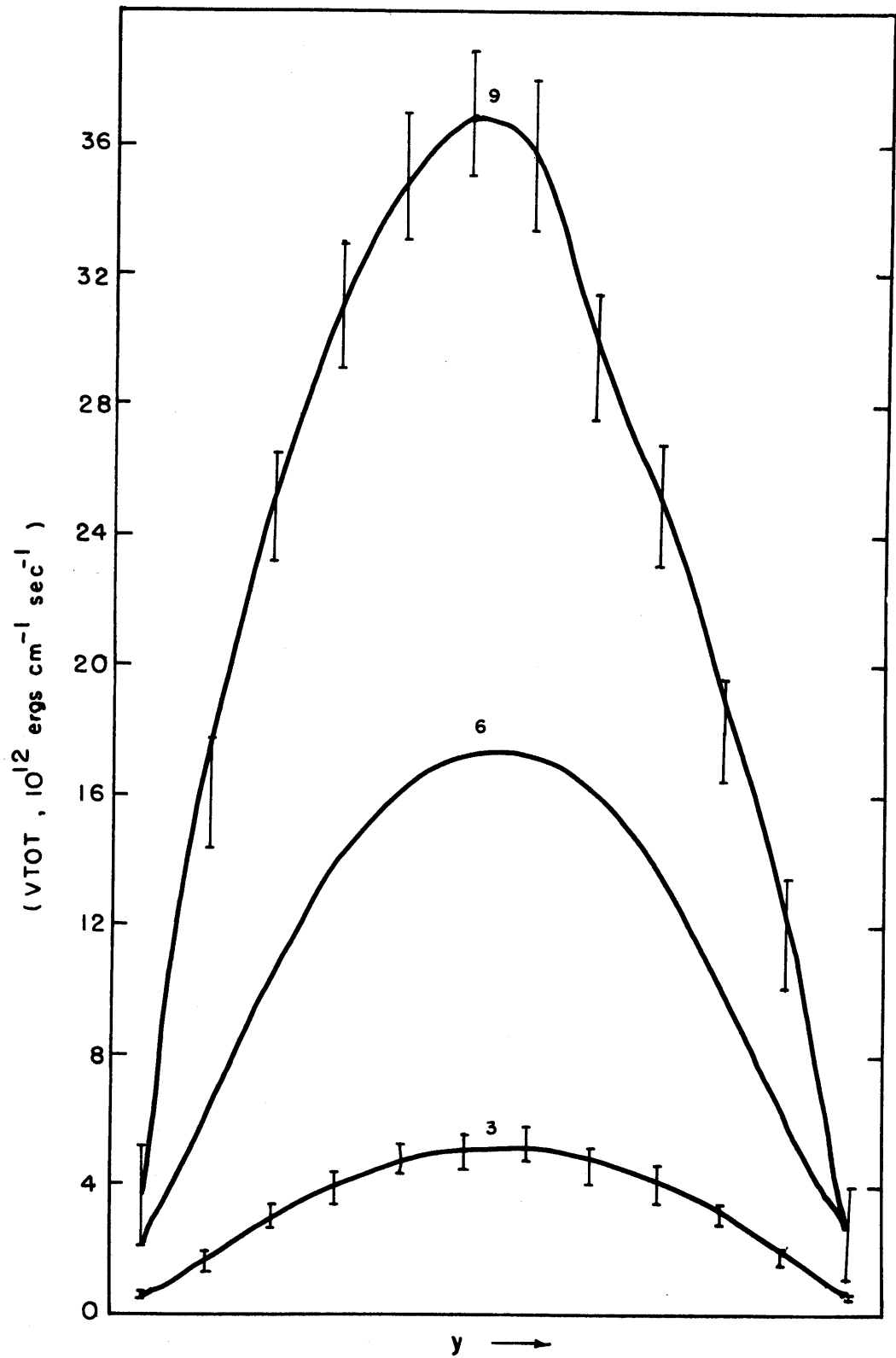


Figure 6.9b. Sensitivity of the total energy transport to the equilibrium absolute meridional temperature gradient.

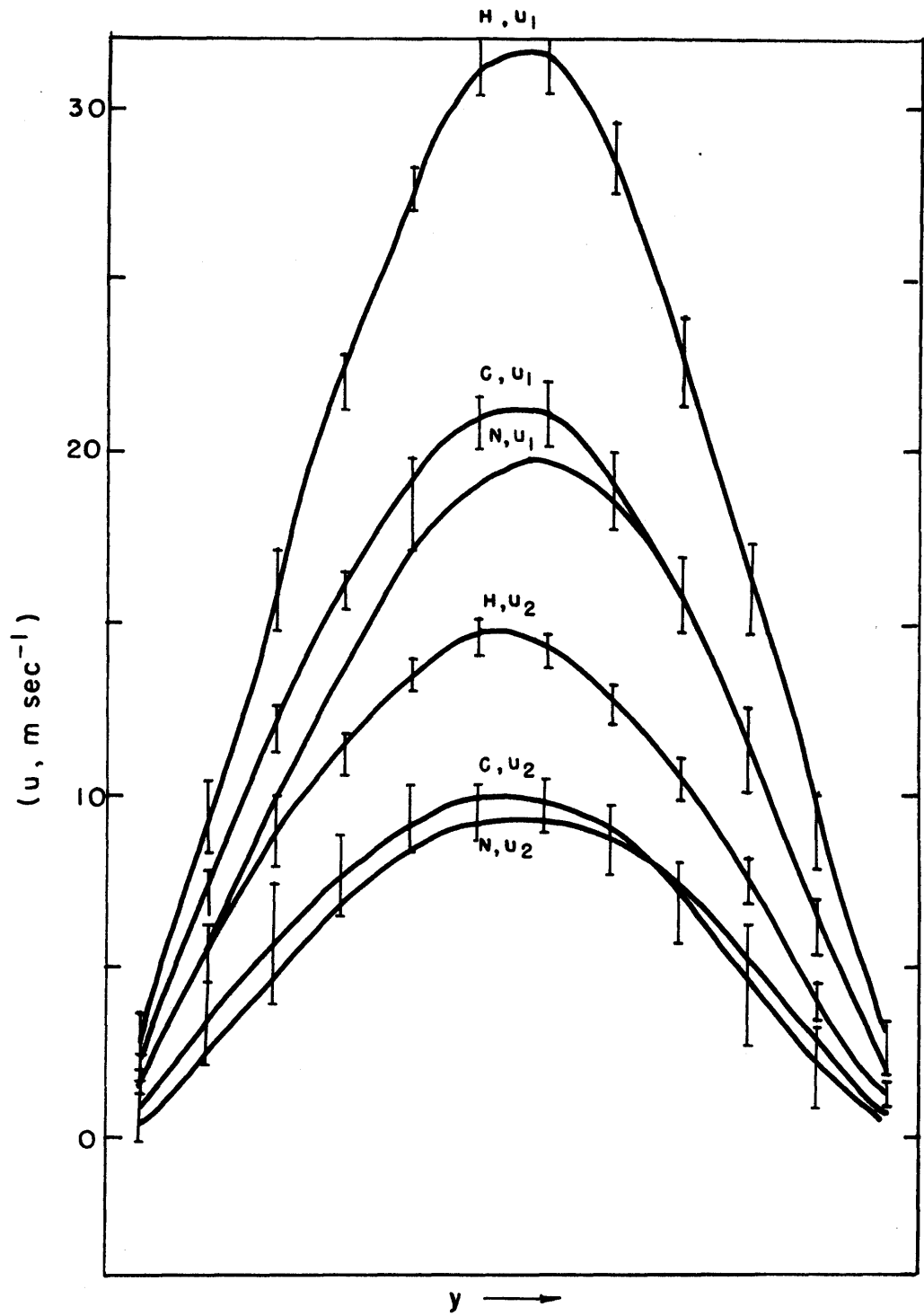


Figure 6.10a. Sensitivity of the upper and lower-level zonal winds to the equilibrium temperature.

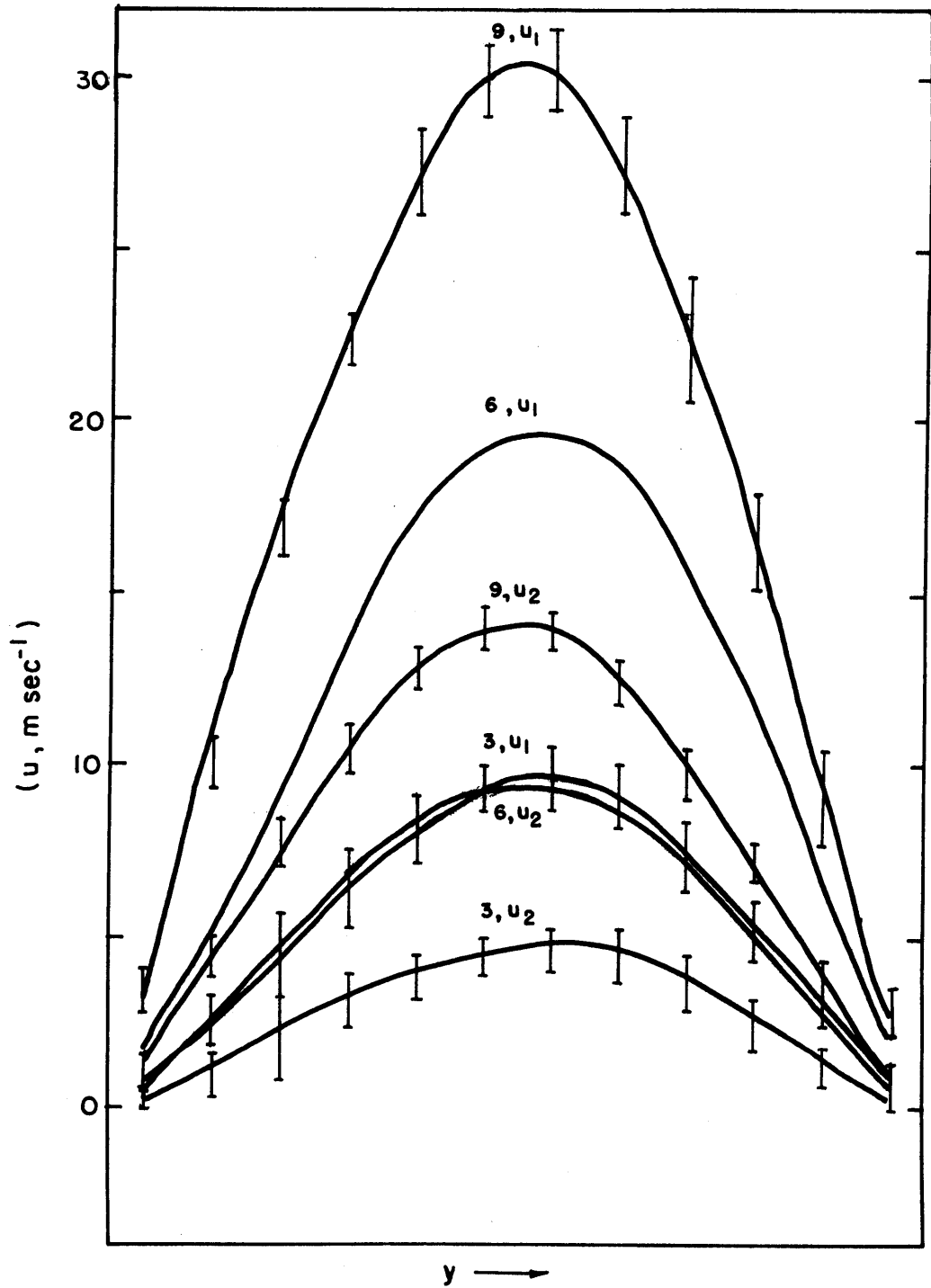


Figure 6.10b. Sensitivity of the upper and lower-level zonal winds to the equilibrium absolute meridional temperature gradient.

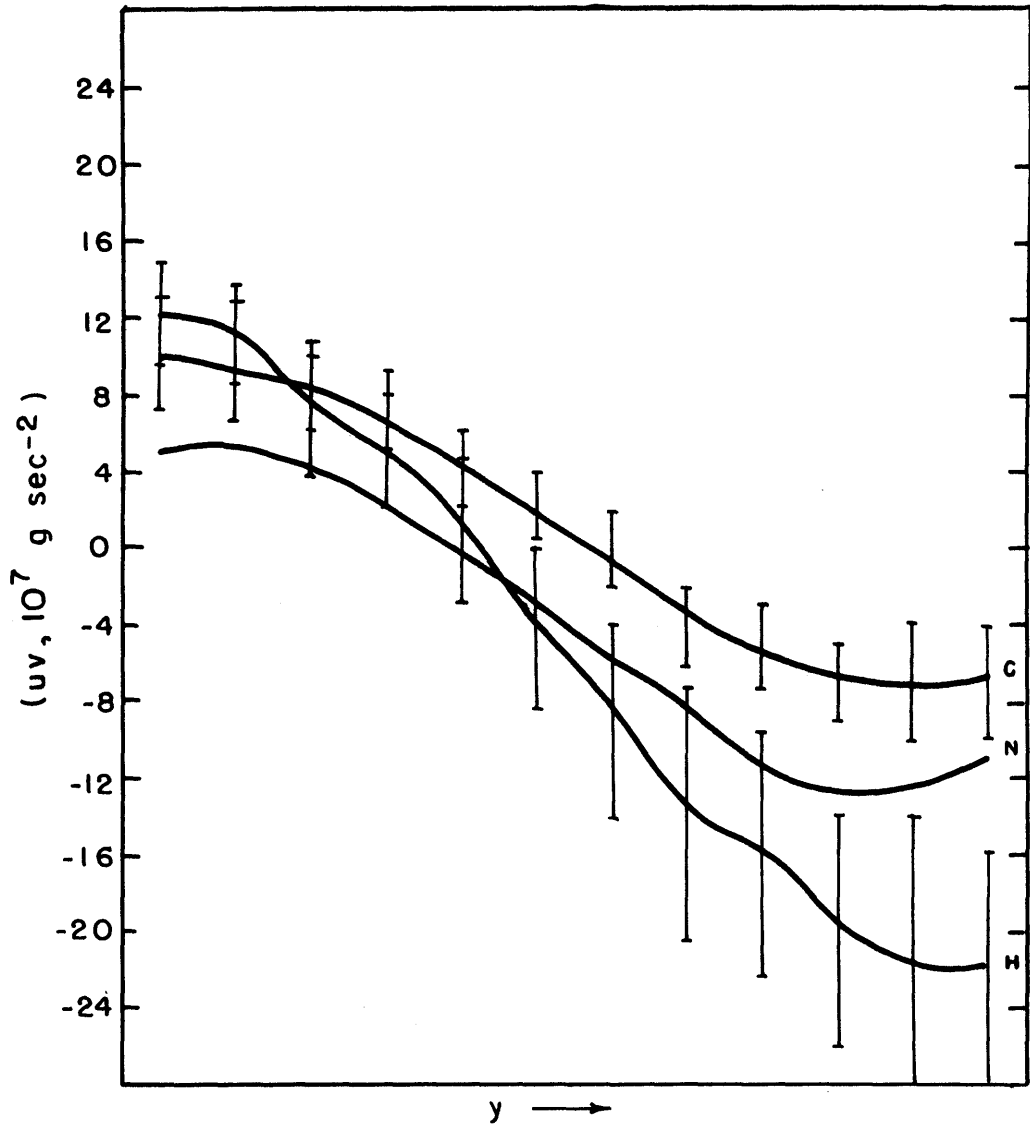


Figure 6.11a. Sensitivity of the transport of zonal momentum to the equilibrium temperature.

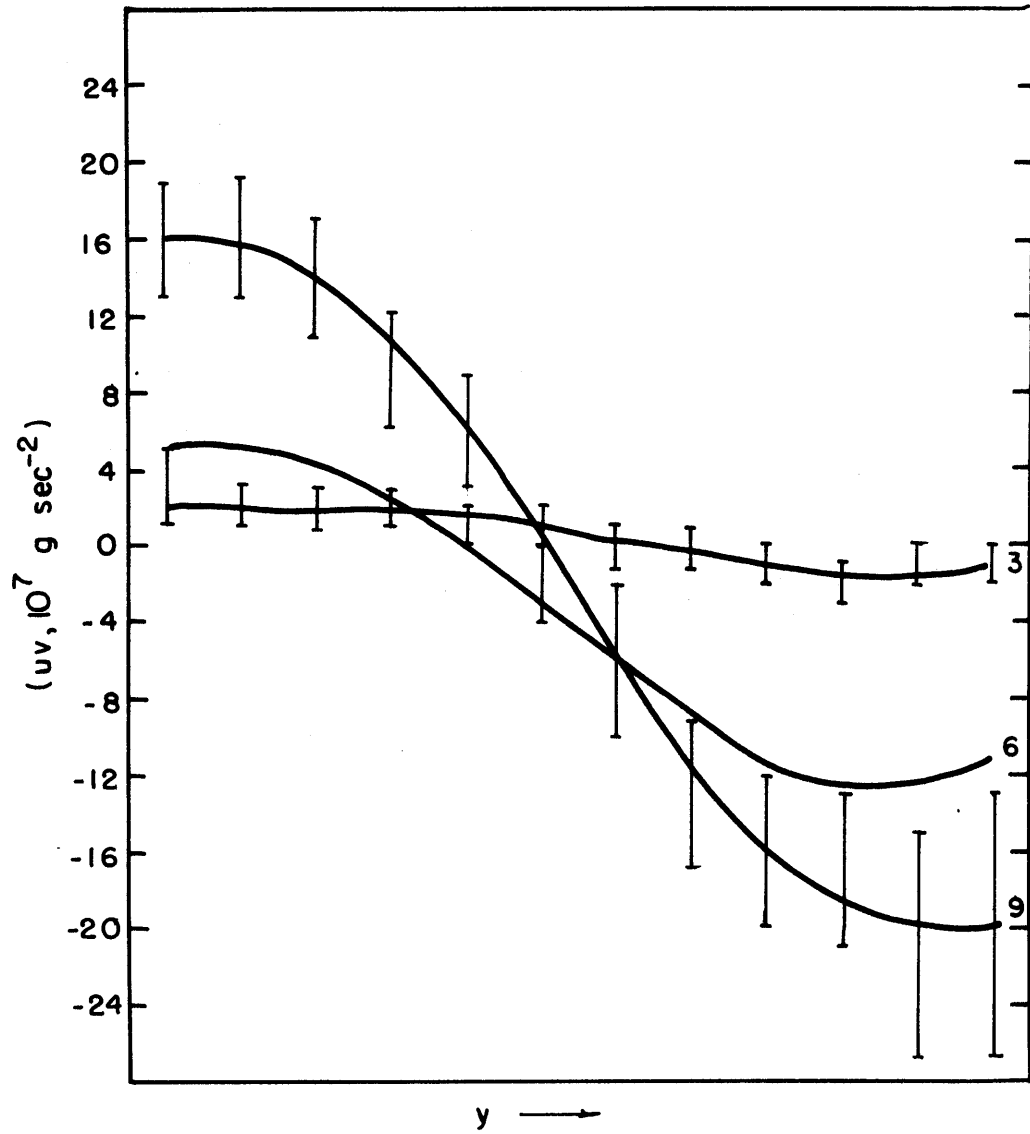
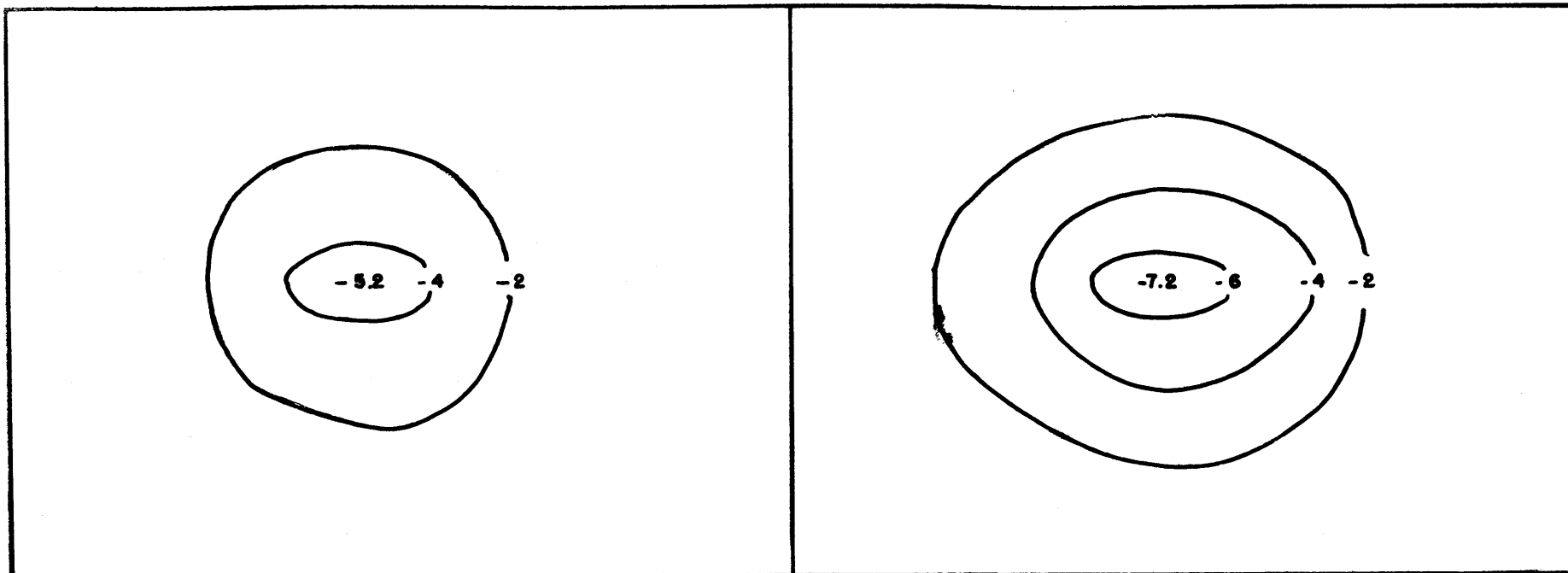
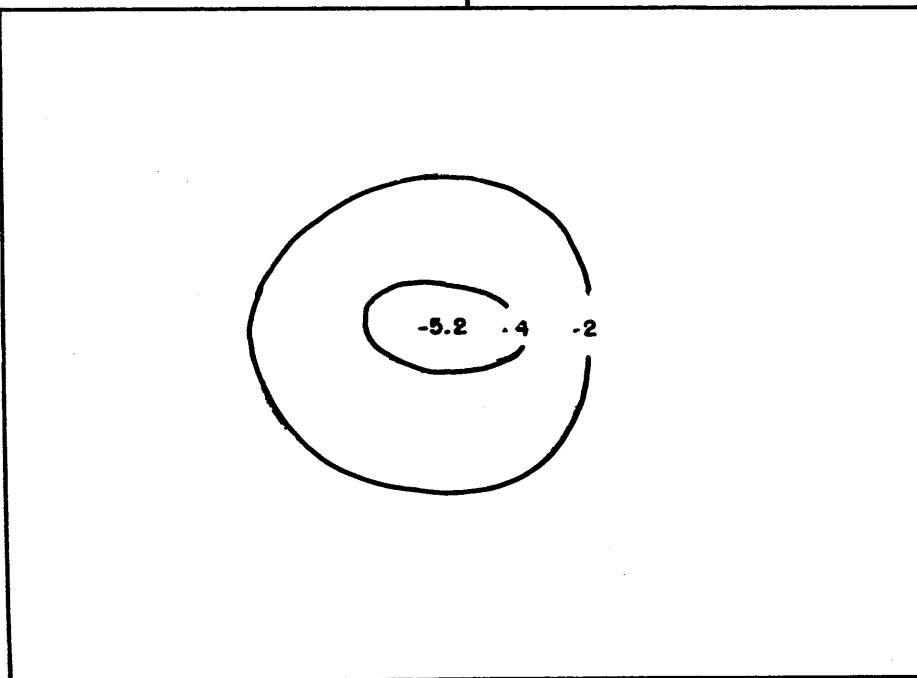


Figure 6.11b. Sensitivity of the transport of zonal momentum to the equilibrium absolute meridional temperature gradient.



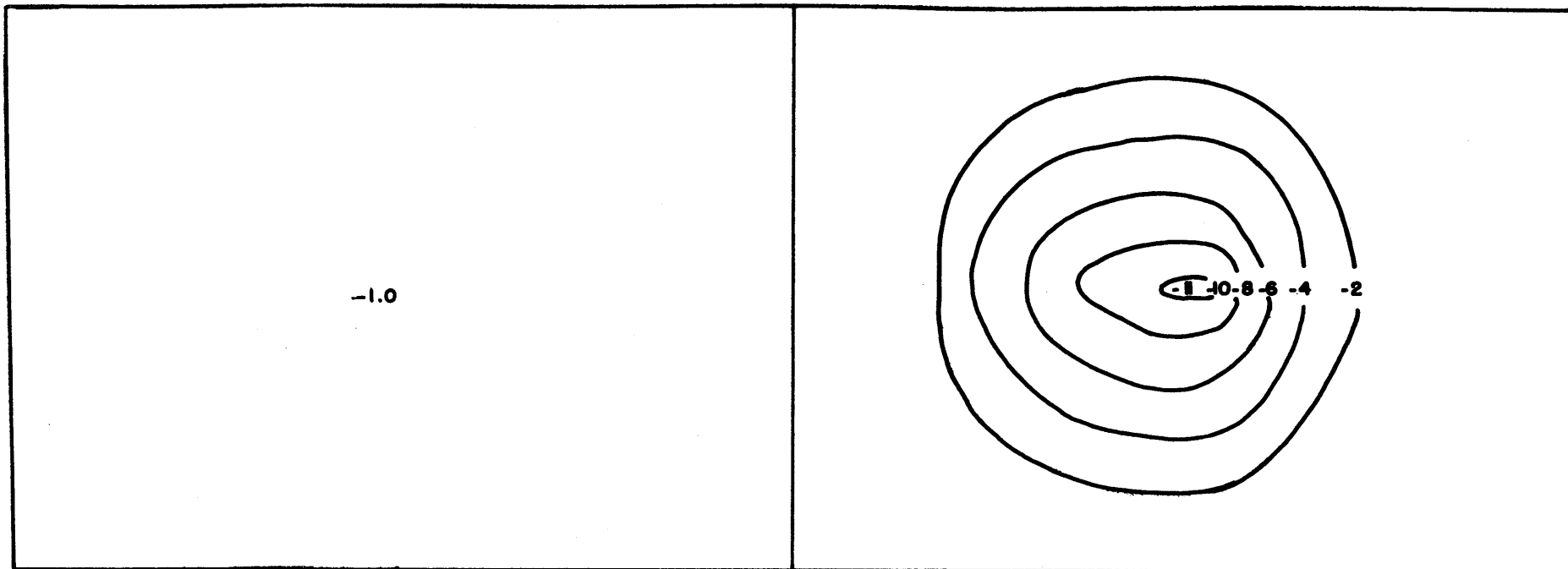
y →
COLD

y →
HOT



y →
NORMAL

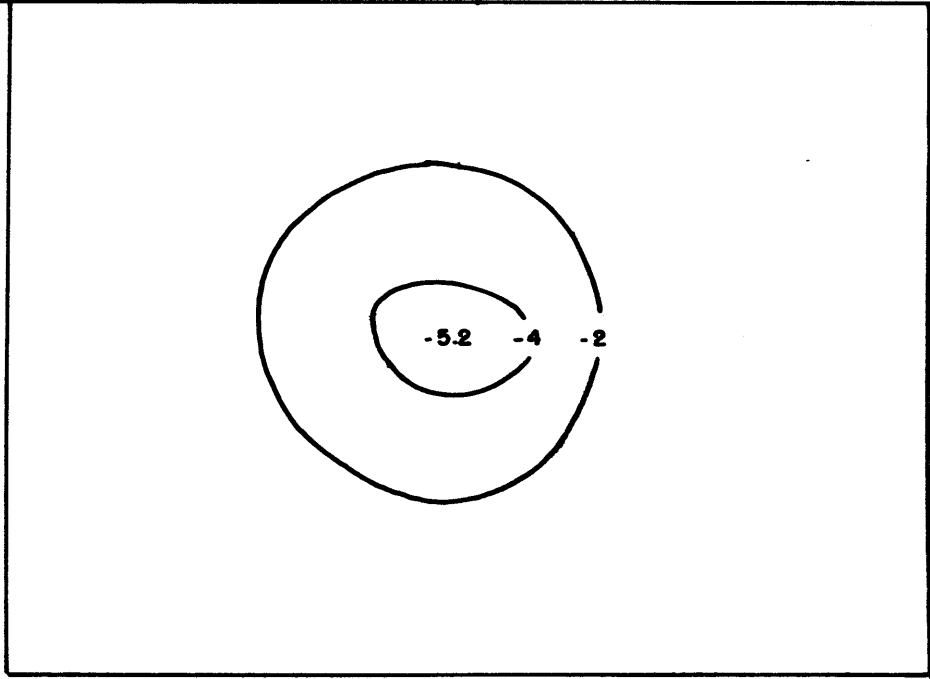
Figure 6.11c. Sensitivity of the mean cell to the equilibrium temperature. Contours placed every $2 \times 10^{12} \text{gsec}^{-1}$. Numbers less than or equal to 0 represent a Ferrell cell.



y →
3

y →
9

Figure 6.11d. Sensitivity of the mean cell to the equilibrium absolute meridional temperature gradient.



y →
NORMAL

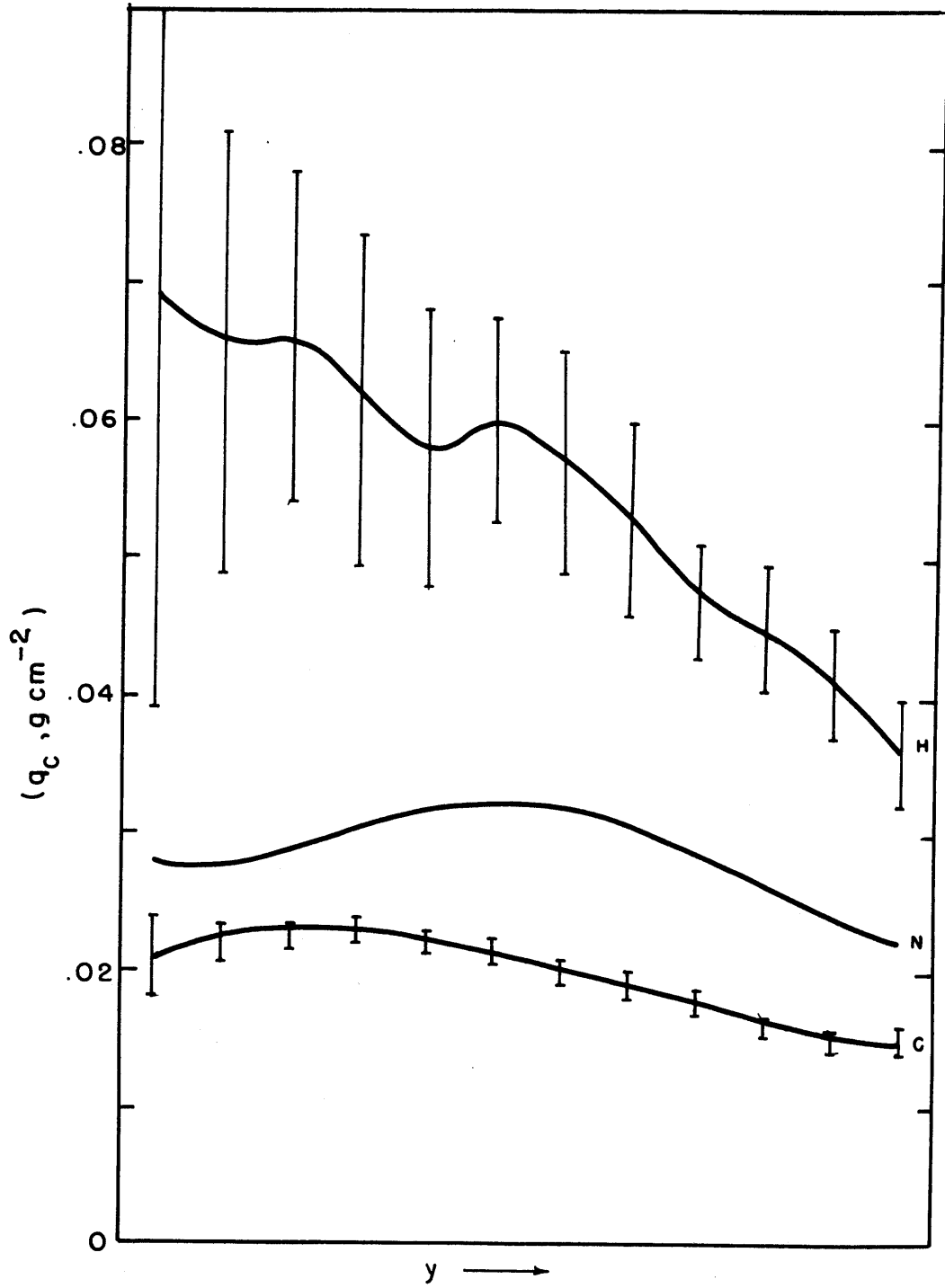


Figure 6.12a. Sensitivity of cloud water in positive condensation regions to the equilibrium temperature.

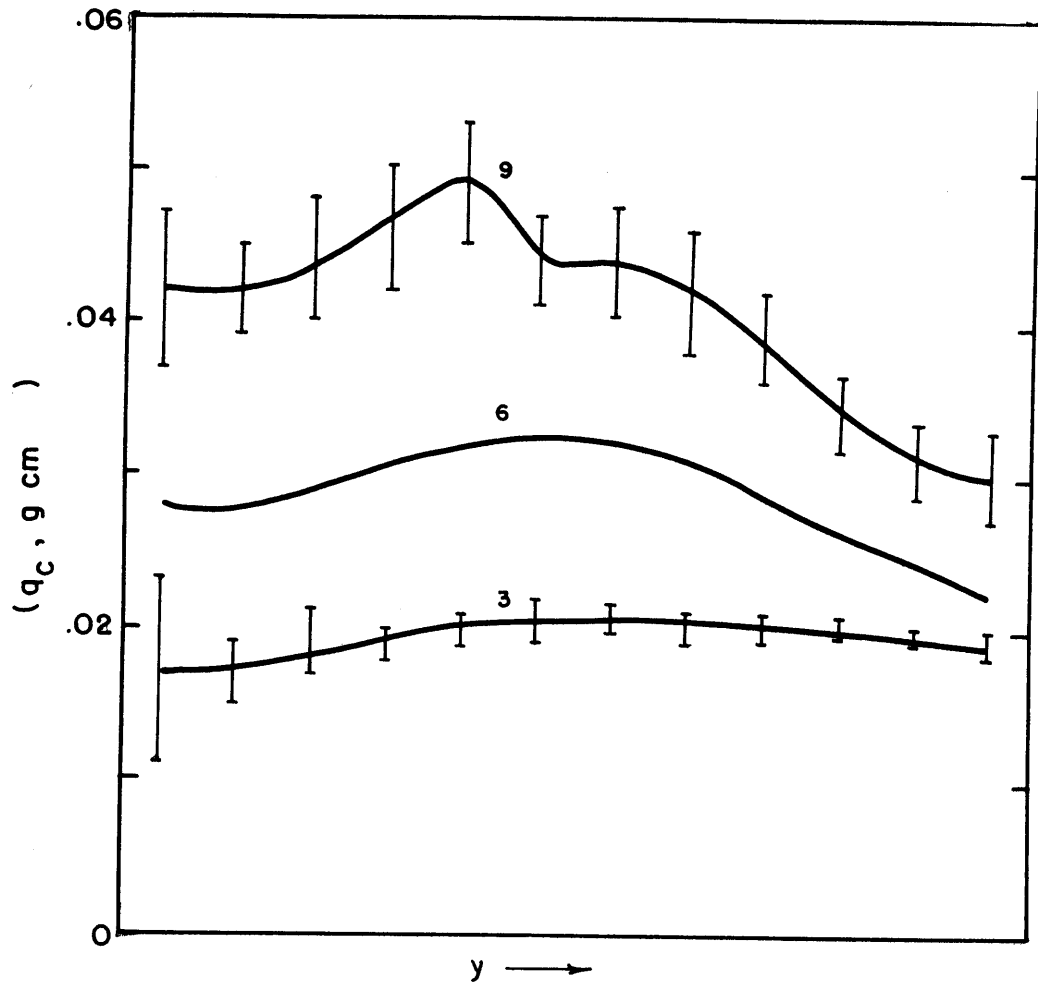


Figure 6.12b. Sensitivity of average cloud water in positive condensation regions to the equilibrium temperature.

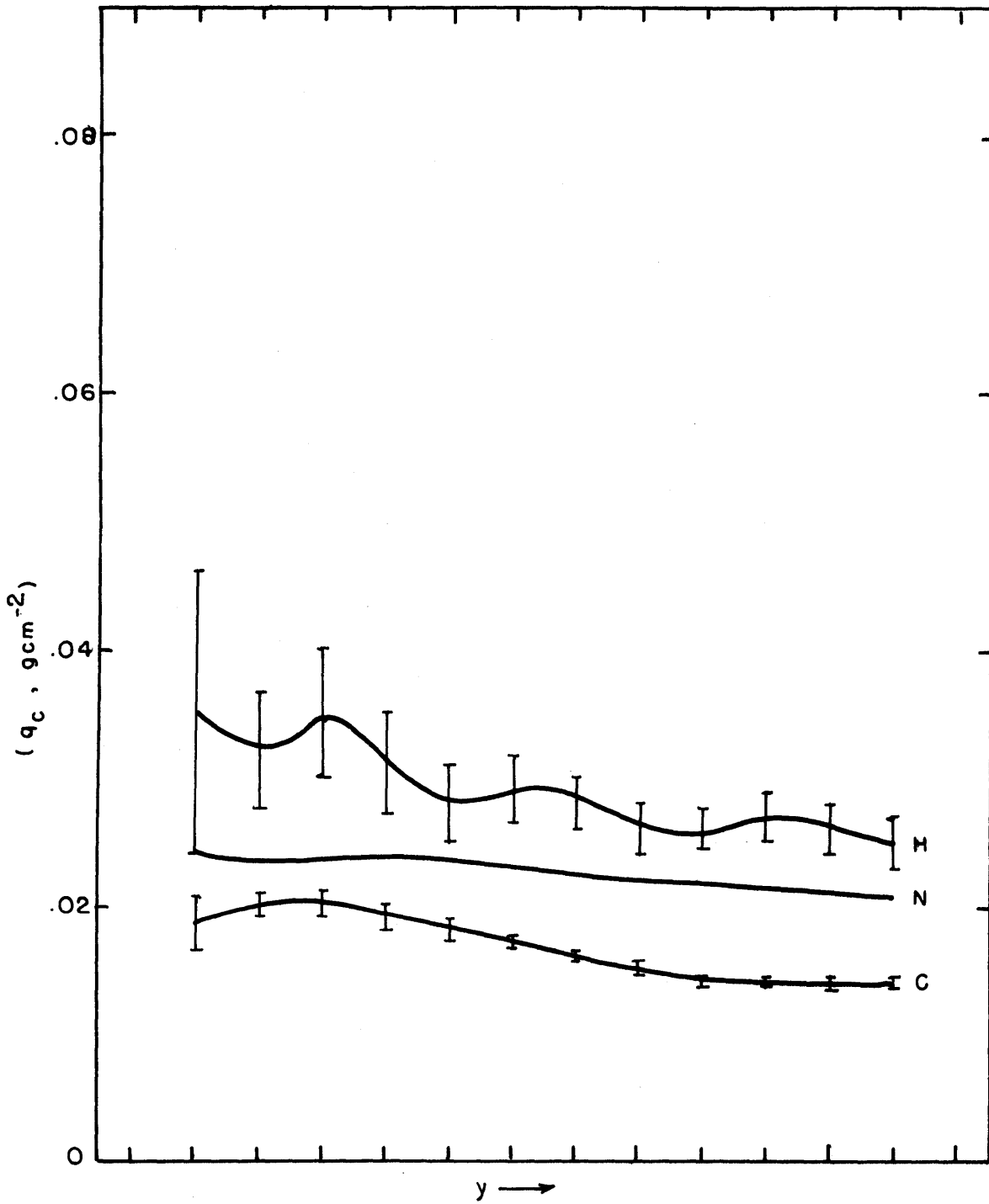


Figure 6.13a. Sensitivity of the average cloud water in the cloudy regions to the equilibrium temperature

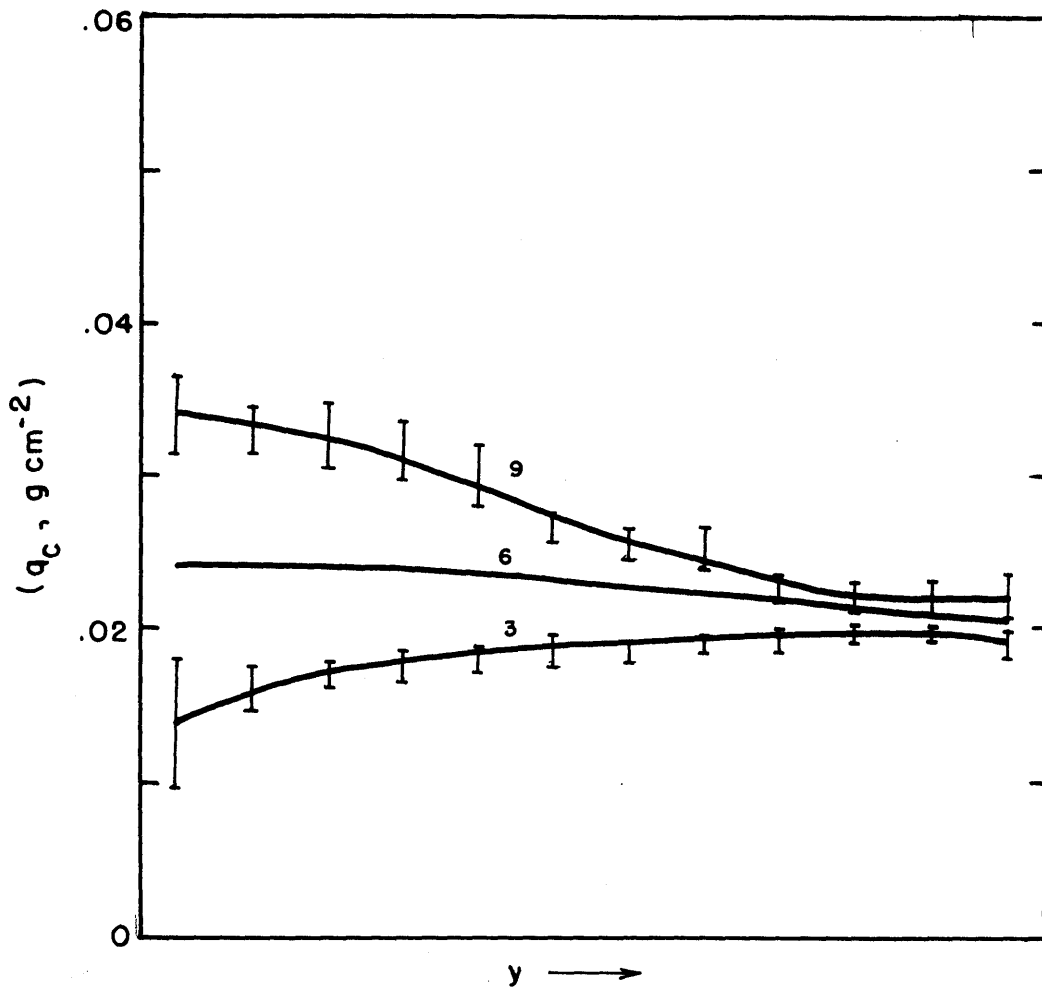


Figure 6.13b. Sensitivity of the average cloud water in the cloudy regions to the equilibrium absolute meridional temperature gradient.

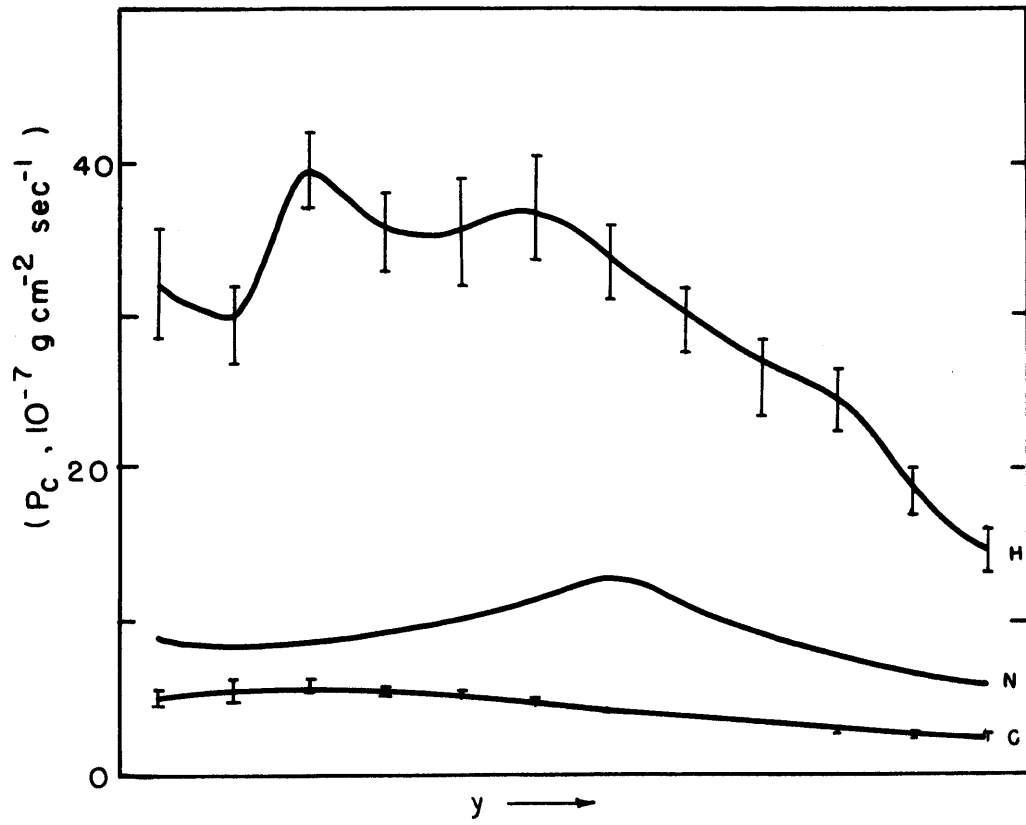


Figure 6.14a. Sensitivity of the precipitation to the equilibrium temperature.

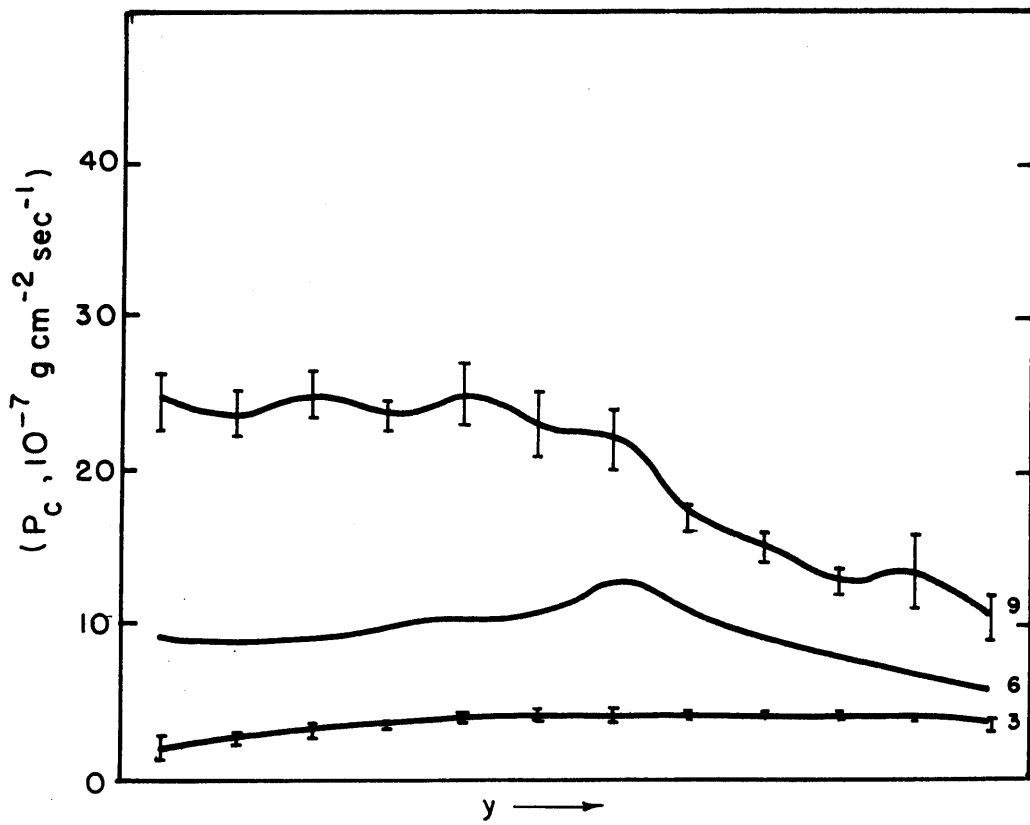


Figure 6.14b. Sensitivity of the precipitation to the equilibrium absolute meridional temperature gradient.

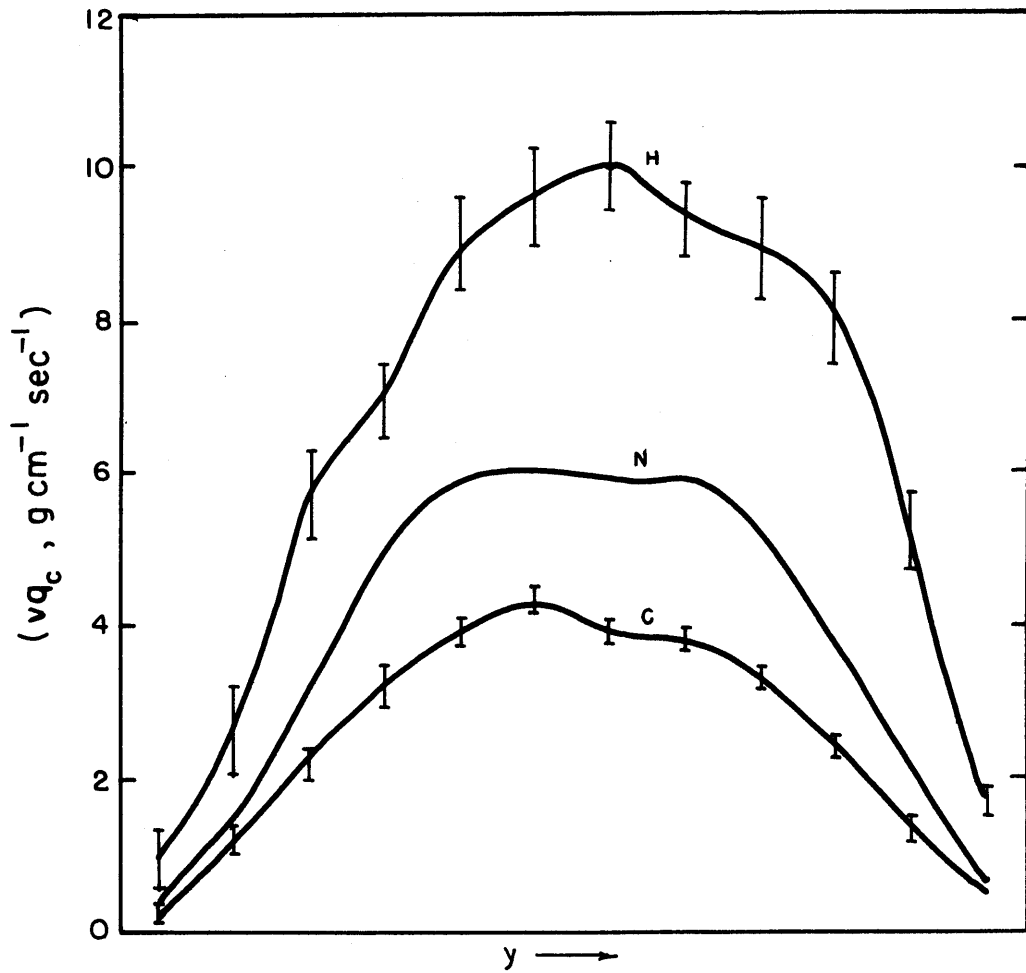


Figure 6.15a. Sensitivity of the meridional transport of cloud water to the equilibrium temperature.

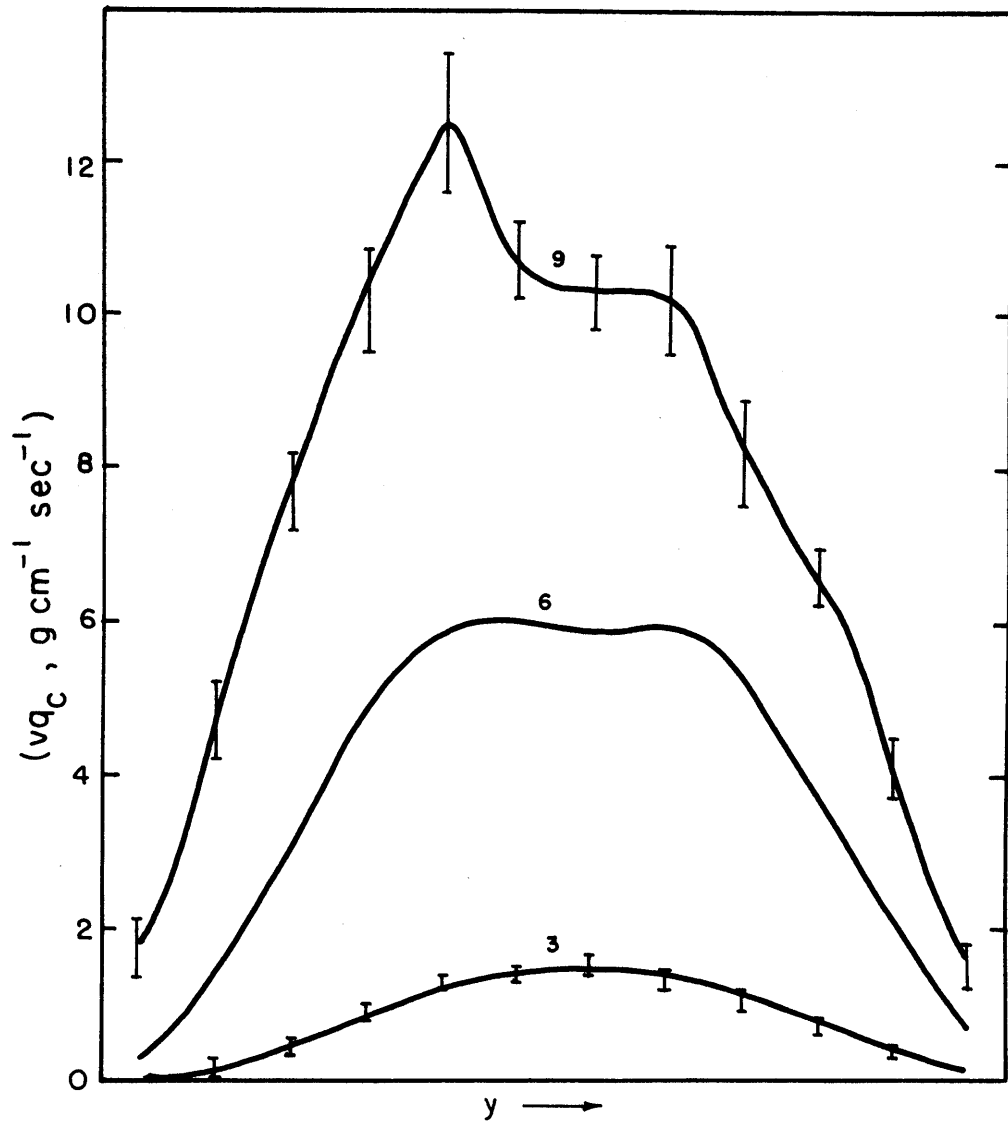


Figure 6.15b. Sensitivity of the meridional transport of cloud water to the equilibrium absolute meridional temperature gradient.

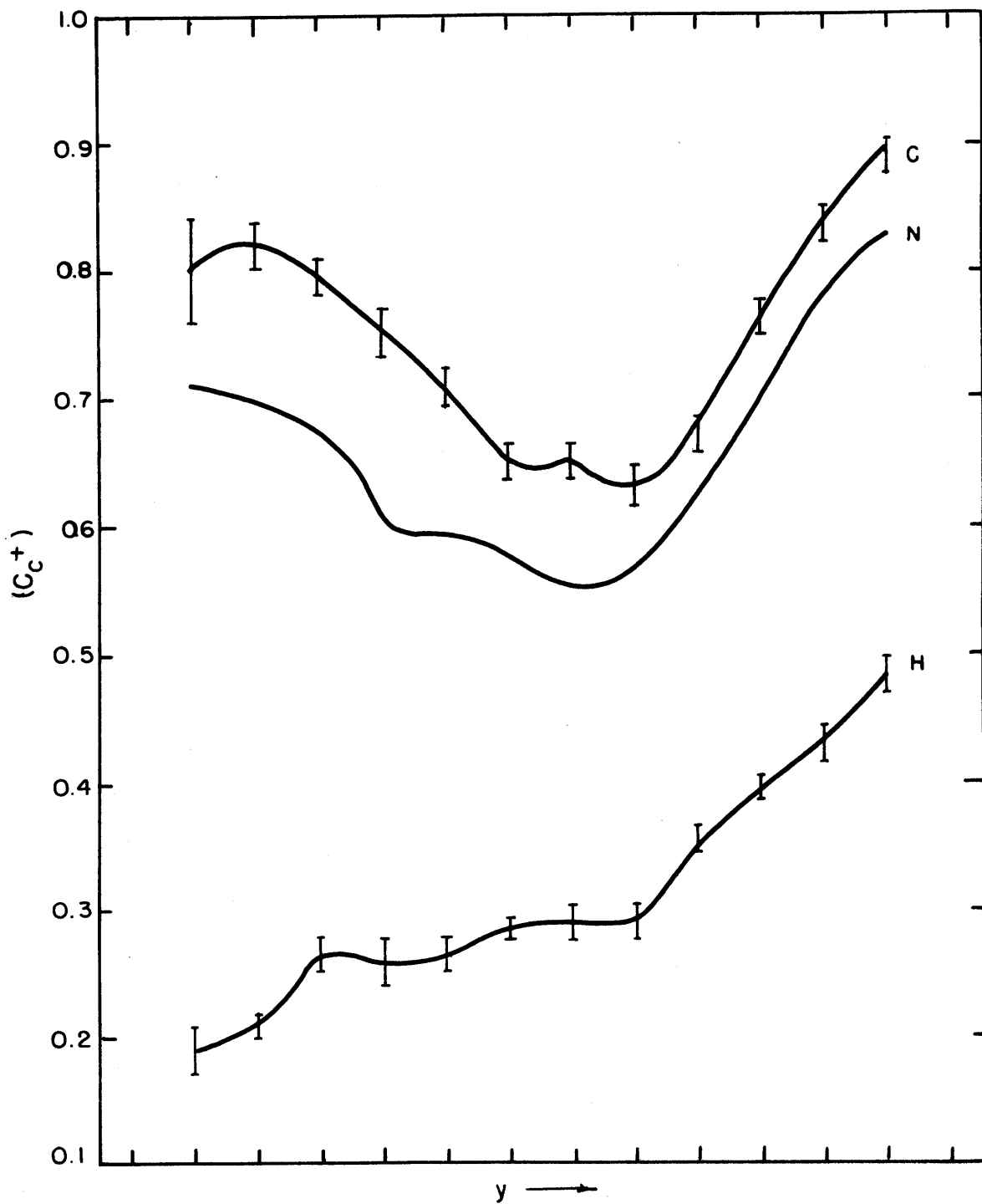


Figure 6.16a. Sensitivity of the fractional coverage of the positive-condensation regions to the equilibrium temperatures

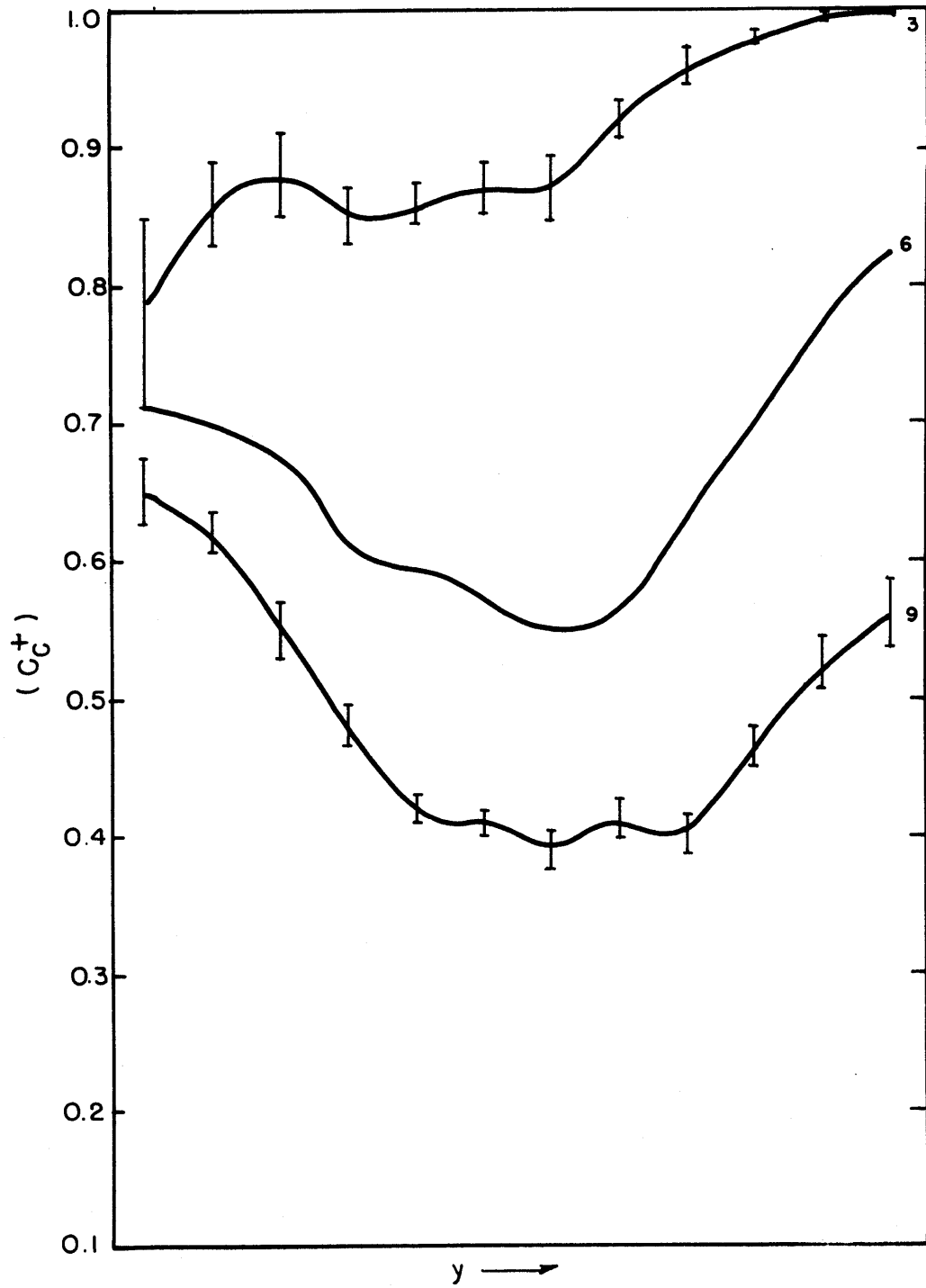


Figure 6.16b. Sensitivity of the fractional coverage of the positive-condensation regions to the equilibrium absolute meridional temperature gradient.

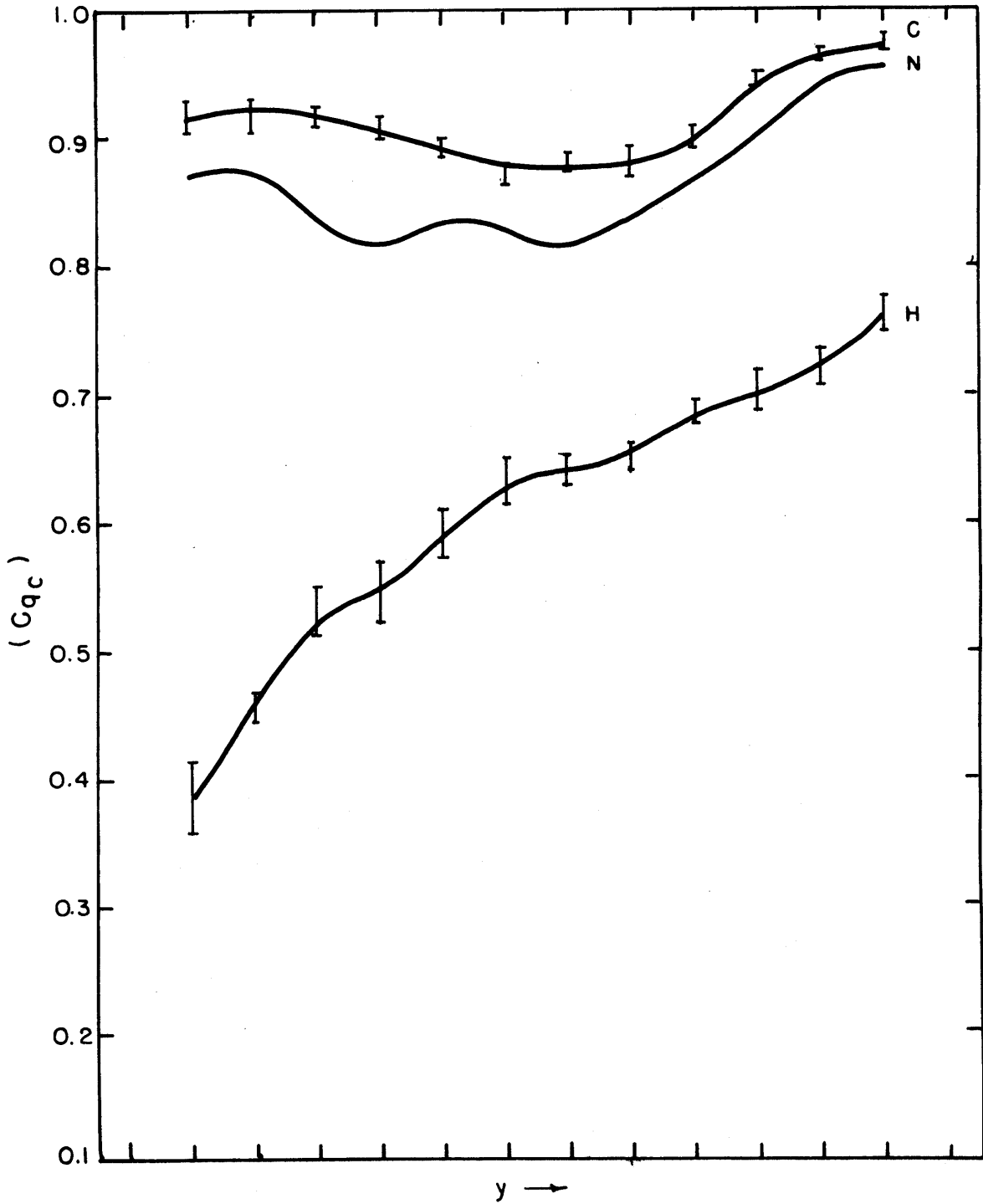


Figure 6.17a. Sensitivity of the total cloud fractional coverage to the equilibrium temperature

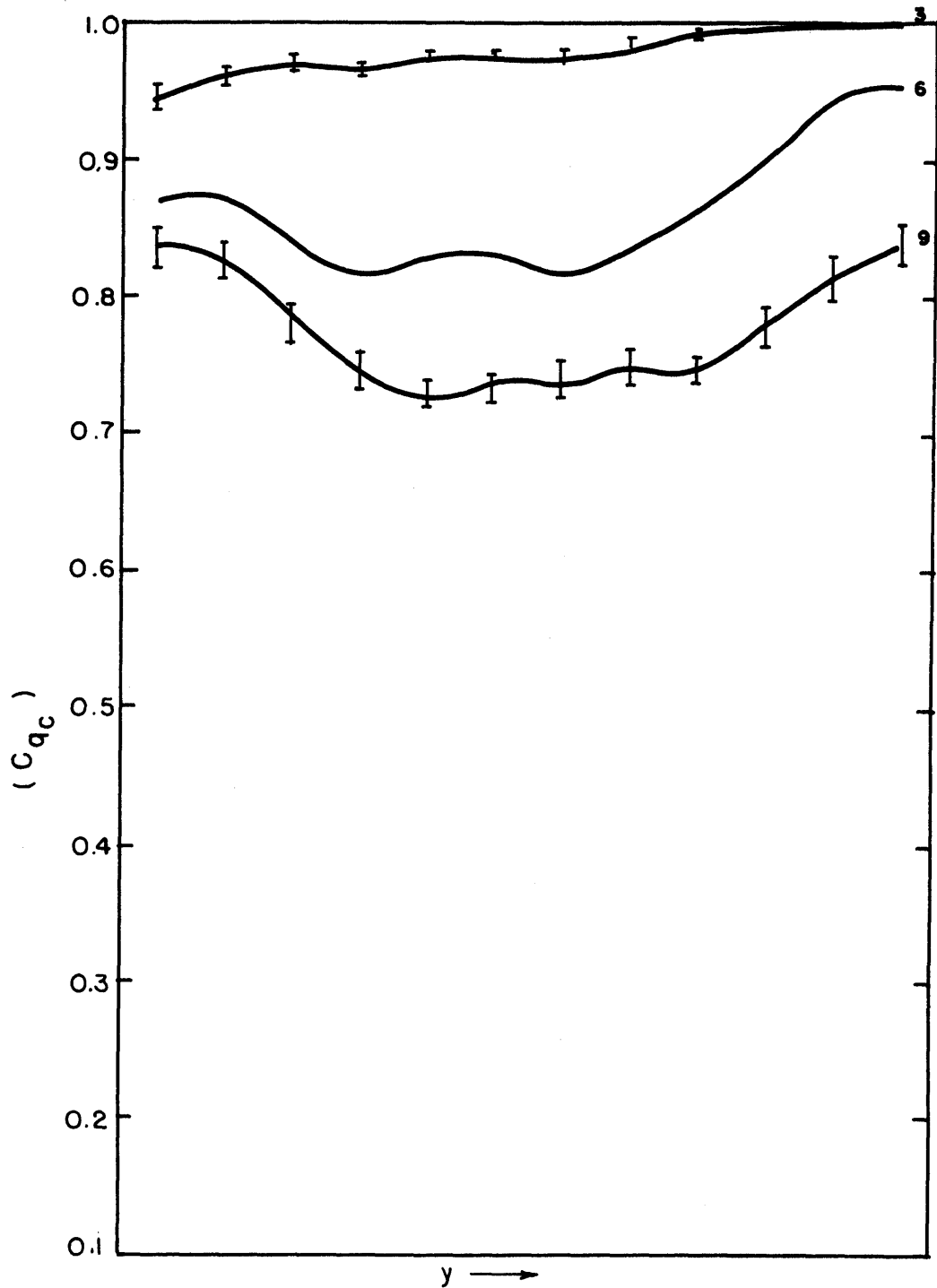


Figure 6.17b. Sensitivity of the total cloud fractional coverage to the equilibrium absolute meridional temperature gradient.

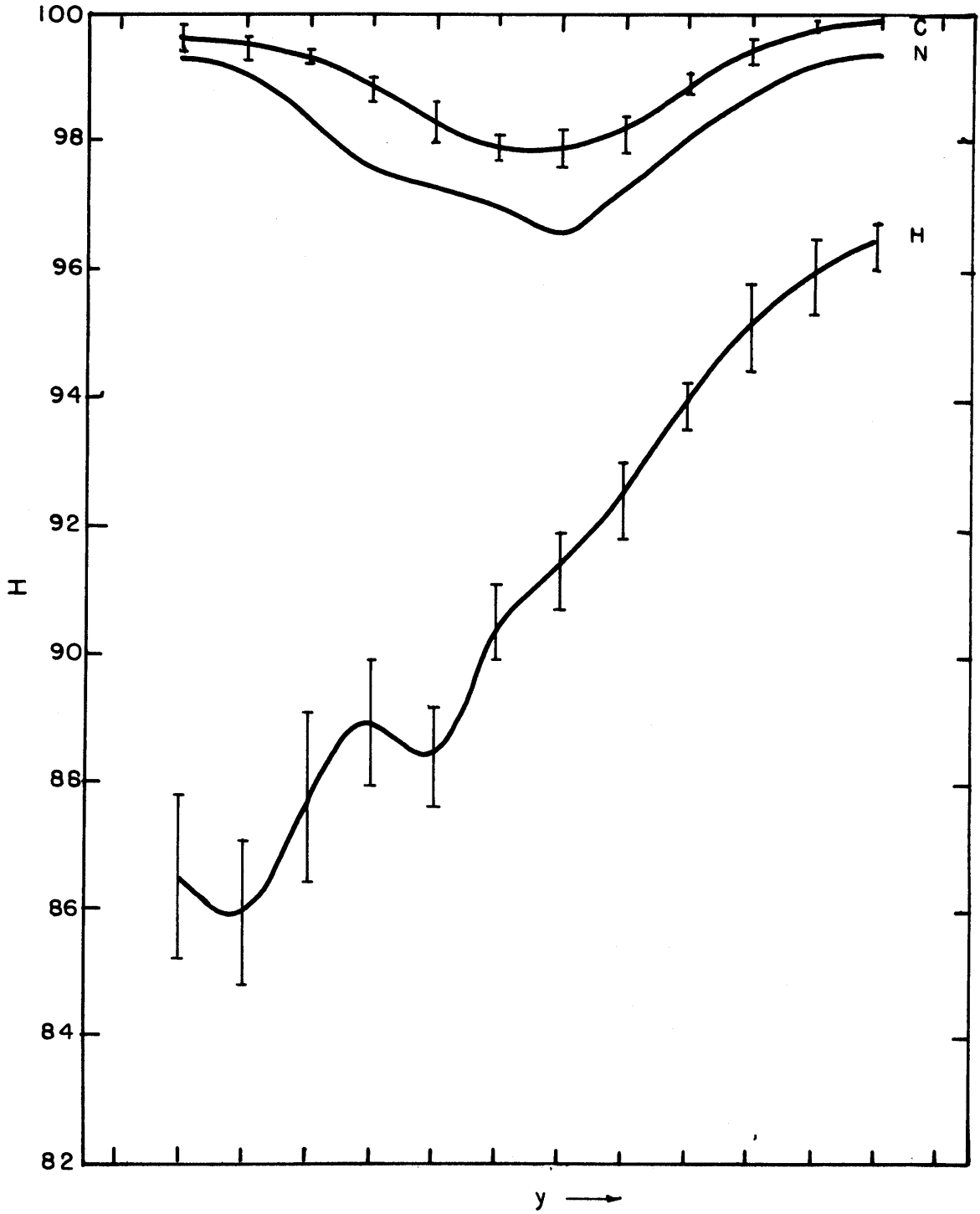


Figure 6.18a. Sensitivity of the relative humidity to the equilibrium temperature.

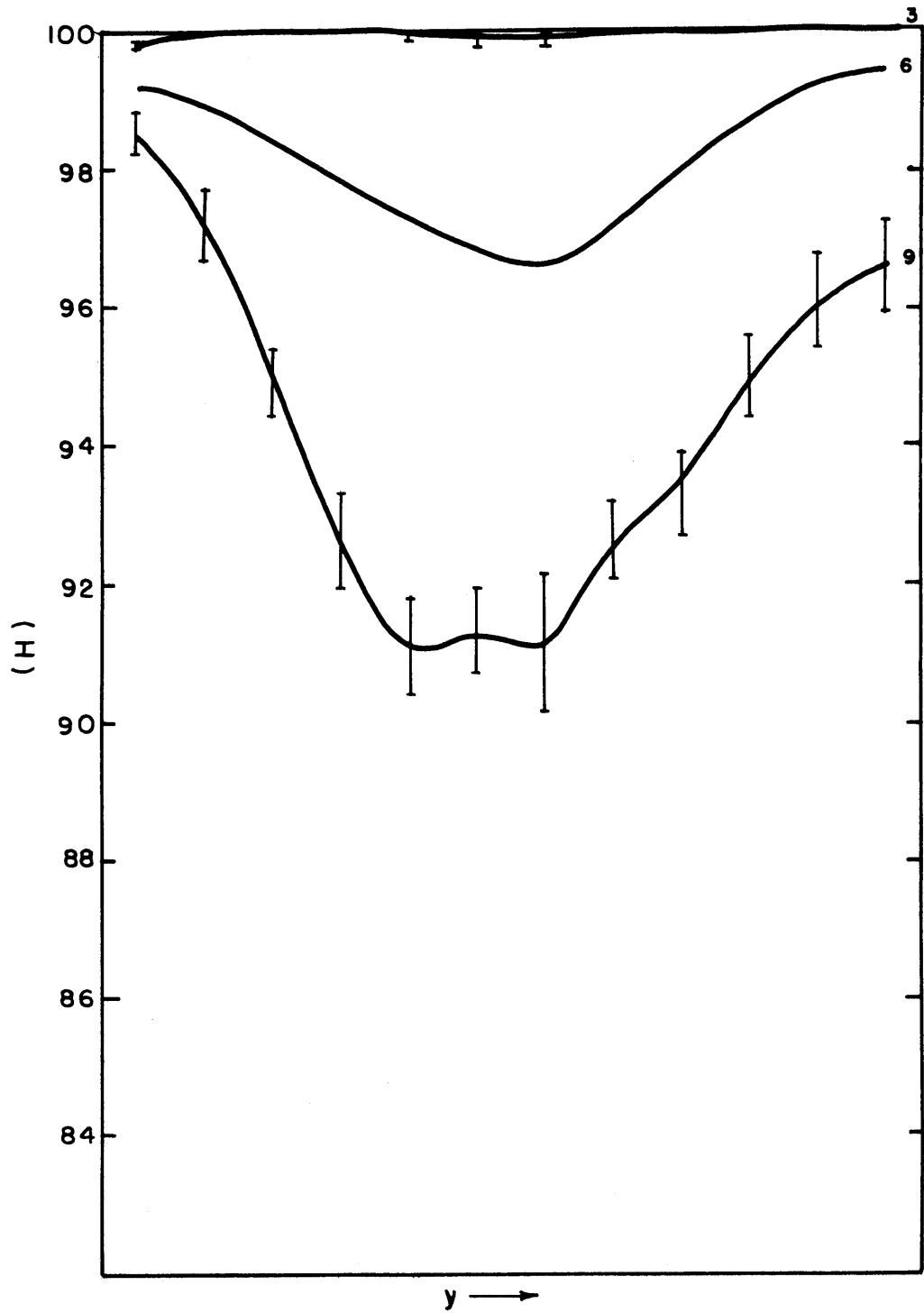


Figure 6.18b. Sensitivity of the relative humidity to the equilibrium absolute meridional temperature gradient.

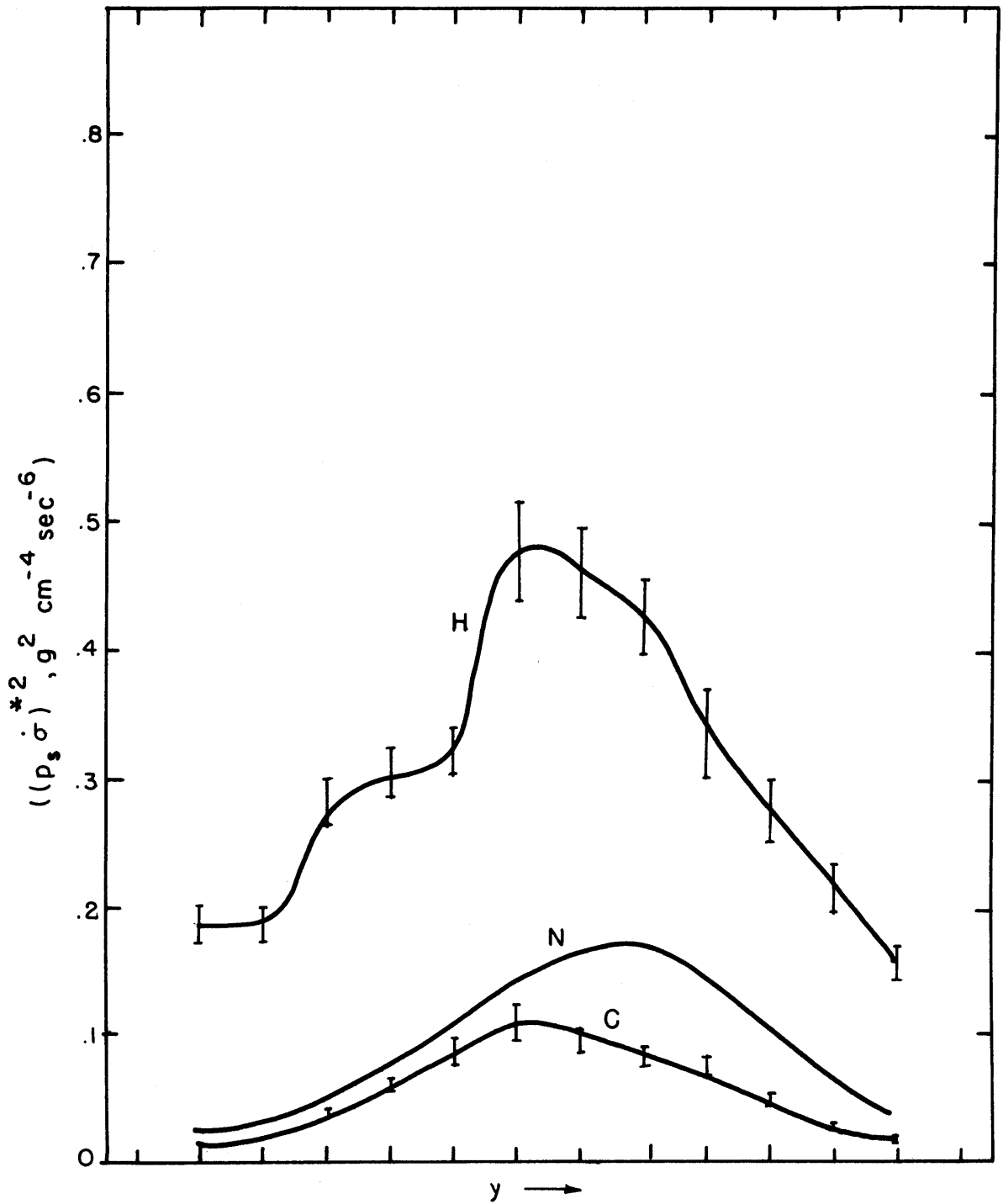


Figure 6.19a. Sensitivity of the eddy vertical velocity to the equilibrium temperature.

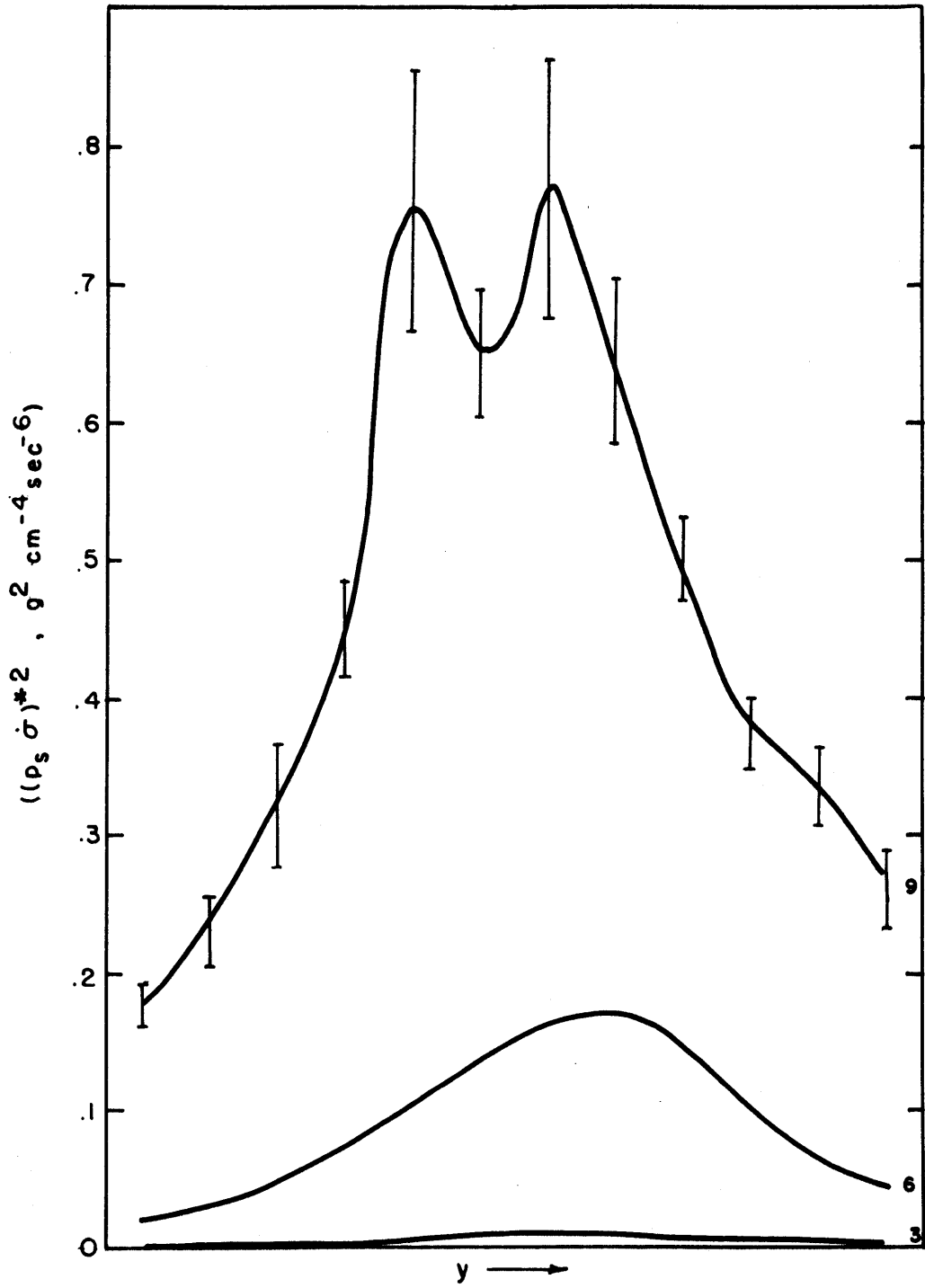


Figure 6.19b. Sensitivity of the eddy vertical velocity to the equilibrium absolute meridional temperature gradient.

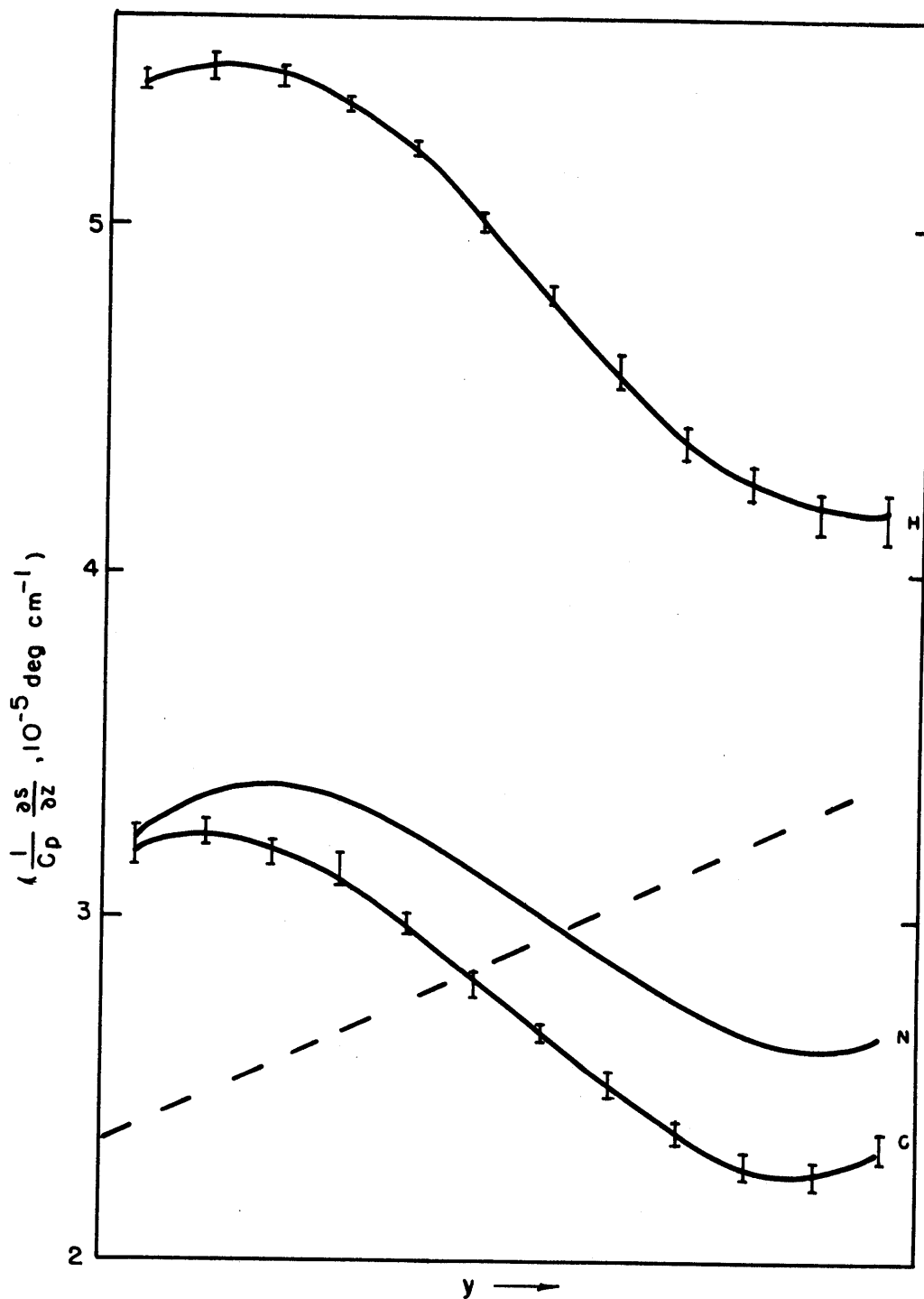


Figure 6.20a. Sensitivity of the atmospheric static stability to the equilibrium temperature.

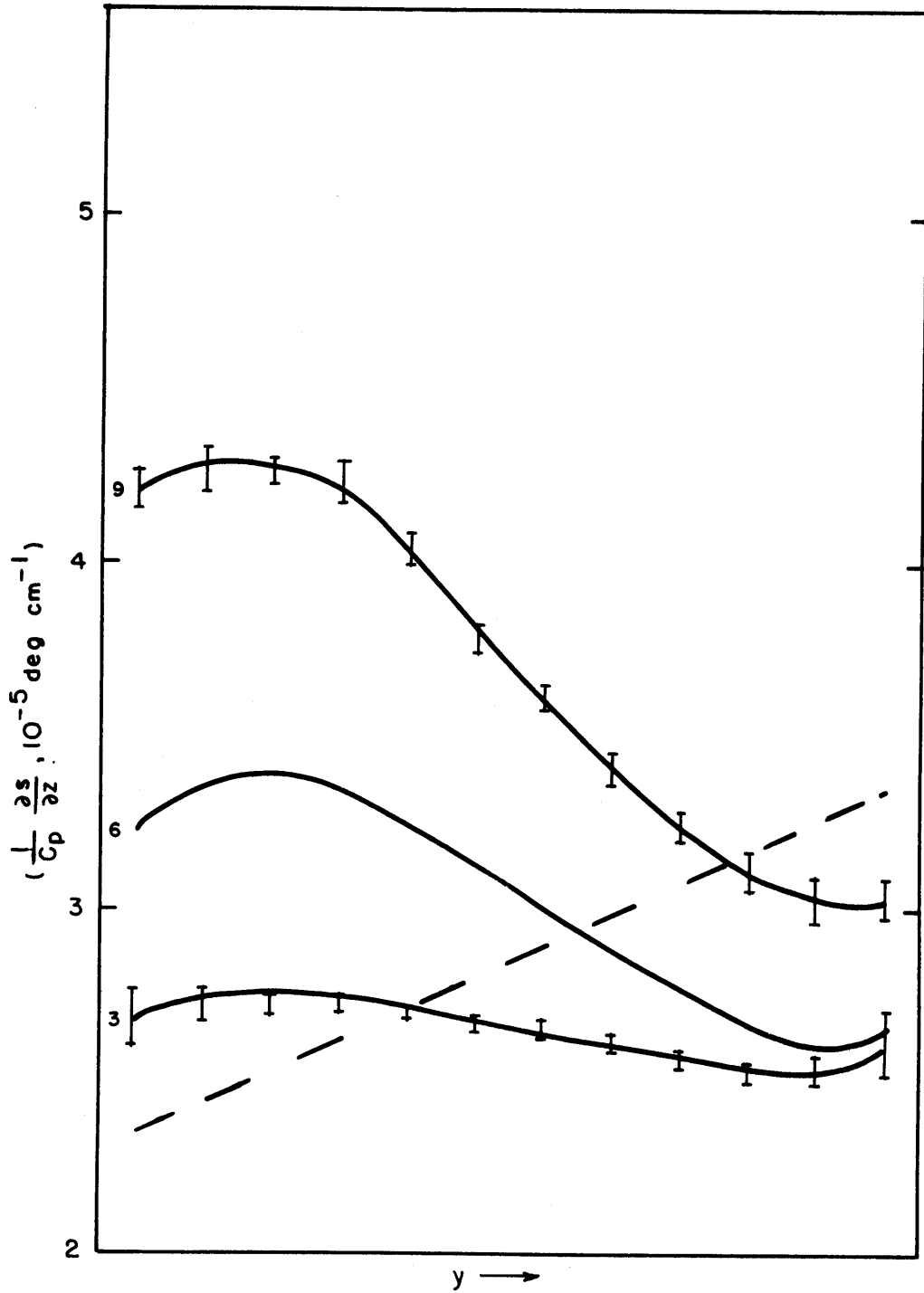


Figure 6.20b. Sensitivity of the static stability to the equilibrium absolute meridional temperature gradient.

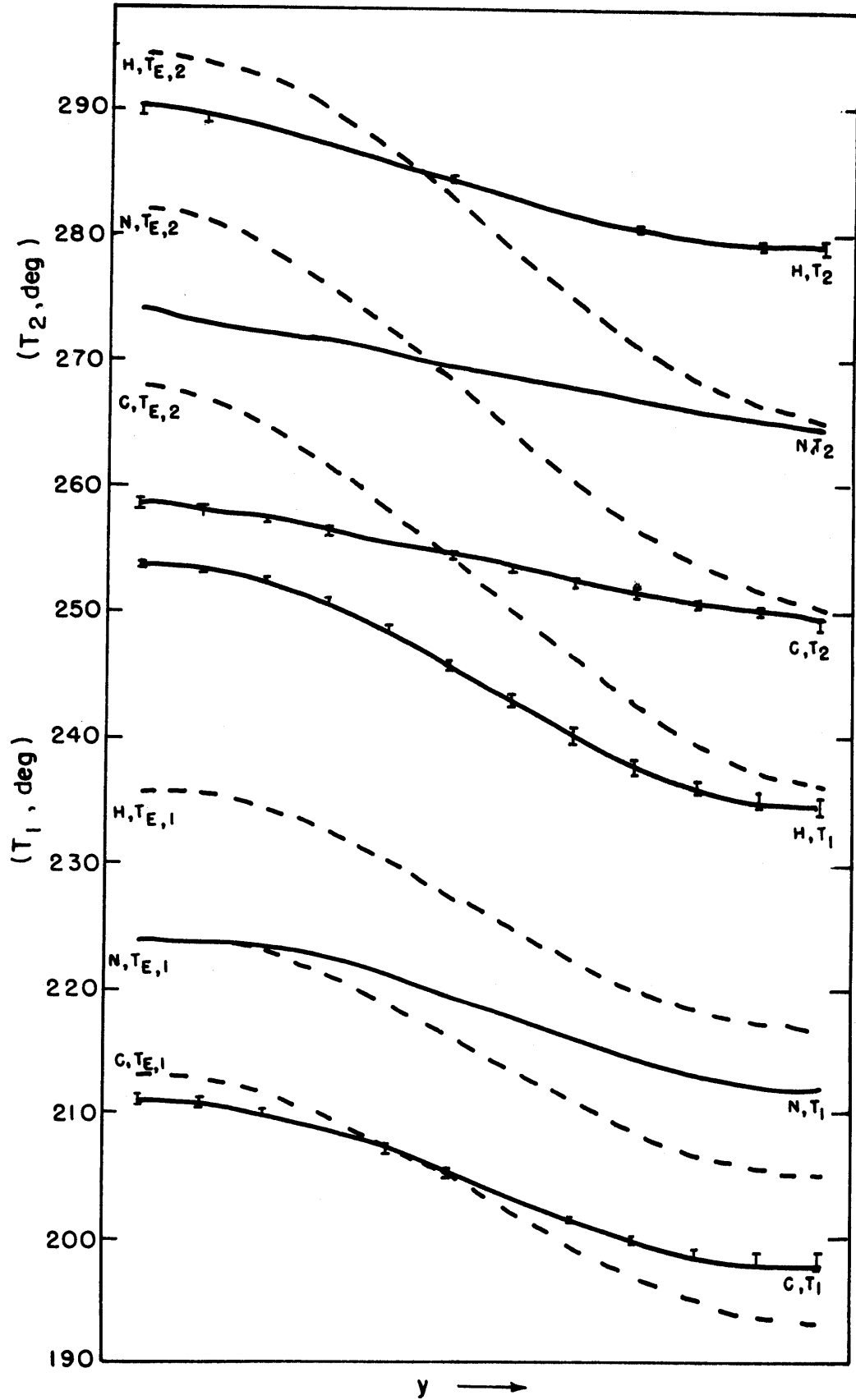


Figure 6.21a. Sensitivity of the upper (1) and lower (2) level temperature to the equilibrium temperature.

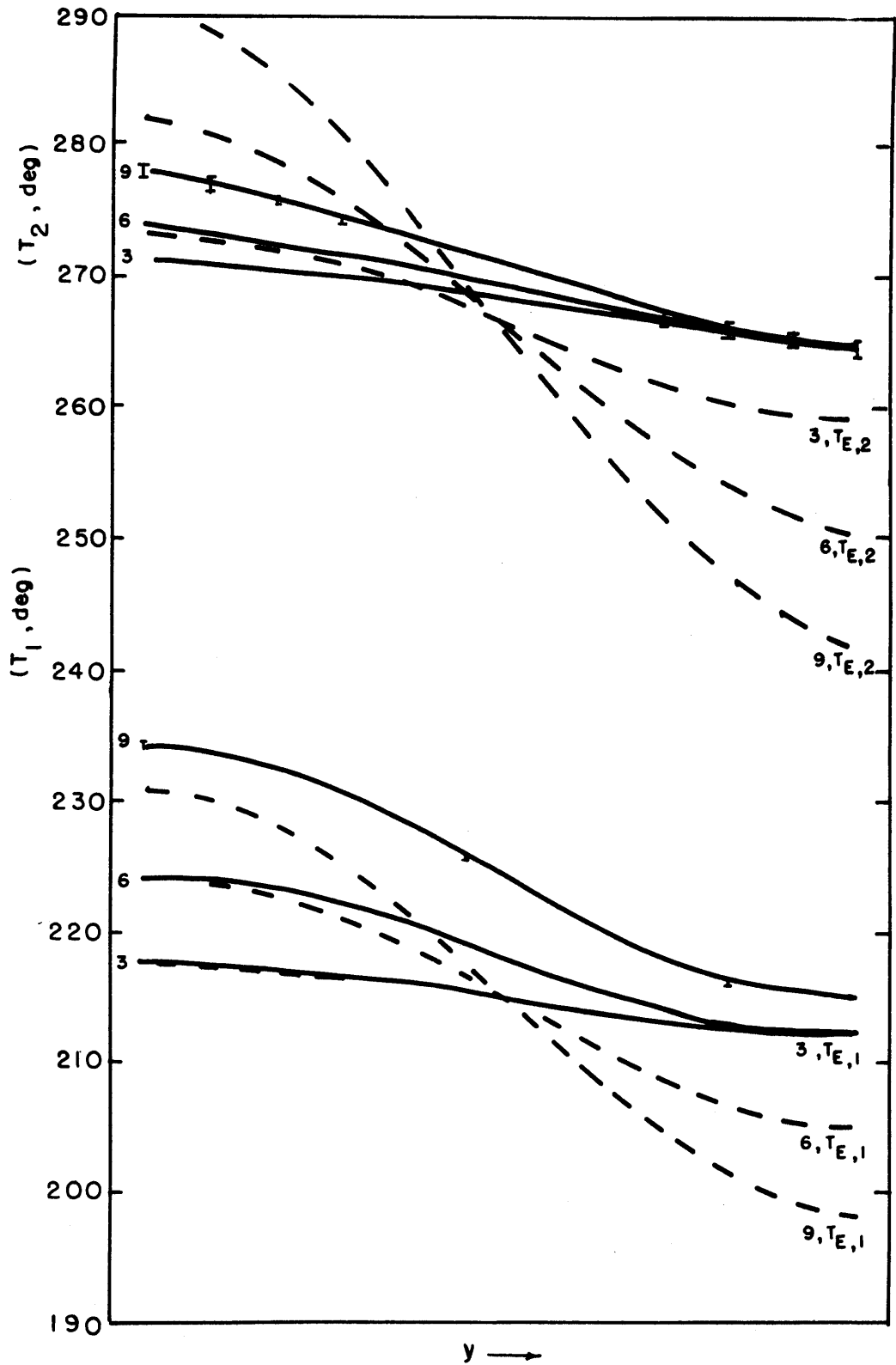


Figure 6.21b. Sensitivity of the upper and lower-level temperatures to the equilibrium absolute meridional temperature gradient.

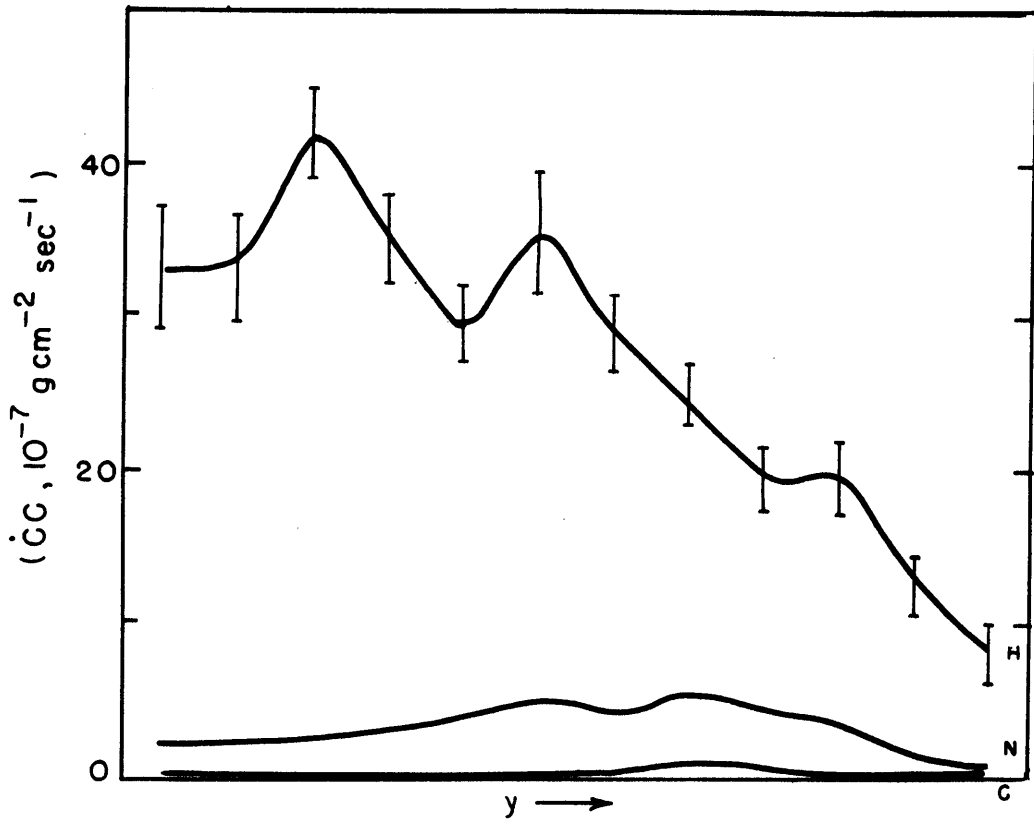


Figure 6.22a. Sensitivity of the convective condensation to the equilibrium temperature.

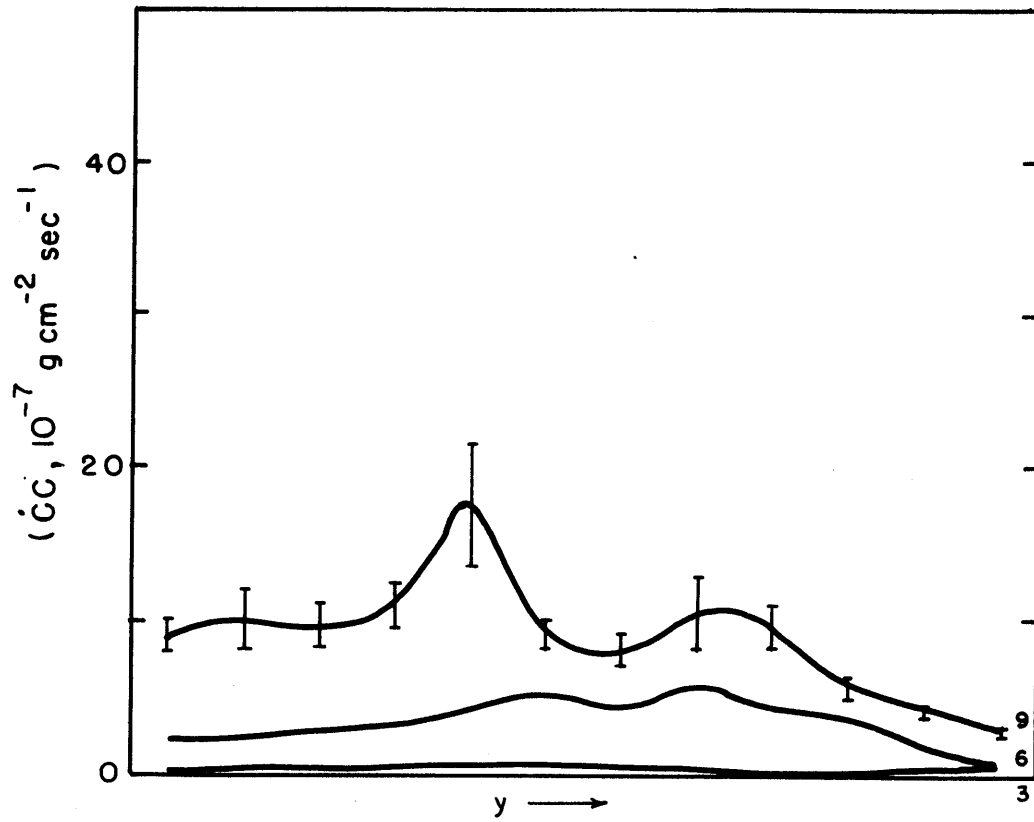


Figure 6.22b. Sensitivity of the convective condensation to the equilibrium absolute meridional temperature gradient.

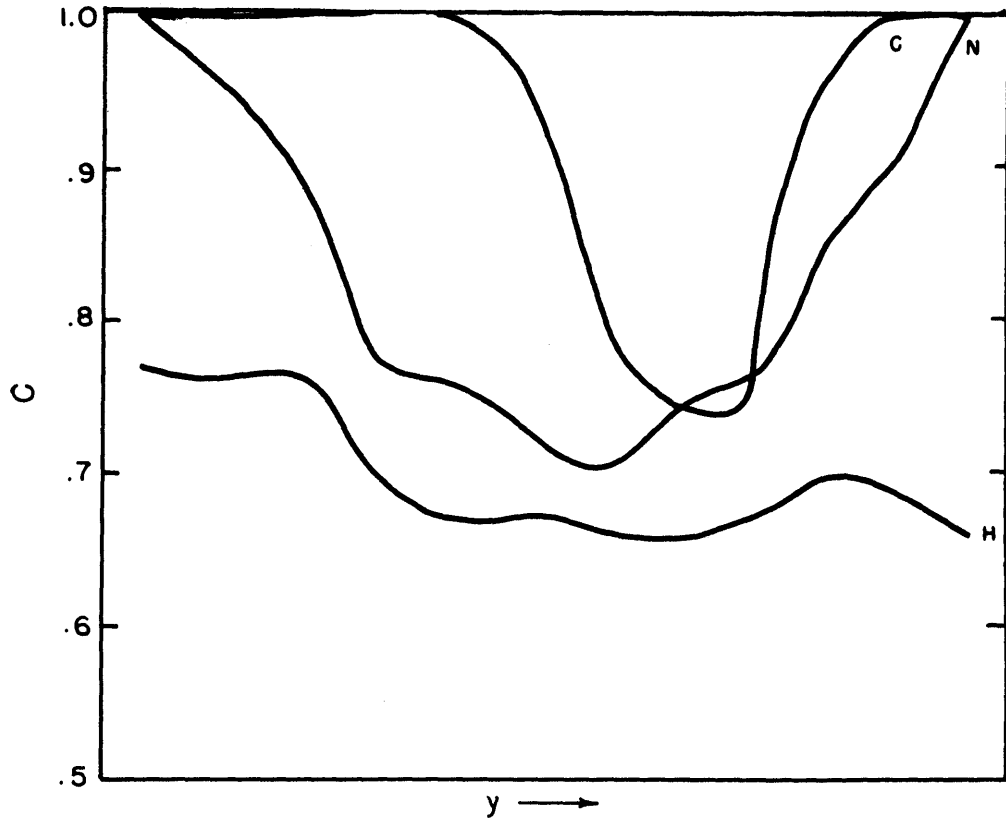


Figure 6.23a. Sensitivity of $C = 1 - \frac{\cos^{-1}(B/W)}{\pi}$ to the equilibrium temperature.

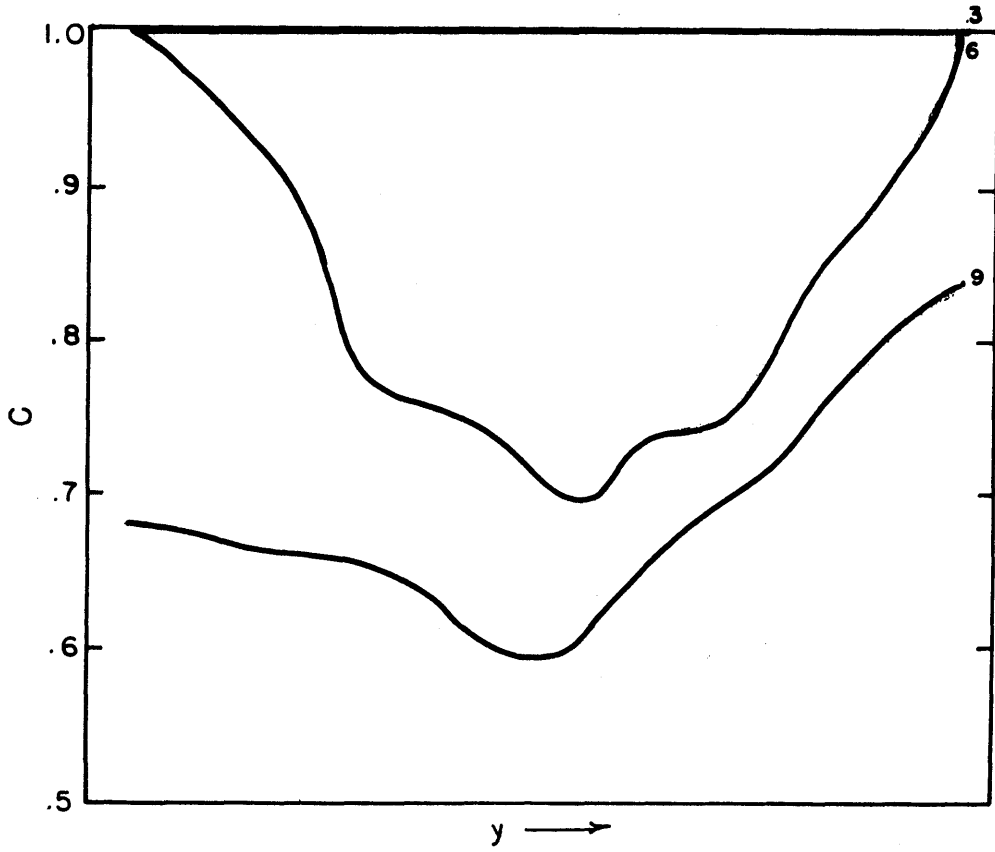


Figure 6.23b. Sensitivity of $C = 1 - \frac{\cos^{-1}(B/W)}{\pi}$ to the equilibrium absolute meridional temperature gradient.

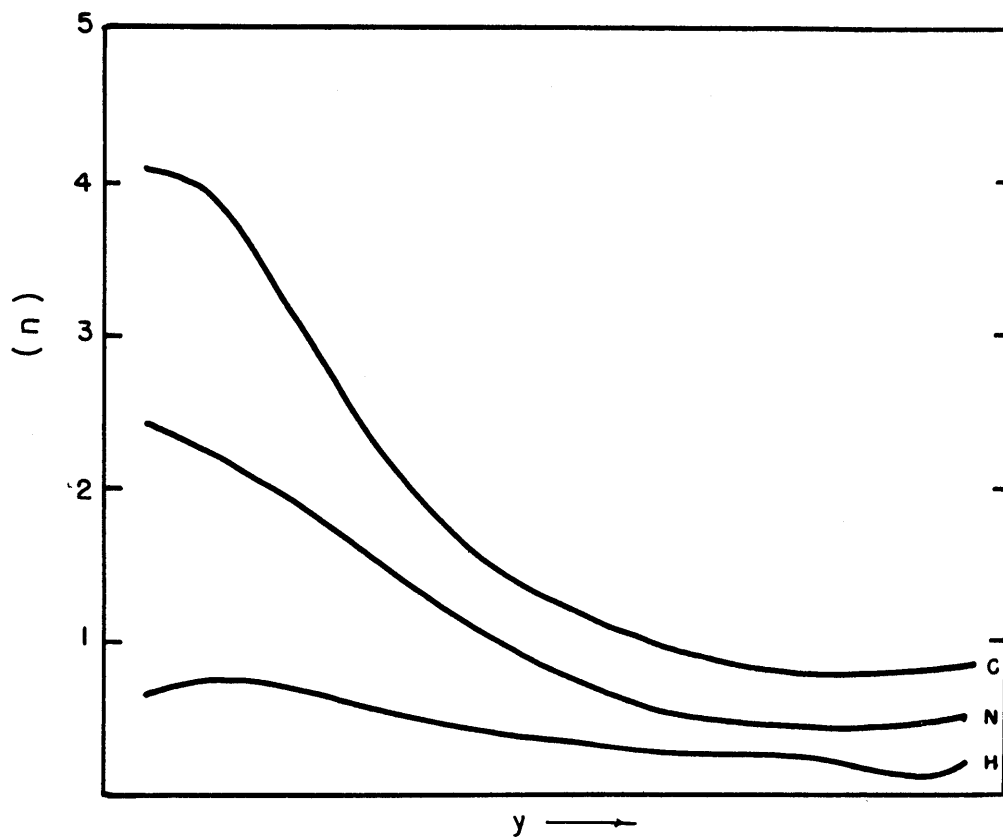


Figure 6.24a. Sensitivity to η to the equilibrium temperature. η is a measure of the ratio of the surface turbulent transport to the atmospheric transport and adiabatic heating.

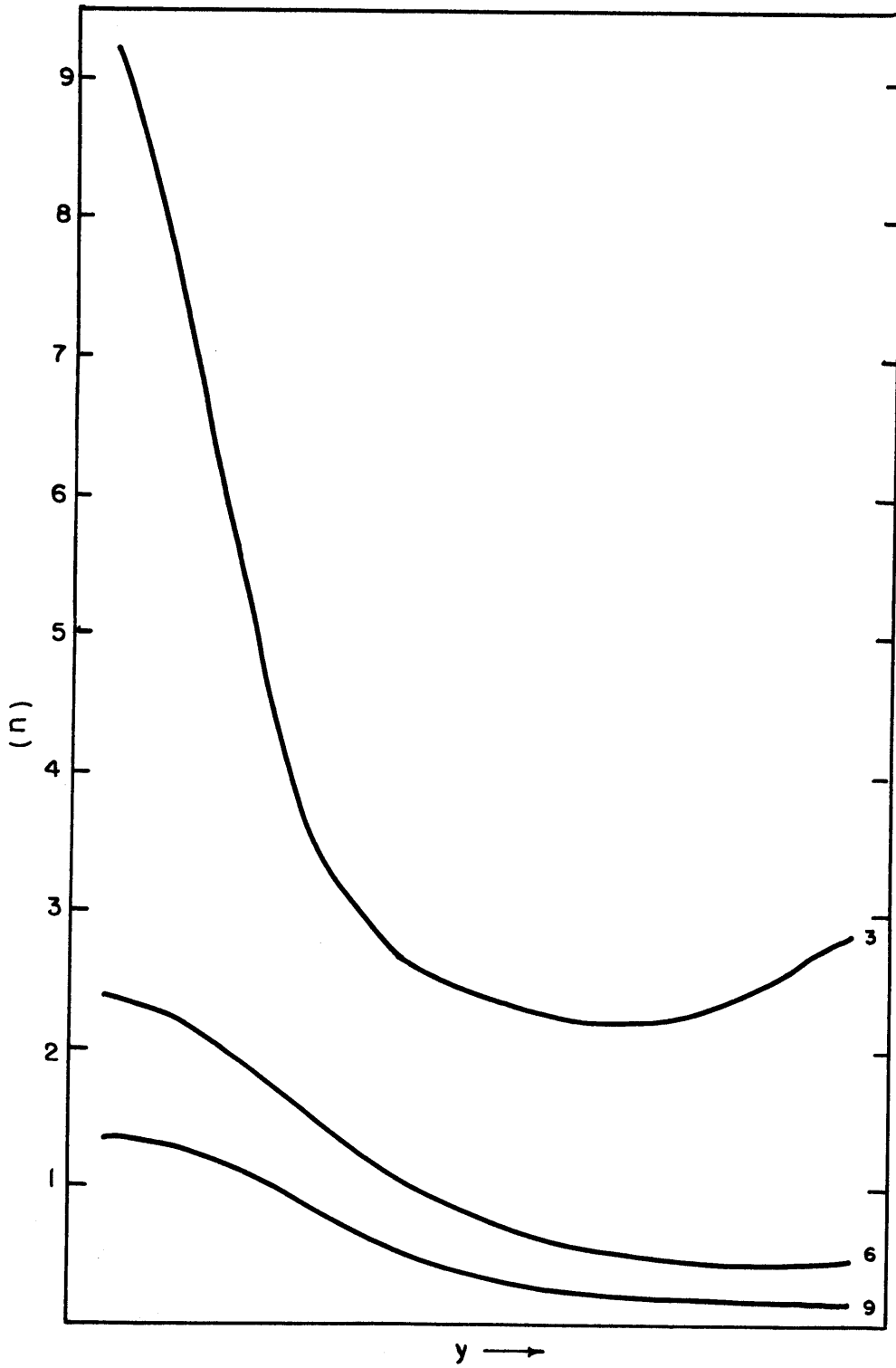


Figure 6.24b. Sensivity of η to the equilibrium absolute meridional temperature gradient.

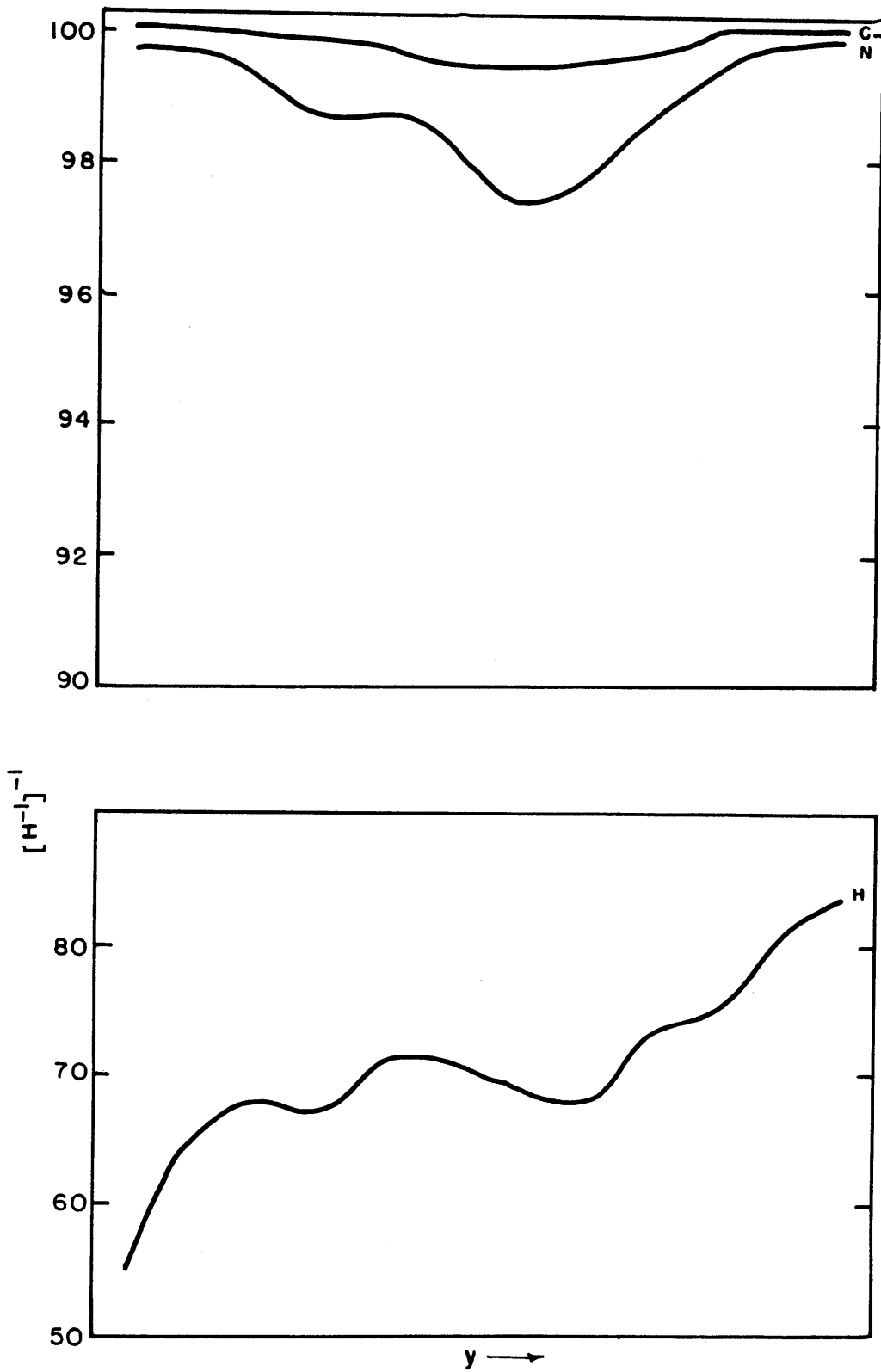


Figure 6.25a. Sensivity of $[H^{-1}]^{-1} = [1 + \frac{1}{\eta}(\frac{\sin\pi C}{\pi} + (1-C)\cos\pi C)]^{-1}$ to the equilibrium temperature.

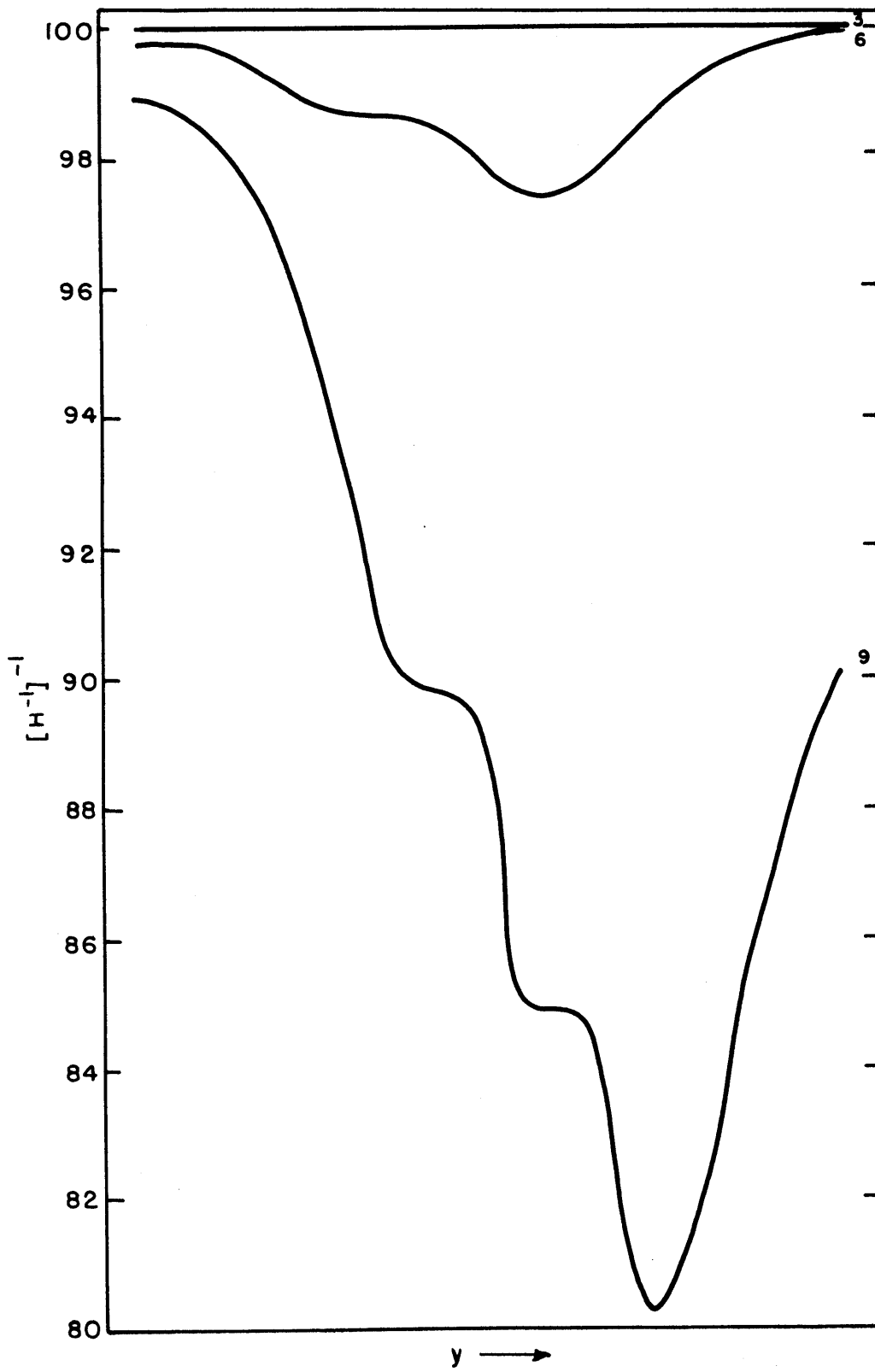


Figure 6.25b. Sensivity of $[H^{-1}]^{-1} = [1 + \frac{1}{\eta}(\frac{\sin \pi C}{\pi} + (1-C)\cos \pi C)]^{-1}$ to the equilibrium absolute meridional temperature gradient.

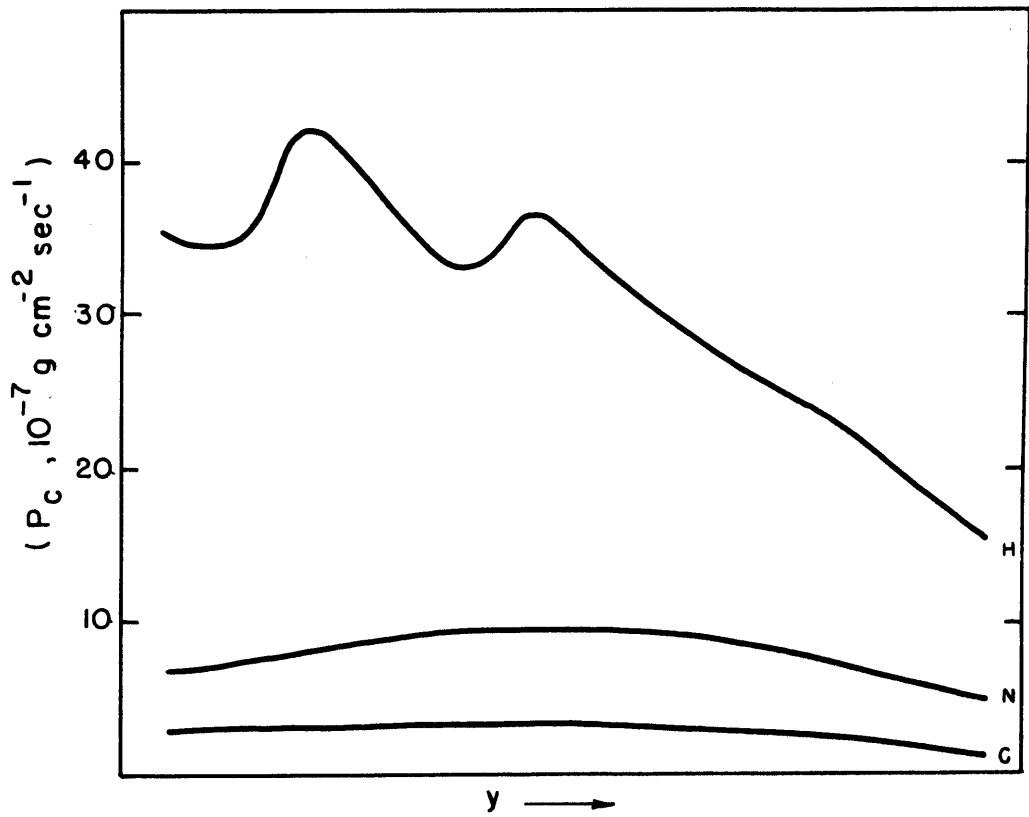


Figure 6.26a. Sensitivity of the calculated precipitation rate of the equilibrium temperature.

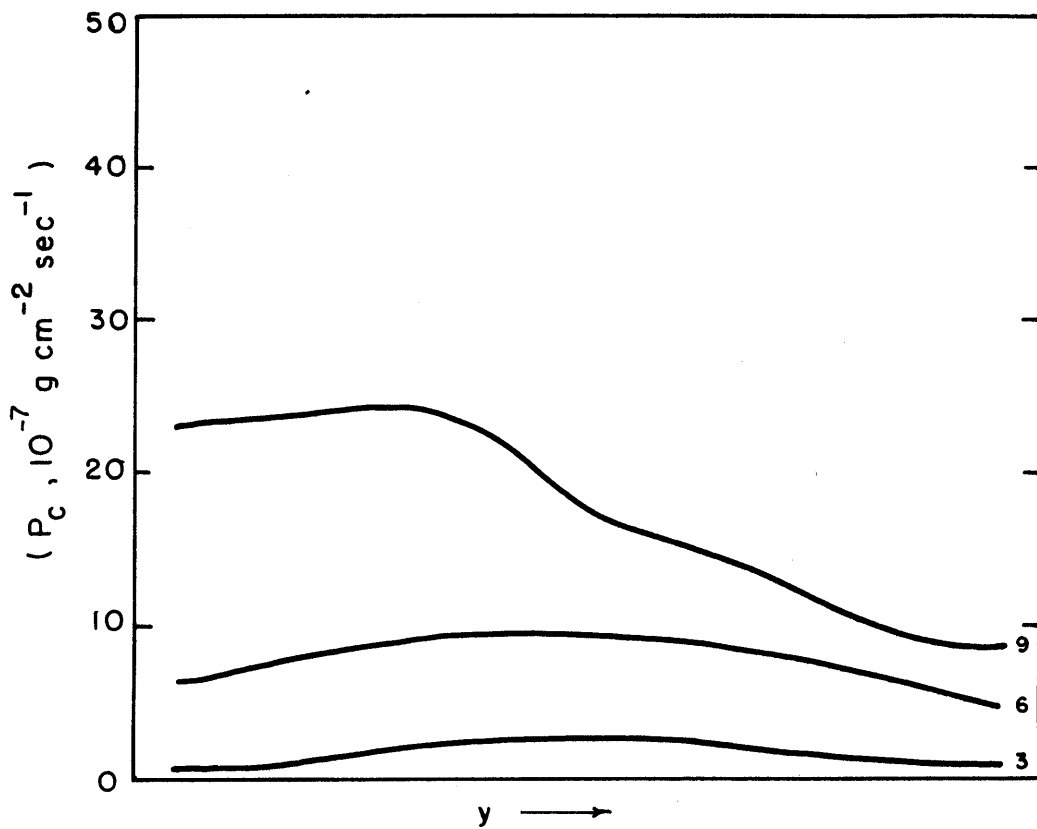


Figure 6.26b. Sensitivity of the calculated precipitation to the equilibrium absolute meridional temperature gradient.

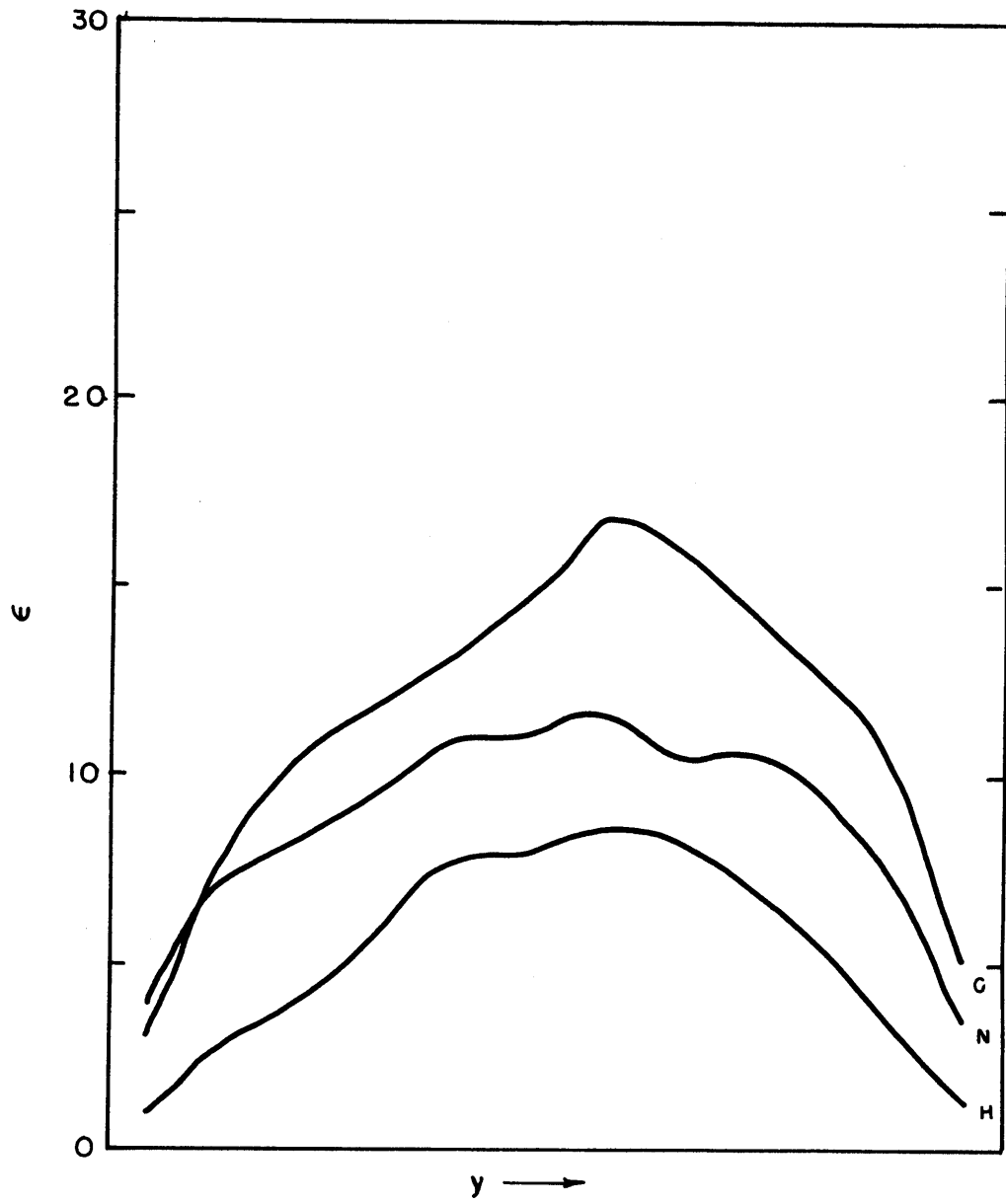


Figure 6.27a. Sensitivity of ϵ to the equilibrium temperature.

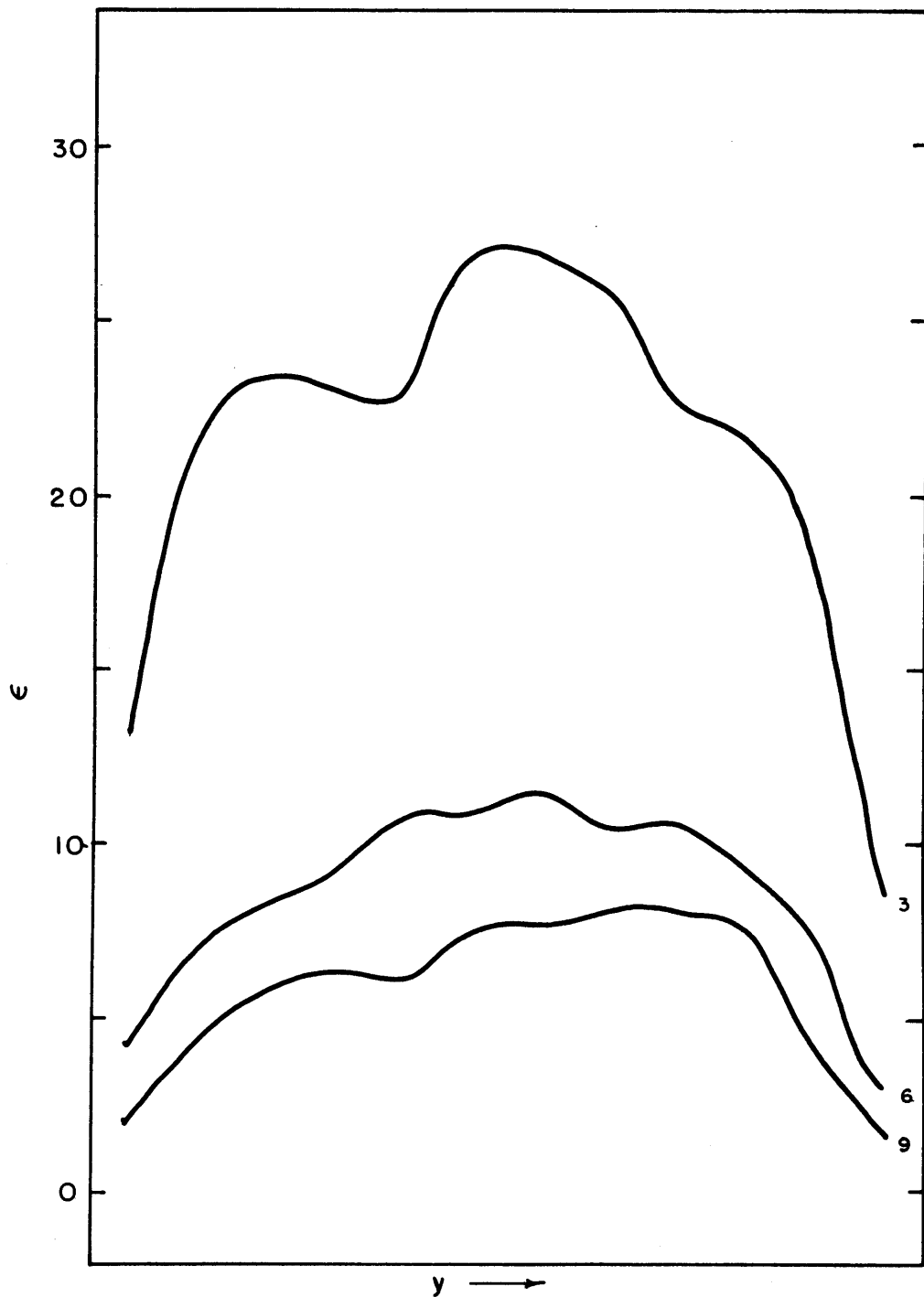


Figure 6.27b. Sensitivity of ϵ to the equilibrium absolute meridional temperature gradient.

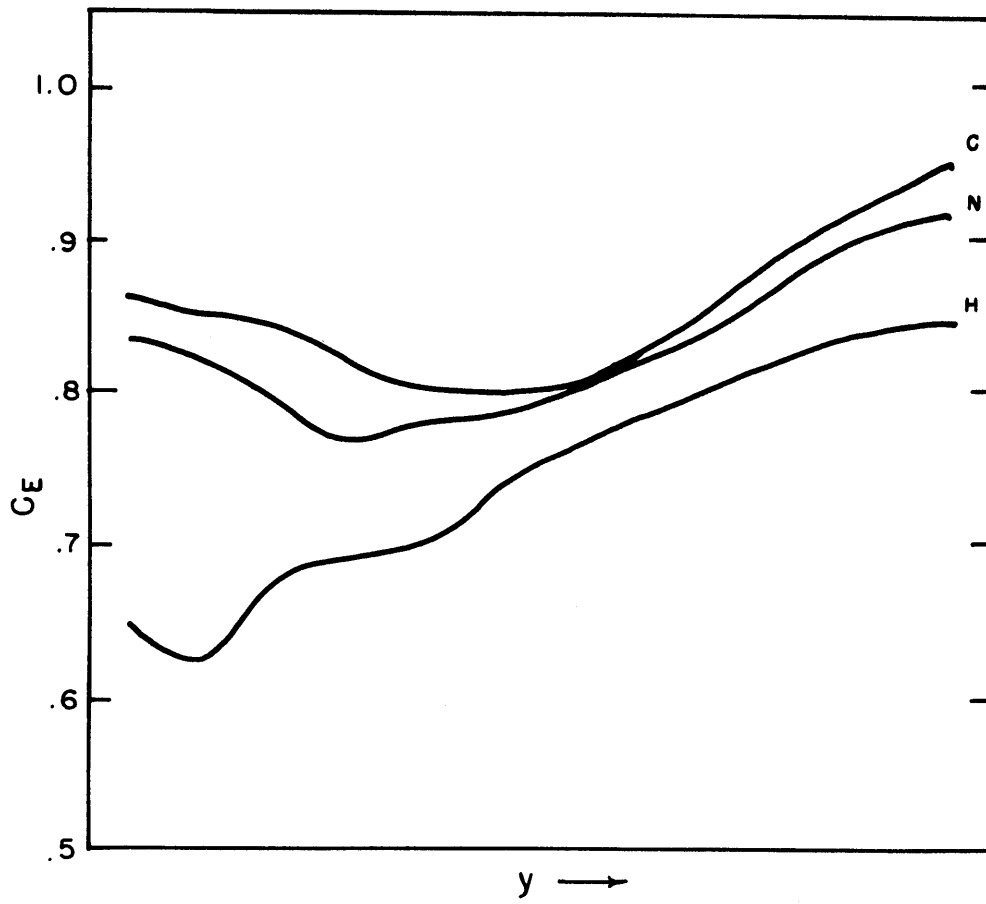


Figure 6.28a. Sensitivity of C_E to the equilibrium temperature.

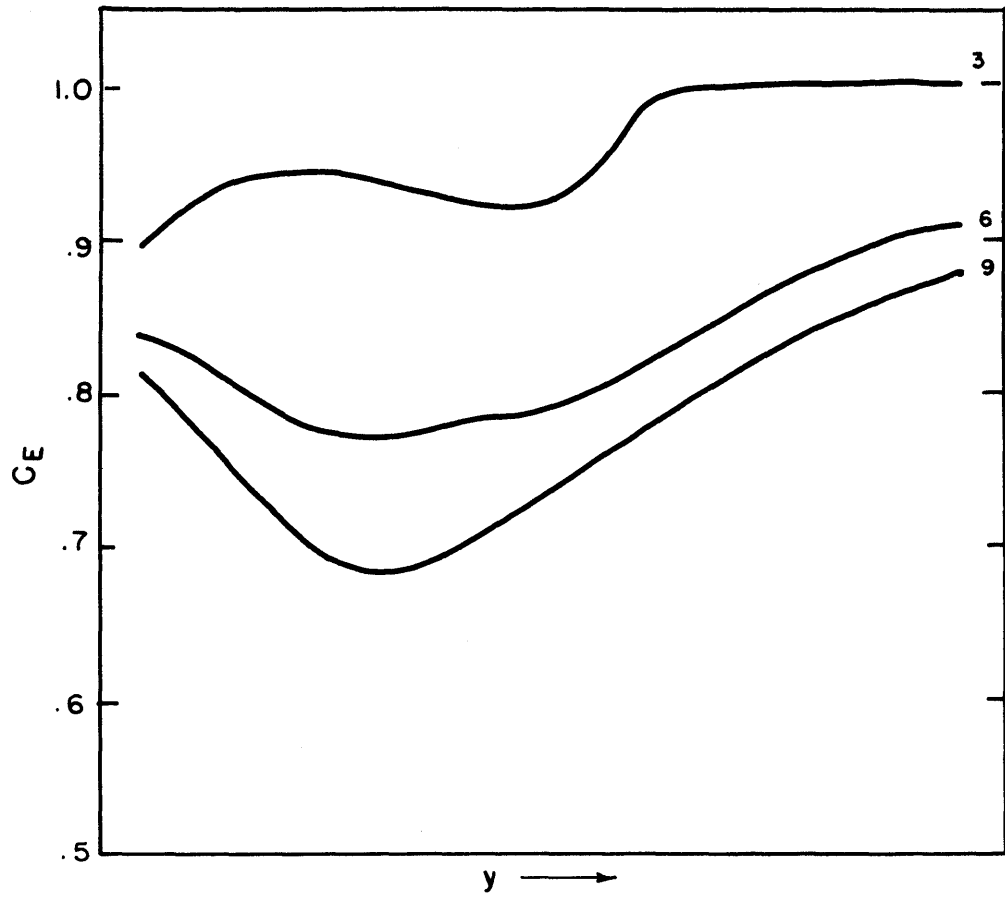


Figure 6.28b. Sensitivity of C_E to the equilibrium absolute meridional temperature gradient.

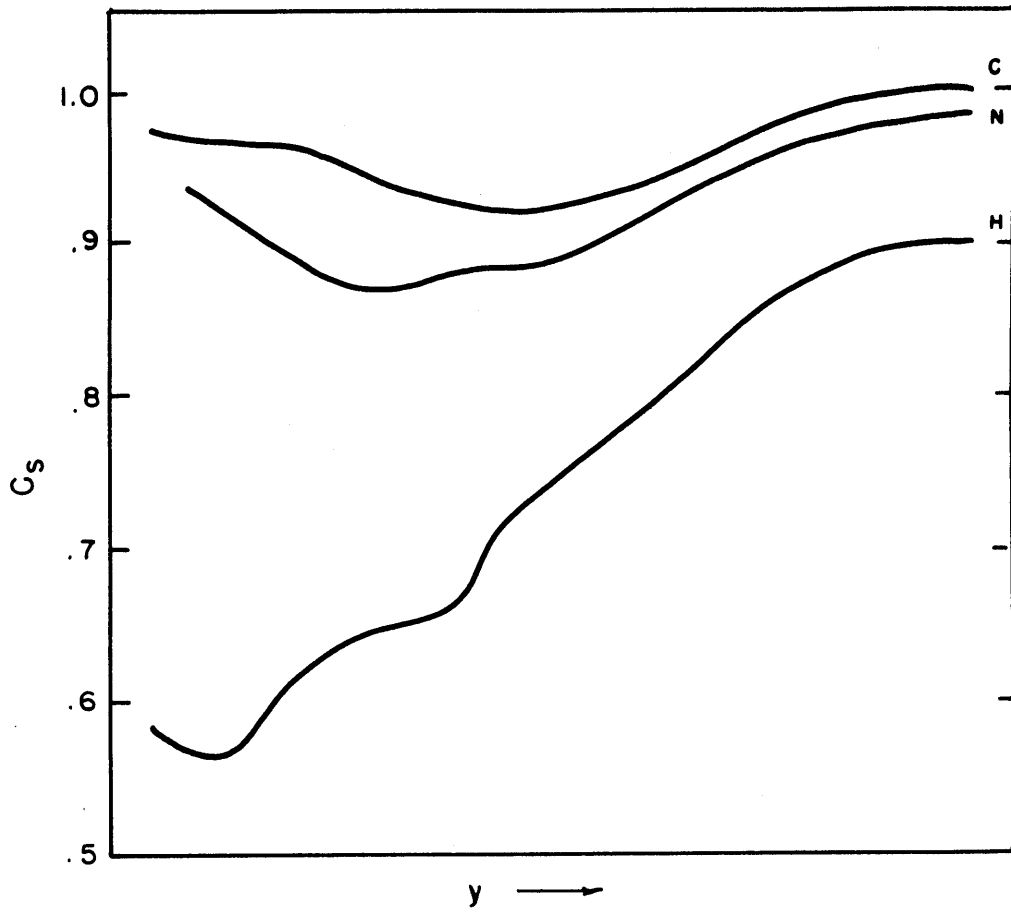


Figure 6.29a. Sensitivity of Sellers' cloud parameterization, C_s , to the equilibrium temperature.

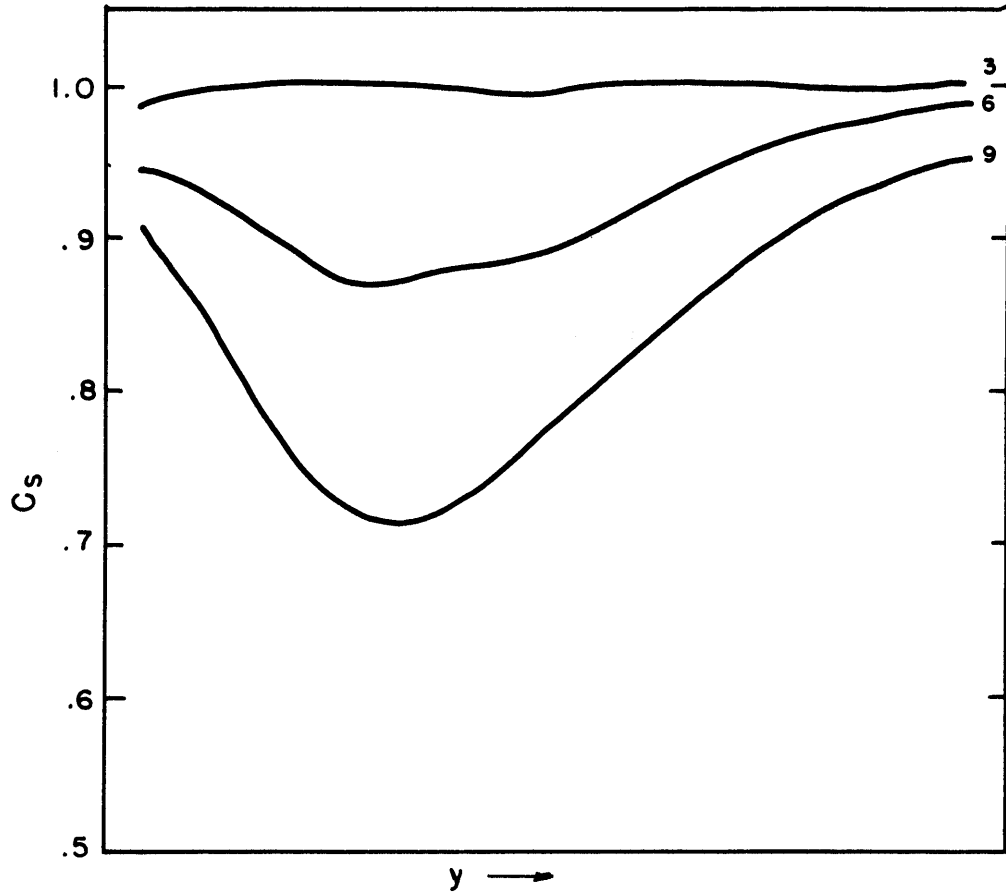


Figure 6.29b. Sensitivity of Sellers' cloud parameterization, C_s , to the equilibrium absolute meridional temperature gradient.

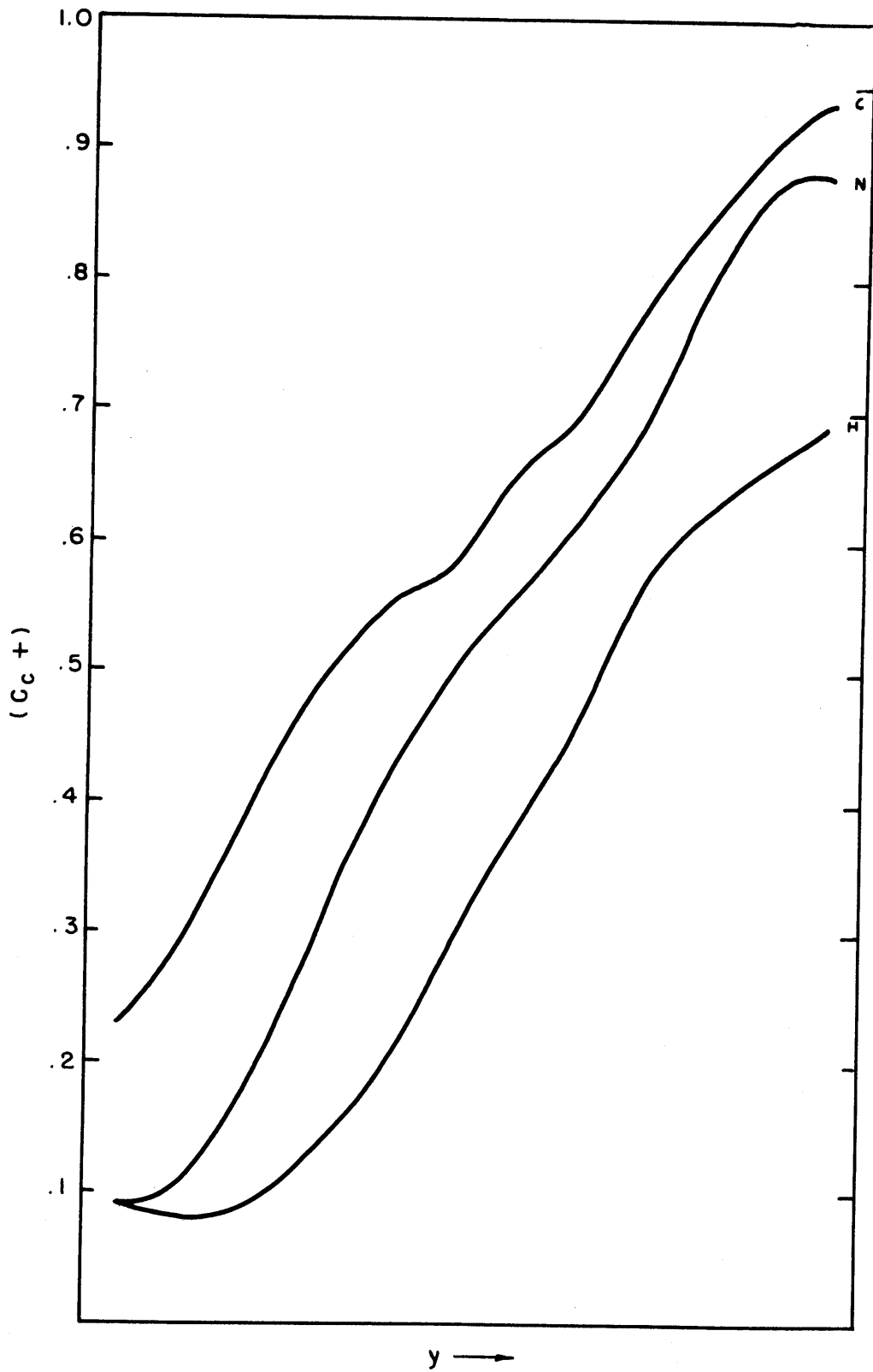


Figure 6.30a. Sensitivity of the fractional coverage of positive-condensation regions to the equilibrium temperature for the experiment with $\tau_2 = 5 \times 10^5 \text{sec}$.

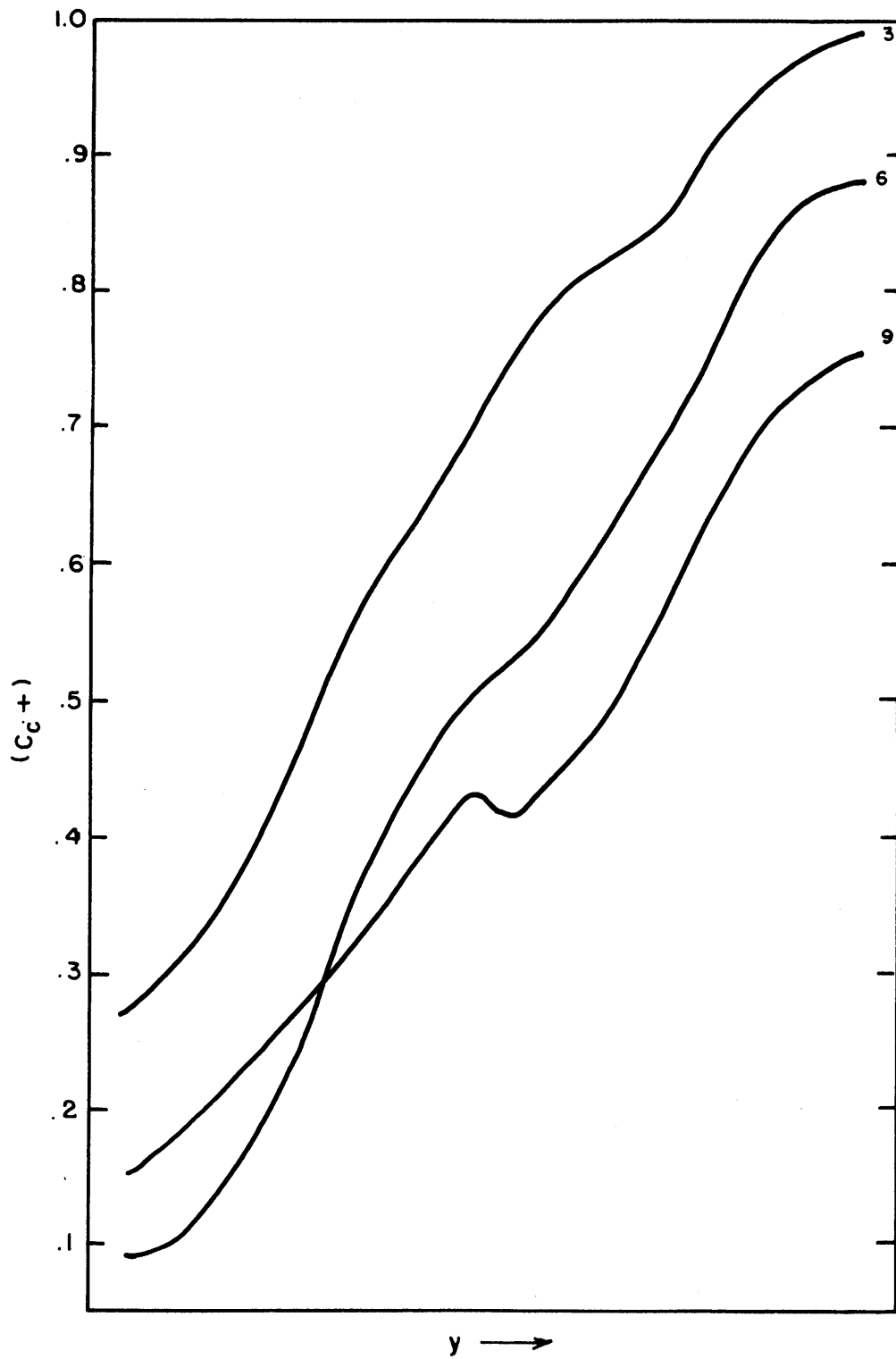


Figure 6.30b. Sensivity of the fractional coverage of positive-condensation regions to the equilibrium absolute meridional temperature gradient for the experiment with $\tau_2 = 5 \times 10^5 \text{sec}$.

7. Summary and Conclusions

In order to determine the sensitivity of an atmospheric hydrologic cycle to the equilibrium temperature, we constructed a numerical model with atmospheric-like behavior that was driven by differential Newtonian heating. The average equilibrium temperature (T_E) of the Newtonian heating was specified for one experiment to be 15° warmer than the T_E of the normal climate ($[T_g] = 280.$) experiment and was specified to be 15° colder in another experiment. These experiments were denoted the hot, normal, and cold climates respectively. Another set of experiments specified the equilibrium absolute meridional temperature gradient ($AMTG_E$) to either be larger by 3×10^{-8} deg cm^{-1} or smaller by 3×10^{-8} deg cm^{-1} than the normal climate - which had an $AMTG_E$ of 6×10^{-8} deg cm^{-1} .

Time-dependent numerical solutions to the primitive equations and equations for water vapor and cloud water were obtained on a self-contained, ocean-covered, mid-latitude two-level, parity-conserving, periodic f plane with sigma and Cartesian coordinates. The equations were integrated for 462.5 days; the last 150 days were time averaged in order to obtain the mean climate for each experiment. Leith's (1973) estimate of the standard deviation of a time average was calculated in order to ensure that various climatic differences were statistically significant.

The model temperatures equilibrated near the T_E of the Newtonian cooling law; however, they were larger on the average because of the latent heat of condensation. Except for the hot climate, the absolute meridional temperature gradient ($AMTG$) was less than the $AMTG_E$ because

of the transport of sensible heat plus potential energy from the southern regions to the northern regions. For the hot climate, enough latent heat was condensed in the southern regions to counteract this transport and the resultant temperature gradient was somewhat larger than the pre-set equilibrium temperature gradient. For the cold climate, the AMTG was less than the $AMTG_E$ but not quite as much as for the normal climate which had more condensation released in middle latitudes than in southern latitudes. Upon increasing the $AMTG_E$ the condensation increased in the southern latitudes but not more than the transport of sensible heat plus potential energy northward and hence the AMTG was less than the $AMTG_E$ but still increased with an increasing $AMTG_E$.

The zonal winds were geostrophically consistent with the AMTG - increasing with an increasing $AMTG_E$ and being largest for the hot climate and slightly larger for the cold climate than for the normal climate. The surface winds also followed the sensitivities of the upper level winds - increasing with an increasing $AMTG_E$ and being largest for the hot climate. On the average, the surface zonal winds were westerly in the computational domain; they were balanced globally by the surface easterlies in the antisymmetric domain and locally by convergence of westerly momentum, from the antisymmetric domain, at the lateral boundaries. A Ferrel circulation was also obtained. By conserving the parity of the dynamical solution on an f plane, we essentially isolated some of the qualitative features of the earth's temperate climatic regime.

Equations for the vertically averaged water vapor and cloud water along with parameterizations for evaporation, condensation, and

precipitation were formulated in terms of the water at the lower level and an ocean-covered surface. One part of the water budget not considered for this study was cloud water at the upper model level; another part not considered was the evaporation of precipitation and sedimenting cloud water in the boundary layer; and another part not considered was fractional cloudiness at one grid point - we discuss fractional cloudiness in terms of the fractional amount of the time that a fractional part of a latitude zone is either condensing or contains cloud water.

Corresponding to an increase of evaporation with an increasing T_E and $AMTG_E$, other water conversions also increased: dew deposition, water-vapor transport, positive condensation, convective condensation, cloud evaporation, cloud-water transport, and precipitation. The resulting equilibrium state had more water vapor content and the cloud water was greatly increased in the cloudy regions. Conversely, fractional coverage of positive-condensation regions, fractional coverage of cloud water, and the relative humidity decreased with increasing T_E and $AMTG_E$.

The increase in cloud-water content with an increasing T_E agreed with Weare and Snell (1974). The decrease in cloud fractional coverage and relative humidity agreed with Schneider and Washington (1973), with Cess (1976), and with Manabe and Wetherald's (1975) - Wetherald and Manabe's (1976) upper-level relative humidity. The quantitative decrease in cloudiness of roughly one percent per degree also agreed with Schneider and Washington and Cess. The decrease in cloudiness and corresponding increase in convective condensation agreed with Sellers' (1976) postulate

that an increase in temperature resulted in less supersaturation stratus-like clouds and more convective-like clouds with a net decrease in cloud area.

We determined that the decrease in cloud fractional coverage and relative humidity with increasing T_E and $AMTG_E$ was due to the increase in the atmospheric eddy subsidence which accompanied an increase in the upward motions (which was suggested by Wetherald and Manabe) along with an increase in the static stability. The slight decrease in the boundary layer temperature difference and the effect of the increased temperature also contributed. These tended to overwhelm the increase in: (1) the surface wind speed and concomitant increase in the turbulent transports; and (2) the increase in the radiative and sensible cooling.

We discussed the effects of horizontal advections on the cloud and relative humidity field by means of the entrainment parameter - so denoted because at the cloud boundary it described the entrainment of dry air. The detrainment of moist air from the cloud was negligible since the relative humidity was identically one everywhere within the cloudy region; only cloud water could be detrained. The parameter was also important in describing, in unsaturated regions, the horizontal advections of moist air into dry regions and advections of dry air into moist regions and, in cloudy regions, the horizontal re-arrangement of cloud water.

Although the entrainment parameter decreased with an increasing T_E and $AMTG_E$, the decrease in the relative humidity in the dry regions may have resulted in a relative entrainment increase. This was deduced

by comparing the decrease in the entrainment to the decrease in the ratio of the surface turbulent transport term to the atmospheric transport and adiabatic heating term. Nonetheless, the decrease in the entrainment parameter with an increasing T_E and $AMTG_E$ indicated that the clouds were becoming more closely associated with ascending motions and that clear skies were becoming more closely associated with descending motions.

Since the horizontal advections were of considerable importance in our numerical model, we did not obtain a good cloud parameterization neglecting them. However, upon eliminating explicit reference to the vertical velocity by substituting an analytical relationship between the vertical velocity and relative humidity, we obtained a better relationship. This is thought to be because the relative humidity is also affected by the transports. Use of the model relative humidity therefore incorporates, indirectly, the effects of the horizontal advections. The cloud formula derived in Chapter 4 had the same qualitative sensitivities as the model clouds - decreasing with increasing T_E and $AMTG_E$ - but Sellers' (1976) formula was shown to have a much better quantitative relationship.

Use of the relative humidity alone gives a fairly good representation of the cloud field although we caution against the use of one relative-humidity formula for all situations. Smagorinsky (1960) has shown that different relations exist between fractional cloud cover and relative humidity at different altitudes. We also showed analytically that simple models of the clouds and relative humidity required an additional parameter that described the intensity of boundary layer transports to

the intensity of atmospheric motions. Entrainment also affected the cloud and relative-humidity relationships. Essentially, cloud coverage had a direct relationship between the relative humidity for constant values of these other parameters. Hence in addition to Smagorinsky's relationships between fractional cloud cover and relative humidity at different altitudes, these other parameters suggest that the relationship may be latitude dependent and that convective clouds may have different relative-humidity and fractional-cloud-cover relationships than stratus clouds.

Although the evidence for a decrease in cloudiness with increasing T_E and $AMTG_E$ was strong for our model, Manabe and Wetherald (1975) and Wetherald and Manabe (1976) obtained an increase in relative humidity in the lower boundary layer (below 800 mb). If there had been model levels in the region where the surface turbulent transports are increasing and where, because of the lower boundary, the vertical velocities and static stabilities increase only negligibly, then we also probably would have obtained an increased relative humidity. Whether or not this would have also increased the fractional cloud cover is unclear since the relationship between the fractional cloud cover and relative humidity was shown to depend on other parameters. For example, for the same fractional cloud cover, increasing surface turbulent transports may correspond simply to an increasing H . The most direct method to resolve this question is to construct a model with more vertical resolution in the boundary layer and to calculate - at least - regions of positive condensation. One should also include some appropriate radiative and sensible heat parameterization more accurate than our Newtonian heating. It is important

to model the boundary layer accurately (I appreciate various comments by Professor Randall on this aspect) since Wetherald and Manabe have pointed out that an increase in low clouds may have more radiatively dominant effects than an equivalent decrease in upper layer cloudiness.

Since the cloud water content is increasing, the detrainment and fractional coverage at the upper level may be increased. Although this may be offset by the increased drying in the regions outside the clouds, the net effect is unknown until a calculation with moisture being carried at two or more levels is done.

The seasonal change of cloudiness that temperate latitudes would have is unclear since for both an increased AMTG and an increased temperature, the cloudiness and relative humidity decreased. A model with seasonal dynamics, that is, one which has both a changing AMTG and a changing temperature is needed to determine relative effects.

The effect of having a surface only partially covered by ocean and the effect of orography was not studied. The distribution of these features on the surface may have important effects and must be included in any model that wishes to predict climate sensitivities directly applicable to the earth.

The effect of the clouds on the local radiative and sensible heating can have an important influence on the equilibrium cloud cover. For example, upon changing the Newtonian time constant a qualitatively different meridional fractional cloud cover structure resulted. However, the average sensitivities remained the same.

The radiative feedbacks that this model would have on the equilibrium sea-surface temperatures if the cloud field were coupled to the radiation field are unclear. Cloud-water contents increase with an

increasing T_E and $AMTG_E$; hence more solar radiation would be reflected back to space. (See Neiburger, 1949, and Paltridge, 1974, for a discussion of cloud albedos.) The fractional coverage of the clouds are decreasing, however, and if the change in cloud albedo is small, more total solar radiation may be absorbed by the earth. Another possible positive feedback is the possible increase in cloud height (Schneider, 1972) due to moist convection. The cloud tops may emit at colder temperatures and accordingly the earth's surface and atmospheric temperature would have to increase in order to achieve planetary radiative equilibrium; on the other hand, the cloud tops may emit at warmer temperatures - in which case the feedback is negative. Another negative feedback is that a decrease in fractional cloud coverage would allow the infrared radiation from the lower and warmer regions of the atmosphere to escape to space more easily.

As was noted previously, a positive feedback need not necessarily destabilize an entire system if other negative feedbacks are also present. For example, if we assume that a change in cloud cover of 2% produces an average decrease in the surface temperature of $.5^\circ$ (Schneider, 1972) and that cloud cover varies less than 2% per degree change in surface temperature, then the decrease in cloudiness with increasing temperature would only amplify any temperature change due to some external cause by a factor less than two. (The strong negative feedback by the temperature overwhelms all other feedbacks.) This means that although climatic assessments, that assume fixed cloudiness, may have qualitatively correct conclusions, they may have quantitative underestimations of the surface temperature effects.

Whether or not clouds amplify or damp the change caused by some external forcing must await computations with a radiative-dynamical model. Cess (1976) suggested that the clouds' negative infrared feedbacks may be so strong that a change in cloud amount may result in little surface temperature change. However, Manabe (private communication) reports that the clouds in his newest model have a positive radiative feedback and noticeable effect on the surface temperature.

Because of the limitations in our small model, we conclude this thesis with the hope that some experiments have been suggested for a larger model.

APPENDIX A

SYMBOLS, SUBSCRIPTS AND OPERATORS

Capital Roman Symbols

- A : general dependent variable
- AMTG : absolute meridional temperature gradient
- AMTG_E : equilibrium absolute meridional temperature gradient
- B : $(C_{DDD}(q_\gamma - 1) - Qq_\alpha)/q_\beta - [\overline{\omega_2}]$
- C : cloud cover, fractional coverage
- C_D : surface drag coefficient = $\min[(1 + 7 \times 10^{-4} |v_s|)10^{-3}, 2.5 \times 10^{-3}]$
- C_{DD} : boundary layer drag coefficient = $C_D/[1 + C_D |v_s| \Delta p / (\rho_s g K)]$
- C_{DDD} : normalized boundary layer drag coefficient = $2C_{DD} g \rho_s |v_s| / P_s$
- C_E : estimated fractional cloud cover (see section 4.2.4)
- C_P : dry air heat capacity at constant pressure, $9.96 \times 10^6 \text{ ergs g}^{-1} \text{ deg}^{-1}$
- C_S : Sellers' (1976) cloud formula
- \dot{C}_{vc} : conversion from vapor to cloud, sec^{-1}
- \dot{C}^+ : positive condensation, sec^{-1}
- \dot{C}^- : negative condensation or cloud evaporation, sec^{-1}
- $\dot{C}\dot{C}$: convective condensation, $\text{g cm}^{-2} \text{ sec}^{-1}$
- E : evaporation, $\text{g cm}^{-1} \text{ sec}^{-2}$
- F_{qi} : flux of water substance, $\text{g cm}^{-2} \text{ sec}^{-1}$
- F_x : frictional force in x direction, cm sec^{-2}

- F_y : frictional force in y direction, cmsec^{-2}
- H : relative humidity
- IM : number of zonal grid points in computational domain
- JM : number of meridional grid points in computational domain
- K : eddy diffusion coefficient in turbulent boundary layer =
 $100|\bar{v}_s| \text{cm}^2 \text{sec}^{-1}$
- L : latent heat of evaporation - condensation, $2.5 \times 10^{10} \text{ ergs g}^{-1}$
- \dot{P} : precipitation, sec^{-1}
- P_c : precipitation, $\text{g cm}^{-2} \text{sec}^{-1}$
- \dot{Q} : diabatic and moist convective heating, $\text{ergs g}^{-1} \text{sec}^{-1}$
- \dot{Q}_c : moist convective heating
- Q : \dot{Q}/C_p , degsec^{-1}
- R : dry air gas constant, $2.87 \times 10^6 \text{ ergs g}^{-1} \text{deg}^{-1}$
- S : lower level static stability, $\frac{1}{2}(\frac{\partial T}{\partial p} + \frac{RT_2}{C_p P_2})$, $\text{deg cm g}^{-1} \text{sec}^2$
- T : temperature, deg
- T_E : radiative-sensible heating equilibrium temperature
- TKE : total kinetic energy, gsec^{-2}
- TPE : total potential energy, gsec^{-2}
- X : east-west domain length, cm
- Y : north-south domain length, cm
- W : amplitude of eddy vertical velocity, $\text{g cm}^{-1} \text{sec}^{-3}$

Capital Greek Symbols

Δ : horizontal difference, cm

Δt : time difference, sec

Δh : $h_2 - h_1$

Δx : east-west difference, cm

Δy : north-south difference, cm

$\Delta \sigma$: sigma difference

Φ : geopotential, $\text{cm}^2 \text{sec}^{-2}$

Ψ_m : symmetric-circulation stream function (y, σ)

Lower-Case Roman Symbols

a_n : part of precipitation function

e : vapor pressure, mb, or exponential

f : coriolis parameter, $1.01 \times 10^{-4} \text{sec}^{-1}$

g : gravitational acceleration, 981 cm sec^{-2}

h : moist static energy, $C_p T + gz + Lq_v$

j : meridional index

k : vertical level indicator

\hat{k} : average zonal wave number of vertical velocity or vertical unit vector

n : time index

p : pressure, $\text{g cm}^{-1} \text{sec}^{-1}$

p_s : surface pressure, $\text{g cm}^{-1} \text{sec}^{-1}$

q_i : water component mixing ratio

q_c : cloud-water mixing ratio

q_p : precipitation mixing ratio

q_α : $\frac{\partial}{\partial T} \ln(q_{v,2}^*)$

q_β : $(\frac{1}{\Delta p} + S q_\alpha)$

q_γ : $q_{v,g}^* / q_{v,2}^*$

q_δ : $(\frac{1}{q_{v,2}^*} + \frac{L}{C_p} q_\alpha)$

s : dry static energy, $C_p T + gz$

\hat{s} : phase speed of zonally propagating vertical-velocity wave

t : time, sec

- u : zonal velocity, cm sec⁻¹
- v : meridional velocity, cm sec⁻¹
- χ : horizontal vector velocity, cm sec⁻¹
- x : east-west direction, cm
- x_n : precipitation function exponent
- y : north-south direction, cm
- z : vertical direction, cm

Lower-Case Greek Symbols

- α : coefficient of smoothing operator, $\text{cm}^4\text{sec}^{-1}$
- α_n : part of precipitation function \dot{P}_1 , sec^{-1}
- δ : finite difference or conditional quantity (See text for relevant details.)
- γ : $1 + \frac{L}{C_p} \frac{\partial q_{v,2}^*}{\partial T}$
- ϵ : entrainment parameter = $\hat{k}(u-\hat{s})/Wq_\beta$
- ζ : generalized horizontal coordinate
- η : relative-humidity parameter, $C_{DDD}q_\gamma/Wq_\beta$
- π : ratio of circumference to diameter of circle
- ρ : atmospheric density, g cm^{-3}
- ρ_0 : atmospheric density at standard temperature and pressure
- σ : pressure divided by surface pressure, vertical coordinate
- $\dot{\sigma}$: $\frac{d\sigma}{dt}$, sec^{-1}
- τ_E : Newtonian time constant, sec
- τ_p : precipitation time constant, sec
- τ_A : upper-level shear stress
- τ_s : surface stress
- ω : $ps\dot{\sigma}$
- ω_1 : $\frac{\omega}{2} + \sigma_1 \left(\frac{\partial p_s}{\partial t} + \underset{\sim}{v}_1 \cdot \nabla p_s \right)$
- ω_2 : $\frac{\omega}{2} + \sigma_2 \left(\frac{\partial p_s}{\partial t} + \underset{\sim}{v}_2 \cdot \nabla p_s \right)$

SUBSCRIPTS

- 1 : level, $\sigma = .25$, $p \sim 2.5 \times 10^5 \text{ g cm}^{-1} \text{ sec}^{-2}$
- 3/2 : level 3/2, $\sigma = .5$
- 2 : level 2, $\sigma = .75$
- c : pertaining to cloud
- g : in the surface layer
- i : water component
- k : general height coordinate
- n : component of precipitation function
- p : precipitation
- q_i : pertaining to a water component
- s : surface layer at anemometer level
- v : vapor
- x : in x direction
- y : in y direction
- E : present equilibrium value
- σ : in σ direction

OPERATORS

$$\overline{(A)} : \int_0^T (A) \frac{dt}{T} \quad : \text{time average}$$

$$\{(A)\} : \int_0^1 (A) \rho_s \frac{ds}{g} \quad : \text{mass-weighted average}$$

$$[(A)] : \int_0^x (A) \frac{dx}{x} \quad : \text{zonal average}$$

$$(\tilde{A}_x) : \int_0^Y (A_x) \frac{dy}{Y} \quad : \text{meridional average}$$

$$[[A]] : [(\tilde{A})] \quad : \text{areal average}$$

$$C_s : \int_0^x \delta(s > 0) \frac{dx}{x} \quad : \text{fractional coverage}$$

$$\{ \overline{(A)} \} : \int_0^T \int_0^x \delta(s > 0) (A) \frac{dx}{x} \frac{dt}{T} \quad : \text{fractional-coverage weighted average}$$

$$(A)^* : (A) - [(A)] \quad : \text{eddy}$$

or

or

APPENDIX B

PARITY BUDGET

In section 2.3 we showed that, for an atmospheric-like dynamical system, odd parity in the stream function was not conserved whereas even parity was conserved. From physical considerations we also know that surface pressure, temperature, and moisture must have, at least, predominantly even parity; since we wish to obtain a system of equations that exactly conserves the parity of the solution, we allow these variables to have only even parity and determine if a conservative system can be found using the following relations

$$A^{\bar{}}(x, y) = \bar{f} A(-x, -y), \quad (\text{B.1a})$$

where

$$A = A^+ + A^-. \quad (\text{B.1b})$$

The parity relationships are as follows:

Tendency

$$\frac{\partial p_s^+}{\partial t} = -\nabla \cdot p_s^+ \int_0^1 \chi^- d\sigma \quad (\text{B.2})$$

Continuity

$$\dot{\sigma} \bar{f} = (\sigma \nabla \cdot p_s^+ \int_0^1 \chi^+ d\sigma - \nabla \cdot p_s^+ \int_0^{\sigma} \chi^+ d\sigma) / p_s^+ \quad (\text{B.3})$$

ω

$$\omega^{\pm} = p_s^{\pm} \dot{\sigma}^{\pm} - \sigma \left\{ \nabla \cdot p_s^{\pm} \int_0^1 \chi^{\pm} d\sigma - v^{\pm} \cdot \nabla p_s^{\pm} \right\} \quad (\text{B.4})$$

Zonal momentum

$$\begin{aligned} \frac{\partial}{\partial t} p_s u^- &= -\nabla \cdot p_s^+ \chi^- u^- - \frac{\partial}{\partial \sigma} p_s^+ \dot{\sigma}^+ u^- + f p_s^+ v^- - \\ &\quad -\nabla \cdot p_s^+ \chi^+ u^+ - \frac{\partial}{\partial \sigma} p_s^+ \dot{\sigma}^- u^+ - p_s^+ F_x^- - \\ &\quad - R \frac{\partial}{\partial x} p_s^+ T^+ - \frac{\partial}{\partial \sigma} p_s^+ \sigma \frac{\partial \Phi^+}{\partial x} \end{aligned} \quad (\text{B.5})$$

Meridional momentum

$$\begin{aligned} \frac{\partial}{\partial t} p_s v^- &= -\nabla \cdot p_s^+ \chi^- v^- - \frac{\partial}{\partial \sigma} p_s^+ \dot{\sigma}^+ v^- - f p_s^+ u^- - \\ &\quad -\nabla \cdot p_s^+ \chi^+ v^+ - \frac{\partial}{\partial \sigma} p_s^+ \dot{\sigma}^- u^+ - p_s^+ F_y^- - \\ &\quad - R \frac{\partial}{\partial y} p_s^+ T^+ - \frac{\partial}{\partial \sigma} p_s^+ \sigma \frac{\partial \Phi^+}{\partial y} \end{aligned} \quad (\text{B.6})$$

Thermodynamic

$$\begin{aligned} \frac{\partial}{\partial t} p_s T^+ &= -\nabla \cdot p_s^+ \chi^- T^+ - \frac{\partial}{\partial \sigma} p_s^+ \dot{\sigma}^+ T^+ + \frac{\omega^+ R T^+}{C_p \sigma} + \\ &\quad + p_s^+ \frac{\dot{Q}^+}{C_p} + \frac{L}{C_p} p_s^+ \dot{C}_{vc}^+ \end{aligned} \quad (\text{B.7})$$

Water

$$\frac{\partial}{\partial t} p_s^+ q_{i,2}^+ = - \nabla \cdot p_s^+ \underline{V}_s^- q_{i,2}^+ - p_s^+ \sum \dot{C}_{i,j,2}^+ + \quad (B.8)$$

$$+ g \frac{\partial}{\partial \sigma} (F_{q_i}^+ + p^+ \nabla_i^+ q_i^+)$$

Hydrostatic

$$\frac{\partial \Phi^+}{\partial \sigma} = - \frac{RT^+}{\sigma} . \quad (B.9)$$

The only possible dynamical system that conserves parity consists of odd parity for the horizontal velocity vector and even parity for all other components. It may be shown that if odd parity for these latter components was physically possible, a parity conserving system could not be found; the above parity arrangement is the only conservative system possible for an f plane.

APPENDIX C

FINITE DIFFERENCE BUDGETS

In the numerical model, a longitudinal point in the computational domain is represented by i with $2 < i < IM1$. $i=1$ refers to the westernmost point - just outside the boundary - and $i=IM2$ refers to the easternmost point - just outside the boundary. A meridional point is represented by j with $2 < j < JM1$. $j=1$ refers to the southernmost point - just outside the boundary - and $j=JM2$ refers to the northernmost point just outside the boundary (see figure 2.5b). For ease in notation we use $A_{i,j} = A^n(i,j,k)$ where the vertical and time indices are understood.

Following Kurihara and Holloway (1967), the total-energy equation of the moist-adiabatic equations integrated over the domain is

$$\frac{d}{dt} \sum_{i=2}^{IM1} \sum_{j=2}^{JM1} \sum_{k=1}^2 p_{s,i,j} \left(C_v T_{i,j} + g z_{i,j} + L q_{v,i,j} + \frac{u_{i,j}^2}{2} + \frac{v_{i,j}^2}{2} \right) \frac{\Delta \sigma}{g} = \quad (C.1)$$

$$\begin{aligned}
 &= \frac{\Delta \sigma}{8g\Delta x} \sum_{j=2}^{JM1} \sum_{k=1}^2 (P_{s,1,j} + P_{s,2,j}) \left\{ \left[(u_{1,j} + u_{2,j}) \times \right. \right. \\
 &\quad \times \left(C_p (T_{1,j} + T_{2,j}) + L (q_{1,j} + q_{2,j}) + \right. \\
 &\quad \left. \left. \frac{(u_{1,j} u_{2,j} + v_{1,j} v_{2,j})}{2} \right) \right] + \\
 &\quad \left. + 2 (\phi_{1,j} u_{2,j} + \phi_{2,j} u_{1,j}) \right\}
 \end{aligned}$$

$$\begin{aligned}
 &- \frac{\Delta \sigma}{8g\Delta x} \sum_{j=2}^{JM1} \sum_{k=1}^2 (P_{s,IM1,j} + P_{s,IM2,j}) \left\{ \left[(u_{IM1,j} + u_{IM2,j}) \times \right. \right. \\
 &\quad \times \left(C_p (T_{IM1,j} + T_{IM2,j}) + L (q_{IM1,j} + q_{IM2,j}) + \right. \\
 &\quad \left. \left. \frac{(u_{IM1,j} u_{IM2,j} + v_{IM1,j} v_{IM2,j})}{2} \right) \right] + \\
 &\quad \left. + 2 (\phi_{IM1,j} u_{IM2,j} + \phi_{IM2,j} u_{IM1,j}) \right\}
 \end{aligned}$$

$$\begin{aligned}
 & + \frac{\Delta \sigma}{\delta q \Delta y} \sum_{i=2}^{IM1} \sum_{k=1}^2 (P_{S,i,1} + P_{S,i,2}) \left\{ \left[(v_{i,1} + v_{i,2}) \times \right. \right. \\
 & \quad \times (C_p (T_{i,1} + T_{i,2}) + L (q_{v,i,1} + q_{v,i,2}) + \\
 & \quad \left. \left. + \frac{(u_{i,1} u_{i,2} + v_{i,1} v_{i,2})}{2} \right) \right] + \\
 & \quad \left. + 2 (\Phi_{i,1} v_{i,2} + \Phi_{i,2} v_{i,1}) \right\}
 \end{aligned}$$

$$\begin{aligned}
 & - \frac{\Delta \sigma}{\delta q \Delta y} \sum_{i=2}^{IM1} \sum_{k=1}^2 (P_{S,i,IM1} + P_{S,i,IM2}) \left\{ \left[(v_{i,IM1} + v_{i,IM2}) \times \right. \right. \\
 & \quad \times (C_p (T_{i,IM1} + T_{i,IM2}) + L (q_{v,i,IM1} + q_{v,i,IM2}) + \\
 & \quad \left. \left. + \frac{(u_{i,IM1} u_{i,IM2} + v_{i,IM1} v_{i,IM2})}{2} \right) \right] + \\
 & \quad \left. + 2 (\Phi_{i,IM1} v_{i,IM2} + \Phi_{i,IM2} v_{i,IM1}) \right\} .
 \end{aligned}$$

The first and second sums on the right hand side of C.1 represent the values at the west-east boundaries. For any variable, the following periodic conditions hold ;

$$A_{1,j} = A_{IM1,j} \quad (C.2a)$$

and

$$A_{2,j} = A_{IM2,j} . \quad (C.2b)$$

Each component in the first sum on the right hand side of C.1 has a negative counterpart; hence the first and second sums vanish. The periodic boundary conditions ensure that whatever leaves or enters on one longitudinal side enters or leaves on the other longitudinal side.

Using the parity relationships in the equations - imposed by the boundary conditions - we show that the third and fourth sums on the right hand side of C.1 vanish at the northern and southern boundaries separately. Consider the southern wall, the parity boundary conditions give

$$A_{i,1}^{\bar{}} = \mp A_{IM2-i,2}^{\bar{}} . \quad (C.3)$$

That is, there is a counterpart equidistant on the other side of a longitudinal midpoint and on the other side of the boundary that is equal in absolute magnitude but, depending on the symmetry of the variable (odd for the horizontal velocity components and even for everything else) negative or positive. Products of variables on either side of the boundary have the following relationships

$$A_{i,1}^{\bar{}} B_{i,2}^{\pm} = \mp A_{IM2-i,2}^{\bar{}} B_{IM2-i,1}^{\pm} \quad (C.4a)$$

and

$$A_{i,1}^{\bar{}} B_{i,2}^{\mp} = \pm A_{IM2-i,2}^{\bar{}} B_{IM2-i,1}^{\mp} . \quad (C.4b)$$

Summing from $i=2$ to $i=IM1$,

$$\sum_{\lambda} A^{\bar{\lambda},1} B^{\lambda,2} = \mp \sum A^{\bar{\lambda},2} B^{\lambda,1}, \quad (C.5a)$$

$$\sum_{\lambda} A^{\bar{\lambda},1} B^{\bar{\lambda},2} = \pm \sum A^{\bar{\lambda},2} B^{\bar{\lambda},1}, \quad (C.5b)$$

$$\sum_{\lambda} (A^{\bar{\lambda},1} + A^{\bar{\lambda},2}) (B^{\lambda,1} + B^{\lambda,2}) = 0, \quad (C.5c)$$

$$\sum (A^{\bar{\lambda},1} + A^{\bar{\lambda},2}) (B^{\lambda,1} + B^{\lambda,2})^n = 0, \quad (C.5d)$$

and

$$\sum (A^{\bar{\lambda},1} B^{\lambda,2} + A^{\bar{\lambda},2} B^{\lambda,1}) (C^{\lambda,1} + C^{\lambda,2}) = 0. \quad (C.5e)$$

In particular, any sum of even parity components multiplied by $(v_{i,1} + v_{i,2})$ and summed from $i=2$ to $i=IM1$ vanishes. The term $(\phi_{i,1} v_{i,2} + \phi_{i,2} v_{i,1})$ also vanishes when summed. Since the same occurs for the northern boundary, the total energy transport into or out of the domain is identically zero.

For the surface-pressure or, equivalently, mass-conservation equation (using the longitudinal periodicity)

$$\frac{\partial}{\partial t} \sum_{\lambda} \sum_j P_{s,\lambda,j} = \frac{\Delta \sigma}{4g\sigma} \sum_j \sum_k (P_{s,\lambda,1} + P_{s,\lambda,2}) (V_{\lambda,1} + V_{\lambda,2}) \quad (C.6)$$

$$- \frac{\Delta \sigma}{4g\sigma} \sum_j \sum_k (P_{s,\lambda,IM1} + P_{s,\lambda,IM2}) (V_{\lambda,IM1} + V_{\lambda,IM2}).$$

The sums on the right hand side vanish because of the meridional velocities.

The parity conditions ensure that the amount of mass and energy that leave or enter on one side of a midpoint of the x-axis at a lateral boundary must have the same amount enter or leave on the other side of the midpoint of the same lateral boundary.

For the zonal momentum (for a frictionless atmosphere) using the longitudinal periodic boundary conditions,

$$\begin{aligned}
 \frac{\partial}{\partial t} \sum_i \sum_j \sum_k p_{s,i,j} u_{i,j} \frac{\Delta\sigma}{g} &= \tag{C.7} \\
 &= \beta \frac{\Delta\sigma}{g} \sum_i \sum_j \sum_k p_{s,i,j} v_{i,j} + \\
 &+ \frac{\Delta\sigma}{8g\Delta y} \sum_i \sum_k (p_{s,i,1} + p_{s,i,2})(v_{i,1} + v_{i,2})(u_{i,1} + u_{i,2}) \\
 &- \frac{\Delta\sigma}{8g\Delta y} \sum_i \sum_k (p_{s,i,jm1} + p_{s,i,jm2})(v_{i,jm1} + v_{i,jm2})(u_{i,jm1} + u_{i,jm2}).
 \end{aligned}$$

The second and third sums on the right hand side of C.7 do not vanish because both u and v have odd parity. The zonal momentum is not conserved within the computational domain at a specific time. If we

consider both the computational domain and its antisymmetric counterpart, however, then zonal momentum in both domains is conserved because the northern (southern) boundary of the computational domain is periodic with the southern (northern) boundary of the antisymmetric domain.

REFERENCES

- Abramowitz, M., and I. A. Stegun, 1964: Handbook of Mathematical Functions. New York, Dover Publications, 1046 pp.
- Arakawa, A., Y. Minty and collaborators, 1974: The UCLA Atmospheric General Circulation Model. Department of Meteorology, UCLA, Los Angeles. [Available from the author at the Department of Meteorology, Los Angeles 90024.]
- Budyko, M. I., 1969: The effect of solar radiation on the climate of the earth. Tellus, 21, 611-619.
- Cess, R. D., 1976: Climate change: An appraisal of atmospheric feedback mechanisms employing zonal climatology. J. Atmos. Sci., 33, 1831-1843.
- Chervin, R. M. and S. H. Schneider, 1976a: A study of the response of NCAR GCM climatological statistics to random perturbations: Estimating noise levels. J. Atmos. Sci., 33, 391-404.
- 1976: On determining the statistical significance of climate experiments with general circulation models. J. Atmos. Sci., 33, 405-412.
- Clapp, P. F., 1964: Global cloud cover for seasons using TIROS nephelometry. Mon. Wea. Rev., 92, 495-507.
- Cunnold, D., F. Alyea, N. Phillips and R. Prinn, 1975: A three-dimensional dynamical-chemical model of atmospheric ozone. J. Atmos. Sci., 32, 170-194.
- Gates, W. L., E. S. Batten, A. B. Kahle, and A. B. Nelson, 1971: A Documentation of the Minty-Arakawa Two-Level Atmospheric General Circulation Model. R-877-ARPA, Rand. [Available from Communications Department, Rand, 1700 Main Street, Santa Monica, CA 90406.]
- Gierasch, P. and R. Goody, 1970: Models of the Venus Clouds. J. Atmos. Sci., 27, 224-245.
- Kasahara, A., and W. M. Washington, 1971: General circulation experiments with a six-layer NCAR model, including orography cloudiness and surface temperature calculations. J. Atmos. Sci., 28, 657-701.
- Kessler, E., 1969: On the distribution and continuity of water substance in atmospheric circulations. J. Atmos. Sci., 28, 657-701.
- Herman, G. and R. Goody, 1976: Formation and persistence of summertime arctic stratus clouds. J. Atmos. Sci., 33, 1537-1553.
- Kraus, E. B., 1973: Comparison between ice age and present general circulations. Nature, 245, 129-133.

- Kurahara, Y., and J. L. Holloway, Jr., 1967: Numerical integration of a nine-level global primitive equations model formulated by the box method. Mon. Wea. Rev., 95, 509-530.
- Landsburg, H. E., 1945: Climatology, Section XII in Handbook of Meteorology. McGraw-Hill, New York, pp. 928-997.
- Leith, C. E., 1973: The standard error of time-average estimates of climatic means. J. Appl. Meteor., 12, 1066-1069.
- London, J., 1957: A study of the atmospheric heat balance. Report, Contract AF 19(122)-165, College of Engineering, New York University. [Available from NTIS.]
- and T. Sasamori, 1971: Radiative energy budget of the atmosphere. Space Res., 11, 639.
- Lorenz, E. N., 1970: Climatic change as a mathematical problem. J. Appl. Meteor., 9, 325-329.
- 1967: The nature and theory of the general circulation. World Meteor. Org.,
- Manabe, S., and F. Möller, 1961: On the radiative equilibrium and heat balance of the atmosphere. Mon. Wea. Rev., 89, 503-532.
- and J. Smagorinsky, J. L. Holloway, and H. M. Stone, 1970: Simulated climatology of a general circulation model with a hydrologic cycle. III. Effects of increased horizontal computational resolution. Mon. Wea. Rev., 98, 175-212.
- , J. Smagorinsky, and R. S. Strickler, 1965: Simulated climatology of a general circulation model with a hydrologic cycle. Mon. Wea. Rev., 93, 769-797.
- and R. F. Strickler, 1964: Thermal equilibrium of the atmosphere with a convective adjustment. J. Atmos. Sci., 21, 361-385.
- and R. T. Wetherald, 1967: Thermal equilibrium of the atmosphere with a given distribution of relative humidity. J. Atmos. Sci., 24, 241-259.
- and ———, 1975: The effects of doubling the CO₂ concentration on the climate of a general circulation model. J. Atmos. Sci., 32, 3-15.
- Marchuk, G. I., 1974: Numerical Methods in Weather Prediction. Academic Press, New York, 277 pp.
- Marshall, J. S. and W. McK. Palmer, 1948: The distribution of raindrops with size. J. Meteor., 5, 1965-1966.

- Miller, D. B. and R. G. Feddes, 1971: Global atlas of relative cloud cover 1967-1970. Joint production by U. S. Dept. of Commerce and U. S. Air Force, Washington, D. C. [Available from NTIS, Springfield, Va. Ap 739 734.]
- Neiburger, U., 1949: Reflection, absorption and transmission of insolation. J. Meteor., 6, 98-104.
- Oort, A. H. and E. M. Rasmusson, 1971: Atmospheric circulation statistics. NOAA professional paper 5. [For sale by the Superintendent of Documents, U. S. Government Printing Office, Washington, D. C. 20402. Price - \$3.00 (paper cover). Stock Number 0317-0045.]
- Newell, R. E., J. W. Kidson, D. G. Vincent and G. J. Boer, 1974: The General Circulation of the Tropical Atmosphere and Interactions with Extratropical Latitudes, Vol. 2. MIT Press, Cambridge, MA, 371 pp.
- Nitta, T. and Y. Ogura, 1972: Numerical simulation of the development of the intermediate-scale cyclone in a moist model atmosphere. J. Atmos. Sci., 29, 1011-1024.
- Paltridge, G. W., 1974: Infrared emissivity, shortwave albedo and the microphysics of stratiform water clouds. J. Geophys. Res., 79, 4053-4058.
- Phillips, N. A., 1957: A coordinate system having some special advantages for numerical forecasting. J. Meteor., 12, 184-185.
- , 1956: The general circulation of the atmosphere: A numerical experiment. Quart. J. Roy. Meteor. Soc., 82, 123-164.
- Sasamori, T., 1975: A statistical model for stationary atmospheric cloudiness, liquid water content and rate of precipitation. Mon. Wea. Rev., 103, 1037-1049.
- Saxon, D. S., 1968: Elementary Quantum Mechanics. Holden-Day, Inc., San Francisco, CA, 426 pp.
- Schneider, S. H., 1972: Cloudiness as a global climatic feedback mechanism: The effects on the radiation balance and surface temperature of variations in cloudiness. J. Atmos. Sci., 29, 1413-1422.
- and R. E. Dickinson, 1974: Climate modeling. Rev. Geophys. Space Phys., 12, 447-493.
- and W. M. Washington, 1973: Cloudiness as a global feedback mechanism. Bull. Amer. Meteor. Soc., 54, p. 742.

- Schutz, C., and W. L. Gates, 1971: Global Climatic Data for Surface, 800 mb, 400 mb: January. R-915 - ARPA, The Rand Corporation, Santa Monica, CA, 180 pp. [Available from The Rand Corporation.]
- and ———, 1972: Global Climatic Data for Surface, 800 mb, 400 mb: July. R-1029 - ARPA, The Rand Corporation, Santa Monica, CA, 180 pp, [Available from The Rand Corporation.]
- Sellers, W. D., 1976: A two-dimensional global climatic model. Mon. Wea. Rev., 104, 233-248.
- Shapiro, R., 1970: Smoothing, filtering and boundary effects. Rev. Geophys. Space Phys., 8, 359-387.
- Shukla, J., 1975: Effect of Arabian sea-surface temperature anomaly on Indian summer monsoon: A numerical experiment. J. Atmos. Sci., 32, 503-511.
- , 1976: On the Dynamics of Monsoon Disturbances. Ph.D. dissertation, Mass. Inst. Tech., 178 pp.
- Shuman, F. G., 1962: Numerical experiments with the primitive equations. Proc. Int. Symp. Num. Wea. Pred., Tokyo, 1960, Meteor. Soc. Japan, 85-107.
- Simpson, J. and V. Wiggert, 1969: Models of precipitating cumulus towers, Mon. Wea. Rev., 97, 471-499.
- Smagorinsky, J., 1960: On the dynamical prediction of large scale condensation by numerical methods. Phys. Precip., Geophys. Mono., 5, Amer. Geophys. Un., 71-78.
- Stommel, H., 1947: Entrainment of air into a cumulus cloud. J. Meteor., 4, 91-94.
- Wetherald, R. T. and S. Manabe, 1975: The effect of changing the solar constant on the climate of a general circulation model. J. Atmos. Sci., 32, 2044-2059.
- Weare, B. C. and F. Snell, 1974: A diffuse thin cloud atmospheric structure as a feedback mechanism in global climate modeling. J. Atmos. Sci., 31, 1725-1734.

BIOGRAPHY

Born in Boulder, CO to Paul C. and Grace D. Roads January 20, 1950

Raised in Lafayette, CO with my brother Paul and my
sisters Nancy, Cynthia, Marilyn, Carol 1950-1968

Awarded Boettcher Scholarship 1968-1972

Attended University of Colorado 1968-1972

Worked at NCAR 1970-1972

Married Anastasia S. Booras August 22, 1970

Inducted into Phi Beta Kappa 1971

Received B.A. in Physics (with distinction) 1972

Awarded NSF Graduate Fellowship 1972-1975

UCAR Fellowship designee 1972

Began graduate work at MIT 1972

Became student member of the AMS 1972

MIT Graduate Student Council Representative 1974-1975

Research Assistant 1975-1977